Transmissiegebaseerde attenuatiecorrectie voor 'time-of-flight'-positronemissie-tomografie

Transmission-Based Attenuation Correction for Time-of-Flight Positron Emission Tomography

Pieter Mollet

Promotoren: prof. dr. S. Vandenberghe, dr. ir. V. Keereman
Proefschrift ingediend tot het behalen van de graad van
Doctor in de Ingenieurswetenschappen: Biomedische Ingenieurstechnieken

Vakgroep Elektronica en Informatiesystemen
Voorzitter: prof. dr. ir. J. Van Campenhout
Faculteit Ingenieurswetenschappen en Architectuur
Academiejaar 2013 - 2014

UNIVERSITEIT
GENT

ISBN 978-90-8578-666-5
NUR 954
Wettelijk depot: D/2014/10.500/12

Department of Electronics and Information Systems
Faculty of Engineering and Architecture
Ghent University

MEDISIP
IBiTech - iMinds
Campus Heymans, Block B
De Pintelaan 185
9000 Ghent
Belgium

Promotors:
Prof. dr. Stefaan Vandenberghe
Dr. ir. Vincent Keereman

Board of examiners:
Prof. dr. ir. Jan Van Campenhout, Ghent University, chairman
Prof. dr. Roel Van Holen, Ghent University, secretary
Dr. Ewout Van Steenkiste, Ghent University
Prof. dr. Michel Defrise, Vrije Universiteit Brussel
Prof. dr. Volkmar Schulz, Aachen University
Prof. dr. Joel Karp, University of Pennsylvania
Prof. dr. Christian Vanhove, Ghent University
Dr. ir. Vincent Keereman, Ghent University
Prof. dr. Stefaan Vandenberghe, Ghent University

This work was supported by the Institute for the Promotion of Innovation through Science and Technology in Flanders (IWT) and the 7th Framework Programme of the European Union through the SUBLIMA project (Grant Agreement No 241711).

Acknowledgements

Many believe that Ph.D. students spent hours in isolation, doing research, and writing a dissertation that finally ends up on a dusty bookshelf in the library. I believe the opposite is true. My work at MEDISIP has been a life-changing experience involving a lot of social contact with many people. Working in this great environment motivated me and made my Ph.D. experience productive and stimulating. Therefore I'd like to begin this dissertation by thanking all of you!

First of all I want to thank my promotors **prof. dr. Stefaan Vandenberghe** and **dr. ir. Vincent Keereman** for their support throughout my Ph.D.. I appreciate all your professional contributions and ideas. **Stefaan**, I'd like to thank you for giving me the opportunity to work as a researcher at MEDISIP. You gave me enough freedom to pave my way in science and you were always available for questions and scientific discussions. Together with **prof. dr. Roel Van Holen** and **prof. dr. Christian Vanhove** you succeed in achieving a high-quality scientific output while managing your team in an informal and friendly way. **Vincent**, thank you for the numerous scientific contributions, the bar visits and your company during our experiments and visits abroad. Your motivation and devotion to your work has inspired me and I still can't believe how you manage to combine all your activities. Especially thanks for sharing a 9-square-meter room with me during the hot summer in New York, July 2011. I wish you the best of luck at the neurology department and hope we can meet once in a while.

I wish to thank all the colleagues at MEDISIP for keeping up the spirit in our research group, the pleasant lunch breaks and drinks in the kitchen. Special thanks to **Pieter**, who has become a true friend and taught me how to print. Thanks for the fun nights out and skiing trips. I wish you the best of luck in your academic career. **Victoria**, for being the first to say ”Moe gij ni werke?” to Mierlootje at 10:30 in the morning. **Nathalie**, for guarding the office during the lunch breaks and organizing the ladies nights. **Willeke** for reinforcing the girl power in our office. **Bert** (a.k.a. kernelinio, burnzy burt) for managing the ICT of our research group and sharing all your conversations in the office next door with us. **Karel** for learning me how to kayak in the Everglades and boosting the scientific output of MEDISIP, now we can relax for some years. **Karen** for being still alive after all your crazy trips in the mountains and geocaching experiences. **Gregor** for being the cutest colleague MEDISIP has ever known. Special thanks to **Chris**, **Benedicte** and **Scharon** at our preclinical imaging facility (Infinity) for supporting our team with multimodality-imaging services. I also like to thank **Anne-Marie**, **Saskia**, **Inge** en **Aaike** for supporting the Ph.D. students. Your work is highly appreciated by many of us. **Ewout**, for your useful insides and unlimited knowledge of nightlife opportunities. Thank you **Roel** for your scientific support and the late night swims at international conferences in Elba and Miami. Also thanks to **Carmen**, **Shandra**, **Lara**, **Faruk**, **Roma** and **Radek**.

Furthermore I'd like to thank some of my former colleagues. **Hendrik** (a.k.a. Rikske, Tony) for distracting me from my work and the many laughs we had. It was a pleasure working with you. I wish you the very best of luck at the medical school. Also thanks to **Samuel**, **Sinem**, **Enrico**, **Tom**, **Erwann**, **Long**, **Steven**, **Hans** and **Ayfer**.

I also like to thank **Joel**, **Amy**, **Gene** from UPENN (Philadelphia) and **Jason**, **David** and **Zahi** from Mount Sinai Hospital for their contributions during my scientific visits abroad. Thanks to all the members of the HYPERimage and SUBLIMA collaborations. Furthermore, I wish to thank the Institute for the Promotion of Innovation by Science and Technology for the financial support through a postgraduate Grant.

Verder wil ik mijn familie bedanken. Vooral mijn **moeder** en **vader**, die me de kansen gaven en me altijd hebben gesteund voor zovele jaren. Veel dank aan mijn **broer** en **zusjes** voor het toffe gezelschap tijdens mijn jeugd, hun inzet voor onze scouts en de leuke familiereizen. Een dikke zoen voor **Jole**, **Jacob** and **Arne**. Verder wens Ik **An**, **Karel** en **Karel** te bedanken, zorg goed voor mijn broer en zusjes! Ook wil ik mijn **schoonouders** bedanken voor de hulp tijdens de drukke periode van mijn doctoraat en tijdens de zwangerschap van

mijn vriendin. Ook veel dank aan al mijn fantastische vrienden: **Veke**, **Jootje**, **Biene**, **Jan**, **Simonneke**, **Bakki**, **Julie**, **Tom**, **Kiki**, **Dietje**, **Koen**, **Laurence** en **Eva** voor de vele uitjes, etentjes en leuke reizen. Graag wil ik ook de leden van **Grace in the Woods** bedanken voor de wekelijkse ontspanning, vele leuke optredens en repetities.

Karootje, dan rest mij enkel nog jou te bedanken. Bedankt om steeds voor mij klaar te staan en voldoende geduld op te brengen tijdens de drukke periodes van mijn doctoraat. Jouw doorzetting en inzet zal me blijven fascineren. Met jou heb ik al veel mooie momenten beleefd en ik kijk alvast heel erg uit naar onze gezinsuitbreiding. Bedankt voor alles!

Pieter
februari 2014
Gent

"No amount of experimentation can ever prove me right; a single experiment can prove me wrong."

Albert Einstein

Table of Contents

Table of Contents **i**

List of Figures **vii**

List of Tables **xix**

List of acronyms **xxiii**

English summary **xxix**

Nederlandstalige samenvatting **xxxv**

1 Introduction **1**
- 1.1 Context 1
- 1.2 Outline 2

2 Positron Emission Tomography **5**
- 2.1 Introduction 5
- 2.2 PET imaging 5
  - 2.2.1 Short history 5
  - 2.2.2 Positron emission 7
  - 2.2.3 The PET scanner 9
    - 2.2.3.1 Gamma detection 9
    - 2.2.3.2 Coincidence detection 10
    - 2.2.3.3 Time-Of-Flight PET 11
  - 2.2.4 Image degrading effects 13
    - 2.2.4.1 Effects related to positron emission physics 13
    - 2.2.4.2 Effects at detection level 15
    - 2.2.4.3 Subject dependent effects 17
  - 2.2.5 Simulation methodology 20
    - 2.2.5.1 Principle of Monte Carlo Simulation 20

2.2.5.2 GATE : Geant Application for Tomographic Emission 21
2.2.6 Clinical PET imaging 22
2.2.6.1 Oncology 23
2.2.6.2 Cardiology 23
2.2.6.3 Neurology 24
2.3 Hybrid imaging 25
2.3.1 PET and Computed Tomography 26
2.3.2 PET and Magnetic Resonance Imaging 26
2.3.2.1 MR-compatible PET detector design 27
2.3.2.2 System design 27
2.3.2.3 Attenuation correction 28
2.3.2.4 Prototypes and clinical systems 28
2.4 Image reconstruction 32
2.4.1 Data representation 32
2.4.1.1 Sinogram data 33
2.4.1.2 List-mode data 34
2.4.2 PET image reconstruction 34
2.4.2.1 Analytical reconstruction 35
2.4.2.2 Iterative reconstruction 37
2.4.2.3 Time-of-flight List-mode reconstruction . . 41
2.4.2.4 Random and scatter compensation 42
2.5 Derivation of the attenuation map in PET/MRI 46
2.5.1 Emission-based techniques 46
2.5.1.1 Simultaneous statistical reconstruction . . . 47
2.5.1.2 Methods based on consistency conditions criteria 47
2.5.2 Transmission-based techniques 49
2.5.3 MR-based techniques 50
2.5.3.1 Segmentation techniques 51
2.5.3.2 Template- and atlas-based techniques . . . 52
2.5.3.3 Emission-based techniques in TOF PET-MRI 53
2.6 Conclusion 55

3 Transmission scanning using an annulus shaped source 57
3.1 Introduction 57
3.2 Proposed method 57
3.2.1 Extraction of transmission data 58
3.2.2 Derivation of the attenuation map 60
3.2.3 Image degrading effects 64

3.2.3.1 Random coincidences 64
3.2.3.2 Scattered coincidences 65
3.2.3.3 Dead-time and random cross-talk 65
3.2.4 Post processing 66
3.2.5 PET image reconstruction 68
3.3 Simulation study 69
3.3.1 PET system simulation 70
3.3.2 Annulus shaped transmission source 71
3.3.3 Human torso phantom 72
3.3.4 Estimation of Radiation Dose 72
3.4 Results 74
3.4.1 PET system simulation 74
3.4.2 Annulus shaped transmission source 75
3.4.2.1 Extraction of transmission data 76
3.4.2.2 Reconstruction of the attenuation map . . 77
3.4.3 NCAT simulation study 77
3.4.3.1 Extraction of transmission data 77
3.4.4 Reconstructed attenuation maps 78
3.4.5 Reconstructed PET images 79
3.4.6 Estimation of Radiation Dose 80
3.5 Discussion 81
3.6 Conclusion 84
3.7 Original contributions 85

4 Phantom experiments **87**
4.1 Introduction 87
4.2 Data corrections 88
4.2.1 Random correction 88
4.2.2 Scatter correction 89
4.2.2.1 Energy-based methods 90
4.2.2.2 TX-based Single Scatter Simulation 91
4.2.3 Count rate correction 95
4.2.4 Noise regularization 96
4.2.5 μ-value scaling 98
4.3 Data acquisition 100
4.3.1 Phantom studies 100
4.3.2 Annulus-shaped transmission source. 101
4.4 Stand-alone transmission scanning 101
4.4.1 Cylindrical water phantom and MRI coil imaging . . 101
4.4.2 Data acquisition 102

- 4.4.3 Results . . . 103
  - 4.4.3.1 Cylindrical water phantom . . . 103
  - 4.4.3.2 MR coil imaging . . . 104
- 4.5 Simultaneous transmission/emission imaging . . . 104
  - 4.5.1 Anthropomorphic torso phantom . . . 105
    - 4.5.1.1 Data acquisition and image reconstruction 106
    - 4.5.1.2 Results . . . 106
- 4.6 Bone imaging . . . 110
  - 4.6.1 Pig head phantom . . . 110
    - 4.6.1.1 Data acquisition . . . 110
    - 4.6.1.2 Results . . . 110
  - 4.6.2 Alderson torso phantom . . . 111
    - 4.6.2.1 Data acquisition . . . 112
    - 4.6.2.2 Results . . . 113
- 4.7 Thoracic imaging . . . 113
  - 4.7.1 Thorax phantom I . . . 114
    - 4.7.1.1 Data acquisition and processing . . . 116
    - 4.7.1.2 Results . . . 117
  - 4.7.2 Thorax phantom II . . . 119
    - 4.7.2.1 Data acquisition . . . 120
    - 4.7.2.2 Results . . . 120
- 4.8 Discussion and conclusion . . . 124
- 4.9 Original contributions . . . 126

5 Clinical imaging experiments 127

- 5.1 Introduction . . . 127
- 5.2 Materials and methods . . . 128
  - 5.2.1 PET/MRI and CT Acquisition protocols . . . 129
    - 5.2.1.1 Brain imaging . . . 129
    - 5.2.1.2 Body imaging . . . 130
  - 5.2.2 PET/MRI and CT co-registration . . . 131
  - 5.2.3 Derivation of the attenuation maps . . . 132
    - 5.2.3.1 CT-based attenuation map . . . 132
    - 5.2.3.2 MR-based attenuation map . . . 133
    - 5.2.3.3 Transmission-based attenuation map . . . 133
    - 5.2.3.4 Truncated TEX/MR-based attenuation map 135
  - 5.2.4 Reconstruction of the PET images . . . 136
    - 5.2.4.1 Brain study . . . 137
    - 5.2.4.2 Thoracic study . . . 137
    - 5.2.4.3 Evaluation of the images . . . 137

5.3 Results . . . 138
  5.3.1 Brain imaging . . . 138
    5.3.1.1 PET/MRI and CT co-registration . . . 138
    5.3.1.2 Extraction of transmission data . . . 138
    5.3.1.3 Reconstructed attenuation map . . . 139
    5.3.1.4 Reconstructed PET image . . . 141
  5.3.2 Body imaging . . . 141
    5.3.2.1 PET/MRI and CT co-registration . . . 141
    5.3.2.2 Extraction of transmission data . . . 141
    5.3.2.3 Reconstructed attenuation maps . . . 144
    5.3.2.4 Reconstructed PET images . . . 145
5.4 Discussion . . . 146
  5.4.1 Brain imaging . . . 146
  5.4.2 Body imaging . . . 150
5.5 Conclusions . . . 152
5.6 Original contributions . . . 152

6 Transmission scanning using fixed line sources 153
6.1 Introduction . . . 153
6.2 Materials and methods . . . 154
  6.2.1 Transmission source . . . 154
  6.2.2 Extraction of transmission data . . . 154
  6.2.3 Derivation of the attenuation map . . . 158
6.3 Simulation study . . . 158
  6.3.1 PET count rate performance . . . 159
  6.3.2 Transmission source . . . 160
  6.3.3 NCAT phantom study . . . 160
6.4 Experimental study . . . 160
6.5 Results . . . 161
  6.5.1 Simulation study . . . 161
    6.5.1.1 PET count rate performance . . . 161
    6.5.1.2 Transmission source . . . 162
    6.5.1.3 NCAT phantom study . . . 163
  6.5.2 Experimental study . . . 166
    6.5.2.1 Reconstructed attenuation maps . . . 168
6.6 Discussion and conclusion . . . 172
6.7 Original contributions . . . 173

7 General conclusion 175
7.1 Summary . . . 175

7.2 Future research 181
7.3 Final conclusion 182

References 183

List of Publications 203

List of Figures

2.1 Timeline showing the most important developments in the history of nuclear medicine. 6

2.2 Positron emission and annihilation, involving the emission of two 511-keV gamma rays in (almost) opposite directions . . 8

2.3 PET geometry designs: detectors mounted on a rotating gantry (a), polygonal (b) or circular detector rings. 9

2.4 Components of a conventional gamma camera. The detector block consists of scintillation crystals, a light guide and an array of photomultiplier tubes. 10

2.5 Coincidence detection: when two photons hit a PET detector within a predefined time window, a coincidence is registered. 11

2.6 The TOF PET principle. The time-of-flight difference Δt is related to the distance $d(= c\frac{\Delta t}{2})$ from the center of the LOR to the annihilation. 12

2.7 Patient with non-Hodgkins lymphoma (140 kg, BMI = 46). Representative transverse, sagittal, and coronal images (not triangulated) for non-TOF reconstruction (top) and the same cross-sectional images for TOF reconstruction (bottom). In each image, the different lesions are seen more clearly in TOF reconstruction than in non-TOF reconstruction. Reprinted with permission [1]. 14

2.8 A coincidence detection system is classified as paralysable or non-paralysable. Paralysable systems can be subdivided in type I and type II systems. Each hit will cause a dead time of the system. In a non-paralysable system a hit is detected only if previous dead times are expired. In a paralysable system all hits are detected, but a coincidence is only accepted if all previous dead times are expired. Additionally, in a type II paralysable system, energy pile-up can cause a rejection of hits. 16

2.9 Coincidence types: true, random and scattered coincidences. 17

2.10 Visual comparison of PET images reconstructed without (a) and with (b) attenuation correction. 20

2.11 GATE simulation of a cylindrical water phantom injected with ^{18}F-FDG. A model of the Philips Gemini TF PET scanner is shown. Green lines represent photon paths. 22

2.12 Male and female digital XCAT phantoms [2] 23

2.13 Frontal (left) and left lateral (right) maximum intensity projections from FDG PET scan in a 46-year-old man with history of melanoma removed from left upper back who then presented with pigmented cutaneous lesions extending from biopsy site to left axilla. Patient was referred for restaging of melanoma. Multiple sites of disease are visible, including local recurrence at biopsy site with in-transit cutaneous metastases (large arrows), left axillary metastases (small arrows), retrosternal metastasis (large arrowhead), and splenic and hepatic metastases (small arrowheads). Reprinted with permission [3]. 25

2.14 Three models for combining PET and MRI systems: sequential (a), a PET insert (b) or fully integrated (c). 29

2.15 Two commercial whole body PET/MRI scanners: the sequential Ingenuity TF PET/MR by Philips Healthcare (a) and fully integrated Biograph mMR by Siemens (b). 30

2.16 A 55-y-old patient with metastatic breast carcinoma. Unremarkable sclerotic lesion (arrow) of left femoral bone on axial CT (A) was diagnosed as metastasis only because it was strongly 18F-FDG-avid on PET/CT (B). Whole-body MRI using T1- weighted fat-suppressed sequence (C) clearly depicts metastasis as contrast enhancing mass (arrowhead). Corresponding PET/MRI image (D) demonstrates precise metabolic-anatomic correlation of this technique for bone imaging. Reprinted with permission [4]. 31
2.17 Overview of section 2.4: different steps involved in the reconstruction of the PET images. 32
2.18 Parameterization of a 3D LOR. 33
2.19 Sinogram projection data of a digital torso phantom. 34
2.20 Back-projection of projection data $p(\cdot)$ into image space. . . 36
2.21 Different steps involved in a typical iterative reconstruction algorithm. 38
2.22 The Single Scatter Simulation method. 44
2.23 Reconstructions of an abdominal PET study. From left to right; top: ML-EM without attenuation correction, FBP and ML-EM with measured attenuation correction, MLAA emission image, absolute difference between MLAA and ML-EM images. Bottom: FBP and ML-EM reconstruction of PET transmission study, MLAA attenuation map, absolute difference between MLAA and ML attenuation maps. Reprinted with permission [5] ©2011 IEEE. 48
2.24 Reconstructions of the attenuation image from simulated data without noise (top row), with noise (middle row), and with more noise (bottom row). From left to right: the true attenuation image, the image estimated by the analytical method, and the references images reconstructed with the maximum-likelihood MLTR algorithm [5] and with FBP. Reprinted with permission [6]. ©Institute of Physics and Engineering in Medicine. Published on behalf of IPEM by IOP Publishing Ltd. All rights reserved. 49
2.25 Different transmission scanning methods for PET. Transmission measured in coincidence mode using ring sources of positron-emitting radionuclide (a) or rotating positron-emitting rods (b). Rotating single-photon source producing LORs between source position and photons detected on opposing side of detector ring (c). 51

2.26 Iterative reconstruction scheme. Reprinted with permission [7] ©2011 IEEE. 53

2.27 Attenuation map and reconstructed activity distributions. Upper row: Initial estimation, second row: estimation after 11 iterations, third row: CT-based reference attenuation and corresponding reconstructed activity, and last row: difference between 11th iteration and CT-based reference, White arrows point to region averaged μ coefficients. (from left to right: transverse, coronal, and sagittal transection). Reprinted with permission [7]. ©2011 IEEE. 54

3.1 Annulus shaped transmission source inserted in a TOF PET scanner. 58

3.2 A blank reference scan (BX-scan) with nothing inside the FOV (a), a cold transmission scan (TX-scan) prior to ^{18}F-FDG-injection (b) and a simultaneous transmission and emission scan (TEX-scan) after ^{18}F-FDG administration (c). The gamma radiation originated from the annulus source is indicated in green, while the radiation from the patient is indicated in red. 59

3.3 TOF-based extraction of transmission data on a particular LOR for a threshold radius τ_1. 61

3.4 Iterative gradient ascent reconstruction. A T-image is created by back-projecting the transmission counts t_i for each LOR i into image space. The current B-image is created by attenuation corrected back-projection of the blank counts b_i using the current estimate of the μ-map. The error between the B- and the T-image is used to update the current μ-map. This process is repeated until convergence is reached. 63

3.5 Random cross-talk composed of two photons originating from two distinct sources. 66

3.6 Global count rate correction to restore inconsistency between blank and transmission scan. The difference in count rate is measured on those LORs which do not suffer from high attenuation and emission contamination. 67

3.7 Segmentation of the reconstructed attenuation map. 68

3.8 GATE model of the TF Gemini PET system. 71

3.9 Transverse slice of the NCAT attenuation (a) and emission distribution (b). Annulus transmission source positioned inside the FOV of a PET Scanner based on the Philips Gemini TF (c). 73

3.10 True, scattered and random count rate performance for GATE Gemini TF model using the NEMA protocol. 74

3.11 (a) True count rate of a blank scan for different transmission (TX) source diameters and activities. (b) Dotted line: percentage of true NEMA emission (EX) count rate during a $\mathrm{TE}_{\mathrm{Nema}}$ scan for different TX source diameters and activities with respect to the maximum count rate measured during a $\mathrm{E}_{\mathrm{Nema}}$ scan. Full line: true transmission count rate during a $\mathrm{TE}_{\mathrm{Nema}}$ scan normalized to the transmission count rate measured at a TX activity level of 80 MBq. 75

3.12 Misclassified emission data with respect to the estimated transmission (ECR) and rejected transmission data with respect to the true transmission data (TRR) for a 40-cm-diameter cylinder (a,c) and 60-cm-diameter (b,d) cylinder. Fractions are calculated for different decision rules (τ_1-values) using an annulus source with a radius of 35 cm (a,b) and 30 cm (c,d). The activity in the cylinders varied from 250 to 750 MBq. The number of transmission events are calculated within a FOV determined by the radius of the cylinder. 76

3.13 Visual comparison of a central slice of the unsegmented (a) and segmented (b) attenuation map derived from a transmission scan of type $\mathrm{TE}_{\mathrm{ncat}}$ and the correct attenuation map (c). 79

3.14 Absolute mean percentage difference of reconstructed SUV values of the E_1-map compared to the SUV-values from the E_2-map 80

3.15 Visual comparison of a central slice of the true tracer distribution (a), reconstructed E_1-map (b) and reconstructed E_2-map (c). 80

3.16 Maximum intensity projection of tracer distribution (a), absorbed dose from transmission scan (b) and absorbed dose from emission scan (c). 81

3.17 Effective total transmission dose as a percentage of the total effective emission dose. A logarithmic scale was used. 82

4.1 Suppression of scattered events using the $SC(\cdot)$ scaling function. Only one factor of the formula in eq. 4.5 is shown. The scaling is applied to both the blank and transmission scan. The method preserves the relation a_i between the true transmission counts $\bar{t}_i$ and true blank scouts $\bar{b}_i$. 90

4.2 Single Scatter Simulation for transmission scanning in coincidence mode. 92

4.3 Calibration of the TX-based SSS algorithm with GATE. . . . 93

4.4 Single Scatter Simulation adapted for the estimation of the TOF-based extracted scattered transmission data. 94

4.5 Summation over coronal and sagittal direction and central transverse slice of the back projected estimated scatter data into image space. Both GATE and SSS estimated scatter are shown. The profiles were calculated for three different threshold values for τ_1. 95

4.6 Relative error of the reconstructed attenuation coefficients in soft tissue, lungs and bone. The attenuation map without scatter correction and with SSS-based scatter correction were compared with the attenuation map derived from a transmission scan were the scatter was rejected. 96

4.7 Reconstructed attenuation map of an anthropomorphic torso phantom without (a) and with noise regularization (b). . . . 98

4.8 Annulus-shaped transmission source 101

4.9 Central transverse (a) and coronal slice (b) of the reconstructed attenuation map of the cylindrical phantom acquired with a TX-scan on the Gemini TF PET/CT system. . 103

4.10 Transverse slice of the TX-based attenuation map (a) and CT image (b) of an MR head coil. 104

4.11 An anthropomorphic torso phantom containing lung and liver compartments and a cardiac and spine insert. 105

4.12 Left to right: central transverse slice of the TX-based (a,c,e) and TEX-based (b,d,f) attenuation maps. Top to bottom: reconstructed attenuation maps without scatter correction (a,b), energy-based scatter compensation (c,d) and SSS-based scatter correction (e,f). 107

4.13 Relative percent difference of reconstructed TX-based attenuation maps (see table 4.5) compared to the CT-based attenuation map. 108

4.14 Relative percent difference of reconstructed TEX-based attenuation maps (see table 4.5) compared to the CT-based attenuation map. 109

4.15 Left to right: central transverse slice of the non attenuation corrected PET image (a), the TEX-based AC PET image (b), the CT-based AC PET image (c) and the difference image between the CT-AC and the TEX-ac PET images (d). 109

4.16 Central transverse and sagittal slices of the TX-based (left) and CT-based (right) attenuation map of the pig phantom. . 111

4.17 VOIs of 4 cm^3 were defined for each tissue: 5 in soft tissue, 5 in the bone structures and 2 in the air cavities. 112

4.18 the Alderson torso phantom. 113

4.19 Coronal (a,b) and sagittal (c,d) slice of the reconstructed TX-based (a,c) and CT-based (b,d) attenuation map of the Alderson torso phantom. 114

4.20 Profile in a slice of the TX-based and CT-based attenuation map showing an increased μ-value close to the ribs and sternum. 114

4.21 Relative difference of the reconstructed TX-based attenuation map compared to the CT-based attenuation maps in VOIs defined in the humerus, rib, spine, sternum, soft tissue and lung tissue. 115

4.22 A thorax phantom contains one lobe of a pig lung and a bovine bone. 115

4.23 Transverse and sagittal slice of the reconstructed CT-based (a) and TEX-based (b) attenuation map. 118

4.24 Transverse slice of the reconstructed TEX-based (a) and CT-based (b) attenuation map. The underestimated attenuation coefficients in the hot lesions are indicated in red. 118

4.25 Transverse slice of the reconstructed PET image with CT-based (a) and TEX-based (b) attenuation correction respectively. Compared to the CT-based AC PET image, a higher uptake in the lungs and a lower uptake in the soft tissue was noticed. 119

4.26 Thorax II phantom: inflated pig lungs (a) and top view of the phantom (b). 119

4.27 Profile of the TEX and EX scan. For each event the location of the annihilations was estimated using the TOF information.121

4.28 Transverse slice of the TX-based attenuation map without scatter correction (a), the TX-based attenuation map with SSS scatter correction (b), the CT-based attenuation map and the MR-based attenuation map (d). Remark: the MR-based attenuation map failed to segment the lungs, because of a lack of similarity with human data. 122
4.29 Transverse slice of the reconstructed PET images from the PET/CT scan ($\mathrm{EX}_{\mathrm{CT}}$) (a), the Ingenuity PET/MR with MR-based attenuation correction ($\mathrm{EX}_{\mathrm{MR}}$) (b) and the TEX-based attenuation corrected PET image ($\mathrm{TEX}_{\mathrm{TX}}$) (c). 123
4.30 Contrast recovery of PET image intensity compared to the PET images derived from the PET/CT scan. 124

5.1 Acquisition and image-processing workflow of brain study. From left to right : PET/MRI and CT acquisition and co-registration, derivation of the CT-based and TEX-based attenuation maps and reconstruction of the PET images using the CT-based and TEX-based attenuation map for attenuation correction. 129
5.2 Acquisition and image-processing workflow of thoracic study. From top to bottom : PET/MRI and CT acquisition, derivation of the CT-based, MR-based and TEX-based attenuation maps and reconstruction of the PET images using the CT-based, MR-based and TEX-based attenuation map for attenuation correction. 131
5.3 Black line represents the scaling function. The histogram model of the CT and TEX-based attenuation coefficients is also shown. 136
5.4 Central sagittal (a,b) and coronal slice (c,d) of the co-registered CT (left) and MRI (right) image of the brain study. 138
5.5 Transverse slice of the estimated annihilation points derived from the TOF information (a). Source positions above the threshold value $\tau_1 = 22$ cm are indicated in green, the source positions that fall within a cylinder of radius $\tau_1 = 22$ cm are indicated in red. The back-projection of the extracted transmission events is also shown (b). 139
5.6 Visual comparison of the TEX-based (right) and CT-based (left) attenuation map of the brain. Central transverse (a,b), coronal (c,d) and sagittal slices (e,f) are shown. 140

5.7 From left to right: transverse slice of the CT-based (a), TEX_{tr}-based (b) and non attenuation corrected (c) PET image of the brain. For the CT-based and TEX_{tr}-based AC PET images, the same thresholds for the color scaling were used. For the non attenuation corrected image the upper threshold was 4 times lower. 141

5.8 Coronal (a) and sagittal (b) slice of the fused PETMRI image using the non-truncated TEX-based attenuation map for attenuation correction. 142

5.9 Relative comparison between the TEX-AC and CT-AC PET images for different VOIs in the brain. The unscaled $\text{TEX}_{\text{tr}}^{**}$ map, unscaled, scatter compensated $\text{TEX}_{\text{tr}}^{*}$ map and scaled TEX_{tr} map were evaluated. 142

5.10 Central transverse (a,b) and coronal slice (c,d) of the coregistered CT (left) and MRI (right) image of the torso of the 6th patient. 143

5.11 Transverse slice of the estimated annihilation points derived from the TOF information. The head (a) and torso (b) region are shown. The threshold value τ_1 is also indicated. . 144

5.12 Unscaled and scaled TEX-based attenuation map and μ-value distribution using histogram matching with predefined distributions for lung and soft-tissue μ-values in both TEX and CT-based attenuation maps for one patient. 145

5.13 Histograms (a,b) and joint histograms (c,d) of the CT- vs TEX_{tr}-map (a,c) and CT- vs MR_{tr}-map (b,d). The joint histograms and histograms were obtained from all patient data combined. 146

5.14 Visual comparison of the TEX-based (left) and MR-based (right) attenuation maps of 3 patients. (a) Central sagittal slice from the lower head/jaw, showing better recovery of the jaw and skull with the TEX-based method. (b) Coronal slice of the torso only shows part of the humerus in the TEX-based attenuation map while the MR-based attenuation map clearly shows truncation artifacts in the arms. (c) Transverse slice of torso indicating segmentation error in the lungs and right humerus with the MR-based method. 147

5.15 Scatter plot of the CT-based attenuation corrected (AC) PET image vs TEX_{tr}-based AC and MR_{tr}-based AC PET image for patient 2-6 (a-e), Absolute mean percentage difference of reconstructed emission values of the TEX_{tr} and MR_{tr}-based AC PET image compared to the CT-based AC map (f). 148
5.16 Central coronal (a,b) and sagittal slice (c,d) of the reconstruction emission data from TEX scan using TEX-based attenuation correction (a,c), from EX scan using MR-based attenuation correction (b,d). 149

6.1 12 Stationary line sources positioned inside the FOV of a PET scanner. In this situation a line source is placed in front of each detector block. The activity, location and number of line sources should be optimized to ensure accurate attenuation coefficients are obtained. 155
6.2 The previously defined TOF-based extraction accepts all events whose estimated annihilation point falls outside a cylinder with radius τ_1 (a). LOR-based selection improves the extraction by ignoring the events marked in red (b). . . . 155
6.3 Distance d_e between event $\{P_1, P_2\}$ and closest line source. 156
6.4 Three situations to clarify the extraction process : Event (a) is classified as transmission data because the distance d_e to the closest line source is smaller than τ_s and the estimated emission point P_s is close to the line source. Event (b) is rejected because d_e is too large. Event (c) is rejected because no line source closer than d_e is found in the direct neighborhood (cylinder with radius τ_s^{TOF}) of the estimated emission point P_e. 157
6.5 Positioning of the line sources inside the FOV of the LaPET scanner. First, 24 holes were drilled in a wooden template at 32 cm off-center radius (a). Next, the template was mounted on the rotating device of the LaPET scanner (b). Finally, the line sources can be fixated in the holes of the wooden template. 161
6.6 Transverse slice of the NCAT attenuation (a) and emission distribution (b). 24 line sources positioned inside the FOV of a PET Scanner based on the LaBr_3 PET design (c). . . . 162
6.7 True, scattered and random count rate performance of GATE LaBr_3 PET model using the NEMA protocol. 162

6.8 True count rate performance of the blank reference scan for different configurations. In the left images, the number of line sources was fixed (6 in (a), 12 in (c) and 24 in (e)) and the position of the line sources varied from 30 to 35 cm. In the right images the position of the line sources was fixed (30 cm in (b), 32.5 cm in (d) and 35 cm in (f)) and the influence of the number of line sources on the true count rate in each configuration was determined. 164

6.9 True NEMA emission count rate and true transmission count rate in function of the transmission activity level during a $\mathrm{TE}_{\mathrm{Nema}}$ scan for a different number of line sources. The transmission count rate was normalized to the count rate simulated at a TX activity level of 100 MBq. The NEMA emission count rate was normalized to the count rate simulated during an $\mathrm{E}_{\mathrm{Nema}}$-scan with an activity level of 500 MBq. 165

6.10 Transverse slices of the reconstructed attenuation maps M_1, M_2 and M_3. The transmission data was acquired with a $\mathrm{T}_{\mathrm{ncat}}$ scan using 6 (a), 12 (b) and 24 (c) line sources respectively. 165

6.11 Error (%) of reconstructed attenuation coefficients compared to the real values for three tissue types. 166

6.12 Percentage of emission and scattered events classified as transmission data. 167

6.13 Transverse slices of the reconstructed attenuation maps M_3, M_5 and M_6 using 24 line sources: a $\mathrm{T}_{\mathrm{ncat}}$ scan containing only transmission data (gold standard)(a) ; a $\mathrm{TE}_{\mathrm{ncat}}$ scan where the TX data was extracted using only TOF information (b);$\mathrm{TE}_{\mathrm{ncat}}$ scan where the TX data was extracted using both TOF as LOR information (c). 167

6.14 Percentage error of reconstructed attenuation coefficients compared to the real values for three tissue types. 168

6.15 Central transverse slice of the reconstructed attenuation maps from table 6.3: M_7: TX-based without LOR-based extraction (a), M_8: TX-based with LOR-based extraction (b), M_9: TEX-based with TOF-based extraction only (c) and M_{10}: TEX-based with both TOF and LOR-based extraction (d). 169

6.16 Error (%) of reconstructed attenuation coefficients for the M_7, M_8, M_9 and M_{10} maps from table 6.3. 169

6.17 Maximum FOV for given line source positions (orange or green) with sampling artifacts caused by the gaps between the detectors (gray area). If the line sources are positioned at the orange spot, a relatively large under-sampled area (gray zone) will cause artifacts in the reconstructed attenuation map. These can be avoided by placing the line source closer to the detector (green spot). 170
6.18 Top: reconstructed attenuation map M_{10} without interpolation (a) and reconstructed attenuation map M_{10} with interpolation (b). The erroneous regions due to the under sampling are indicated with blue spheres. The errors introduced by the interpolation are indicated with the red arrows. Bottom: detected counts from line source 0: matrix representation of detections before interpolation (c), matrix representation after interpolation (d). 171

List of Tables

2.1 Abbreviated list of positron-emitting isotopes with their half-life and production method. 8
2.2 PET detectors. 11
2.3 Positron range in water (FWHM in mm) for commonly used positron emitting radio-isotopes [8, 9]. 14
2.4 Overview of the attenuation coefficients at 511 keV of the most relevant tissues. 19
2.5 Abbreviated list of positron-emitting isotopes, tracer compounds and their typical applications. 24

3.1 Blank scans (B_x), simultaneous transmission/emission scans (TE_x) and emission scans (E_x) using GATE. All scans had an acquisition time of 3 minutes. 70
3.2 FDG-PET uptake (SUV) and attenuation coefficients for different tissue types. 72
3.3 Relative error (%) of attenuation coefficient of water (0.097 cm^{-1}) for three cylindrical phantoms of 20-cm, 40-cm, 60-cm-diameter filled with 250 to 750 MBq of FDG. A 30 and 35-cm-radius annulus transmission source was used. 77
3.4 First column : collected trues, randoms, delays, annulus scatter and phantom scatter during a simulation of type TE_{ncat}. Second column: percentage of collected counts after extractions. In the first row, only LORs who pass through a FOV of 57 cm are considered. 78
3.5 Percentage mean difference in μ-values (%) in VOIs of different tissues compared to the correct values (table 3.2). . . 79
3.6 Simulated effective dose (mSv) for different tissue types during transmission and emission scanning. During the transmission scans, an annulus transmission source with different activities was used. 81

4.1 Overview of phantom studies acquired on the Gemini TF PET/CT scanner and the Ingenuity TF PET/MRI scanner. The type of PET scanning (transmission only TX, simultaneous transmission/emission TEX or emission only EX) is also shown. Additionally, we indicate whether CT or MRI data of the phantom was available. 99
4.2 Overview of the PET acquisition of the initial experiments on the Gemini TF PET/CT system. 102
4.3 Reconstructed attenuation coefficients (mm^{-1}) of water for cylindrical water phantom. 102
4.4 Overview of PET acquisition on the Gemini TF PET/CT system using the anthropomorphic torso phantom. 105
4.5 Reconstructed attenuation coefficients (mm^{-1}) of lung, soft-tissue and bone in the anthropomorphic torso phantom. The scatter correction method applied is also shown. 108
4.6 Mean reconstructed attenuation coefficients (mm^{-1}) in VOIs defined in the air cavities, soft tissue and bone of the pig phantom. 111
4.7 Overview of measurements on the Gemini TF PET/CT. . . . 117
4.8 Overview of the total counts and total activity of the acquisitions listed in table 4.7 117
4.9 Mean reconstructed attenuation coefficients (mm^{-1}) for VOIs defined in the pig lungs, bovine bone and water container. 118
4.10 Reconstructed attenuation coefficients (mm^{-1}) of water for cylindrical water phantom. 121
4.11 Overview of reconstructed PET images. For the first two reconstructions our in house reconstruction software was used. The last two PET images were obtained from the Ingenuity PET/MRI scanner and the Discovery PET/CT. 123

5.1 Patient weight (kg), injected activity (MBq) 80-90 minutes prior to PET/MRI acquisition and acquired bed positions during PET/MRI acquisition. 130
5.2 TEX- MR- and CT-based reconstructed attenuation maps. . 136
5.3 Mean reconstructed μ-values (mm^{-1}) in VOIs defined in white/grey matter, bone structures and air cavities. (**) indicates that the attenuation map was neither scaled nor compensated for scatter. For The TEX^{*}_{tr} scatter compensation was implemented. For the TEX_{tr}-map both μ-value scaling and scatter compensation were applied. 140

5.4 Transmission rejection rate (%) and emission contamination rate (%) for 5 patients. Rates are averaged over all bed positions. 143
5.5 Mean and mean standard deviation of reconstructed μ-values (mm^{-1}) in lung and soft-tissue for CT, unscaled and scaled TEX-based attenuation map for all patients. Predefined μ-values assigned in the MR-based method are also shown. 144
5.6 First three rows: mean normalized similarity (%) between reconstructed PET images of 5 patients using 3 different truncated attenuation maps (CT-map, $\mathrm{TEX_{tr}}$-map, $\mathrm{MR_{tr}}$-map). Last three rows: mean normalized similarity (%) between TEX- and MR-based AC PET images and similarity between PET images reconstructed using the non-truncated (TEX-map, MR-map) and truncated ($\mathrm{TEX_{tr}}$-map, $\mathrm{MR_{tr}}$-map) attenuation maps. Similarities were measured over all patient data combined. 149

6.1 Blank scans (B_x), simultaneous transmission/emission scans (TE_x) and emission scans (E_x) using GATE. All scans had an acquisition time of 3 minutes. 159
6.2 6 attenuation maps reconstructed from the $\mathrm{T_{ncat}}$,$\mathrm{TE_{ncat2}}$,$\mathrm{TE_{ncat}}$ data sets. 163
6.3 4 attenuation maps reconstructed from the TX and TEX data acquired on the LaPET scanner. 168

List of acronyms

A

AC	Attenuation Correction
ACF	Attenuation Correction Factor
APD	Avalanche PhotoDiode

B

BGO	Bismuth Germanate
BX	Blank reference scan

C

CRC	Contrast Recovery Coefficient
CT	Computed Tomography

D

DOI	Depth Of Interaction
DWI	Diffusion Weighted Imaging

E

ECR	Emission Contamination Rate

F

FBP	Filtered BackProjection
FDG	FluoroDeoxyGlucose
fMRI	functional MRI
FOV	Field Of View
FWHM	Full Width at Half Maximum

G

GATE	GEANT Application for Tomographic Emission
GEANT4	Geometry And Tracking 4

H

HU	Hounsfield Units

L

LOR	Line Of Response
LSO	Lutetium oxyorthosylicate
LYSO	Lutetium-Yttrium oxyorthosylicate

M

MC	Monte Carlo
MAP	Maximum A Posteriori
ML-EM	Maximum Likelihood - Expectation Maximization
MRF	Markov Random Field
MRI	Magnetic Resonance Imaging

N

NCAT	NURBS-based Cardiac Torso phantom

O

OSEM	Ordered Subsets Expectation Maximization

P

PET	Positron Emission Tomography
PMMA	Poly Methyl MethAcrylate
PMT	PhotoMultiplier Tube

R

ROI	Region Of Interest

S

SiPM	Silicon PhotoMultiplier
SPECT	Single Photon Emission Computed Tomography

SSS	Single Scatter Simulation
SUV	Standardized Uptake Value

T

TOF	Time-Of-Flight
TX	Transmission scan
TEX	Simultaneous transmission/emission scan
TRR	Transmission Rejection Rate

U

UTE	Ultrashort Echo Time

V

VOI	Volume-Of-Interest

English summary

Nederlandstalige samenvatting

English summary

The work presented in this dissertation is situated in the field of nuclear medicine, specifically in Positron Emission Tomography and the combination of PET with Magnetic Resonance Imaging (MRI). Emission Tomography is based on the tracer principle which states that a molecule labeled with a radioactive isotope participates in the metabolic activity of the human body in a similar way as the non-radioactive molecule. The tracer is injected in the patient and the distribution of this tracer is reconstructed by detecting the radiation that originates from the radioactive isotopes. In PET, positron emitting isotopes are used. After emission, the positron travels a short distance until a positronium is formed. Almost immediately an annihilation with an electron occurs and two gamma photons are emitted in opposite direction. The two gamma photons are detected with a polynomial ring of PET detectors surrounding the patient and the coincidence electronics register the photon-pair in a list-mode or sinogram data format. Subsequently, the tracer distribution or PET image is reconstructed with an analytical or iterative method. Advances in detector technology allow current systems to measure the difference in arrival times of two photons in coincidence. Although this Time-Of-Flight (TOF) information is not exact, the reconstruction can be improved significantly, yielding more accurate PET images in a shorter time span.

Absolute quantification in PET is difficult to obtain due to the physical properties of positron emission, inefficiencies at the detection level and interactions of the radiation with the subject being investigated. One of the major image degrading effects is photon attenuation. To correct for attenuation, the distribution of the tissue-dependent attenuation coefficients at 511 keV within the Field Of View (FOV) needs to be determined. This information is stored in an attenuation map and can be used during reconstruction to correct the PET data for attenuation.

PET imaging has evolved into multimodal imaging techniques where func-

tional PET is combined with anatomical imaging techniques such as Computed Tomography (CT) and MRI. PET/CT is widely used in clinical practice for the diagnosis and follow-up of various diseases. CT provides anatomical landmarks which improves the interpretation and diagnostic accuracy of the PET images. The detectors measure the average linear attenuation of the X-rays between the tube and the detectors. Hence, CT-images can easily be transformed into attenuation maps at 511 keV using scaling techniques. In the last decade, there is a growing interest in combining PET with MRI. PET/MRI is expected to be a promising imaging technique for applications where a high soft-tissue contrast is desired such as in brain imaging or imaging of parenchymal abdominal organs. Additionally, MRI can provide functional information complementary to functional PET through the use of techniques such as MR spectroscopy, diffusion weighted imaging or functional MRI (fMRI). From a hardware perspective, most issues related to combining PET and MRI are solved and fully integrated PET/MRI systems exist today. On the software side, attenuation correction (AC) remains a major issue. MRI signals correlate with proton densities and relaxation properties of tissue. Contrary to CT, a direct conversion from MRI intensity values to attenuation coefficients is not applicable. Hence MR-based attenuation correction relies on segmentation and atlas registration techniques to derive an estimate of the attenuation map. These methods have some major drawbacks related to lung/bone imaging, inter and intra-patient variability of attenuation coefficients, imaging of flexible MRI coils and truncation of the arms. Alternative approaches exist: in stand-alone PET, transmission scans with orbiting rot sources were used to derive the attenuation coefficients at 511 keV. Additionally, complex algorithms allow the use of the emission data to derive the attenuation coefficients.

In this work a new MR-compatible method to derive the attenuation map in a TOF PET scanner is proposed. The technique works as follows: a transmission source containing a positron emitter is placed inside the FOV of the PET scanner. First a blank reference scan is acquired. During this scan neither the patient table nor the patient are inside the FOV and the photons originating from the transmission source are only attenuated by air. Subsequently, the patient is positioned on the table and moved inside the FOV of the PET scanner. A transmission scan (TX-scan) is acquired. During this scan, the photons will be attenuated by any object inside the FOV. By comparing the data acquired during the blank scan and the transmission scan in an iterative algorithm, an attenuation map can be derived. Additionally, when the transmission data and emission data are acquired simultaneously (TEX scan), the TOF capabilities of the PET scanner can be used to extract the transmission data. Hence, no acquisition time of the PET or MRI scanner is lost for the purpose of attenuation correction. The method was evaluated in three steps: first with simulation studies, second with experimental data acquired on state-of-the-art PET/MRI and PET/CT systems and finally, with clinical data acquired on the sequential Ingenuity TF PET/MRI from Philips Healthcare.

In the simulation study, the accuracy of the transmission-based technique was evaluated with simultaneous transmission/emission scans of the human torso region. For this purpose a model of the Gemini TF PET scanner (Philips Healthcare) and an annulus-shaped transmission source were designed in GATE. A digital torso was generated with the NCAT software. Both the attenuation map and the tracer distribution map were generated. The results obtained from the simulation study indicate that accurate attenuation coefficients (below 4% relative error in all tissues) can be obtained with a 3 minute TEX-scan using an annulus shaped transmission source filled with 18 MBq of ^{18}F-FDG. Subsequently, the attenuation map is used to correct the PET data for attenuation. The reconstructed PET image was compared to the actual tracer distribution and the following quantification errors were obtained: below 9% inside the lungs and bone tissue, 4.3% in a lesion inside the lungs and below 3% in the myocardium and soft tissue.

Further validation was done with phantom studies on state-of-the-art TOF PET/CT and TOF PET/MRI scanners. Contrary to simulation studies, working with experimental data does not allow any simplification of the PET acquisition process. Image degrading effects will influence the accuracy of the reconstructed attenuation maps and the PET images. Correction methods were proposed to compensate for these effects. In all studies random coincidences were compensated with the delayed window method. The mismatch between the count rate performance of the blank and transmission scan was corrected with a global correction factor and noise was regulated during reconstruction by minimizing the total variation in the attenuation map. For the compensation of scattered transmission events, two methods were proposed. The first method suppresses coincidences in which the energy of the photons are low compared to a given threshold. In the second method the scatter was estimated with a fast simulation technique, called Single Scatter Simulation. Results show that better results are obtained when the scattered transmission events are corrected using the SSS method. In total six phantom studies were presented into four groups: stand-alone TX scanning, simultaneous TEX scanning, bone imaging and thoracic imaging. In the first group two transmission studies were done: a TX scan of a cylindrical water phantom and a TX scan of a MRI head coil. For the second group an anthropomorphic torso phantom was used. We made a comparison between the TX-based and the TEX-based attenuation map. Next, we evaluated how well our method is able to recover bone structures with a TX scan of the head of a pig and the Alderson torso phantom. Finally, two thorax phantoms containing tissue recovered from a cow and pig were presented. In the last study we compared our TEX-based AC method with a standard CT-based AC method and the MR-based AC method installed in the Ingenuity TF PET/MRI scanner. Four major conclusions were drawn from the phantom studies. First, all phantom studies indicate that correction methods for image degrading effects are required in order to obtain accurate attenuation coefficients at 511 keV. Second, when the transmission and emission data are acquired simultaneously, scattered and true emission data might contaminate the extracted transmission data yielding inaccurate attenuation coefficients. This was observed with the second and the fourth group of phantom studies. Improvements can be made by increasing the activity inside the transmission source. Thirdly, the TX and TEX-based methods are able to visualize any object inside the FOV. Finally, to achieve absolute PET quantification, correcting for the attenuation of gamma rays in bone tissue is mandatory. This was illustrated with the third group of studies. Large bone structures were visible in the attenuation maps. Smaller bone structures or soft bone tissue characterized by a lower attenuation coefficients are more difficult to distinguish from the surrounding tissue.

Subsequently, an evaluation on clinical data was performed. In total 6 patient studies were investigated on the sequential Ingenuity TF PET/MRI scanner and Brilliance CT scanner (Philips Heathcare) available at Mount Sinai Hospital in New York, USA. The patients studies included one brain study and 5 studies of the head/neck and upper torso region. In the brain study, the accuracy of the TEX-based AC PET image obtained from the TEX scan was compared with the CT-based AC PET image obtained from the same data set. A relative error of 6.5% to 13% was obtained in VOIs defined in the thalamus, cerebellum, frontal lobe, occipital lobe and white matter. For the thoracic studies, TEX-based AC was compared with a standard CT-based and the three-segment MR-based AC method. Results show that for bone, the relative error of the TEX-based AC PET images compared the CT-based AC PET images was 18.7% lower than the error obtained in the MR-based AC PET image. For the lungs and soft tissue, an improvement below 5% was reported. Overall, a better performance was obtained with the TEX-based methods. However, these results were only possible when a μ-value scaling method was applied to the attenuation maps to compensate for the inaccuracy due to the scatter and emission contamination in the transmission data.

Finally, we improved the transmission-based technique by replacing the annulus-shaped transmission source with a fixed number of stationary line sources. Similar to the annulus-based method, the attenuation maps are derived with an iterative gradient ascent algorithm using a blank reference scan and a simultaneous transmission and emission scan. Because only a fixed number of line sources are used, the extraction of transmission data can be improved by rejecting those Lines-Of-Responses (LORs) which do not pass close to at least one line source. Additionally, TOF information can be used the reject unwanted data. The method was first evaluated with a simulation study in GATE. For this purpose we build a model of a $LaBr_3$ TOF PET scanner and generated a digital torso phantom from the NCAT software. First we compared the LOR-based extraction of the transmission data with the TOF-based method that was used in the annulus-based studies. Simulation studies show that for a setup with 24 line sources, the Emission Rejection Rate (ECR) improves from 1.13% to 0.45%. The fraction of scattered emission data misclassified as transmission data decreases from 4.32% to 2.29%. A quantitative improvement of the attenuation coefficients of 10-25% was obtained in all tissue types. Only random correction and count rate correction was applied. Finally, the method was evaluated with a phantom study on the $LaBr_3$ TOF PET scanner installed at the radiology department at the University of Pennsylvania (UPENN), Philadelphia. A TX and TEX scan of an anthropomorphic torso phantom was acquired. The relative error of the reconstructed attenuation coefficients in both the TX-based and the TEX-based attenuation map was less than 10% in all tissues. The best results where obtained for bone tissue with a relative error below 5%. In this study scattered transmission and emission events were not compensated.

Nederlandstalige samenvatting

De technieken beschreven in dit proefschrift zijn van toepassing op beeldvorming binnen de nucleaire geneeskunde, meer specifiek, voor de combinatie van positronemissietomografie (*Positron Emission Tomography, PET*) met magnetische resonantiebeeldvorming (*Magnetic Resonance Imaging, MRI*). Emissietomografie is gebaseerd op het speurstof-principe, waarbij een radioactief isotoop wordt ingebouwd in een molecule zonder de fysiologische eigenschappen ervan te wijzigen. De speurstof wordt toegediend aan de patiënt, de straling afkomstig van de radioactieve isotopen wordt gedetecteerd door de PET-scanner en de verdeling van de stof wordt vervolgens gereconstrueerd. In PET maakt men gebruik van isotopen die positronen produceren bij verval. Het positron zal na emissie een korte afstand afleggen en vervolgens na interactie met een elektron een positronium vormen. Bijna onmiddellijk zal een annihilatie plaatsvinden waarbij een paar gammafotonen worden geproduceerd die in tegengestelde richting uitgezonden worden. Deze gammastralen worden gedetecteerd door een ring van PET-detectoren. Met behulp van analytische of iteratieve methoden kan men vervolgens de verdeling van de speurstof in het lichaam reconstrueren. Huidige PET-detectoren laten toe om het tijdsverschil (*Time-Of-Flight, TOF*) tussen de aankomsttijden van de twee fotonen te meten. Ook al is deze informatie niet exact, door deze tijdsinformatie te includeren in de reconstructie kan men in een kortere tijdspanne een betere beeldkwaliteit verkrijgen.

Het verkrijgen van kwantitatieve PET-beelden wordt bemoeilijkt door een aantal effecten die eigen zijn aan het verval van de isotopen, ontstaan bij de detectie of registratie van het fotonpaar of afhankelijk zijn van eigenschappen van de objecten of patiënten die worden onderzocht. Eén van de belangrijkste effecten is fotonattenuatie. Om hiervoor te corrigeren, dient de verdeling van attenuatiecoëfficiënten binnen het beeldvolume gekend te zijn. Deze verdeling wordt opgeslagen in een attenuatiemap en kan gebruikt worden tijdens de reconstructie om te corrigeren voor attenuatie.

PET-beeldvorming is gedurende de laatste tien jaar geëvolueerd tot multimodale beeldvorming, waarbij functionele PET gecombineerd wordt met anatomische beeldvormingstechnieken zoals computertomografie (*Computed Tomography, CT*) of MRI. PET/CT is een veel gebruikte techniek in klinische praktijk voor de diagnose en opvolging van verschillende aandoeningen. De meeste toepassingen situeren zich binnen de oncologie, neurologie en cardiologie. Anatomische beeldvorming met CT biedt de mogelijkheid om de interpretatie en de diagnostische nauwkeurigheid van de PET-beelden te verbeteren. De detectoren meten de attenuatie van de X-stralen uitgezonden door een röntgebron. Bijgevolg kunnen CT-beelden gemakkelijk herschaald worden om zo een attenuatiemap voor 511 keV-fotonen te bekomen. Recent wordt veel onderzoek verricht naar de combinatie van PET met MRI. Er wordt verwacht dat PET/MRI een interessante techniek kan zijn voor toepassingen waarbij contrast in zachte weefsels een belangrijke rol speelt, zoals in de hersenen of het abdomen. Bovendien kan de MRI-scanner gebruikt worden voor functionele beeldvorming zoals MR-spectroscopie, diffusie gewogen beeldvorming of functionele MRI (fMRI). Recente detectortechnologie laat reeds toe om beide modaliteiten te combineren. Wat de beeldreconstructie betreft, vormt attenuatiecorrectie nog steeds een groot probleem. MR-signalen zijn gerelateerd aan de protondensiteit en relaxatie-eigenschappen van weefsels. In tegenstelling tot CT, kan men de MR-beelden niet op eenvoudige wijze transformeren naar een attenuatiemap. Bijgevolg wordt er bij MR-gebaseerde methodes vaak gebruik gemaakt van segmentatie of atlas-gebaseerde technieken. Deze methodes vertonen echter problemen bij de segmentatie van botweefsel en de longen of het in beeld brengen van de MRI-coils. Verder houdt men geen rekening met de hoge inter- en intra-variabiliteit van de attenuatiecoëfficiënten in weefsels. Bovendien kan men met MRI vaak slechts een beperkt beeldvolume reconstrueren. Transmissiebeeldvorming vormt een alternatieve methode om de attenuatiemap te bepalen in PET/MRI. Toen PET nog niet gecombineerd werd met CT, werd meestal een roterende transmissiebron gebruikt. Bovendien kan de emissiedata zelf gebruikt worden om via complexe algoritmes de verdeling van de attenuatiecoëfficiënten te schatten.

In dit onderzoek werd een nieuwe MR-compatibele methode ontwikkeld om de verdeling van de attenuatiecoëfficiënten van de patiënt in een TOF-PET-opname te bepalen. De methode werkt als volgt: een speurstof wordt geïnjecteerd in een transmissiebron die vervolgens in de PET-scanner wordt geplaatst. Vooreerst wordt een referentie-scan opgenomen. Tijdens deze scan worden enkel gammafotonen afkomstig van de transmissiebron opgemeten, zowel de patiënt als het bed bevinden zich buiten het beeldvolume. Bijgevolg worden de fotonen enkel door de lucht geattenueerd. Vervolgens wordt de patiënt op het bed geplaatst en binnen het beeldvolume gebracht. Een transmissie-scan (TX-scan) wordt opgenomen. Tijdens deze scan zullen de fotonen afkomstig van de transmissiebron door de patiënt en het bed geattenueerd worden. Door de PET-data gemeten tijdens de transmissie-scan te vergelijken met de data opgenomen tijdens de referentie-scan kan de verdeling van de attenuatiecoëfficiënten bepaald worden. Indien de transmissie- en emissiedata simultaan opgemeten worden (TEX-scan), kan de tijdsinformatie (TOF) aangewend worden om de transmissiedata van de emissiedata te scheiden. Hierdoor hoeft men geen PET- of MRI-acquisitietijd te verliezen voor het afleiden van de attenuatiemap. De methode werd geëvalueerd in drie fasen: in de eerste plaats met simulatiestudies, vervolgens met experimentele data opgenomen met de Gemini TF PET/CT en de Ingenuity TF PET/MRI-scanners en finaal met patiëntenstudies opgenomen met de Ingenuity TF PET/MRI-scanner.

In een simulatiestudie in GATE werd de methode geëvalueerd met simultaan opgemeten transmissie- en emissiedata van een humaan torsofantoom. Hiervoor werd eerst een model van de Gemini TF PET-scanner ontwikkeld. Vervolgens werd een transmissiebron gedefinieerd in de vorm van een annulus. De bron werd geïnjecteerd met 18 MBq ^{18}F-FDG. Een referentie-scan van 3 minuten werd gesimuleerd. Vervolgens werd een gedigitaliseerd humaan torsofantoom verkregen met behulp van het NCAT-softwarepakket. Zowel de verdeling van de speurstof als de attenuatiecoëfficiënten werden bepaald. Het fantoom werd in het beeldvolume gebracht en een simultane transmissie- en emissie-scan werd gesimuleerd. Met behulp van tijdsinformatie werd de transmissiedata van de emissiedata gescheiden. Resultaten tonen aan dat met deze opstelling accurate attenuatiemappen verkregen werden (een relatieve fout van minder dan 4% in alle weefsels). Vervolgens werd de attenuatiemap aangewend om de PET-data te corrigeren voor attenuatie. De volgende relatieve fouten t.o.v. de correcte verdeling van de speurstof werden bekomen: minder dan 9% in botweefsel en de longen, 4.3% in een lesie in de longen en minder dan 3% in het myocardium en zachte weefsels.

In een tweede fase werd experimentele data opgemeten met state-of-the-art TOF-PET/CT- en TOF-PET/MRI-scanners. Hiervoor werden fantomen gebruikt. In tegenstelling tot simulatiestudies, kan men bij reële studies de PET-opname niet vereenvoudigen. Beelddegraderende effecten zullen onvermijdelijk de kwaliteit van de attenuatiemappen en de uiteindelijke PET-beelden beïnvloeden. Om dit te voorkomen werden verschillende correctiemethodes voorgesteld. In alle studies werden de willekeurige coïncidenties gecompenseerd met behulp van de *delayed window*-methode. Het verschil tussen de *count rate*-performantie van de referentie- en transmission-scan werd gecorrigeerd met een globale correctiefactor en voor de reductie van ruis werd gekozen voor een regularisatie tijdens de reconstructie. In dit werk werden twee methodes voorgesteld voor de compensatie van de verstrooide coïncidenties afkomstig van de transmissiebron. In de eerste methode tracht men de invloed van de verstooide coïncidenties te verminderen door coïncidenties gevormd door fotonen met een lage energie te onderdrukken. In de tweede methode wordt de fractie verstrooide coïncidenties op elke interactielijn (*Line-Of-Response, LOR*) geschat met behulp van een snelle simulatiemethode, *Single Scatter Simulation (SSS)*. Uit de resultaten van de studies bleek dat de tweede methode de meest accurate attentiecoëfficiënten oplevert. In totaal werden zes fantoomstudies opgenomen. Deze studies werden onderverdeeld in vier groepen: TX-beeldvorming, simultane TEX-beeldvorming, beeldvorming van de botstructuren en torsostudies. De eerste groep bestaat uit twee studies: een TX-scan van een cilinder gevuld met water en een TX-scan van een MR-coil. In de tweede groep werd een TX- en TEX-scan van een antropomorfisch torsofantoom opgenomen en de gereconstrueerde attenuatiemappen werden met elkaar vergeleken. Vervolgens werd onderzocht in welke mate onze techniek bot kan onderscheiden van de omgevende weefsels. Binnen deze groep werden twee studies uitgevoerd: een TX-scan van de kop van een varken en een TX-scan van het Alderson torsofantoom. De laatste groep omvat twee torsostudies. Voor beide fantomen werden weefsels van dieren gebruikt. In de laatste studie werden drie methodes voor het bepalen van de attenuatiemap vergeleken: TEX-gebaseerd, CT-gebaseerd en MR-gebaseerd. De laatste methode is een drie-segment-methode geïnstalleerd op de Ingenuity TF PET/MRI-scanner. Tot slot kan met vier belangrijke conclusies trekken uit deze studies. Ten eerste, alle fantoomstudies tonen aan dat de correctie voor de beelddegraderende effecten noodzakelijk zijn. Ten tweede, wanneer de transmissie- en emissiedata simultaan opgenomen worden, kan de misclassificatie van de ware en verstrooide emissiedata leiden tot een foutieve schatting van de attenuatiecoëfficiënten. Dit werd opgemerkt in de studies uit de tweede en vierde groep. Men kan dit eventueel voorkomen door de concentratie van de activiteit in de transmissiebron te verhogen. Ten derde, de TX- en TEX-gebaseerde methode is in staat alle objecten binnen het beeldvolume te reconstrueren. Ten laatste, om de kwantitatieve PET-beeldvorming te verzekeren dient de PET-data gecorrigeerd te worden voor de attenuatie van fotonen in botstructuren. Dit werd geïllustreerd met de studies uit de derde groep. Visuele inspectie toont aan dat verschillende grotere botstructuren herkenbaar zijn in de attenuatiemappen. Kleine structuren of botweefsel gekenmerkt door een lagere attenuatiecoëfficiënt zijn moeilijker te onderscheiden van de omgevende weefsels.

Vervolgens werd de methode getest op humane data. In totaal werden zes patiëntenstudies opgemeten met de sequentiële Ingenuity TF PET/MRI-scanner en de Brilliance CT-scanner. Beide toestellen zijn beschikbaar in het Mount Sinai ziekenhuis in New York. Er werd een onderscheid gemaakt tussen één studie van de hersenen en vijf studies van de thorax. In de eerste studie onderzochten we de verschillen tussen de TEX-gebaseerde AC en de CT-gebaseerde AC door PET-beelden te vergelijken in de voornaamste regio's in de hersenen. Een kwantitatief verschil van 6.5% tot 13% werd verkregen in de thalamus, het cerebellum, de frontale kwabben, de occipitale kwabben en de witte materie. Voor de studies van de humane thorax, werd de TEX-gebaseerde methode vergeleken met zowel de CT-gebaseerde alsook de MR-gebaseerde methode. Voor botweefsel was het kwantitatief verschil tussen de TEX-gebaseerde AC PET-beelden en de CT-gebaseerde AC PET-beelden 18.7% minder dan het kwantitatief verschil tussen de MR-gebaseerde AC PET-beelden met de CT-gebaseerde AC PET-beelden. Voor de longen en het zachte weefsel was dit verschil 5%. Deze goede resultaten kon men echter enkel bekomen door de TEX-gebaseerde attenuatiemappen te herschalen met de histogramgebaseerde schalingstechniek.

Tenslotte werd de transmissiegebaseerde techniek verbeterd door de annulus-vorm te vervangen door een vast aantal stationaire lijnbronnen. Net als bij de annulus-transmissie-methode, wordt een attenuatiemap bekomen door een referentie-scan te vergelijken met een transmissie-scan in een iteratief algoritme. Omdat nu lijnbronnen worden gebruikt kan men echter de scheiding van de transmissiedata in een TEX-scan op basis van tijdsinformatie (TOF-gebaseerde methode) verbeteren door ook die LORs te verwijderen die geen enkele lijnbron doorkruisen (de LOR-gebaseerde methode).

De methode werd eerst geëvalueerd met een simulatiestudie in GATE. Hiervoor werd een model van een prototype LaBr$_3$ TOF-PET-scanner gedefinieerd, alsook de lijnbronnen die dienst doen als transmissiebron. Vervolgens werd een gedigitaliseerd humaan torsofantoom verkregen met behulp van het NCAT-softwarepakket. Eerst werd de LOR-gebaseerde methode voor de extractie van de transmissiedata vergeleken met de TOF-gebaseerde methode. Resultaten tonen aan hoe bij een configuratie van 24 lijnbronnen de misclassificatie van de emissiedata (*Emission Rejection Rate, ECR*) verbetert van 1.13% tot 0.45%. Voor de misclassificatie van de verstrooide emissiedata werd een vermindering van 4.32% tot 2.29% bekomen. Een kwantitatieve verbetering tussen 10% en 25% werd gezien in de attenuatiecoefficienten van botweefsel, de longen en zachte weefsels. Hierbij werd enkel gecorrigeerd voor willekeurige coïncidenties en *count rate* effecten. Verder werd de methode toegepast op een fantoomstudie met de $LaBr_3$ TOF-PET-scanner, beschikbaar in de afdeling radiologie van de Universiteit van Pennsylvania (UPENN), Philadelphia. Hiervoor werd een antropomorf torsofantoom gebruikt. Er werd een TX- en TEX-scan opgemeten. De relatieve fout van de attenuatiecoëfficienten in zowel de TX- als de TEX-gebaseerde attenuatiemappen was minder dan 10% in alle weefsels. De beste resultaten werden bekomen in het botweefsel, waar een relatieve fout onder de 5% werd gezien. Ook hier werd niet gecorrigeerd voor de verstrooide coïncidenties.

Chapter 1

Introduction

1.1 Context

The work presented in this dissertation is situated in the field of nuclear medicine. In our research we mainly focus on Positron Emission Tomography (PET). PET imaging is based on the tracer principle which states that a molecule labeled with a radioactive isotope participates in the metabolic activity of the human body in a similar way as the non radioactive molecule. In PET imaging, radioisotopes that undergo positron emission decay are used. The tracer is injected in the patient and the radiation is detected by a PET scanner. Subsequently, an analytical or iterative algorithm is applied to reconstruct the tracer distribution. PET is a functional imaging technique characterized by a very high sensitivity and low spatial resolution. Additionally, PET image degrading effects compromise the diagnostic accuracy. One of the major effects is photon attenuation. In order to improve the diagnostic accuracy, PET imaging has evolved into multi-modality imaging were PET scanners are combined with anatomical imaging techniques such as Computed Tomography (CT) or Magnetic Resonance Imaging (MRI). Today, PET/CT has been the method-of-choice for hybrid imaging in clinical practice. CT-images provide anatomical landmarks which improve the interpretation of the PET images and the CT-image can be converted easily into attenuation maps using a bilinear scaling technique. Lately, there is also a growing interest in combining PET and MRI. MRI has several advantages over CT. MRI exhibits an excellent soft tissue contrast and provides complementary functional information through the use of techniques such as MR spectroscopy, diffusion weighted imaging or functional MRI (fMRI). Finally, MRI does not impose additional radiation exposure to the patient and fully simultaneous PET/MRI is feasible. To obtain comparable PET image quality in PET/MRI as in PET/CT, one of the major difficulties that needs to be addressed is the correction of the PET image for photon attenuation. The probability of photon attenuation depends on the electron density of tissues while the MRI signals are related to proton densities and relaxation properties. A direct conversion is therefore not possible. Most research groups rely on segmentation and/or atlas registration techniques to derive attenuation maps with acceptable quality. However, for the MR-based methods the notion of prior knowledge about the attenuation coefficients or anatomical properties of the patients remain.

Other methods can be used to obtain an attenuation map. In standalone PET, a transmission scan was used to derive the attenuation map. For this purpose, orbiting pin sources or ring source of a long-live positron emitter were used. Later single sources like ^{137}Cs were used. These sources are characterized by higher energies which improves tissue penetration and single photon methods allow higher collection rates and therefore shorter scan times.

In this work we propose to derive the attenuation map from a transmission scan using an annulus-shaped source or a fixed number of stationary line sources. The transmission source is filled with a solution containing a positron emitter and is positioned inside the FOV of the PET scanner. First a blank reference scan is acquired. Subsequently, the patient in placed on the table and moved inside the bore of the PET scanner and a transmission scan is acquired. By using Time-Of-Flight (TOF) information the transmission scan can be acquired simultaneously with the emission data reducing the total acquisition time. Additionally, no MRI scanning time is needed for the purpose of attenuation correction.

1.2 Outline

The PET imaging technique is presented in chapter 2. We start with a brief history, followed by a detailed explanation of the physics of positron emission and the PET scanner as a coincidence detection device. Subsequently, the PET image degrading effects and simulation methodology are discussed and finally the primary clinical applications of PET are presented. Next we show how PET evolved into hybrid imaging techniques such as PET/CT and PET/MRI. Thirdly, we present how the acquired PET data can be reconstructed into a PET image. Finally, we discuss the major goal of this work, namely, how the attenuation map can be derived in a TOF PET/MRI system in order to correct the PET data for attenuation.

In chapter 3 we introduce a transmission-based attenuation correction technique using a positron emitting source. First the basic concepts of the method are described. Next, we give an overview of the simulation models that were used to validate the method followed by the results obtained. Additionally, the transmission radiation dose delivered to the patient is discussed.

In the next chapter the method is evaluated with experimental data on the Gemini TF PET/CT and Ingenuity TF PET/MR scanners. First we discuss how to compensate for the image degrading effects compromising the accuracy of the reconstructed attenuation coefficients. Next an overview of all the phantom studies is given. Subsequently, each phantom study is discussed in detail and a quantitative evaluation of the reconstructed attenuation maps as well as PET images are presented. Finally, we discuss the results and draw the most important conclusions.

Further validation is presented in chapter 5 with clinical data of 6 patients. One human brain study and 5 thoracic studies are presented. First we give an overview of the PET/MR and CT data acquisitions as well as the image co-registration and the methods that were used to derive the attenuation maps from all three modalities. Subsequently, for both the brain and thoracic studies, a quantitative evaluation of the reconstructed attenuation maps and PET images is presented. In the brain study, the transmission-based attenuation maps were compared with the CT-based attenuation map while in the thoracic studies we also include a comparison to the MR-based attenuation maps obtained from the software installed on the sequential TOF PET/MRI scanner.

In chapter 6 we introduce a different approach by replacing the annulus shaped transmission source with a fixed number of positron emitting line-sources. First we discuss how the data is acquired and the transmission data is extracted. Next we present a simulation study in GATE using an NCAT torso phantom. This simulation study was used to validate the method and compare the reconstructed attenuation maps to results obtained from the annulus-based approach. Finally, the method was evaluated with a phantom study on the $LaBr_3$ PET scanner available in the radiology department at the University of Pennsylvania (UPENN), Philadelphia, USA. For this purpose an anthropomorphic torso phantom was used. The results obtained from the transmission experiments are presented and discussed at the end of the chapter.

A general overview of the most important results obtained during this thesis, along with a conclusion and future research possibilities is given in the final chapter.

Chapter 2

Positron Emission Tomography

2.1 Introduction

In this chapter we will provide an overview of the scientific background relevant to this work. First the basic concepts of Positron Emission Tomography (PET) and its use in nuclear medicine are described. We will show how Time-Of-Flight (TOF) technology has improved PET as a diagnostic tool and give an overview of the physical limitations of a PET acquisition system. In the next section, we will introduce multimodal imaging, in particular we will show how advances in technology and biomedical science have led to the integration of functional PET imaging with other imaging modalities such as Computed Tomography (CT) or Magnetic Resonance Imaging (MRI). The basic principles of PET image reconstruction are introduced in the third section. The final section is dedicated to attenuation correction in PET, the core subject of this work.

2.2 PET imaging

2.2.1 Short history

A timeline of the most important events that have led to the development of the first PET scanner can be found in figure 2.1. Emission tomography (ET) is based on the tracer principle, proposed by George de Hevesy in 1911 [10]. This principle states that an atom in a molecule which takes part in

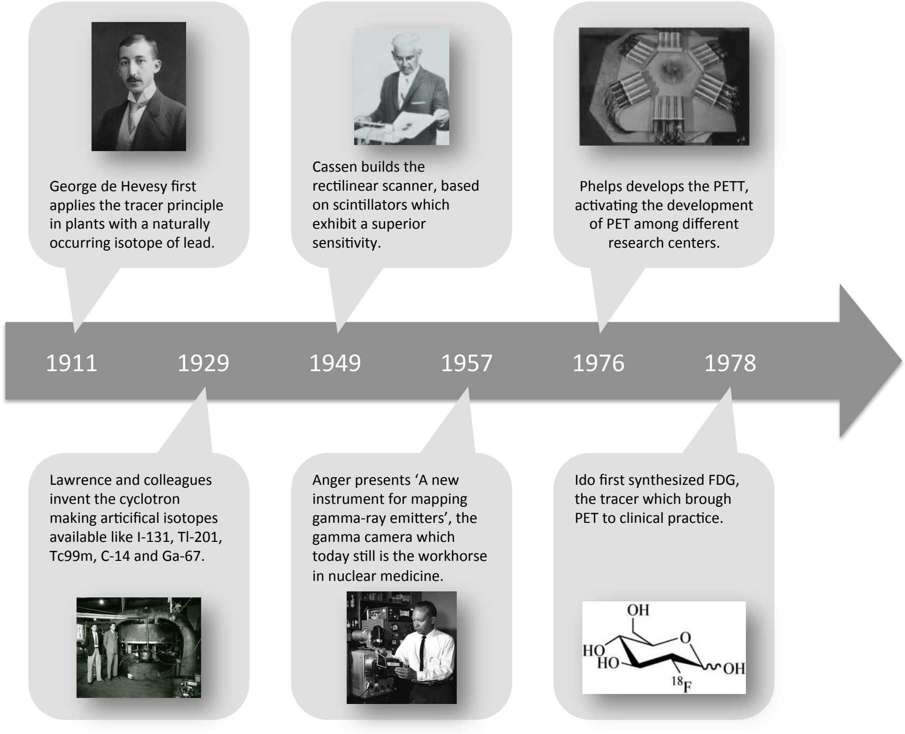

George de Hevesy first applies the tracer principle in plants with a naturally occurring isotope of lead.

Lawrence and colleagues invent the cyclotron making articifical isotopes available like I-131, Tl-201, Tc99m, C-14 and Ga-67.

Cassen builds the rectilinear scanner, based on scintillators which exhibit a superior sensitivity.

Anger presents 'A new instrument for mapping gamma-ray emitters', the gamma camera which today still is the workhorse in nuclear medicine.

Phelps develops the PETT, activating the development of PET among different research centers.

Ido first synthesized FDG, the tracer which brough PET to clinical practice.

Figure 2.1: Timeline showing the most important developments in the history of nuclear medicine.

the metabolism of an organism can be replaced by one of its radioactive isotopes. By detecting the radiation from these isotopes, the distribution of the tracer can be reconstructed. ET encompasses two main imaging techniques: Positron Emission Tomography (PET) and Single Photon Emission Computed Tomography (SPECT). Both techniques use radioactive isotopes to image physiological processes in the body. In the earliest research, naturally occurring radioisotopes were used. New tracers became available in the 1930s with the development of the first cyclotron by Lawrence and colleagues in Berkeley, California [11]. Although World War II temporarily halted the production of radioactive isotopes, progress resurged partially due to the development of the nuclear reactor during the Manhattan project. Later, two important inventions in the 1950s contributed to the origin of body organ imaging in nuclear medicine: the rectilinear radioisotope scanner by Benedict Cassen and colleagues at UCLA [12] and the gamma camera by Hal Anger and colleagues in Berkeley, California [13]. Cassen assembled the first automated scanning system to image thyroid gland after administration of radioiodine (^{131}I). The scanner was widely used in the late 50s until the early 70s when organ-specific radiopharmaceuticals were developed. The development of the Anger camera led to the design of the first SPECT system and might be regarded as the most important milestone in the development of ET. Later in 1959, coincidence imaging capabilities were added to the camera [14]. Finally, in 1976 the first PET scanner, the PETT III, was developed by Michael E. Phelps and his team with the support of the Department of Energy and NIH [15]. In the late 1970s, the tracer Fluor-Deoxyglucose (FDG) labeled with ^{18}F was first synthesized by Tatsuo Ido and Al Wolf at the Brookhaven National Laboratory [16]. ^{18}F-FDG PET had a significant clinical impact, especially in oncology. During the late 90s and early 2000, PET scanners were combined with Computed Tomography (CT) and widely spread in hospitals around the world.

2.2.2 Positron emission

The tracer principle is based on the insight that a molecule in which an atom is replaced by one of its radioactive isotopes participates in the physiological processes of organs in the same way as the non-radioactive molecule. The distribution of the tracer can be reconstructed by detecting the emission of gamma rays, caused by the decay of the radioactive compound. This concept offers two major benefits when imaging the biological activity in the body: the measurements are non-invasive and picomolar concentrations of substances can be measured due to the high sensitivity.

In PET imaging, the radiopharmaceutical does not emit gamma rays directly. Positron emission is a form of β-decay by which a proton p in an unstable nucleus is converted into a neutron n involving the emission of a positron e^+ and an electron neutrino v_e:

$$p \rightarrow n + e^+ + v_e + E_k \text{ MeV} \tag{2.1}$$

After emission, the positron possesses a certain amount of kinetic energy (E_k), depending on the isotope used. The emitted particle will travel freely, colliding with other atoms and thereby lose energy. When thermal energies are reached, the positron will interact with an electron and form a positronium. At that instance, an annihilation occurs. The combined mass of the positron and the electron is transformed in high-energy gamma rays that travel in (almost) opposite directions. According to Einstein's E=mc^2

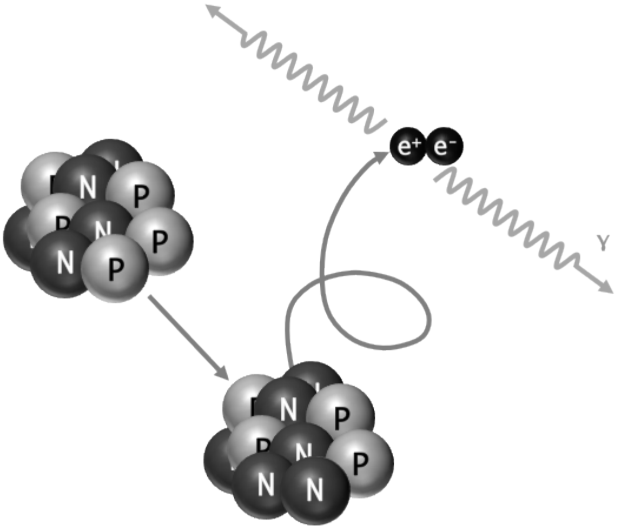

Figure 2.2: Positron emission and annihilation, involving the emission of two 511-keV gamma rays in (almost) opposite directions

equation, each gamma photon has an energy of 511 keV. The process is illustrated in figure 2.2.

Examples of the important positron emitters, their half-life and production method are shown in table 2.1. Because of their relatively short half-lives, a cyclotron has to be available on site for some isotopes. Other isotopes require a specific generator (^{68}Ga, ^{82}Rb). An overview of their applications can be found in section 2.2.6.

^{15}O	^{13}N	^{11}C	^{18}F	^{82}Rb	^{68}Ga
2 min	11 min	20 min	110 min	75 sec	68 min
On-site	On-site	On-site	Cyclotron	Generator	Generator
Cyclotron	Cyclotron	Cyclotron	Regional distribution	^{82}Sr/Rb	^{68}Ge/Ga

Table 2.1: Abbreviated list of positron-emitting isotopes with their half-life and production method.

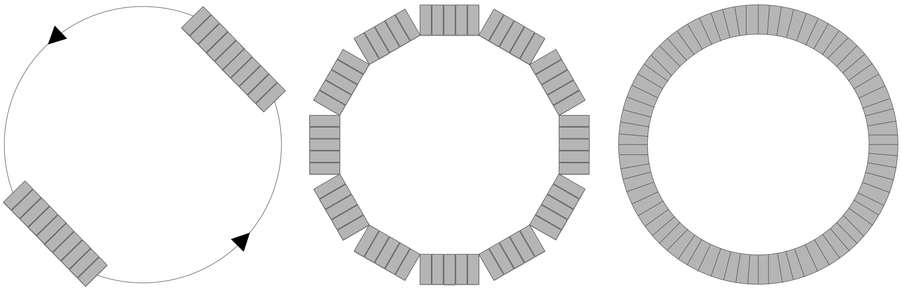

Figure 2.3: PET geometry designs: detectors mounted on a rotating gantry (a), polygonal (b) or circular detector rings.

2.2.3 The PET scanner

2.2.3.1 Gamma detection

PET systems generate images of the distribution of tracers by detection of gamma photons produced after positron annihilation. The gamma rays are detected by a ring of detectors surrounding the patient. Although PET detectors can be organized in different ways (see figure 2.3), today most clinical systems have a polygonal configuration with multiple rings covering an axial extent in the range of 15 to 25 cm. The fundamental components of a conventional PET detector are illustrated in figure 2.4. When gamma photons hit the scintillation crystals they transfer some of their energy through the process of Compton scatter and/or the photoelectric effect. The energy deposited in the crystal is converted to visible or ultraviolet (UV) light. Scintillation materials have a number of properties that are important to PET imaging. To increase the probability of absorption, the crystals should have a high density, ensuring high stopping power. Second, high light output is desirable to achieve both high energy resolution and high detection efficiency. A third important property of scintillation crystals is the shape of the scintillation pulse. A short rise time of the light pulse and the absence of afterglow is needed to allow operation at high gamma count rates. Common scintillation crystals used in PET today have these characteristics [17, 18]. Most of them are inorganic single-crystal scintillators, such as Sodium Iodide doped with Thallium (NaI:Tl), Bismuth Germinate (BGO), Lutetium Orthosilicate (LSO), Lutetium-yttrium oxyorthosilicate (LYSO) or Lanthanum halide ($LaBr_3$:Ce).

A light guide then spreads the scintillation light to the photomultiplier

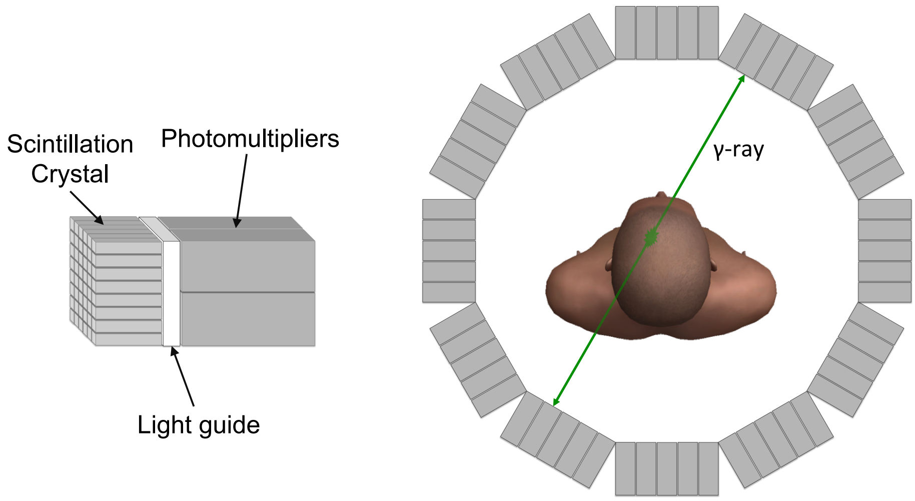

Figure 2.4: Components of a conventional gamma camera. The detector block consists of scintillation crystals, a light guide and an array of photomultiplier tubes.

tubes (PMTs) which convert the optical photons to electric signals. Because of their size (typically 2-3 inches), PMTs are not directly coupled to one crystal but generally cover multiple scintillation crystals. The relative proportion of light on each PMT allows identification of the crystal where the scintillation occurred ([13, 19–21]). The energy and incidence time are also estimated from the PMT pulse. Although PMTs are commonly used in emission tomography because of their high gain, fast response and low noise, PMTs are sensitive to magnetic fields and the size of the PMTs does not allow one-to-one coupling of one crystal to one PMT thereby limiting the ability to manufacture high spatial resolution detectors. With the development of fully integrated PET/MRI in mind, these drawbacks have led to the investigation of alternatives to the PMTs such as the avalanche photodiodes (APDs) and more recently, the silicon photomultiplier (SiPM)[22–28]. An overview of the characteristics of these photon detectors is shown in table 2.2

2.2.3.2 Coincidence detection

The detection of the two gamma photons within a short time frame is registered as a coincidence. The concept of coincidence detection is illustrated in figure 2.5. Once a gamma photon is detected a coincidence circuitry is

	Temperature sensitive	MR-sensitive	Timing resolution
PMT	No	Yes	High
APD	Yes	No	Low
SiPM	Yes	No	High

Table 2.2: PET detectors.

activated. A coincidence is registered if a second photon is detected within a predefined time window (typically 5 - 20 ns). The coincidence is assigned to the line connecting the two detectors triggered by the incident gamma rays. This line is called the Line Of Response (LOR). Today most clinical systems operate in 3D mode, allowing coincidence detection between detectors lying in any ring combination. Some PET detectors will also register the difference in arrival time of the two photons in coincidence. This Time-Of-Flight (TOF) difference can provide extra information on the location of the electron-positron annihilation (see section 2.2.3.3).

2.2.3.3 Time-Of-Flight PET

In conventional PET the location of the annihilation on the LOR can not be determined. In the reconstruction an equal probability for all positions along the LOR is assumed. In TOF PET, the difference in arrival time of the two photons is also registered. This time-of-flight difference Δt is directly related to the distance $d (= c\frac{\Delta t}{2})$ from the center of the LOR to the annihilation as shown in Figure 2.6. However, the measured time difference is not known with infinite precision and therefore the exact location of photon

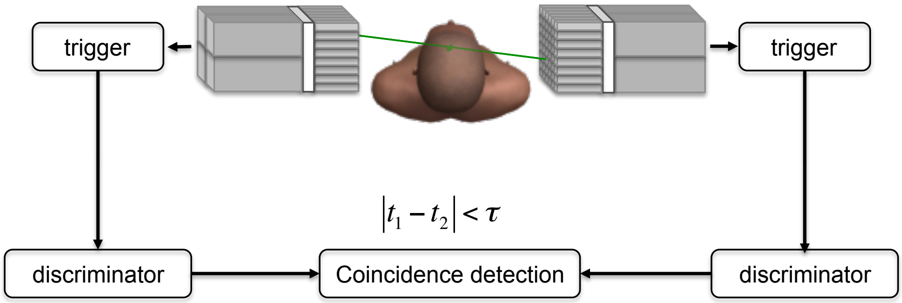

Figure 2.5: Coincidence detection: when two photons hit a PET detector within a predefined time window, a coincidence is registered.

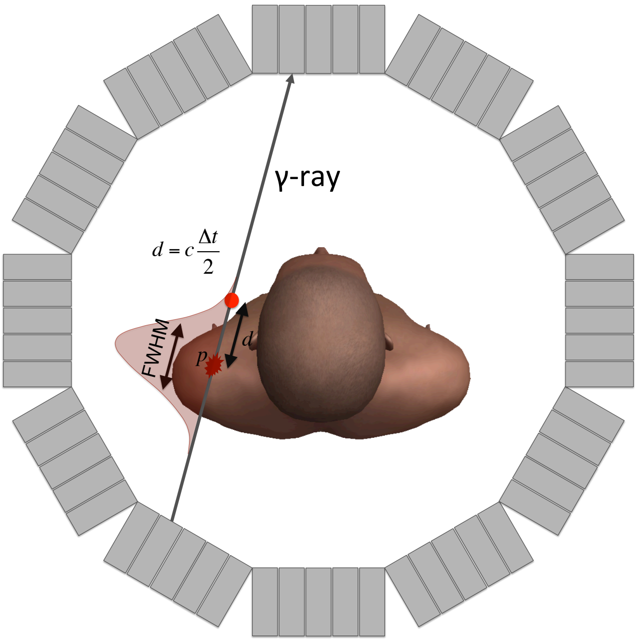

Figure 2.6: The TOF PET principle. The time-of-flight difference Δt is related to the distance $d(= c\frac{\Delta t}{2})$ from the center of the LOR to the annihilation.

emission is not known. This limitation is characterized by the timing resolution $\Delta\tau$ which is determined by the FWHM (Full Width at Half Maximum) of the distribution of Δt given emission point p (figure 2.6):

$$\Delta x \; (= FWHM) = c\frac{\Delta\tau}{2} \tag{2.2}$$

In the early 1980s, the feasibility of TOF PET was introduced [29–31]. Although timing resolutions between 470 and 750 ps were reached with CsF and BaF_2 scintillators, poor spatial resolution and sensitivity caused by the low density, low light output and low photoelectric fraction of the scintillators limited the use of TOF PET to research systems. Since the development of new scintillators in the 1990s, such as LSO, a new generation of TOF PET scanners was designed [32, 33]. The first commercial TOF PET scanner was introduced in 2006 by Philips [34]. Current TOF PET systems are characterized by a TOF resolution of 500 to 600 ps. Recently, a TOF resolution below 400 ps was obtained with a prototype TOF PET scanner equipped with cerium-doped lanthanum bromide ($LaBr_3$) scintilla-

tors [35–37].
It has been shown in a number of studies that TOF leads to a significant improvement of the PET image quality, particularly for oncology applications [1, 38, 39]. A significant improvement in signal-to-noise (SNR) and contrast recovery in both phantom studies, as well as in patients has been reported. In patient studies, the best improvement was obtained for larger patients with lower contrast lesions [39]. The use of TOF allows faster and more uniform convergence during reconstruction while good image quality is achieved for shorter acquisition times. This implies that TOF is desirable in routine clinical practice where the reconstruction time is often limited or in situations were fewer counts are collected such as respiratory gating or dynamic imaging. The clinical benefit of TOF PET is illustrated in figure 2.7 which shows a patient with non-Hodgkin's lymphoma. The higher uptake value in the TOF-based image reconstruction illustrates the superiority of TOF over non-TOF PET.

2.2.4 Image degrading effects

The accuracy of PET imaging is affected by a number of image degrading effects. Some of these effects depend on the physical properties of positron emission and determine the physical limitation of PET imaging. Others are system dependent and occur at the detection level. Most of these can be reduced to some degree by improving the detector technology or adapting the system design parameters. A final type of effects will depend on the subject being imaged. Additional knowledge such as anatomy might be required to correct for these effects . A detailed overview of all effects and their correction methods are discussed here.

2.2.4.1 Effects related to positron emission physics

Positron range and acollinearity

Positron emitters have physical characteristics that limit the spatial resolution of the PET system. Before annihilation, positrons travel a certain distance from the emission point. This finite positron range defines an inherent spatial limitation which is not present in conventional single photon emission techniques. Examples of the positron range in water for different isotopes is shown in table 2.3. The positron range has a limited effect on the resolution in human studies. Additionally, acollinearity of the emitted gamma photons results in an angular uncertainty ($\sim 0.23^\circ$) which also affects the PET resolution, especially when the diameter of the scanner is

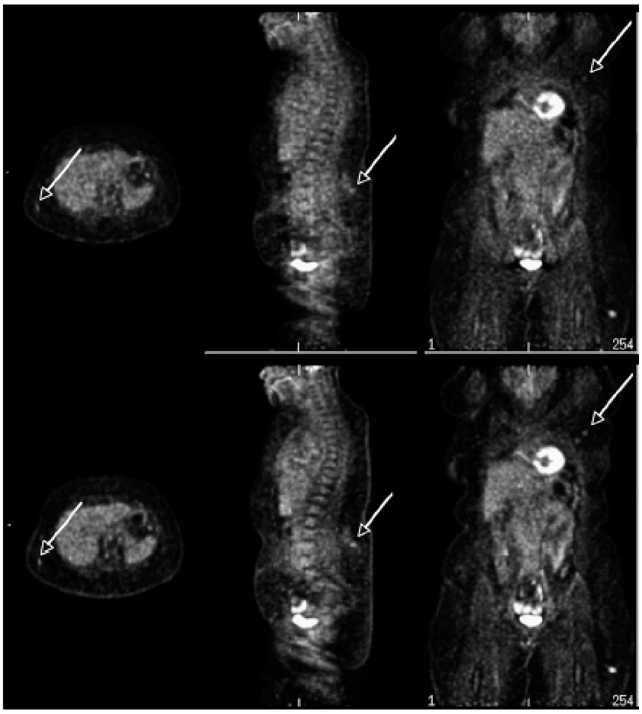

Figure 2.7: Patient with non-Hodgkins lymphoma (140 kg, BMI = 46). Representative transverse, sagittal, and coronal images (not triangulated) for non-TOF reconstruction (top) and the same cross-sectional images for TOF reconstruction (bottom). In each image, the different lesions are seen more clearly in TOF reconstruction than in non-TOF reconstruction. Reprinted with permission [1].

large: a resolution blur close to 2 mm for a diameter of 90 cm.

Poisson noise

Radioactive decay and consequently the emission of positrons is a randomly occurring process and is therefore subject to statistical fluctuations. Literature shows how radioactive decay can best be described with Poisson

Isotope	^{15}O	^{13}N	^{11}C	^{18}F	^{82}Rb	^{68}Ga
FWHM in mm	1.5	1.4	1.1	1.0	1.7	1.7

Table 2.3: Positron range in water (FWHM in mm) for commonly used positron emitting radio-isotopes [8, 9].

statistics [40, 41]. The Poisson nature of radioactive decay, causes noise in reconstructed PET images which is hard to avoid. Post smoothing techniques can be applied, although this could hide important small lesions and thereby influence the diagnostic accuracy. More complex reconstructions include prior information in the algorithm to regulate noise.

2.2.4.2 Effects at detection level

Intrinsic resolution and parallax error

The physical size of the crystals plays a dominant role on the intrinsic resolution of the PET detector due to the fact that the position of interaction within the crystal is not determined. Another resolution limiting effect is the parallax error which worsens the resolution of the reconstructed PET image when a larger fractions of the gamma photons enter the crystals at oblique angles. The resolution of current clinical PET scanners is in the range of 4-6 mm. To avoid resolution broadening, the depth of interaction (DOI) of the gamma photons needs to be accurately determined and the crystal size can be reduced. The physical effects limiting the resolution can also be modeled in the image reconstruction to improve the resolution of the PET images.

Dead-time effects

The performance of PET detectors is limited by the rate at which incoming hits can be processed. Multiple photon interactions can cause a pulse pile up in the PMTs when light pulses overlap significantly. Additionally, electronic devices will need a minimum amount of time to process incoming events and define their energy and timing. As a result, some events will be missed. The amount of missing events is related to the probability that some events will occur within a certain time frame. This probability increases at higher countrates. The time for which a detector is unavailable for photon detection is called the dead time. Dead times are typically in the order of 50 to 900 ns, depending on the detector technology used.

A detection system can be classified as paralysable or non-paralysable. In a non-paralysable system, if a hit is registered then the detector ignores all hits during deadtime τ. A paralysable detector registers every hit and only accepts coincidences if all previous dead times are expired. Subsequently, paralysable systems can be subdivided in type I or type II systems. The difference between the three categories is shown in figure 2.8. Suppose that τ represents the dead time of the system. As τ seconds are needed to process pulse 1, pulse 2 will not be detected by a non-paralysable nor

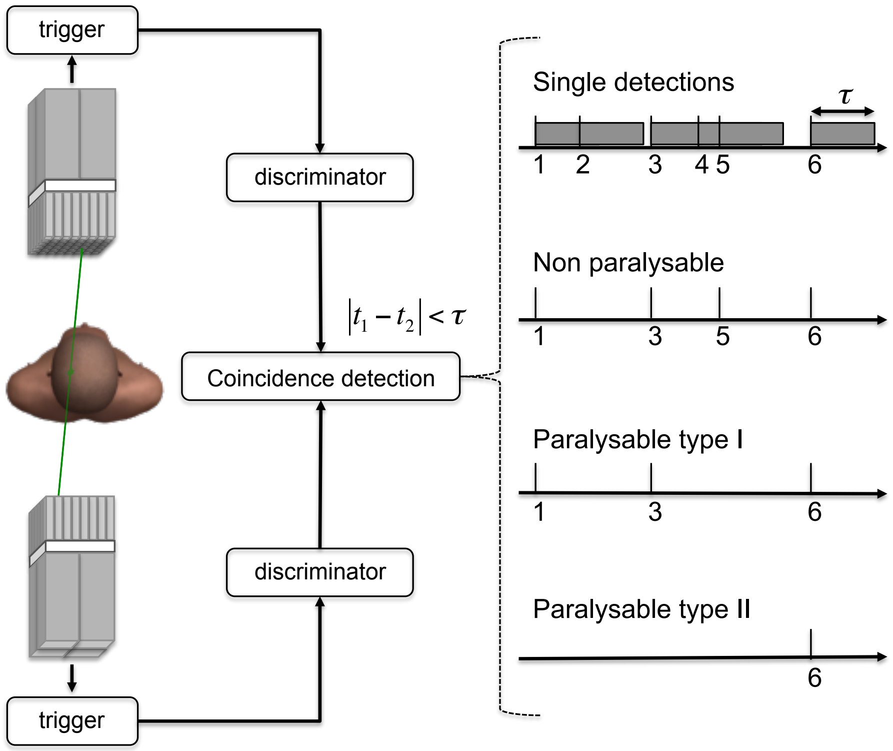
trigger
discriminator
$|t_1 - t_2| < \tau$
Coincidence detection
discriminator
trigger
Single detections
τ
1 2 3 4 5 6
Non paralysable
1 3 5 6
Paralysable type I
1 3 6
Paralysable type II
6

Figure 2.8: A coincidence detection system is classified as paralysable or non-paralysable. Paralysable systems can be subdivided in type I and type II systems. Each hit will cause a dead time of the system. In a non-paralysable system a hit is detected only if previous dead times are expired. In a paralysable system all hits are detected, but a coincidence is only accepted if all previous dead times are expired. Additionally, in a type II paralysable system, energy pile-up can cause a rejection of hits.

by a paralysable system. A type II paralysable system will not detect pulse 1 because the energies of pulse 1 and 2 are added and the total energy falls out of the energy window. This pile-up is ignored in a paralysable type I system. When pulse 4 is initiated, a dead time is only initiated in a paralysable system, whereas the pulse is ignored in the non-paralysable system. Pulse 5 will therefore only be detected on the non-paralysable system. Dead time effects should be considered during reconstruction in order to obtain absolute quantification.

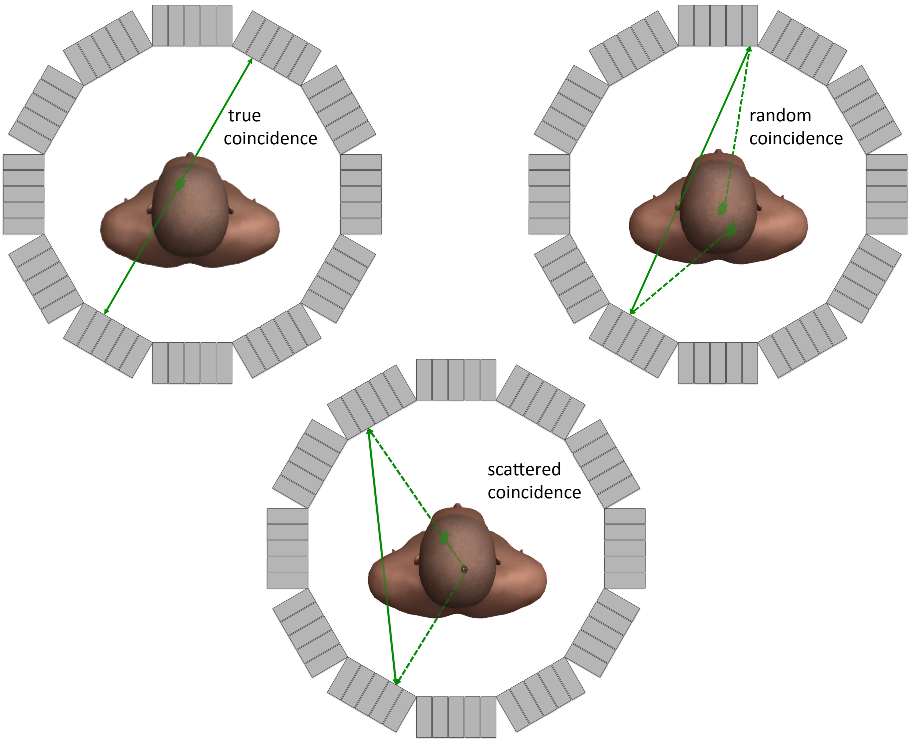

Figure 2.9: Coincidence types: true, random and scattered coincidences.

2.2.4.3 Subject dependent effects

Random and scattered coincidences

Coincidence events can be classified in 3 categories : true, scattered and random events. A random coincidence is one where the two gamma photons arise from two distinct annihilations. While both the true and scattered coincidence type arise from one annihilation, a scattered event is registered when at least one photon has undergone at least one Compton scattering prior to detection. Since a photon changes its direction and loses energy during Compton scattering, it is likely that the scattered coincidence is assigned to the wrong LOR. The three coincidence types are illustrated in figure 2.9.

Random events add unwanted coincidences to the measured data causing a degradation of the quantitative accuracy and contrast recovery in the reconstructed PET image. The amount of random coincidences can be estimated from the singles rate on the PET detectors. The random coincidence rate r_{ij} on the LOR (L_{ij}) defined by crystal pair $\{i, j\}$ can be calculated by:

$$r_{ij} = 2\tau s_i s_j, \tag{2.3}$$

where 2τ is the coincidence time window and s_i and s_j the singles rate on crystal i and j respectively. More commonly, the random fraction is estimated using the delayed window technique [42]. When the first photon is detected a delayed window is opened in parallel with the normal coincidence window. The delayed window has the same length but is shifted in time to ensure only photon pairs emitted from two different annihilations are detected within it. The estimated random fraction can then be used to pre-correct the data before reconstruction. Although this method removes bias it will amplify the noise if no additional smoothing is applied.

Scattered coincidences adversely affect PET image quality by introducing a quantification bias as well as reducing spatial resolution. The quantification bias is typically removed by estimating the scatter and subtracting it from the measured data. Most clinical systems apply algorithms based on theoretical models using the Klein-Nishina formula [43]. This method is called Single Scatter Simulation (SSS) and only gives an estimate of the single scatter along each LOR. Multiple scatter is then also included by multiplying the single scatter estimation with a correction factor. As the scatter distribution is object dependent, information about the anatomy of the patient as well as the emission distribution is required.

Attenuation

After annihilation, the 511 keV photons will travel through tissue before the detectors are reached. During their path, there is a possibility that the photons will interact with matter through the process of Compton scatter or the photoelectric effect. Only a fraction of the emitted photon pairs will therefore hit the detector. This effect is known as attenuation. The fraction of photons that will be transmitted through a slice of homogeneous tissue of thickness L is given by the attenuation factor (AF):

$$AF = e^{-\mu L} \tag{2.4}$$

Where μ represents the tissue-dependent attenuation coefficient. The attenuation coefficient is related to the electron density of the tissue and the energy of the photon. An overview of the attenuation coefficients at 511

Tissue type	μ cm^{-1}
Lung	0.0267
Adipose tissue	0.0927
Soft tissue	0.0968
Liver	0.0977
Spongious bone	0.1100
Cortical bone	0.1300

Table 2.4: Overview of the attenuation coefficients at 511 keV of the most relevant tissues.

keV of the most relevant tissues is given in table 2.4. When two photons in coincidence, emitted from annihilation point *a* travel through a path of continuous attenuation before hitting detectors d_1 and d_2 respectively, the line integral is taken :

$$AF = e^{-\int_{d_1}^{a} \mu(s)ds - \int_{a}^{d_2} \mu(s)ds} = e^{-\int_{d_1}^{d_2} \mu(s)ds} \tag{2.5}$$

The attenuation factor is the product of the probability of attenuation of the two photons in coincidence. Attenuation influences the quantitative accuracy of the PET image. Figure 2.10 depicts the difference between a PET image which is not corrected for attenuation with the same PET data, reconstructed with attenuation correction applied. Attenuation correction is implemented in the reconstruction process. For this purpose the attenuation map, defining the attenuation coefficient at 511 keV for each voxel inside the PET image is used. More details on how the attenuation map can be derived are discussed in section 2.5.

Motion

Motion of the patient or physiological motion of the organs can reduce the PET image quality. For example, respiratory and cardiac motion causes significant motion blur and artifacts in thoracic PET imaging. Typically, motion correction is done by gated imaging [44–46]. For each gate, only data within a specific time frame will be used for reconstruction. The gates are set according to the respiratory or cardiac cycle. Other techniques for tracking motion have also been investigated and proven to be very useful in brain imaging [47].

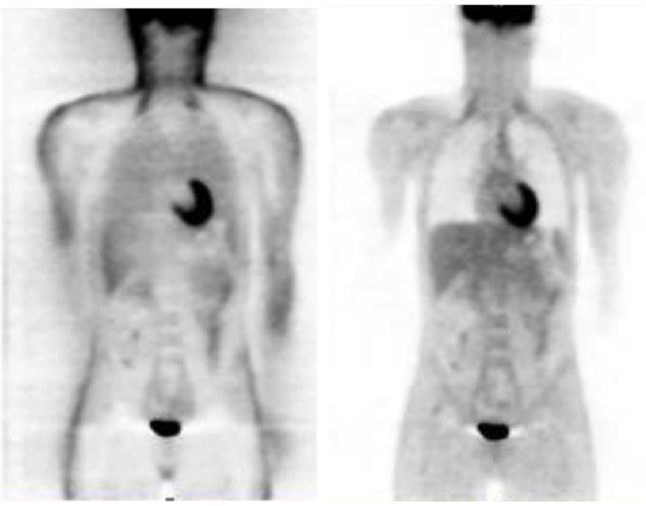
(a) (b)

Figure 2.10: Visual comparison of PET images reconstructed without (a) and with (b) attenuation correction.

2.2.5 Simulation methodology

Simulation methods provide a useful way of evaluating new PET instrumentation or imaging methods without the need to perform time consuming, costly and complicated experiments with real systems. Dedicated simulation packages with accurate and fast emulation of underlying physical processes have therefore become indispensable for instrument designers.

2.2.5.1 Principle of Monte Carlo Simulation

Monte Carlo methods try to solve statistical problems by numerical calculation based on random variable sampling. The use of random sampling to simulate complex systems is not new and has been applied to many fields. In the field of particle physics, interactions between particles were interpreted using cross sections as probabilities. The name "Monte Carlo" refers to a casino in Monaco, which was famous for the random nature of their games offered [48]. H. O. Anger was the first designer to use Monte Carlo techniques in nuclear medicine for the simulation of the physical response of his new scintillation camera [49].

In a Monte Carlo simulation a solution is determined by random sampling of the physical interactions involved in a stochastic process through the use of a pseudo-random number generator. This mechanism involves repetitive calculations, and probability density functions describing each process are required. Depending on the variety of interactions considered, different degrees of realism can be obtained. In the context of positron emission tomography these interactions are positron emission, positron-electron annihilation, Compton scatter, photoelectric effect, photon detection, etc. Sometimes the less important interactions are simplified or neglected to reduce computational complexity. As an example, the process of annihilation could be simplified by only simulating back-to-back gamma photons thereby ignoring positron range and acollinearity. The method generates simulated data close to the data we would obtain in a real situation. Because of the random nature, each outcome will be different if a different seed for the random number generator is chosen.

2.2.5.2 GATE : Geant Application for Tomographic Emission

A well known and validated Monte Carlo simulator for emission tomography is GATE [50]. The software package is based on the physics library GEANT4 developed at the European Organization for Nuclear Research (CERN). In this dissertation we intensively used the simulator to evaluate PET system design and new methods in PET. The major limitation of the software is the high computational cost. Recently, acceleration methods have become available [51]. In our work, simulations were mostly used to illustrate or prove the feasibility of a PET imaging method. Therefore, the models were simplified to allow relatively fast emulation of the PET acquisition process. For example, positron range and acollinearity were neglected. Figure 2.11 shows an acquisition of a cylindrical water phantom of 30 cm diameter and 70 cm length injected with 250 MBq of ^{18}F-FDG. In this simulation a model of the Gemini TF PET scanner from Philips Healthcare was used.

In order to evaluate the performance of a new PET design or imaging method in terms of spatial and temporal resolution, sensitivity, analytical phantoms such as cylinders, spheres or point sources are used. To mimic a clinically relevant situation more complex phantoms are required. GATE allows including anthropomorphic phantoms in the simulation. The first digital anthropomorphic phantoms were derived from high resolution CT data [52]. Later, the MCAT and NCAT phantoms were developed [2, 53]. Recently a new version of the phantom, called the XCAT phantom was introduced [54]. In Figure 2.12 the XCAT male and female phantom is shown. The phantom can be generated using a software package. Many detailed structures can be included to tune the phantom for a particular

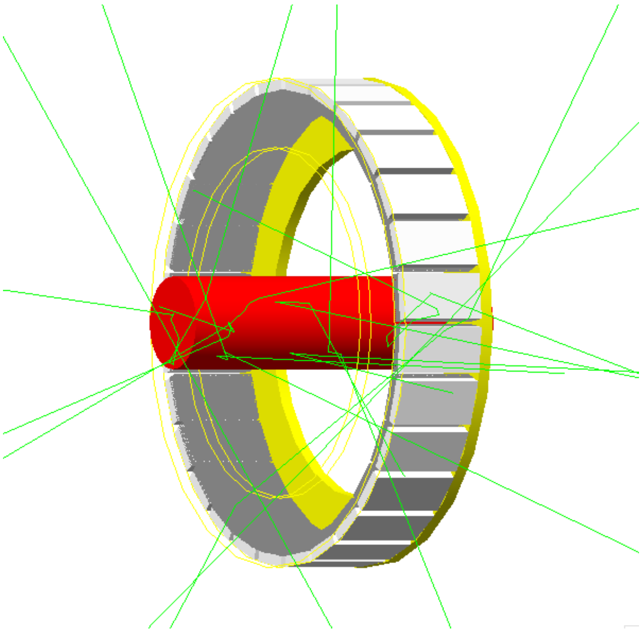

Figure 2.11: GATE simulation of a cylindrical water phantom injected with ^{18}F-FDG. A model of the Philips Gemini TF PET scanner is shown. Green lines represent photon paths.

need. In our work, only the main organ volumes were included while heart and respiratory motion was neglected.

2.2.6 Clinical PET imaging

PET is a functional imaging technique that provides information about the biochemical and physiological processes in the human body. Typically, a change in these processes precedes structural changes when the body is in a disease state. Therefore, PET imaging could permit an earlier diagnosis. The information can also be useful for prognosis and therapy follow up. Non-invasive PET imaging started as a research tool in the late 1970s. Because of technological advances and the production of a wide range of tracers, PET became an important clinical tool for the diagnosis, staging and monitoring of disease in patients. A short list of PET tracers involved in these applications is shown in table 2.5. In this section some of the important clinical applications of PET are discussed. The interested reader is referred to following papers covering more detail: [3, 55, 56].

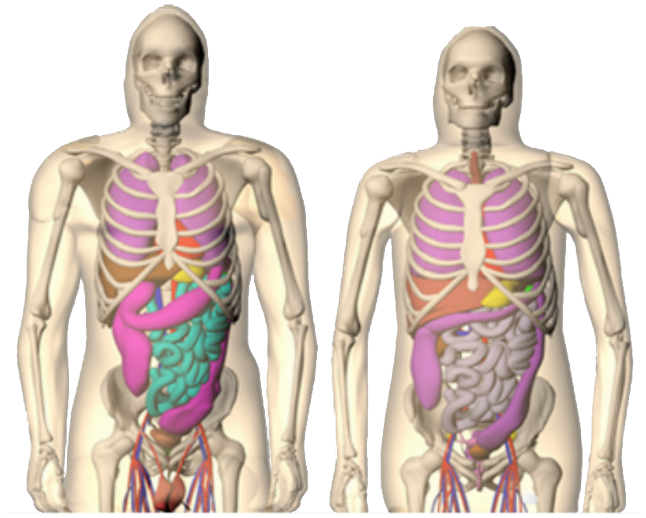

Figure 2.12: Male and female digital XCAT phantoms [2]

2.2.6.1 Oncology

In clinical oncology, PET imaging is used for tumor detection and differentiation between benign and malignant tumors, tumor staging, restaging and detection of recurrent disease. Clear benefit is obtained with ^{18}F-FDG PET in the assessment of patients with lung, lymphoma, colon, and melanoma cancer. ^{18}F-FDG uptake has been shown in tumors of the head and neck, ovary, breast, musculoskeletal system, and neuroendocrine system as well [57]. Figure 2.13 shows the maximum intensity projections of a FDG-PET scan of a patient with melanoma. Metastases are detected in the left axilla, skin, retrosternal region, liver and spleen.

Other than ^{18}F-FDG, ^{18}F-FMISO can be used for imaging tumor hypoxia, ^{18}NaF for bone metastases, ^{11}C-Acetate and ^{11}C-choline for prostate cancer , etc. For a complete overview the reader is referred to [56].

2.2.6.2 Cardiology

PET imaging has become a useful diagnostic tool to determine the vascular condition of the heart. Cardiac PET imaging provides accurate assessment of the blood flow and metabolism of the myocardium as well as the risk of developing cardiac disorders such as coronary artery disease and myocardial viability [55, 58]. In conventional cardiac PET imaging ^{82}Rb and ^{13}N-

Isotope	Tracer	Function	Application
^{11}C	Methionine	Protein synthesis	Oncology
^{11}C	Flumazenil	Benzodiazepine Receptor antagonist	Epilepsy
^{13}N	Ammonia	Blood perfusion	Myocardial perfusion
^{82}Rb	Ammonia	Blood perfusion	Myocardial perfusion
^{15}O	Carbon dioxide	Blood perfusion	Brain activation Studies
^{15}O	Water	Blood perfusion	Brain activation Studies
^{18}F	Fluoro-deoxy-glucose	Glucose metabolism	Oncology, cardiology, Neurology
^{18}F	Fluoride ion	Bone metabolism	Oncology
^{18}F	Fluoro-mizonidazole	Hypoxia	Oncology, response to radiotherapy

Table 2.5: Abbreviated list of positron-emitting isotopes, tracer compounds and their typical applications.

ammonia are used for myocardium perfusion imaging and ^{18}F-FDG PET can be used to visualize ischaemic heart disease in the myocardium.

2.2.6.3 Neurology

Brain activity can be imaged by measuring the amount of oxygen-rich blood flowing to various regions inside the brain. For this purpose dihydrogen oxide labeled with the ^{15}O isotope can be administered to the patient. Because of the short half-life (2.03 min) a cyclotron has to be available on site. A more practical approach is to use ^{18}F-FDG, as brain utilizes glucose in its metabolism. Measuring the brain activity can be useful for a number of applications. An early diagnosis of the **Alzheimer disease** can be detected by a decrement in cerebral blood flow, oxygen utilization and glucose metabolism in the parietal and temporal lobes [59]. An early diagnosis may help identify individuals at risk, and allow initiation of therapy to slow down disease progress. **Parkinsons disease** is the result of loss of dopaminer-

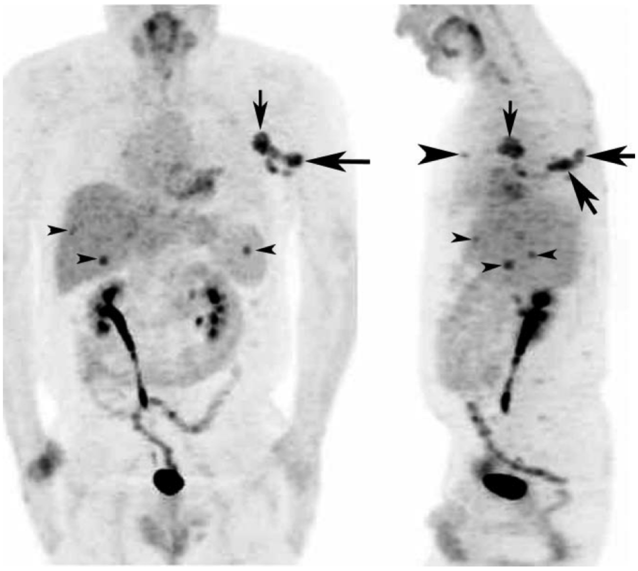

Figure 2.13: Frontal (left) and left lateral (right) maximum intensity projections from FDG PET scan in a 46-year-old man with history of melanoma removed from left upper back who then presented with pigmented cutaneous lesions extending from biopsy site to left axilla. Patient was referred for restaging of melanoma. Multiple sites of disease are visible, including local recurrence at biopsy site with in-transit cutaneous metastases (large arrows), left axillary metastases (small arrows), retrosternal metastasis (large arrowhead), and splenic and hepatic metastases (small arrowheads). Reprinted with permission [3].

gic neurons in the substantia nigra which can be detected with ^{18}F-DOPA PET and ^{18}F-FDG PET. ^{11}C-FMZ PET can be useful in localizing the epileptogenic focus when investigating **partial epilepsy**. Finally, PET-FDG imaging shows changes in the brain function beginning many years before clinical presentation of the **Huntington's disease** [60].

2.3 Hybrid imaging

Hybrid imaging involves combining multiple imaging modalities to improve the diagnostic accuracy and/or to introduce new applications. The last decade a lot of research has focused on combining functional imaging techniques, such as PET and SPECT, with anatomical imaging techniques, such as CT and MRI. Initially, the imaging modalities were combined by acquiring both images separately, followed by co-registration with software. Today, almost perfect registration is achieved by developing sequential designs or fully integrated systems. In this section we will discuss state-of-the-art PET/CT and PET/MRI hybrid imaging.

2.3.1 PET and Computed Tomography

The usefulness of PET as a diagnostic tool is limited by its poor spatial resolution and the absence of clear anatomical landmarks. Correlating PET images with structural images derived from CT significantly improves diagnostic accuracy [61–63]. As an additional advantage, CT images can easily be scaled to attenuation maps at 511 keV to correct the PET data for attenuation, hereby replacing the lengthy transmission scans which were acquired prior to the emission scan in stand-alone PET. Today, most PET centers have a sequential PET/CT scanner installed. Numerous studies have shown the benefit of PET/CT hybrid imaging. Bar-Sholam et al. assessed the additional value of hybrid PET/CT over stand-alone PET and stand-alone CT with a study of 204 cancer patients with 586 sites suspicious of disease [64]. An improved diagnostic interpretation of 49% of cancer patients and 30% of sites was reported. The additional value includes precise lesion characterization, lesion localization and lesion detection. In 14% of cancer patients, combined PET/CT had an impact on the patient management which included referral and planning of surgery, chemotherapy, radiotherapy, exclusion of cancer and guidance in invasive diagnostic procedures. In another study which involved 91 patients with histologically proven malignancy and 190 suspected sites of disease, Israel et al. reported improvements in accuracy using PET/CT [63]. They conclude that hybrid PET/CT provides new diagnostic opportunities and both structural changes as increased cell metabolism should be considered in PET imaging. All systems nowadays are combined PET/CT systems.

2.3.2 PET and Magnetic Resonance Imaging

Magnetic Resonance Imaging (MRI) can also be used as an anatomical imaging technique in combination with functional PET. MRI has a high anatomical resolution and its soft-tissue contrast is superior to CT [65–67]. Therefore MRI is expected to be the method-of-choice for diagnostic problems in oncology associated with soft-tissue regions (e.g., tumors in the pelvis, the head-and-neck region, or the brain.) [66, 68–70]. Secondly, while CT delivers a significant amount of radiation dose to the patient, radiation exposure will be limited in a combined PET/MRI system. This is especially important in pediatric studies were radiation dose is a matter of great concern. Thirdly, PET and MR systems can be fully integrated enabling simultaneous acquisition, creating an opportunity for motion correction, multi-modal tracers, etc. [71]. Additionally, MRI is more than an anatomical imaging technique and true value may therefore be found in simultaneous acquisition of PET with functional MRI imaging techniques (e.g., Diffusion Weighted Imaging (DWI), Dynamic contrast-enhanced MRI, fMRI and MR spectroscopy).

Despite the great potential of PET/MRI, three major issues have prolonged the implementation of fully integrated PET/MRI systems into clinical practice. The first is adapting the PET detectors to make them MR-compatible; second, choosing a proper design for the integration of the PET and the MRI scanner, and finally, creating attenuation maps for accurate PET imaging. These issues will be discussed in the remainder of this section.

2.3.2.1 MR-compatible PET detector design

Traditional PET detectors, based on PMTs, are sensitive to magnetic fields. Optical fibers can be used to guide the light outside the magnetic field for detection with PMTs[72, 73] or the PMTs are replaced with avalanche photodiodes (APDs) [74–76]. The disadvantage of the APDs is that these detectors have bad timing characteristics and their performance is temperature dependent. Lately, Silicon Photon Multipliers (SiPM) have been proposed which allows the integration of fast PET detectors in a MR environment [77–79] and enable TOF measurement. At the crystal level, Lutetium oxyorthosilicate (LSO) and Bismuth germinate (BGO) have been shown to have similar and the lowest magnetic susceptibility showing no significant artifacts on the MRI images [80].

2.3.2.2 System design

The method-of-choice for combining PET and MRI depends on a trade-of between the cost and the clinical usage of the system. Today, three models of system design are considered (see figure 2.14): first, a sequential setup similar to the current PET/CT systems, second, a removable PET insert placed inside the bore of the MR system, third, a fully integrated PET/MRI system allowing simultaneous acquisition.

A sequential design is the most straightforward and least challenging way to combine a PET and a MRI system. The patient is placed on a table that moves through the MRI and PET FOV. From a hardware perspective, no magnetic field-insensitive PET detectors are required and most interference can be solved with limited shielding. On the software side, limited adaptation will be needed to allow interaction between both systems and automate the co-registration process. The major disadvantage of this construct is the inability to perform simultaneous PET/MRI imaging which can lead to longer acquisition times and co-registration errors due to patient motion.

Simultaneous PET/MRI can be achieved by placing a PET insert inside the bore of the MRI scanner. However, because of space limitations this approach is limited to brain imaging. An even more challenging approach is to fully integrate the PET detector and electronics within the MRI system. Different approaches have been investigated. The first approach relies on the use of a split superconducting magnet. The magnet is split in two elements leaving a gap in which a PET scintillator ring can be inserted. In a field-cycled PET/MRI system, the PET acquisition takes place during certain temporal frames free of magnetic field. Therefore two separate and dynamically controllable magnets are used. Subsequently, the PET detector ring can also be integrated between the gradient and the body coil of the MR. Most issues with this design option are related to the limited space available leading to significant constraints on the PET system.

2.3.2.3 Attenuation correction

Attenuation correction remains one of the major issues in PET/MRI. Contrary to CT, the attenuation map can not directly be derived from the MRI image, due to the fact that MR signals correlate with proton densities and relaxation properties of tissue. Possible solutions to this problem rely on segmentation or atlas registration techniques, transmission-based techniques or on the emission data itself. The reader is referred to section 2.5 for more details.

2.3.2.4 Prototypes and clinical systems

Pre-Clinical systems

The first MR-compatible PET detectors were developed by Cherry's group at UCLA [81]. An 38-mm diameter LSO ring was constructed and installed within a 0.2-T MRI scanner [72]. 4-m long optical fibers were used to guide the light from the scintillator to the PMTs located outside the magnet where the magnetic field was below 10 mT. A similar system was used by Carson et

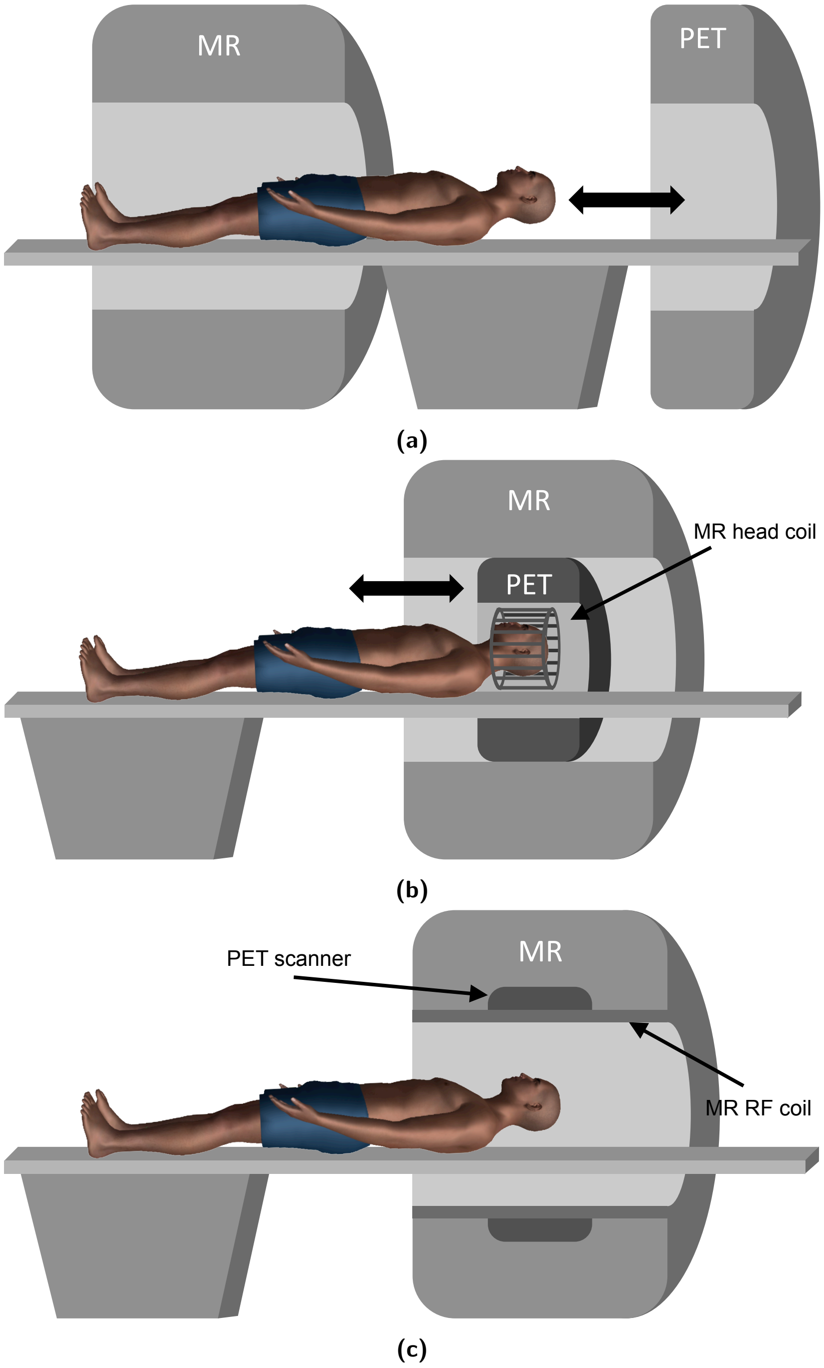
MR
PET
MR
MR head coil
PET
PET scanner
MR
MR RF coil

(a)

(b)

(c)

Figure 2.14: Three models for combining PET and MRI systems: sequential (a), a PET insert (b) or fully integrated (c).

al. (1998), who reported the first simultaneously acquired PET/MRI images for small animals [82] and Raylman et al. where 20-layered crystal blocks were inserted into a 1.5T clinical MRI scanner [83]. A major drawback of these PET inserts is the signal loss due to the long light guides [84, 85]. In addition, a lot of space is consumed by the optical fibers.

In the work of Pichler and Catana et al., APDs have been used to replace the magnetic-sensitive PMTs [85, 86]. Later, Schlyer et al. mounted an APD-based PET detector, called the RatCap, on the animal head and acquired simultaneous PET/MRI data [87].

The introduction of fully integrated systems started with the split magnet approach applied by Lucas et al. on a 1 T actively shielded superconducting magnet [75]. A 8-cm gap in the radial direction was used to house 24 12x12 LYSO block detectors. A field-cycled small animal PET/MRI was demonstrated at the 2007 Society of Nuclear Medicine Meeting [88].

Clinical systems

The first clinical system was based on a removable APD-based brain PET

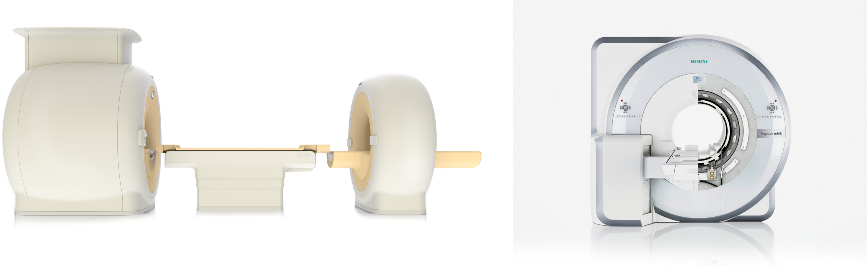

(a)

(b)

Figure 2.15: Two commercial whole body PET/MRI scanners: the sequential Ingenuity TF PET/MR by Philips Healthcare (a) and fully integrated Biograph mMR by Siemens (b).

scanner that fits into a 3 T clinical Magnetom Trio MRI scanner (Siemens Medical Solutions) [85, 89, 90]. Recently, more research has been done on the development of whole body PET/MRI systems. Two commercial whole-body PET/MRI systems are currently available : the Ingenuity sequential TOF PET/MRI (Philips Healthcare) and the Biograph mMR fully integrated PET/MRI from Siemens (figure 2.15). The Ingenuity combines a Gemini TOF PET scanner with an Achieva 3T X-series MRI system in a sequential setup. A rotating patient table is installed in between both scanners to switch from one modality to the other. The Biograph mMR is the first fully integrated PET/MRI system. The PET detectors are APD-based allowing operation in a high magnetic field. Hence, truly simultaneous acquisition of PET and MRI data is possible. A downside of the APD technology is that the detectors are not TOF capable. Despite all issues related to hybrid PET/MRI imaging, a study of Drzezga et al. [91] demonstrates the feasibility of PET/MRI in clinical practice. 32 patients with different oncologic diagnoses underwent a PET/CT and subsequent PET/MRI scan. Quantitative analysis showed a high correlation between the mean Standardized Uptake Value (SUV) measured with both systems in lesions and background tissue. Although some studies indicate the superiority of combined PET/MRI over PET/CT for specific applications, evidence in literature is limited and evaluation of the benefits of PET/MRI is still ongoing [4, 70, 92]. An example demonstrating the advantage of combined MR and PET over PET/CT is depicted in figure 2.16: a transverse slice of the torso of a 55-y-old patient with metastatic breast carcinoma is shown.

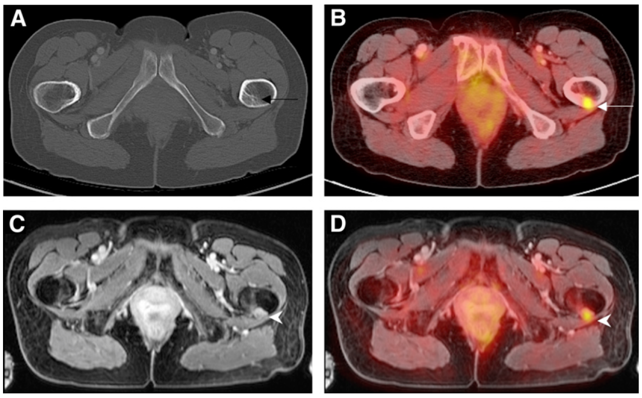

Figure 2.16: A 55-y-old patient with metastatic breast carcinoma. Unremarkable sclerotic lesion (arrow) of left femoral bone on axial CT (A) was diagnosed as metastasis only because it was strongly 18F-FDG-avid on PET/CT (B). Whole-body MRI using T1- weighted fat-suppressed sequence (C) clearly depicts metastasis as contrast enhancing mass (arrowhead). Corresponding PET/MRI image (D) demonstrates precise metabolic-anatomic correlation of this technique for bone imaging. Reprinted with permission [4].

2.4 Image reconstruction

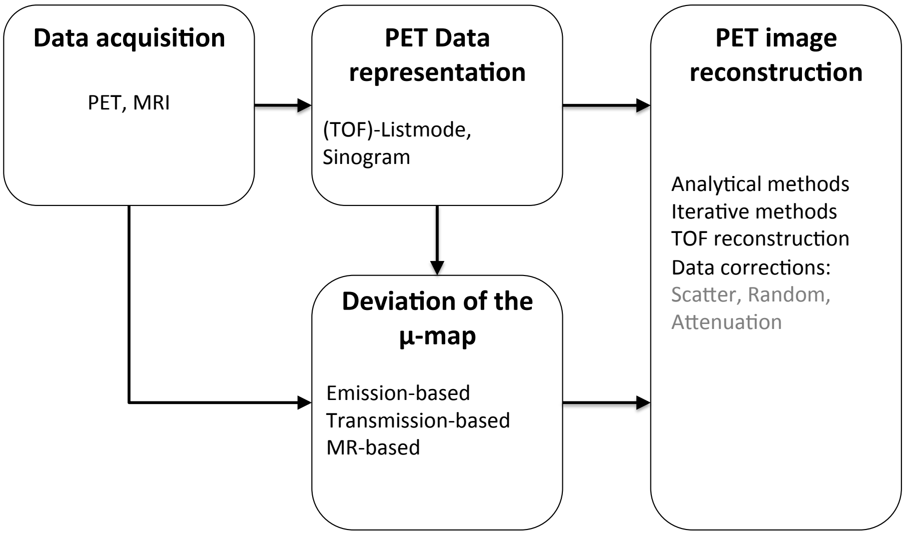
Data acquisition
PET, MRI
PET Data representation
(TOF)-Listmode, Sinogram
PET image reconstruction
Analytical methods
Iterative methods
TOF reconstruction
Data corrections:
Scatter, Random, Attenuation
Deviation of the µ-map
Emission-based
Transmission-based
MR-based

Figure 2.17: Overview of section 2.4: different steps involved in the reconstruction of the PET images.

In this section we will describe the different steps that are needed to obtain a PET image from the acquired PET data. First we will describe how the PET data can be organized. Secondly, an overview of the most common reconstruction algorithms are presented as well as the corrections that are required to improve image quality. An overview of the reconstruction process is shown in figure 2.17. The derivation of the attenuation map, required for the purpose of attenuation correction, is discussed in section 2.5.

2.4.1 Data representation

The acquired PET data can be organized in different ways before the reconstruction takes place. Two classes of data representations are commonly used in practice: sinogram projection data and list-mode event data. The method-of-choice highly depends on the amount of information we want to preserve for each detection and determines the reconstruction method.

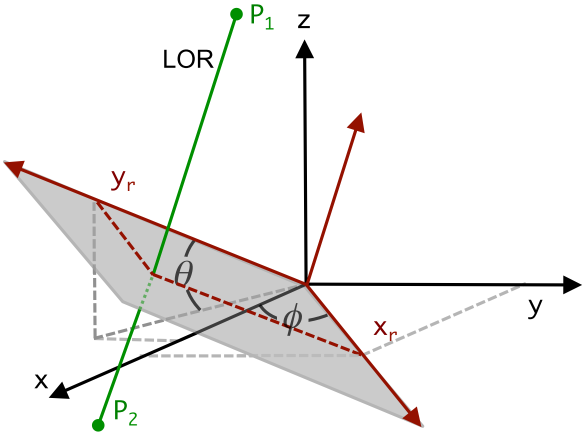

Figure 2.18: Parameterization of a 3D LOR.

2.4.1.1 Sinogram data

The detected coincidences can be histogrammed into a 4D matrix where each element represents a Line-Of-Response. An LOR is uniquely defined by its angles of orientation $\{\phi, \theta\}$ and the shortest distances between the LOR and the center of the FOV (coordinates $\{x_r, y_r\}$) (see figure 2.18). Given the end point coordinates P_1 (x_1, y_1, z_1) and P_2 (x_2, y_2, z_2) of the LOR, the parameters can be calculated as follows :

$$\begin{aligned} \phi &= tan^{-1}\left(\frac{x_1 - x_2}{y_2 - y_1}\right) \\ x_r &= x_1 \cos\phi + y_1 \sin\phi \\ \theta &= tan^{-1}\left(\frac{(x_1 - x_2)\sin\phi - (y_1 - y_2)\cos\phi}{z_2 - z_1}\right) \\ y_r &= x_1 \cos\theta \cos\phi - y1 \cos\theta \sin\phi + z1 \sin\theta \end{aligned} \tag{2.6}$$

Sinograms provide a useful way to interpret and view raw PET data. A row in one slice of a 2D sinogram represents parallel projections along a given angle. Conversely, a particular voxel j in image space corresponds to a sinusoidal path in the sinogram, representing each LOR passing through voxel j. For example, figure 2.19 illustrates how a small hot spot inside the left lung is translated into a sinusoidal wave in a 2D sinogram.

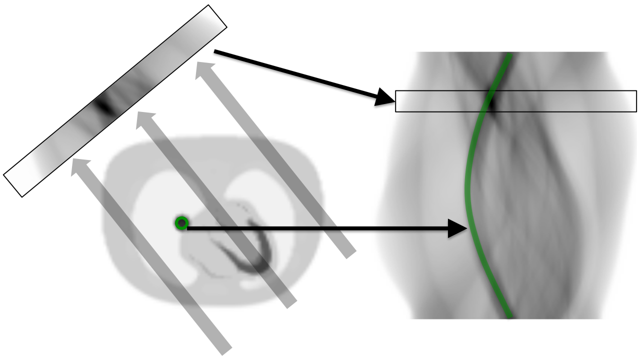

Figure 2.19: Sinogram projection data of a digital torso phantom.

Sinograms are also an easy way to process the projection data prior to reconstruction. Interpolation techniques can be used to estimate missing data (due to gaps in the detectors) or random correction can easily be done by subtracting the delayed sinogram from the prompt sinogram. Sinograms become very large when data is acquired in 3D mode. Additionally, for short scanning times, this data representation is very inefficient as many sinogram bins will contain zeros.

2.4.1.2 List-mode data

The detected coincidences can also be stored as events in a list-mode data file. This allows more flexibility as additional information such as photon energy and timing can be included. Secondly, list-mode processing is efficient for sparse datasets because empty LOR bins are neither stored nor processed. The major disadvantage of list-mode data is that it is not amenable to analytical methods without first binning the events into a standard sinogram data format. Additionally, some correction methods such as scatter and random correction might require conversion to sinogram format.

2.4.2 PET image reconstruction

PET image reconstruction is performed to obtain a three-dimensional (3D) image of the tracer distribution. PET scanners count the number of coincident events p_{ij} between crystal pairs $\{i, j\}$, modeled as a Poisson variable with mean value:

$$< p_{ij} >= \int_{FOV} f(x,y,z)\,\Omega_{ij}(x,y,z)\;dx\;dy\;dz \tag{2.7}$$

where $f(\cdot)$ denotes the tracer distribution. The probability of detecting an emission originated from a point (x, y, z) in the FOV on detector pair $\{i, j\}$ is modeled through the sensitivity function $\Omega(\cdot)$. We assume a stationary tracer concentration which is negligible outside the FOV. The reconstruction problem consist of recovering $f(\cdot)$ from the measured data p_{ij}. If each LOR is modeled as a line connecting the center of the front faces of the two crystals, eq. 2.7 can be modified using line integrals along L_{ij} connecting detector pair $\{i, j\}$:

$$< p_{ij} >= \int_{L_{ij}} f(x(s),y(s),z(s))\;ds \tag{2.8}$$

In the remainder of this chapter we will present methods to solve the problem analytically or with an iterative algorithm.

2.4.2.1 Analytical reconstruction

An estimate of the tracer distribution can be obtained by a process called back-projection, which is the adjoint to eq. 2.8 and is defined by :

$$f(x,y,z) = \int_{-\theta}^{\theta}\int_{0}^{\pi} p(x_r, y_r, \phi, \theta)\;d\phi\;cos\theta\;d\theta, \tag{2.9}$$

with

$$\begin{aligned} x_r &= x\;cos\phi + y\;sin\phi \\ y_r &= (x\cos\phi - y\sin\phi)\cos\theta + z\sin\theta \end{aligned}$$

Practically, back-projection is performed by placing a constant value of $p(x_r, y_r, \phi, \theta)$ into the voxels along the appropriate LOR:

$$f^*(x,y,z) = p(x_r, y_r, \phi, \theta), \forall\{x,y,z\} \in L_{ij} \tag{2.10}$$

This process is repeated for all possible orientations and radial distances (see figure 2.20).

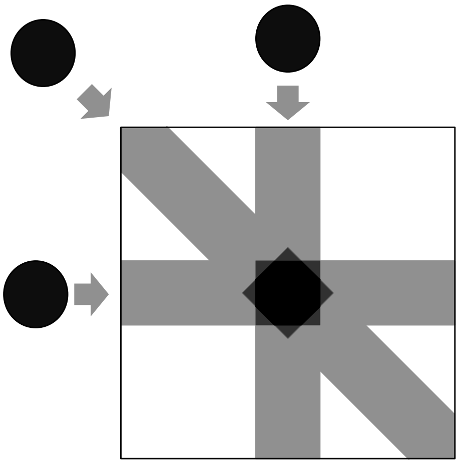

Figure 2.20: Back-projection of projection data $p(\cdot)$ into image space.

The problem with simple back-projection is that the reconstructed image shows star-shaped artifacts. To solve this issue, a method called Filtered Back Projection (FBP) was proposed [93]. FBP was based on the insight that the Fourier transform of the two-dimensional projection $p(x_r, y_r; \phi, \theta)$ is equivalent to a slice of the three-dimensional Fourier transform of $f(\cdot)$:

$$F^*(v_x, v_y, v_z; \phi, \theta) = P(v_{xr}, v_{yr}; \phi, \theta)\delta(v_{zr}) \tag{2.11}$$

This results is know as the back-projection or Fourier slice theorem. If we now consider a continuous sampling in ϕ and θ we have :

$$f(\mathbf{r}) = \int_{-\theta}^{\theta} \int_{0}^{\pi} \mathcal{F}^{-1}\{F^*(v_x, v_y, v_z; \phi, \theta)\}\ d\phi\ cos\theta\ d\theta \tag{2.12}$$

with $\mathbf{r} = (x, y, z)$. Image distortion can then easily be avoided by including a filter before the back-projection:

$$f(\mathbf{r}) = \int_{-\theta}^{\theta} \int_{0}^{\pi} \mathcal{F}^{-1}\{G(v_{x_r}, v_{y_r}, \phi, \theta)\mathcal{F}\{p(x_r, y_r, \phi, \theta)\}\}\ d\phi\ cos\theta\ d\theta \tag{2.13}$$

Back projection methods require continuous sampling of the projection data $p(\cdot)$. Additionally, analytical methods assume that the data are pre-corrected for various image degrading effects such as random coincidences, scatter and attenuation. For these reasons, iterative methods are more attractive (see next section). However, Filtered back-projection (FBP) remains important because of its linear nature allowing control of the spatial resolution and noise correlations in the reconstruction, which is an advantage for quantitative data analysis.

2.4.2.2 Iterative reconstruction

Because the data measured with the PET scanner represents a sampled version of the continuous domain definition, eq. (2.8) can be approximated with a system of linear equations:

$$< \mathbf{p} >= \mathbf{Hf} \tag{2.14}$$

Where each element f_j, $j = 1, \cdots, N$ of $\mathbf{f}$ represents a voxel in image space, p_i the number of counts detected on LOR i, $i = 1, \cdots, M$ and $\mathbf{H}$ the MxN system matrix. The reconstruction problem can be stated as follows: Find the tracer distribution $f(\cdot)$, given the measured projection data $p(\cdot)$, information about the PET acquisition system (the system matrix $\mathbf{H}$) and, possibly, a statistical model of the data and the tracer distribution.

Many approaches exist to solve Eq. (2.14). All of them provide criteria to indicate which image, among all possible solutions, is to be considered as the best candidate to represent the true tracer distribution. These criteria then determine which computational technique is best suited. In general, the solution is found using an iterative approach as follows (see figure 2.21):

- An **initial estimate** of the tracer distribution is generated. FBP could be used, but usually all voxels are set to the same value.
- An estimate of the projection data on each LOR is made by a process called **forward projection**. The projection simulates the PET acquisition system.
- The forward projected data is then compared to the measured data
- Finally the error, measured in the previous step is **back-projected** into image space and the current estimate of the tracer distribution is updated.
- The previous three steps are repeated until convergence is reached.

With the introduction of more computational power, iterative reconstruction algorithms have become more popular. Compared to analytical methods, iterative reconstruction improves the overall image quality by allowing

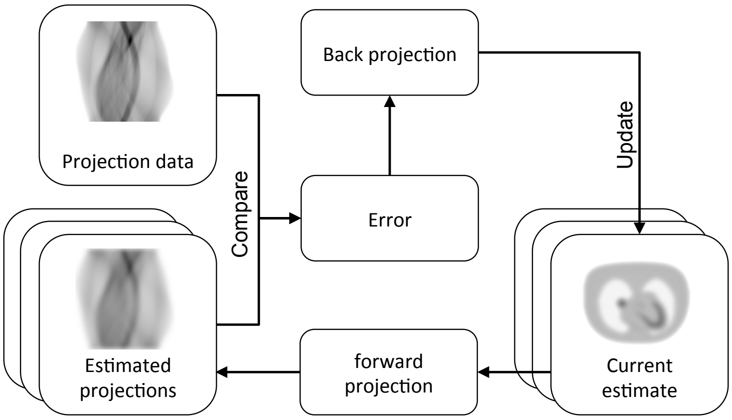

Figure 2.21: Different steps involved in a typical iterative reconstruction algorithm.

more accurate modeling of the PET acquisition system. Additionally, statistical techniques can be used to control noise.

Maximum Likelihood - Expectation Maximization (ML-EM)

Because of the Poisson nature of radioactive decay, the photon detections obey the Poisson distribution, provided that no corrections have been applied to the data. The probability of detecting p_i counts on LOR i, given the tracer distribution $\mathbf{f}$ is given by:

$$\mathcal{P}\{p_i; \mathbf{f}\} = \frac{\bar{f}_i^{p_i} exp(-\bar{f}_i)}{p_i!} \tag{2.15}$$

where $\bar{f}_i = \sum_{j=1}^{N} h_{ij} f_j$. The combined probability can be described as:

$$\mathcal{P}\{\mathbf{p}; \mathbf{f}\} = \prod_{i=1}^{M} \frac{\bar{f}_i^{p_i} exp(-\bar{f}_i)}{p_i!} \tag{2.16}$$

The maximum likelihood (ML) formulation, propose by R. A. Fisher (1921) gives an indication of which solution $\hat{\mathbf{f}}$ has greatest statistical consistency with the observed data by maximizing the likelihood $\mathcal{L}(\mathbf{f}) = \mathcal{P}\{\mathbf{p}; \mathbf{f}\}$:

$$\hat{\mathbf{f}} = \arg\max_{\mathbf{f}} \mathcal{P}\{\mathbf{p}; \mathbf{f}\} \tag{2.17}$$

By taking the logarithm of the object function, and omitting $(p_i!)$ the maximum likelihood criterion can be simplified:

$$\log \mathcal{L}(\mathbf{f}) = \arg\max_{\mathbf{f}} \left[\sum_{i=1}^{M} p_i \log \bar{f}_i - \bar{f}_i \right] \tag{2.18}$$

The solution can be found using the following ML-EM algorithm:

$$\hat{f}_j^{(k+1)} = \frac{\hat{f}_j^{(k)}}{\sum_m h_{mj}} \sum_i h_{ij} \frac{p_i}{\sum_n h_{in} \hat{f}_n^{(k)}} \tag{2.19}$$

With k the iteration number, i the LOR index and j, m and n the voxel indices. The different steps depicted in figure 2.21 can be recognized in the algorithm :

- The **forward projection** gives an estimate of the measured data p_i:

$$\sum_n h_{in} \hat{f}_n^{(k)} \tag{2.20}$$

- The estimated projections and measured data are then compared by calculating the ratio:

$$\frac{p_i}{\sum_n h_{in} \hat{f}_n^{(k)}} \tag{2.21}$$

- The error ratio is then back-projected into image space:

$$\sum_i h_{ij} \frac{p_i}{\sum_n h_{in} \hat{f}_n^{(k)}} \tag{2.22}$$

- finally, the back-projected data is normalized:

$$\frac{1}{\sum_m h_{mj}} \sum_i h_{ij} \frac{p_i}{\sum_n h_{in} \hat{f}_n^{(k)}} \tag{2.23}$$

LOR-dependent correction factors, such as attenuation, scatter fraction, detector efficiency can be modeled in **H**. The reader is referred [94] for more information about the derivation of this algorithm.
The ML-EM algorithm is widely used in clinical practice and research because of its simplicity and easy implementation. Additionally, non negative values are enforced by the multiplicative error and update step. Although convergence is predictable and consistent, a usable solution may require 30 to 100 iterations. A second shortcoming is that the ML criterium yields noisy reconstructed images for high iteration numbers.

Accelerated algorithms

The iterative approach described above can be very computation-intensive. Typically many iterations are required to obtain good image quality. Additionally, each iteration requires many forward and back-projection operations. One approach to significantly accelerate the reconstruction algorithm is the use of ordered subsets. This technique divides the data into O subsets following a certain order. Eq. 2.19 is then applied to each subset:

$$\hat{f}_j^{(k+1)} = \frac{\hat{f}_j^{(k)}}{\sum\limits_{m \in S_o} h_{mj}} \sum_{i \in S_o} h_{ij} \frac{p_i}{\sum\limits_{n} h_{in} \hat{f}_n^{(k)}} \tag{2.24}$$

Were back-projection is only performed for the projection data belonging to subset S_o. At each update, a different subset is selected. Ordered Subset Expectation Maximization (OS-EM) significantly improves speed as fewer iterations are required compared to ML-EM. However, care should be taken when defining the subset. The solution must be shared by all subsets to ensure convergence.

Bayesian methods

The ML formulation does not consider any prior knowledge about the probability of a particular solution to exist. Because finding **f** given the measured data p_i is an ill-posed inverse problem, many images can provide a valuable solution. Among those solutions, we might want to find the one with the lowest noise possible. A Bayesian approach might help in achieving this goal. The maximum a posteriori (MAP) criterion can be expressed as :

$$\hat{\mathbf{f}} = \arg\max_{\mathbf{f}} \mathcal{P}\{\mathbf{f}; \mathbf{p}\} = \arg\max_{\mathbf{f}} \frac{\mathcal{P}\{\mathbf{p}; \mathbf{f}\} \cdot \mathcal{P}\{\mathbf{f}\}}{\mathcal{P}\{\mathbf{p}\}} \tag{2.25}$$

By taking the logarithm and ignoring $\mathcal{P}\{\mathbf{p}\}$ (not a function of $\mathbf{f}$) the MAP criterion is modified:

$$\hat{\mathbf{f}} = \arg\max_{\mathbf{f}} [\log \mathcal{P}\{\mathbf{p};\mathbf{f}\} + \log \mathcal{P}\{\mathbf{f}\}] \tag{2.26}$$

An energy function $U(\mathbf{f}) = \log \mathcal{P}\{\mathbf{f}\}$ can now be utilized to penalize image solutions that do not possess expected properties. The solution can be found using the following MAP algorithm :

$$\hat{f}_j^{(k+1)} = \frac{\hat{f}_j^{(k)}}{\sum_m h_{mj} + \beta \frac{\partial U(\mathbf{f})}{\partial f_j}|_{f_j=\hat{f}_j^{(k)}}} \sum_i h_{ij} \frac{p_i}{\sum_n h_{in}\hat{f}_n^{(k)}}, \tag{2.27}$$

with β a positive weighting parameter which controls the influence of the penalty.

2.4.2.3 Time-of-flight List-mode reconstruction

In section 2.4.2.2 we described how the PET image can be reconstructed given the projection data $\mathbf{p}$ and the system matrix $\mathbf{H}$. When TOF is used, each event contains information about the difference in arrival time of the two photons in coincidence, which allows a more precise localization of the positron annihilation. This additional information introduces an additional dimension in the sinogram format. As a consequence,TOF PET systems mostly use a list-mode format to organize the projection data and each event is processed individually during reconstruction. To include TOF information in the reconstruction, the ML-EM algorithm (eq. 2.19) is modified as follows:

$$\hat{f}_j^{(k+1)} = \frac{\hat{f}_j^{(k)}}{\sum_m h_{mj}} \sum_e h_{i_e j} g_e(j) \frac{1}{\sum_n h_{i_e n} g_e(n) \hat{f}_n^{(k)}} \tag{2.28}$$

Where i_e represents the LOR index for the e^{th} list-mode event. For each event e, both within the back- and forward projection operations, the coefficients of the system matrix $\mathbf{H}$ are multiplied by a TOF kernel $g_e(\cdot)$ centered at the TOF difference Δt_e along the LOR and defined by:

$$g_e(j) = \frac{1}{\sqrt{2\pi}\sigma} \exp\left(-\frac{(d_{i_e j} - \Delta x_e)^2}{2\sigma^2}\right) \tag{2.29}$$

with $\Delta x_e = c\frac{\Delta t_e}{2}$ and $d_{i_e j}$ the distance from the center of LOR i_e to the center of voxel j. σ is related to the TOF resolution $\Delta\tau$ (FWHM) by :

$$c\frac{\Delta\tau}{2} = \sqrt{2\sigma^2(4\ln 2)} \tag{2.30}$$

In analytical reconstruction methods a technique called Confidence Weighting (CW) is mostly used. It has been shown that CW has good noise properties compared to other TOF reconstruction kernels [95]. However, better results are obtained when adaptive, object dependent weighting kernels are used [96].

2.4.2.4 Random and scatter compensation

During a PET acquisition, all types of coincidences are stored. In order to achieve absolute quantification, scattered and random coincidences need to be removed from the data. However, the limited energy resolution does not allow to exactly classify the scattered events and there is no way to determine if two photons originated from different annihilation events. Therefore correction methods which try to estimate the scattered and random coincidences are used.

Random compensation

Random events can be estimated using a delayed window method [97]. The delayed events are included and marked in the list-mode data. Random compensation can be done by subtracting the back-projection from the update factor each time a delayed event is processed:

$$\hat{f}_j^{(k+1)} = \frac{\hat{f}_j^{(k)}}{\sum_m h_{mj}} \sum_e h_{i_e j} g_e(j) \frac{w_{i_e}}{\sum_n h_{i_e n} g_e(n) \hat{f}_n^{(k)}} \tag{2.31}$$

Where w_{i_e} equals -1 if the event is marked as a delayed event and $w_{i_e} = 1$ otherwise. Additive methods are easy to implement as they do not require any binning of the data into a sinogram. However, Poisson noise will be amplified and special care is needed to regulate the noise to ensure sufficient image quality. Additionally, this approach might introduce negative values in the reconstructed images. A better approach is to bin the delayed coincidences in a sinogram and pre-process the sinogram to suppress noise. Subsequently, the sinogram can be used as an estimate during the forward projection of the estimated emission data :

$$\hat{f}_j^{(k+1)} = \frac{\hat{f}_j^{(k)}}{\sum_m h_{mj}} \sum_e h_{i_e j} g_e(j) \frac{1}{\sum_n h_{i_e n} g_e(n) \hat{f}_n^{(k)} + r_{i_e}} \tag{2.32}$$

Where r_{i_e} represents the random estimate for LOR i.

Scatter compensation

In 3D PET imaging the fraction of scattered events can become very large [98, 99]. Compensating for scatter is therefore mandatory. Scatter correction is typically done by modeling the scatter process [100, 101]. For this purpose the Klein-Nishina formula is used :

$$\frac{d\sigma}{d\Omega} = \frac{Zr_0^2}{2} \frac{1+\cos^2\theta}{[1+\gamma(1-\cos\theta)]^2} \left[1 + \frac{\gamma^2(1-\cos\theta)^2}{(1+\cos^2\theta)[1+\gamma(1-\cos\theta)]}\right]$$

with $\gamma = E/m_0c^2$, E the energy of the incident photon, m_0c^2 the rest mass of the electron, r_0 the classical electron radius and Z the atomic number of the scattering atom. The formula gives the probability of scattering through angle Ω, from which the single scatter distribution can be estimated. A major drawback of this approach is that the model requires an estimate of the true tracer and object density distributions. Because only an estimate of the true emission is available at the time of reconstruction, and the estimate is contaminated by scatter, the scatter distribution is estimated using an iterative algorithm. A technique that is commonly used in practice, easy to implement and computationally efficient is the Single Scatter Simulation method [100]. The algorithm works as follows : first the object density distribution or attenuation map is sampled to derive a scatter point. Subsequently, the line integrals through the activity distribution and density distribution connecting the scatter point to each detector of the PET scanner is calculated. Finally the scatter fraction on each LOR is calculated using eq. 2.33 and the line-integrals are added to a single scatter sinogram. This process is repeated for each sampled scatter point. Figure 2.22 illustrates the simulation model. The method is fast as the line integrals through the activity and density distributions only needs to be calculated once. When TOF is used, the simulation process becomes more complicated as the scattered fraction on a particular LOR depends on the distance from the emission point to the center of the total path from D_1 through S to D_2. In [95] Watson et al. propose to extend the model to

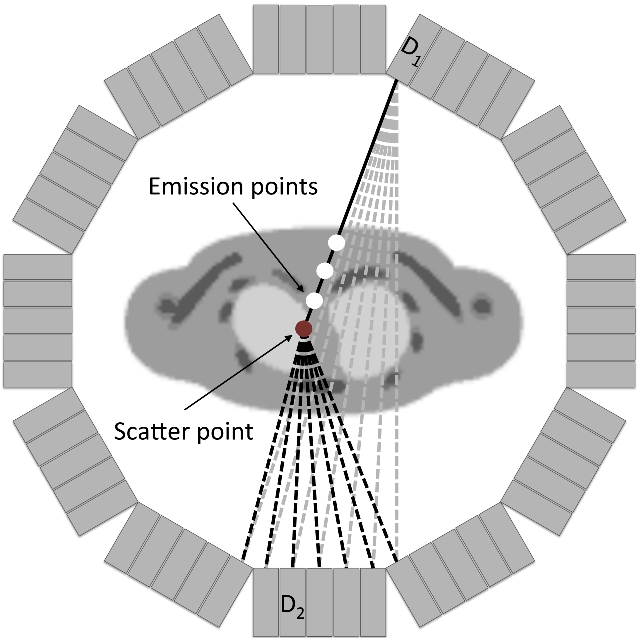

Figure 2.22: The Single Scatter Simulation method.

include TOF and estimate the scatter distribution for multiple time bins.

Finally the estimated scatter sinogram can be used in the reconstruction as follows :

$$\hat{f}_j^{(k+1)} = \frac{\hat{f}_j^{(k)}}{\sum\limits_m h_{mj}} \sum_e h_{i_e j} g_e(j) \frac{1}{\sum\limits_n h_{i_e n} g_e(n) \hat{f}_n^{(k)} + r_{i_e} + s_{i_e}(\Delta t_e)} \tag{2.33}$$

Where $s_{i_e}(\Delta t_e)$ represents the TOF-dependent scatter estimate on LOR i_e.

Other methods than the analytical SSS method include energy-based methods [102–104] and function fitting [105–107]. Energy-based methods commonly use two energy windows during the PET acquisition, one over the scatter region (lower energies) and one over the photon peak (511 keV). The scatter fraction can be estimated from the data acquired in the first energy window. Subtraction from the prompt data will provide proper scatter correction. In another approach a smooth estimate of the scatter sinogram is estimated by fitting a function to the data measured outside the contour of the patient after random correction. This method assumes that the events outside the patient are due to scatter. The major drawback of this method is that local variations of the activity distribution and object density are not considered.

2.5 Derivation of the attenuation map in PET/MRI

In order to correct the PET image for attenuation and scatter, an attenuation map needs to be generated. Since the advent of PET/CT, the attenuation map can be derived from the CT-images [61, 108, 109]. Contrary to PET transmission data, CT images contain less noise, have higher resolution and can be acquired in a short time span, at the expense of a higher radiation dose. In a combined PET/MRI scanner, no CT is available. Hence, the attenuation map should be derived using a different method. In this section we will summarize the different methods that have been proposed so far. These approaches can be divided into three categories : emission-based, transmission-based and MR-based methods.

The attenuation correction technique must fulfill some requirements to achieve adequate PET quantification. First, the reconstructed attenuation coefficients should be accurate and the attenuation map should be free of artifacts. Second, the method should be MR compatible and the acquisition time of the PET or MRI scanner for the purpose of attenuation correction should be limited. Finally, the method should be able to visualize any object inside the FOV. As we will see throughout this section, it is difficult to develop a method that meets all these requirements.

2.5.1 Emission-based techniques

One way to address the problem is to derive the attenuation map from the emission data itself. For this, three classes of methods have been proposed. The first approach is to use segmentation techniques to cluster the voxels of the uncorrected emission map into regions of approximately constant attenuation. For each region a tissue-depend attenuation coefficient at 511 keV is assigned [110, 111]. For this purpose an active contour finding algorithm is typically used. As non-attenuation corrected images show high contrast between the skin and the rest of the body, the body contour can be extracted easily. To improve classification a very short transmission scan can be included. The second class of techniques attempts to derive quantitative attenuation coefficients from the emission projections using simultaneous reconstruction of the activity and attenuation distribution. The last class of methods tries to reconstruct the attenuation independently using consistency conditions. In the remainder of this section we will discuss the latter two approaches.

2.5.1.1 Simultaneous statistical reconstruction

Emission-based reconstruction of attenuation coefficients started with the work of Censor et al. [112] in which the PET image and the attenuation map were reconstructed by alternating iterations using only the emission projections. In Nuyts et al. [5] this idea was improved to a constrained maximum likelihood (ML) approach which takes into account the Poisson nature of the data and enables the use of a-priori knowledge about the attenuation of human tissue. This method is referred to as MLAA, which stands for Maximum Likelihood reconstruction of Attenuation and Activity. Results of an abdominal PET study are depicted in figure 2.23. The absolute difference between the emission distributions reconstructed using MLAA and ML-EM with measured attenuation correction mainly contains noise with a mean squared error of 28% of the mean or 6.5% of the maximum from the ML-EM image. Although these approaches would eliminate the use of transmission scanning, it has been shown that the emission data alone does not determine the attenuation correction factors [113]. The success is limited by the inherent crosstalk between the two unknown variables [5, 114]. This can easily be seen if we consider a tracer distribution and an attenuation medium which are both radially symmetrical. However, it is known that TOF reconstruction is more robust than non-TOF reconstruction when attenuation correction is not accurate or not applied at all [115] and recent research shows that by including TOF information, one can determine the attenuation sinogram by the emission data up to a constant scaling factor [6]. This was illustrated with an analytical method using simulated 2D PET data (see figure 2.24).

2.5.1.2 Methods based on consistency conditions criteria

To avoid the cross-talk, the attenuation map can also be reconstructed without the need to reconstruct the activity distribution. This can be done by applying a set of mathematical conditions which the attenuation corrected data should satisfy. Most of these conditions were derived from X-ray CT and are valid for the Radon transform. For example, the zeroth condition (zeroth moment) states that the sum of the data in each projection of a 2D sinogram should be constant, independent of the projection angle. A more complex condition is defined by the first moment which is the sum of the data in each bin multiplied by the distance of that bin from the

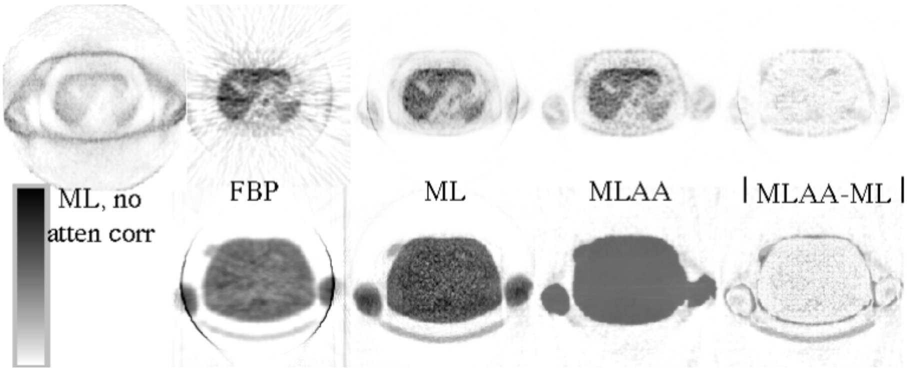

Figure 2.23: Reconstructions of an abdominal PET study. From left to right; top: ML-EM without attenuation correction, FBP and ML-EM with measured attenuation correction, MLAA emission image, absolute difference between MLAA and ML-EM images. Bottom: FBP and ML-EM reconstruction of PET transmission study, MLAA attenuation map, absolute difference between MLAA and ML attenuation maps. Reprinted with permission [5] ©2011 IEEE.

origin. It has been shown that the consistency conditions can be used to estimate the parameters for a uniform elliptical attenuation distribution for two-dimensional PET data [116]. This work was later extended to three dimensional correction using a single template [117].

However, certain difficulties may appear when the measured data are not in the range of the imaging operator because of noise, discretization errors or other physical factors, which is certainly the case with 3D PET data. Additionally, instability of the solution can be caused by the ill-posedness of the problem. Therefore these techniques are mostly used in situations where either it is impractical to acquire transmission data or there is significant misalignment between the transmission data and emission data.

In 2000, Bronnikov et al. [118] presented an approach that strengthened the paradigm of the consistency conditions by discretization of the problem. This approach ensures natural regularization of the problem and it can easily be applied in various scanner configurations, including 3D PET acquisition. Additionally, the discretization allows the method to take into account the influence of physical factors, such as scattered coincidences, a finite detector resolution and the system response.

Later, in 2007, the consistency formulations were revised and modified in order to take into account the characteristics of the PET imaging operator [119]. Results indicate that some consistency conditions can be violated

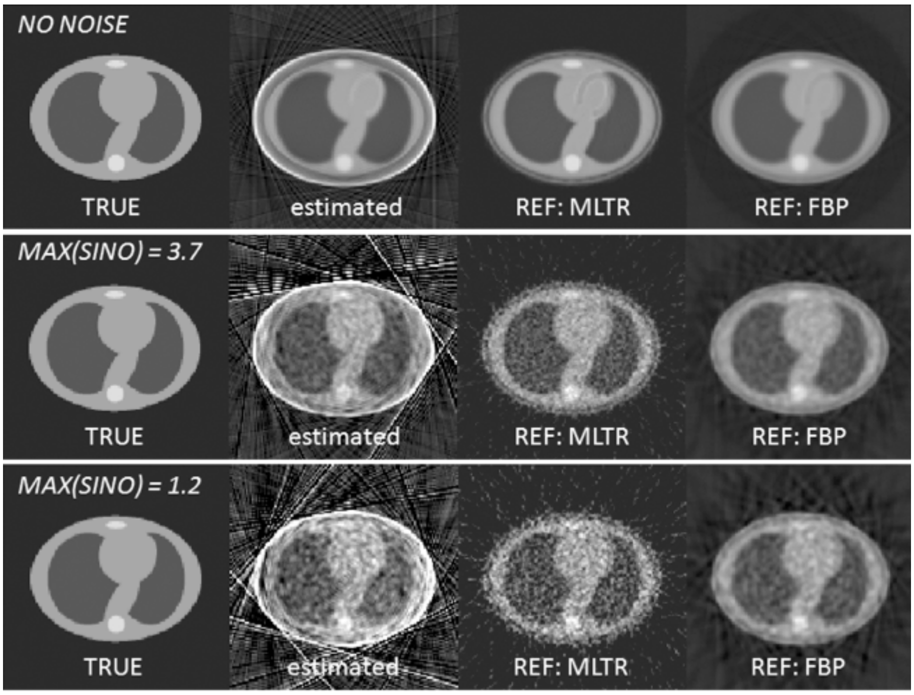

Figure 2.24: Reconstructions of the attenuation image from simulated data without noise (top row), with noise (middle row), and with more noise (bottom row). From left to right: the true attenuation image, the image estimated by the analytical method, and the references images reconstructed with the maximum-likelihood MLTR algorithm [5] and with FBP. Reprinted with permission [6]. ©Institute of Physics and Engineering in Medicine. Published on behalf of IPEM by IOP Publishing Ltd. All rights reserved.

at the 10% level. However, these modified conditions have not yet been applied for the purpose of attenuation correction of real PET data.

2.5.2 Transmission-based techniques

Photon attenuation can also be measured by inserting a positron-emitting source inside the field-of-view of the PET scanner. The emitted photons will travel through tissue and only a fraction will be transmitted depending on the electron density of the tissue. The amount of attenuation is then calculated by comparing the number of transmitted photons with the number we would detect when the photons only travel through air (blank scan). More specific, the attenuation a_i on LOR i relates the measured signal t_i

with the signal b_i that would be measured in absence of attenuation:

$$t_i = a_i b_i, \text{ with } a_i = e^{(-\sum_j \mu_j l_{ij})} \tag{2.34}$$

Where μ_j is the attenuation coefficient of tissue j and l_{ij} the intersection length of LOR i with tissue j. The measurements b_i are often referred to as the blank scan while t_i are the number of events collected during the transmission scan.

The use of an external radionuclide source was first proposed in 1952 by Mayneord [120]. Later this method was refined which enabled its use in conjunction with conventional emission scanning [121]. At that time, transmission images were used to match anatomical contours to the radionuclide distribution measured by the scanner. Only in the 1970s, when the first PET systems were developed, transmission scanning was adapted for the purpose of attenuation correction. Different transmission scanning geometries were proposed in literature (figure 2.25). The first PET systems used a ring source of ^{68}Ga/^{68}Ge with a half-life of 68 min and 270.8 days respectively. The ring was mechanically moved into the FOV and photons were collected in coincidence mode. This design was later replaced by continuously rotating rod sources, which could be collimated and therefore reduce scatter contaminating the transmission data. Additionally, rotating sources facilitate separation of emission and transmission data enabling post-injection transmission or even simultaneous emission/transmission scanning. The positron emitters were then replaced with single-photon sources like ^{137}Cs with a half-life of 30.2 years and energy of 662-keV. The higher energy of ^{137}C-sources improves tissue penetration and single photons can be recorded at a higher collection rate.

Depending on the choice of geometry and source type, the transmission data can be acquired before (pre-injection [122]), during (simultaneous [123, 124]), or after (post-injection [125]) the emission scan. Simultaneous scanning is highly desirable in clinical practice, it reduces scanning time and improves the spatial co-registration between the attenuation map and emission map. The disadvantage is the crosstalk between the transmission and emission data, leading to less accurate attenuation coefficients.

2.5.3 MR-based techniques

When PET and MRI are combined in a fully integrated system, no CT will be available for accurate attenuation correction. Although a transmission scan could be used, many research groups focus on the derivation of the

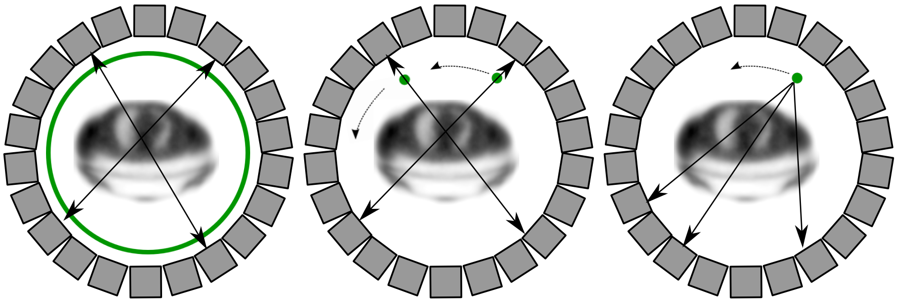

Figure 2.25: Different transmission scanning methods for PET. Transmission measured in coincidence mode using ring sources of positron-emitting radionuclide (a) or rotating positron-emitting rods (b). Rotating single-photon source producing LORs between source position and photons detected on opposing side of detector ring (c).

attenuation map based on the MRI data. However, a number of difficulties are encountered with MRI-based attenuation correction. First, MRI signals correlate with proton densities and relaxation properties of tissue. Hence, a direct conversion from a MRI image to the electron density of tissue is not possible. Secondly, some specific tissue types, such as lung and cortical bone have almost no signal on conventional MRI images due to the very short transverse relaxation time (T_2). Therefore it is hard to distinguish these tissues from air, although their relative attenuation coefficients differ significantly. Finally, during an MRI acquisition, the RF coils may cause significant photon attenuation and should be included in the attenuation map. A template can be used when working with fixed coils, but special considerations need to be taken when working with flexible coils. Perhaps complex deformation methods can be used in combination with fiducial markers to obtain a deformed template of the coil attenuation.

2.5.3.1 Segmentation techniques

One way to address the problem of MR-based attenuation correction is to segment an MRI image in different tissue classes and assign predefined attenuation coefficients. Here we present the voxel-based segmentation approaches that are used today, all based on different MR images. The first method uses conventional T1 weighted MR images for the segmentation of air, soft tissue, skull and lung tissue. Brain PET was the earlier application in which direct segmentation was used to derive the attenuation map.

Zaidi et al. developed a Fuzzy c-means clustering algorithm applied to T1-weighted spin-echo images for the classification of air, brain tissue, skull, nasal sinuses and scalp [126]. Unfortunately, manual intervention was required for the segmentation of the skull. A more sophisticated method was proposed by Wagenknecht et al. [127]. Prior knowledge about the relative position of the regions was used to improve the segmentation. Later, direct segmentation was also used in whole body PET/MRI imaging [128, 129]. However, most of these methods do not consider bone, since air, bone and lung tissue are not distinguishable in conventional T1-weighted MRI. This issue was solved when Ultrashort echo time (UTE) sequences were utilized to visualize regions with very short spin-spin relaxation times T2 [130–133]. These methods show promising results on brain studies. Keereman et al. acquired five human brain PET/CT and MRI datasets and an average error on the resulting PET images of 5% was obtained. Berker et al. used a UTE triple echo sequence, combining UTE for the detection of bone and Dixon gradient echoes for water-fat separation [133, 134]. In their study a maximum classification error in the segmented attenuation maps of 18.9% was obtained [133].

2.5.3.2 Template- and atlas-based techniques

The attenuation map can be derived by first registering the patient specific MRI image to a template MRI image. The inverse transformation is then applied to a template attenuation map. This idea of template matching, initially proposed by Montandon and Zaidi in 2004 [135], was first applied to brain PET/MRI by Rota Kops et al. in 2007 [136]. In this work, T_1-weighted MRI images were used. The method was tested with 4 subjects in their first study and 30 subjects in a follow-up study [136, 137]. An average error of less than 5% in 3 cortical and 3 subcortical regions of interest and a maximum error of 10% in a region of interest were reported. Later, a more advanced method was developed by Hoffmann et al. [138]. First an atlas of MR-CT data sets was created. The patient specific T_1-weighted MRI image is then co-registered to all MRI images from the atlas, the same transformations are applied to the CT images. Finally, in each voxel, a pseudo CT value is derived by taking a weighted average of all co-registered CT images. The weighting factors are derived from the regional image information. The method was evaluated on both brain and whole-body data [138, 139]. An average error in PET quantification of 3.2% was obtained in 10 clinically relevant volumes of interest in the brain. The method performed better than segmentation techniques on whole body data, but still showed

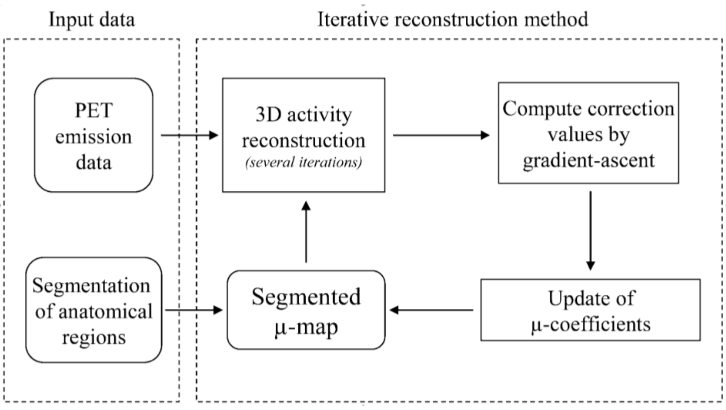
Input data
Iterative reconstruction method
PET emission data
3D activity reconstruction (several iterations)
Compute correction values by gradient-ascent
Segmentation of anatomical regions
Segmented μ-map
Update of μ-coefficients

Figure 2.26: Iterative reconstruction scheme. Reprinted with permission [7] ©2011 IEEE.

large quantification errors of 10% or more, especially in lung tissue. In the work of Johannson et al. MR-CT correspondences were trained to generate pseudo CT images. For this purpose two different UTE and one T2-weighted MR image were used. They validated their method with brain scans of 5 patients. A mean absolute error of 137 Hu was reported for the CT value in the pseudo CT images.

2.5.3.3 Emission-based techniques in TOF PET-MRI

In a TOF PET/MRI system emission-based techniques could be combined with MR imaging to improve the accuracy of the attenuation map. Salomon et al. investigated how emission based techniques can be used to reconstruct attenuation coefficients of previously defined connected anatomical regions [7]. In their method, they attempt to simultaneously reconstruct the attenuation and activity distribution where only the connected regions are adapted instead of reconstructing on a voxel-by-voxel basis. A general scheme is given in figure 2.26. This approach leads to increased robustness as the number of possible outcomes is significantly reduced. Furthermore, no additional anatomical *a priori* information such as organ models is included. This way, the method is not affected by the inter-patient variability of the anatomical structure of the tissues. The method was evaluated with five patient studies from data acquired on the sequential Ingenuity TF PET/MR scanner (Philips Healthcare). The reconstructed attenuation map and emission distribution of one patient study is shown in figure 2.27.

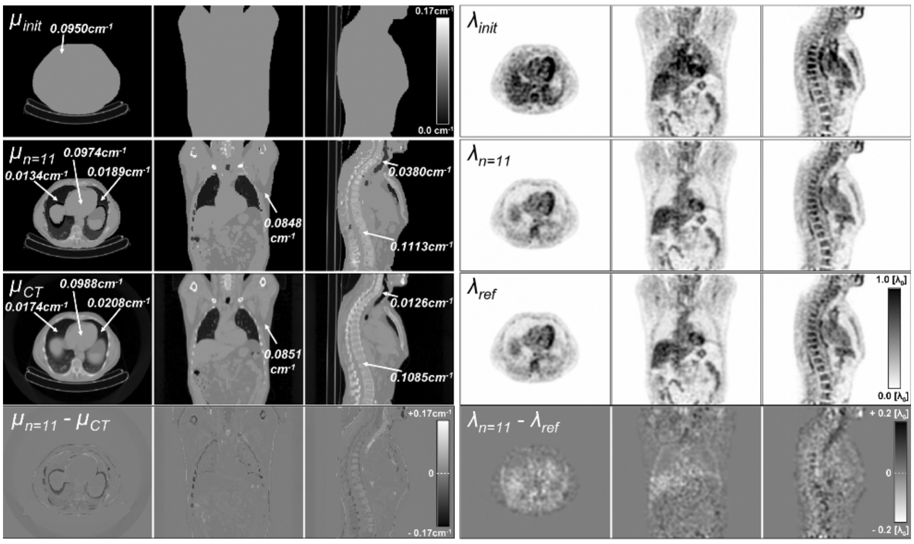
μ_{init}
0.0950cm-1
0.17cm-1
0.0 cm-1
$\mu_{n=11}$
0.0974cm-1
0.0134cm-1
0.0189cm-1
0.0848 cm-1
0.0380cm-1
0.1113cm-1
μ_{CT}
0.0988cm-1
0.0174cm-1
0.0208cm-1
0.0851 cm-1
0.0126cm-1
0.1085cm-1
$\mu_{n=11}$ - μ_{CT}
+0.17cm-1
0
- 0.17cm-1
λ_{init}
$\lambda_{n=11}$
λ_{ref}
1.0 [λ_0]
0.0 [λ_0]
$\lambda_{n=11}$ - λ_{ref}
+ 0.2 [λ_0]
0
- 0.2 [λ_0]

Figure 2.27: Attenuation map and reconstructed activity distributions. Upper row: Initial estimation, second row: estimation after 11 iterations, third row: CT-based reference attenuation and corresponding reconstructed activity, and last row: difference between 11th iteration and CT-based reference, White arrows point to region averaged μ coefficients. (from left to right: transverse, coronal, and sagittal transection). Reprinted with permission [7]. ©2011 IEEE.

The reconstructed attenuation coefficients were compared to the CT-based attenuation and an absolute mean difference of 0.005 cm^{-1} (<20%) in the lungs, 0.0009 cm^{-1} (< 2%) in fatty tissue and 0.0015 cm^{-1} (<2%) in blood and muscles was obtained. The averaged deviations between the estimated activity using the reconstructed and the CT-based attenuation are as follows: bony tissue :-10.3%, blood and muscles : -2.9%, fatty tissue : -2.0%.

Some problems occur when using conventional MR images as anatomical information. Different tissue classes show a reduced region homogeneity especially in the ribs and the lungs as well as backbone and the surrounding tissue. This could be avoided if the reconstruction algorithm allows to update the segmented MR-image based on the PET emission data. Additionally, in the study of Salomon et al. misalignment between the PET and MR images was observed which is avoided in a simultaneous PET/MRI scan. Another problem was caused by the limited FOV of the MRI scanner. This issue was solved by estimating the body contour using only PET emission data.

The proposed method provides a robust attenuation correction method derived from TOF PET data and segmented MR images without the use of additional anatomical information or prior knowledge about the attenuation coefficients. Further research needs to focus on the use of novel techniques such as UTE to improve the tissue classification to avoid segmentation artifacts in the reconstructed attenuation and activity distribution.

2.6 Conclusion

In this chapter we introduced the medical imaging modalities that are used throughout this work. The main topic of this work was covered in the last section. In this section we reviewed the different methods that can be used to derive the attenuation map in a PET/MRI system. MR-based methods were discussed as well as methods based on PET transmission and emission data. Despite the progress made so far, some major challenges remain. First, the use of predefined information about the attenuation coefficients of tissues or the anatomy of the patient should be avoided. Second, all relevant tissues and materials, such as air, soft tissue, lung, bone, MRI coils and patient bed should be considered. Finally, the method should be robust, fast and fully automated to allow its use in clinical practice. Today, there is still no method which solves all these issues. In the next chapters we will present a transmission-based approach which addresses most of these problems. The method is MR-compatible, does not require additional PET/MRI acquisition time for the purpose of attenuation correction, the technique is able to visualize any object inside the FOV of the scanner and the attenuation coefficients at 511 keV are measured directly, avoiding the use of predefined attenuation coefficients or segmentation techniques.

Chapter 3

Transmission scanning using an annulus shaped source

3.1 Introduction

In the previous chapter we gave an overview of the current approaches to correct for attenuation in a (TOF) PET/MRI system. Emission-based, transmission-based and MR-based methods were discussed. In this chapter a new transmission-based approach to derive the attenuation map is proposed. First we give a general overview of the method and its application to current TOF PET systems with moderate TOF resolution. Next, the iterative algorithm, used to reconstruct the attenuation map is derived. Finally, the concept is evaluated with simulation studies using GATE. This chapter should be regarded as a proof of concept, demonstrating the potential of this method in ideal circumstances. In the next chapters, the method will be evaluated with experimental and clinical data.

3.2 Proposed method

In order to measure the transmission of 511 keV photons through tissue, a transmission source is installed inside the bore of a TOF PET scanner. Conventionally transmission scanning was performed using a rotating positron emitting source in coincidence mode (e.g. ^{68}Ge; ^{68}Ga) or a rotating single-photon source (e.g. ^{137}Cs)[140, 141]. Although these methods have proven to give accurate attenuation maps, using rotating sources in future PET/MRI systems is difficult because of the reduced bore size and

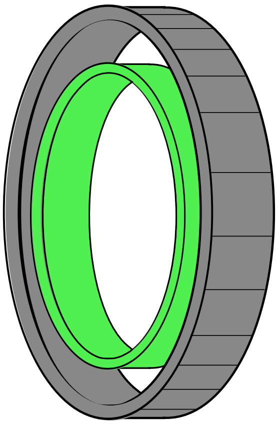

Figure 3.1: Annulus shaped transmission source inserted in a TOF PET scanner.

the presence of the strong magnetic field. In this work we propose to use an annulus shaped source with a thickness of less than 3 mm covering the whole axial FOV of the scanner. The source is filled with a water solution of ^{18}F-FDG, the same radio-pharmaceutical as administered to the patient. In future systems other sources with a long half-life like ^{68}Ge may be considered. Figure 3.1 shows the setup of a typical PET scanner equipped with an annulus shaped transmission source.

The acquisition protocol works as follows: First a blank reference scan is acquired. During this initial scan, 511 keV photons originating from the annulus will only be attenuated by air and the annulus itself. Secondly, the patient is positioned inside the PET scanner. A transmission scan is acquired and photons coming from the annulus will be attenuated by the patient. By comparing the data acquired from the transmission scan and the blank scan, an attenuation map can be derived. Depending on whether the transmission scan was performed prior or after tracer administration the transmission scan is called a cold transmission scan (TX-scan) or a simultaneous transmission and emission scan (TEX-scan) respectively. An overview of the three types of scans is shown in figure 3.2.

3.2.1 Extraction of transmission data

During a TEX-scan 511 keV photons originating from the patient (emission data) as well as photons coming from the transmission source (transmission data) are detected. For the purpose of reconstruction of the attenuation

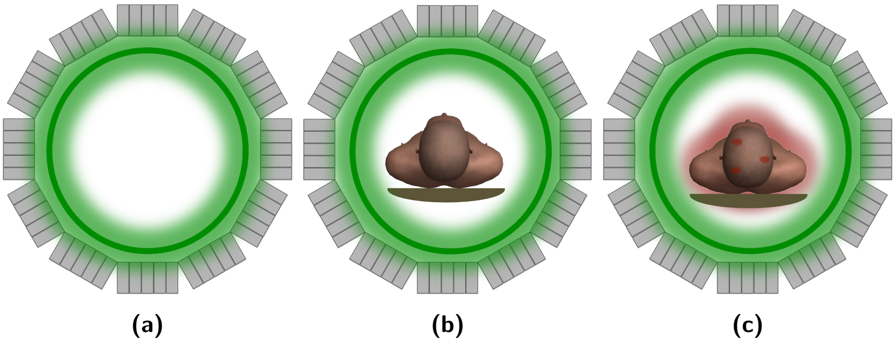

Figure 3.2: A blank reference scan (BX-scan) with nothing inside the FOV (a), a cold transmission scan (TX-scan) prior to ^{18}F-FDG-injection (b) and a simultaneous transmission and emission scan (TEX-scan) after ^{18}F-FDG administration (c). The gamma radiation originated from the annulus source is indicated in green, while the radiation from the patient is indicated in red.

map, only the transmission data is needed. To separate the transmission data from the emission data we need to know for each coincidence where the photon-pair was created. In a perfect TOF PET system, for each measured coincidence the difference Δt in detection times between the 2 photons in coincidence is known. This time difference can be used to calculate the location of the annihilation along a Line-of-Response (LOR):

$$\begin{aligned} \gamma &= .5(1 - \frac{c.\Delta t}{d_i}) \\ x_s &= x_1 + \gamma(x_2 - x_1) \\ y_s &= y_1 + \gamma(y_2 - y_1) \\ z_s &= z_1 + \gamma(z_2 - z_1) \end{aligned} \tag{3.1}$$

where c is the speed of light, (x_1, y_1, z_1) and (x_2, y_2, z_2) are the coordinates of the detection points of the event, d_i the distance between the detection points and (x_s, y_s, z_s) the source location. Knowing where the photons are coming from, the transmission data can easily be extracted.

The limited timing capabilities of current PET detectors limit the accuracy of the extraction of transmission data from the simultaneous emission/transmission data set. For a given source at position p the calculated source positions using eq. 3.1 will be distributed around p according to a kernel whose FWHM is defined by the timing resolution of the system (figure 3.3). A timing resolution of less than 66 ps is necessary to get sub-centimeter position resolution. Current commercially available TOF PET systems are characterized by good time-of-flight resolutions ($\simeq$ 500 ps) and there is still room for improvement [142, 143]. Because of the limited timing resolution it will be unclear for some events whether the photons came from the patient or from the transmission source. Therefore we propose the following hard decision rule (see figure 3.3):

- Choose a threshold radius τ_1
- Use the measured TOF difference (Δt) of each event to calculate the estimated source location of the positron emission
- If the location is outside a cylinder of radius τ_1 centered at the FOV center ($x_s^2 + y_s^2 > \tau_1^2$), the event is classified as part of the transmission data
- Else, the coincidence is classified as emission

Using this hard decision rule will have two consequences. First, not all transmission data will be extracted from the measured data. The amount of rejected transmission data will be evaluated using the **Transmission Rejection Rate**:

$$\mathbf{TRR} = \frac{\#\text{rejected true transmission events}}{\#\text{total true transmission events}} \tag{3.2}$$

If τ_1 is chosen to be the diameter of the annulus, on average 50% of the transmission data will be lost on each line of response. Secondly, emission events originated at locations close to the threshold radius τ_1 will be classified as transmission data. This contamination will be evaluated using the **Emission Contamination Rate**:

$$\mathbf{ECR} = \frac{\#\text{misclassified emission events}}{\#\text{estimated transmission events}} \tag{3.3}$$

In order to decrease this effect, τ_1 should be chosen as large as possible. It is clear that these two conditions are in conflict and a trade-off has to be made.

3.2.2 Derivation of the attenuation map

In a transmission scan, the attenuation factor a_i for LOR i relates the measured signal t_i to the signal b_i that would be measured in absence of

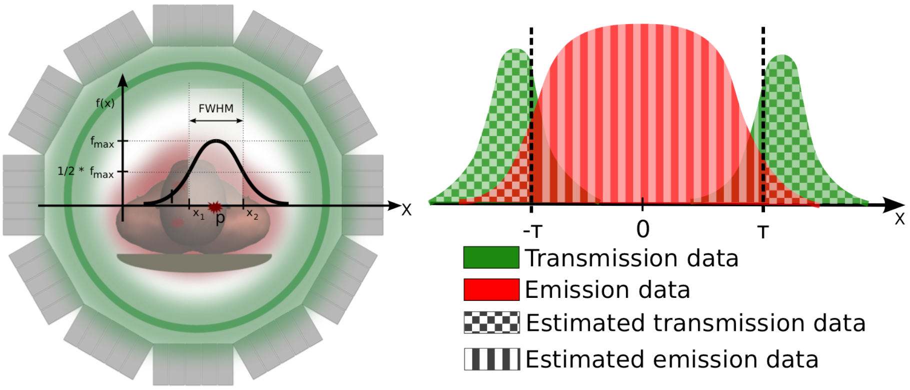

Figure 3.3: TOF-based extraction of transmission data on a particular LOR for a threshold radius τ_1.

attenuation :

$$t_i = a_i b_i \tag{3.4}$$

The signal b_i can be measured using a blank scan or can be derived with the simulation package GATE. The attenuation on LOR i can easily be calculated as $a_i = t_i/b_i$. However, only a small amount of activity is introduced into the annulus source which will lead to low statistics on many LORs, particularly on LORs passing through tissues with a high attenuation coefficient. This renders the problem ill-posed. Consequently, we calculate the attenuation by maximizing the log-likelihood function for emission tomography [5, 94, 144]:

$$L(\boldsymbol{\lambda}_a, \boldsymbol{\mu}) = \sum_i (-a_i y_i(\boldsymbol{\lambda}_a) + t_i ln(a_i y_i(\boldsymbol{\lambda}_a))), \tag{3.5}$$

where $\boldsymbol{\lambda}_a = (\lambda_{a,1}...\lambda_{a,J})$ is the activity distribution inside the annulus source, $\boldsymbol{\mu} = (\mu_1...\mu_J)$ the attenuation coefficients, J the number of voxels in the reconstruction matrix and $y_i(\boldsymbol{\lambda}_a)$ the estimated counts in absence of attenuation. In our situation $y_i(\boldsymbol{\lambda}_a)$ can be replaced with b_i:

$$L(\boldsymbol{\mu}) = \sum_i (-a_i b_i + t_i ln(a_i b_i)) \tag{3.6}$$

The function L is now concave in $\boldsymbol{\mu}$ [94, 144]. In this study we used a gradient ascent algorithm that attempts to maximize $L(\boldsymbol{\mu})$ as a function of

μ [5, 145]:

$$\mu_j^{k+1} = \mu_j^k + \alpha(1 - \frac{\sum_i c_{ij} t_i}{\sum_i c_{ij} a_i^k b_i}) = \mu_j^k + \alpha(1 - \frac{T_j}{B_j^k}) \tag{3.7}$$

with

$$\begin{aligned} t_i &= \text{ measured true transmission counts on LOR } i \\ b_i &= \text{ measured blank counts on LOR } i \\ c_{ij} &= \text{ sensitivity of detecting activity from voxel } j \text{ on LOR } i \\ a_i^k &= e^{(-\sum_m l_{im}\mu_m^k)}\text{, the current estimate of the attenuation on LOR } i \\ l_{im} &= \text{ the intersection length of LOR } i \text{ with voxel } m \\ \alpha &= \text{ a relaxation parameter} \end{aligned} \tag{3.8}$$

The reconstruction process can be described as follows : first the image T ($T_j = \sum_i c_{ij} t_i$) is calculated by back-projecting the counts t_i measured during the transmission scan into the voxels. Secondly, a B-image is derived, but this time the counts b_i are weighted with the current estimate of the attenuation a_i^k along LOR i. Finally, a voxel-by-voxel error ratio of the B and T-image is calculated and used to update the attenuation. The second and the last step are repeated until μ_j^k converges. The reconstruction process is summarized in figure 3.4.

In current TOF PET systems the transmission data needs to be extracted using the hard decision rule with threshold parameter τ_1. Due to this decision, transmission data will be lost and if τ_1 is to small, emission data will contaminate the transmission data. Suppose $\hat{t}_i$ represents the number of true transmission counts on LOR i after extraction of the transmission data and $\hat{b}_i$ represents the number of blank counts extracted when the same decision rule is applied. Equation (3.7) is modified as follows:

$$\mu_j^{k+1} = \mu_j^k + \alpha(1 - \frac{\sum_i c_{ij} \hat{t}_i}{\sum_i c_{ij} a_i^k \hat{b}_i}) \tag{3.9}$$

Now we need to prove that $\hat{t}_i = a_i \hat{b}_i$ is still valid if we assume that $t_i = a_i\ b_i$. Suppose $\hat{t}_i = \epsilon_i t_i$. ϵ_i depends on the threshold value τ_1 and the distribution of the estimated source locations on LOR i (figure 3.3). This distribution only depends on the activity distribution in the transmission source and the timing resolution of the system and is independent of the attenuation on

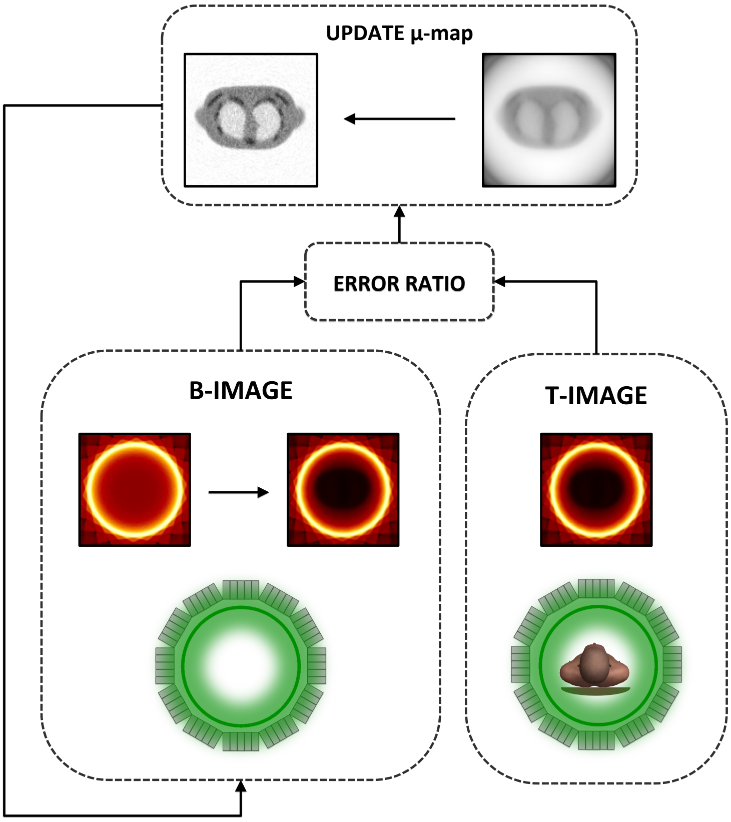

Figure 3.4: Iterative gradient ascent reconstruction. A T-image is created by back-projecting the transmission counts t_i for each LOR i into image space. The current B-image is created by attenuation corrected back-projection of the blank counts b_i using the current estimate of the μ-map. The error between the B- and the T-image is used to update the current μ-map. This process is repeated until convergence is reached.

this particular LOR. This implies that $\hat{b}_i = \epsilon_i b_i$ and therefore $\hat{t}_i = a_i \hat{b}_i$. Therefore, only those events of the blank scan whose estimated source location falls outside a cylinder of radius τ_1 will be back-projected during the second step of reconstruction in order to estimate $\hat{B}_j = \sum_i c_{ij} \epsilon_i a_i b_i$.

When a list-mode format is used to store the acquired or simulated data, eq. 3.9 can easily be converted to list-mode format :

$$\mu_j^{k+1} = \mu_j^k + \alpha(1 - \frac{\sum\limits_{e \in \widehat{\mathrm{TX}}} c_{i_e j}}{\sum\limits_{e \in \widehat{\mathrm{BX}}} c_{i_e j} a_i^k}), \tag{3.10}$$

with e the event index in the list-mode file, i_e the LOR event e belongs to, and $\widehat{\mathrm{TX}}$ and $\widehat{\mathrm{BX}}$ the extracted transmission and blank data using the TOF-based extraction method.

3.2.3 Image degrading effects

The algorithm described in eq. 3.10 can be used to derive the attenuation map from a transmission scan in ideal circumstances. However, when working with real data, some effects may decrease the accuracy of the reconstructed attenuation coefficients and the overall quality of the attenuation map. In this section we will define these effects and the possible solutions on how to control their influence in the reconstruction process.

3.2.3.1 Random coincidences

Compared to 2D PET, 3D PET acquisitions suffer from an increase in the number of random coincidences. The presence of these randoms in the blank and transmission data influences the reconstructed attenuation coefficients. In this work, randoms are estimated using a delayed windowing technique. The delayed events are then subtracted from the collected prompt data during reconstruction :

$$\mu_j^{k+1} = \mu_j^k + \alpha(1 - \frac{\sum_i c_{ij} \hat{t}_{i,p} - \sum_i c_{ij} \hat{t}_{i,d}}{\sum_i c_{ij} a_i^k \hat{b}_{i,p} - \sum_i c_{ij} a_i^k \hat{b}_{i,d}}), \tag{3.11}$$

where indices p and d represent prompt (trues, randoms and scatter) and delayed data respectively.

3.2.3.2 Scattered coincidences

Besides random events, correction for scattered events is mandatory to obtain accurate attenuation coefficients at 511 keV. Scatter estimation will be discussed in the next chapter. If the fraction of the extracted prompt transmission events scattered in the patient and the annulus source ($\hat{s}_{t,i}$) and the fraction of the extracted prompt blank events scattered in the annulus source ($\hat{s}_{b,i}$) are estimated, the following corrections can be implemented:

$$\mu_j^{k+1} = \mu_j^k + \alpha(1 - \frac{\sum_i c_{ij}\hat{t}_{i,p}(1-\hat{s}_{t,i}) - \sum_i c_{ij}\hat{t}_{i,d}}{\sum_i c_{ij}a_i^k\hat{b}_{i,p}(1-\hat{s}_{b,i}) - \sum_i c_{ij}a_i^k\hat{b}_{i,d}}) \tag{3.12}$$

3.2.3.3 Dead-time and random cross-talk

The performance of a PET system highly depends on the characteristics of the detectors and readout electronics. Each detector will need a minimum amount of time to process incoming events and during coincidence processing, no further coincidences may be accepted. This effect of "dead time" compromises the performance of the system when the photon flux increases. Dead time effects will therefore differ between the TEX-scan and the initial blank scan.

During a simultaneous acquisition of emission and transmission data, there is a possibility that two photons originating from the two distinct sources (patient or transmission source) will be combined in the coincidence processing chain. We will refer to this effect as random cross-talk (see figure 3.5). Although these coincidences are compensated with the random correction method random cross-talk will cause less detections of true transmission events compared to a stand-alone transmission scan.

The presence of dead time effects and random cross-talk implies that the difference between the back-projection B_j and T_j in eq. 3.7 is not only related to attenuation. The reconstruction algorithm should be adapted to include these additional effects. The attenuation effect will be negligible on those LORs which do not intersect with the patient. On these LORs, the difference in count rate between the blank and transmission data is only related to dead-time and random cross-talk. Subsequent to the random correction, we propose to count the number of extracted events in both blank and transmission scan which are outside a FOV of radius τ_2. The ratio

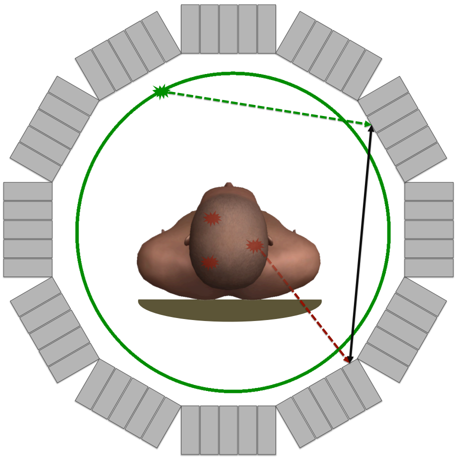

Figure 3.5: Random cross-talk composed of two photons originating from two distinct sources.

of those counts is then used as a global count rate consistency correction factor in the reconstruction :

$$\mu_j^{k+1} = \mu_j^k + \alpha(1 - \frac{\hat{T}_j}{\beta_{\tau_2} \hat{B}_j^k}), \quad \beta_{\tau_2} = \frac{\sum_{>\tau_2} t_i}{\sum_{>\tau_2} b_i} \tag{3.13}$$

The value of τ_2 is chosen higher than τ_1 to remove emission contamination from the calculated counts. The process is illustrated in figure 3.6.

3.2.4 Post processing

Although we have presented a framework on how dead-time, random cross-talk, scatter and random coincidences can be corrected, other effects such as the Poisson nature of radioactive decay, and the low amount of activity inside the transmission source, may increase the variance in the reconstructed attenuation map. To avoid noise propagation in the reconstructed emission image during attenuation correction, a segmentation technique is applied to the reconstructed attenuation maps as a post processing step.

In order to segment the reconstructed attenuation maps into different tissues a Markov Random Field (MRF) technique based on a Gaussian Mix-

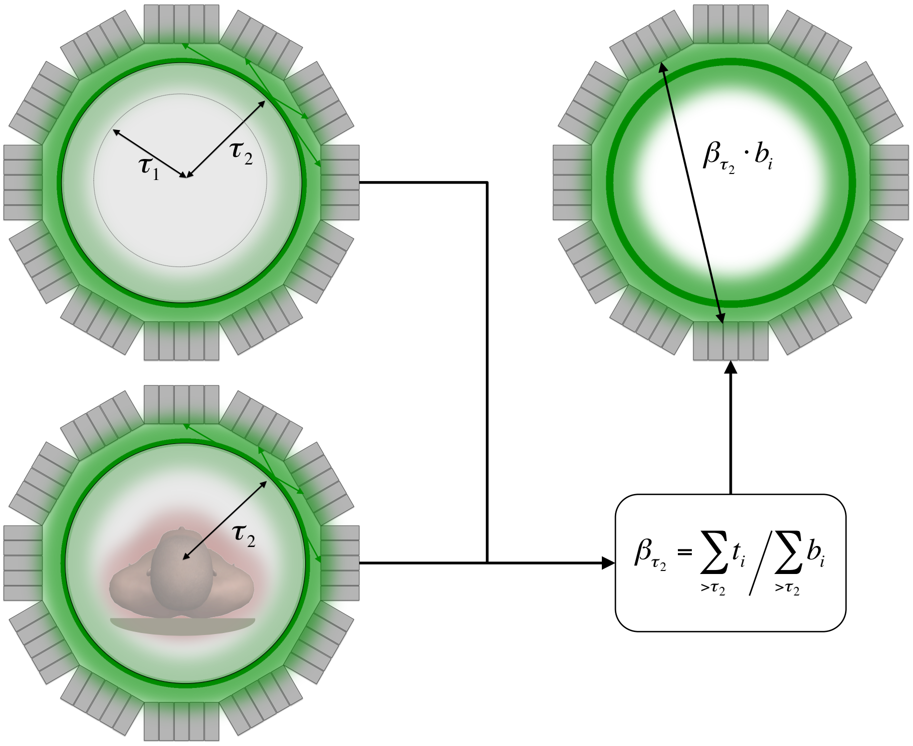
τ_1
τ_2
$\beta_{\tau_2} \cdot b_i$
τ_2
$\beta_{\tau_2} = \sum_{>\tau_2} t_i \Big/ \sum_{>\tau_2} b_i$

Figure 3.6: Global count rate correction to restore inconsistency between blank and transmission scan. The difference in count rate is measured on those LORs which do not suffer from high attenuation and emission contamination.

ture (GM) model was used. First the maps were smoothed using a Gaussian kernel. To fit a GM model to the histogram of the image data we applied the Expectation Maximization (EM) algorithm to estimate the number of Gaussian mixtures and their corresponding parameterization [146]. Labels were assigned to each voxel using Iterated Conditional Modes (ICM) and spatial correlations between the neighboring voxel labels were taken into account using MRF priors. After segmentation, mean attenuation coefficients are calculated for each region. As the PET acquisition introduces partial volume effects that cause a smoothing of attenuation coefficients at the edges between different tissues, the mean coefficients for the segmented regions will be overestimated in tissue of low attenuation and vice versa. To solve this issue, a smaller region *r* is calculated for each region *R* by using morphological operations (erosion). These smaller regions will not include tissue borders and are used as a mask to calculate mean attenuation coeffi-

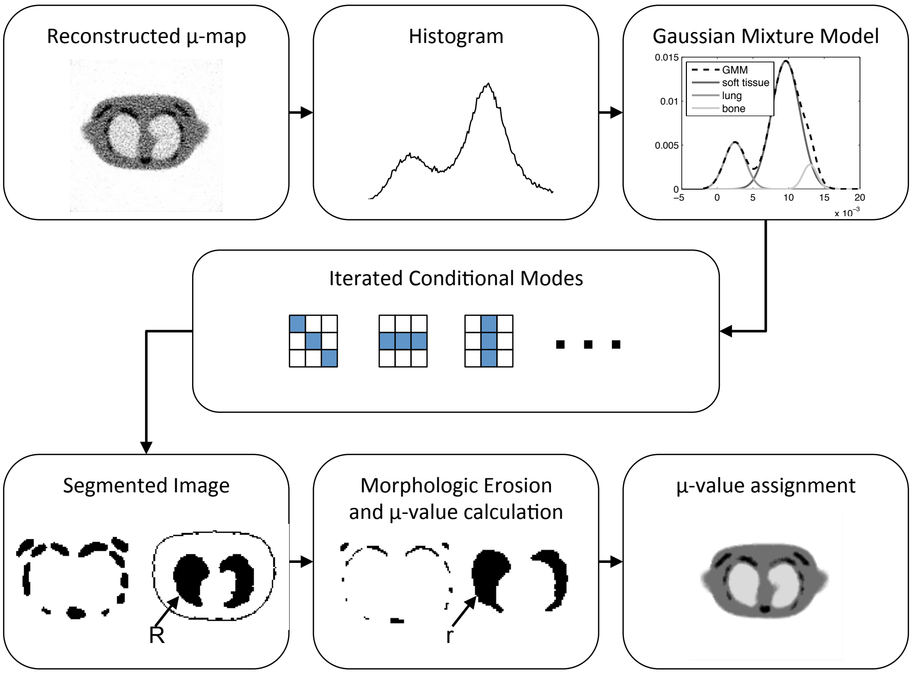
Reconstructed μ-map
Histogram
Gaussian Mixture Model
0.015
0.01
0.005
0
−5
0
5
10
15
20
x 10^-3
GMM
soft tissue
lung
bone
Iterated Conditional Modes
Segmented Image
R
Morphologic Erosion and μ-value calculation
r
μ-value assignment

Figure 3.7: Segmentation of the reconstructed attenuation map.

cients within the original reconstructed image. Finally, the calculated means are assigned to the bigger regions R. The complete process is depicted in figure 3.7.

3.2.5 PET image reconstruction

Finally, the PET image is reconstructed. Attenuation effects are compensated using the reconstructed segmented attenuation map derived from the blank and TEX-scan measured on a TOF PET system with moderate TOF resolution. The log-likelihood function from (3.5) can be modified to include both transmission and emission data :

$$L(\lambda_p, \lambda_a, \mu) = \sum_i (-\bar{t}_i + t_i ln(\bar{t}_i)), \tag{3.14}$$

with

$$\bar{t}_i = a_i \sum_k c_{ik}(\lambda_{p,k} + \lambda_{a,k}),$$

and where $\boldsymbol{\lambda}_p = (\lambda_{p,1}...\lambda_{p,J})$ is the activity distribution inside the patient and $\boldsymbol{\lambda}_a = (\lambda_{a,1}...\lambda_{a,J})$ the activity distribution in the annulus-shaped transmission source. As $\boldsymbol{\mu}$ is now known, the function is concave in $\boldsymbol{\lambda} = \boldsymbol{\lambda}_p + \boldsymbol{\lambda}_a$ and can be maximized by applying a number of iterations of the ML-EM routine [94, 144] which can be converted to TOF list-mode reconstruction as in [147]:

$$\lambda_j^{k+1} = \frac{\lambda_j^k}{\sum_i c_{ij}} \sum_e c_{i_e j_{\Delta t_e}} \frac{1}{\sum_n c_{i_e n_{\Delta t_e}} a_{i_e} \lambda_j^k}, \tag{3.15}$$

where $\sum_i c_{ij}$ is the summation of sensitivity c_{ij} over all possible LORs, i_e is the LOR index of event e and Δt_e the time bin. It is important to note that for the reconstruction of the emission distribution, no emission data needs to be extracted. The iterative reconstruction uses both transmission and emission events.

3.3 Simulation study

To investigate the proposed method, several simulation studies were performed with GATE [50]. In this section the different steps that were taken to perform these studies will be described. First we defined an accurate model of the Philips Gemini TF PET scanner (Philips Medical Systems, Cleveland, USA). We have chosen this model as it is combined with a Philips Achieva 3T MR into the first sequential whole-body TOF PET/MRI [148]. Secondly, the activity of the transmission source was determined. Then the influence of the diameter of the source and threshold value τ_1 on the TOF-based extraction was evaluated and thirdly, the method was validated with a simulation study using the digital NCAT torso phantom. Finally a digital phantom of the lower torso and abdomen was used to estimate the radiation dose delivered to the patient by the transmission source. Because the dosimetry simulations were conducted during the second term of this work a newer version of NCAT software, the XCAT package, was used. An overview of all GATE simulations can be found in table 3.1. In this chapter we will refer to each simulation type with their names B_x,TE_x or E_x.

Scan type	Annulus (activity, radius)	Phantom (type, total activity)
E_{Nema}	-	NEMA cylinder, 50-1050 MBq
B	0-148 MBq, 30-35 cm	-
TE_{Nema}	0-74 MBq, 30-35 cm	NEMA cylinder, 500 MBq
TE_{20}	18 MBq, 30-35 cm	20-cm cylinder, 250-750 MBq
TE_{40}	18 MBq, 30-35 cm	40-cm cylinder, 250-750 MBq
TE_{60}	18 MBq, 30-35 cm	60-cm cylinder, 250-750 MBq
TE_{ncat}	18 MBq, 35 cm	NCAT phantom, 44.5 MBq
E_{ncat}	-	NCAT phantom, 44.5 MBq
T_{xcat}	18-74 MBq, 35 cm	XCAT phantom, 0 MBq
E_{xcat}	-	XCAT phantom, 86.4 MBq

Table 3.1: Blank scans (B_x), simultaneous transmission/emission scans (TE_x) and emission scans (E_x) using GATE. All scans had an acquisition time of 3 minutes.

3.3.1 PET system simulation

The PET scanner is composed of a full ring of 28 sectors with a diameter of 90.34 cm. Each module contains a 23 x 43 array of 4 x 4 x 22 mm^3 LYSO crystals. In the actual system, signal readout is performed by a hexagonal array of PMTs. When a photon is detected, digitization is done by analog-to-digital converters for each PMT, corresponding to an equivalent integration time of 90 ns [34]. The signal readout was modeled in GATE with a paralysable dead time of 90 ns on the singles chain. A paralysable coincidence dead time of 150 ns was also included. The timing resolution of the system was set to 600 ps.

An overview of the GATE model is shown in figure 3.8. To validate our Monte Carlo model, simulations of type E_{Nema} were done in accordance with the NEMA NU 2-2001 protocols [149]. In this work we used the standard 20 x 70-cm cylindrical phantom containing a 70 cm long line source at 4.5 mm from the central axis filled with ^{18}F-FDG. The total activity ranged from 50 to 1050 MBq. GATE results were compared to experimental data derived from NEMA measurements on the Philips Gemini TF PET/MRI system.

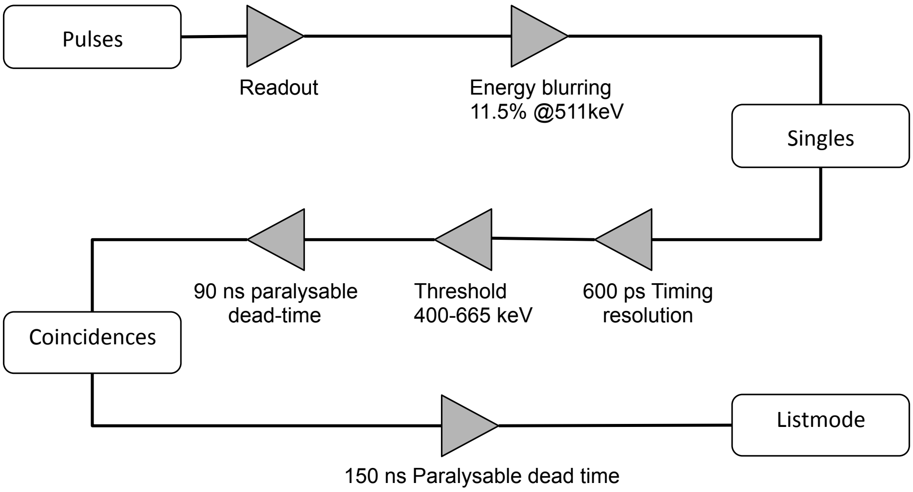
Pulses
Readout
Energy blurring
11.5% @511keV
Singles
600 ps Timing resolution
Threshold 400-665 keV
90 ns paralysable dead-time
Coincidences
150 ns Paralysable dead time
Listmode

Figure 3.8: GATE model of the TF Gemini PET system.

3.3.2 Annulus shaped transmission source

In this section we describe how the optimal parameters for the transmission source were derived. When the annulus transmission source is inserted in the FOV of the scanner, the PET count rate performance is expected to decrease. The count rate performance during the blank scans (B) and simultaneous transmission/emission scans of type $\mathrm{TE}_{\mathrm{Nema}}$ were evaluated in function of the parameters of the transmission source. The simultaneous scans were derived from NEMA simulations using the 20-cm-diameter cylindrical phantom with the transmission source inside the FOV. Based on the results obtained from these simulations, the optimal amount of activity for this study was determined.

Because of the limited timing resolution, emission and transmission data will be misclassified during the TOF-based extraction process (figure 3.3). We evaluated the influence of the diameter of the source and the parameter τ_1 on the extraction of transmission data using simultaneous transmission/emission scans of type TE_{20}, TE_{40}, TE_{60}. To mimic a whole-body imaging situation, three cylindrical phantoms of 20-cm, 40-cm and 60-cm-diameter and 70 cm length were used. The phantoms were filled with water and injected with ^{18}F-FDG varying from 250 MBq to 750 MBq. In all three simulation types two different annulus transmission sources with an inner

Tissue type	SUV	Attenuation coefficient (mm^{-1})
Lung	0.48	0.00248
Soft tissue	1.67	0.00960
Bone	1.55	0.01700
Myocardium	5.00	0.00960
Lesion	6.00	0.00960

Table 3.2: FDG-PET uptake (SUV) and attenuation coefficients for different tissue types.

radius of 30 and 35 cm were used. Next, we evaluated the influence of the erroneous separation of emission and transmission data on the reconstructed attenuation maps of the three cylinders. The mean attenuation coefficient of water was compared with the real attenuation coefficient of water (0.097 cm^{-1}) found in literature.

3.3.3 Human torso phantom

The method was validated with a simulation study using the digital NCAT phantom (TE_{ncat}, E_{ncat}) [2]. Thirty-two 4 mm slices of the torso were segmented into different tissue types including one lesion inside the lungs. The phantom was injected with 6.5 MBq/kg of ^{18}F-FDG, 60 minutes prior to scanning. Table 3.2 shows the FDG-PET uptake values (SUV) and attenuation coefficients assigned to each tissue. A central slice of the tracer distribution and attenuation map is shown in figure 3.9. The NCAT phantom has a maximum lateral outside dimension of 57 cm and weighs 10 kg. A 35-cm-radius transmission source filled with 18MBq of ^{18}F-FDG was used. A 3 minutes blank and simultaneous transmission/emission scan was acquired.

3.3.4 Estimation of Radiation Dose

Prior to PET acquisition, the patient is injected with a radiopharmaceutical. The internal radiation dose delivered to the patient is of great concern, especially when the PET system is combined with a CT scanner. The absorbed dose is defined by the mean energy deposited by ionizing radiation to matter per unit of mass. The SI unit of absorbed dose is Gray (1 Gy

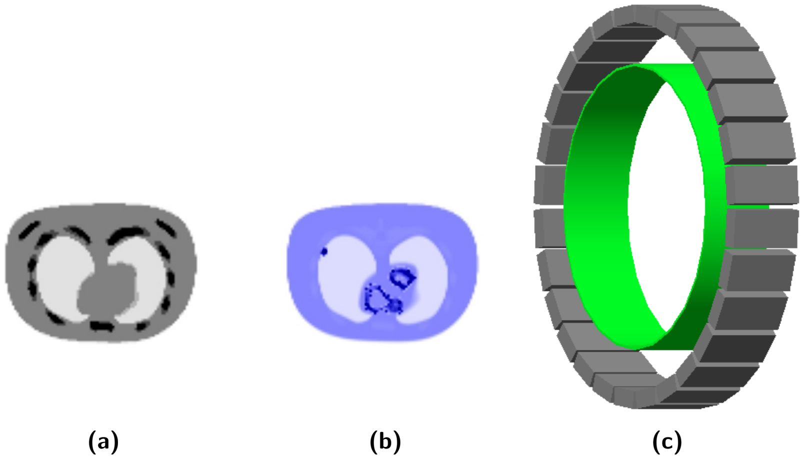

Figure 3.9: Transverse slice of the NCAT attenuation (a) and emission distribution (b). Annulus transmission source positioned inside the FOV of a PET Scanner based on the Philips Gemini TF (c).

$= 1\frac{J}{kg}$). The equivalent dose depends on the radiation type and can be derived from the absorbed dose as follows:

$$H_t = W_r D_{t,r} \tag{3.16}$$

where $D_{t,r}$ is the dose delivered by radiation type r averaged over tissue t and W_r the weighting factor for radiation type r. The SI unit for equivalent dose is sievert (Sv). Some tissues like bone marrow are more sensitive to radiation than others, therefore the effective dose is calculated by summation of tissue equivalent doses weighted with a factor W_t, which takes into account the radiation sensitivity of each organ being irradiated:

$$E = \sum W_t H_t \tag{3.17}$$

The transmission method described in this chapter increases the dose as an additional positron emitting source is inserted in the PET FOV. Although the amount of activity inside the source is limited and the patient is only exposed to radiation during the PET acquisition, the radiation dose should be kept as low as possible. We estimated the radiation dose to different tissues by simulating an XCAT phantom in GATE. Fifty 4-mm slices of the lower torso and abdomen region were segmented into different tissues. Three transmission scans of type T_{XCAT} were acquired. For each scan a different amount of activity was injected in the transmission source: 18,

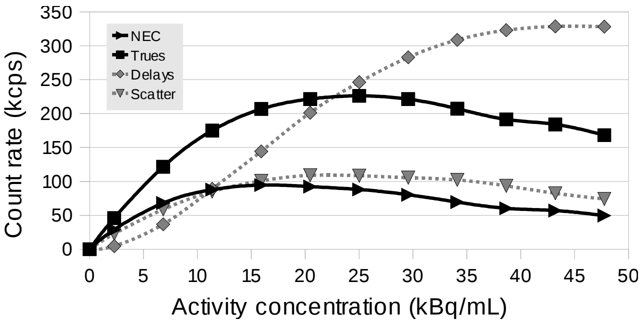

Figure 3.10: True, scattered and random count rate performance for GATE Gemini TF model using the NEMA protocol.

37 and 74 MBq respectively. Next, the phantom was injected with 8.6 MBq/kg of ^{18}F-FDG and an emission scan (E_{XCAT}) was acquired. To mimic a clinically relevant situation, lesions were inserted in the liver, colon and spine. All lesions had a contrast of 8:1 to the activity in muscle tissue. For each scan the radiation dose absorbed by the patient was simulated. Finally, the effective dose in each tissue type and the total effective dose was calculated. For this purpose tissue depended weighting factors W_t were obtained from the International Commission on Radiological Protection (ICPR) recommendation [150].

3.4 Results

3.4.1 PET system simulation

The system performance was evaluated using the Noise Equivalent Count Rate (NECR) defined as [151]:

$$NECR = \frac{T^2}{T + S + 2R}, \tag{3.18}$$

where T, S and R are the rates of true, scattered, and random coincidences within the boundaries of the object scanned. Figure 3.10 summarizes the results from count rate simulations for a 20 x 70-cm cylindrical NEMA phantom. The NECR curve shows a peak value of 94 kcps which occurs at an activity concentration of 15.7 kBq/ml. Ojha *et al.* [148] reports a peak NECR rate of 110 kcps at the same activity concentration.

3.4.2 Annulus shaped transmission source

Figure 3.11 shows the true count rate performance of the blank scans and simultaneous transmission/emission scans of type TE_{Nema}. Increasing the transmission (TX) activity in a simultaneous transmission/emission scan will influence the count rate performance of the emission as shown in figure 3.11b. Figure 3.11 also shows that changing the radius of the source from 30 cm to 35 mm does not have a huge impact on the emission for transmission activities below 80 MBq. Influences on the emission count rate should be avoided and placing the transmission source closer to the detectors makes it easier to extract the transmission data from the emission data. In our work the annulus source is filled with 18 MBq of FDG. The emission count rate drops to 86% of the count rate obtained without transmission source. Although 18 MBq seems low, results will show that accurate attenuation maps can be derived.

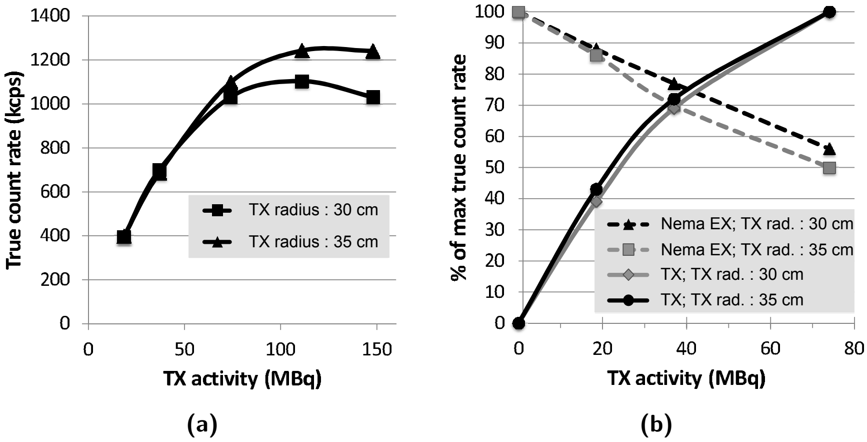

Figure 3.11: (a) True count rate of a blank scan for different transmission (TX) source diameters and activities. (b) Dotted line: percentage of true NEMA emission (EX) count rate during a TE_{Nema} scan for different TX source diameters and activities with respect to the maximum count rate measured during a E_{Nema} scan. Full line: true transmission count rate during a TE_{Nema} scan normalized to the transmission count rate measured at a TX activity level of 80 MBq.

The TOF-based extraction of transmission data and the reconstruction of the attenuation map was first evaluated with phantom studies using uniform water cylinders. For each study the ECR, TRR and reconstructed μ-values are reported.

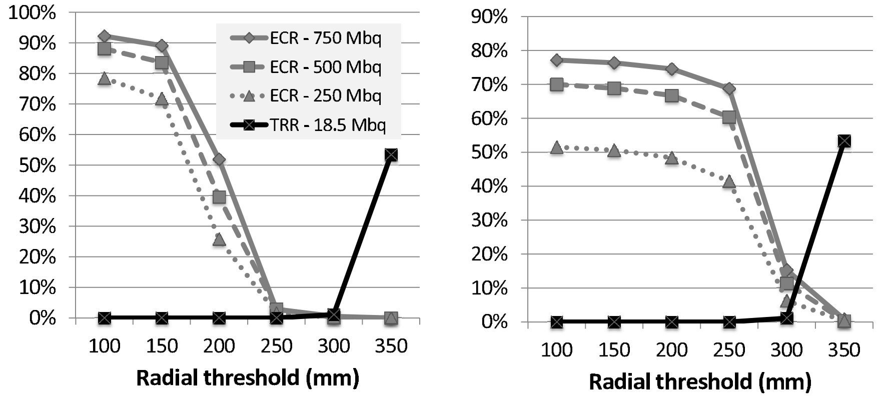

(a) Cyl.: 40 cm /TX: 35 cm

(b) Cyl.: 60 cm /TX: 35 cm

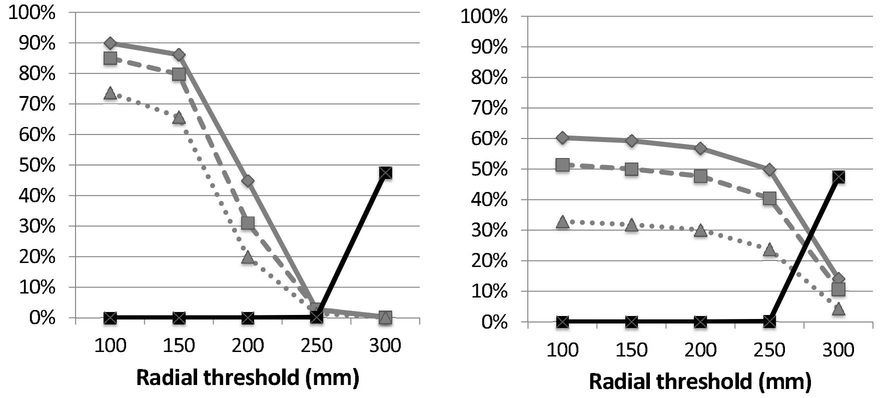

(c) Cyl.: 40 cm /TX: 30 cm

(d) Cyl.: 60 cm /TX: 30 cm

Figure 3.12: Misclassified emission data with respect to the estimated transmission (ECR) and rejected transmission data with respect to the true transmission data (TRR) for a 40-cm-diameter cylinder (a,c) and 60-cm-diameter (b,d) cylinder. Fractions are calculated for different decision rules (τ_1-values) using an annulus source with a radius of 35 cm (a,b) and 30 cm (c,d). The activity in the cylinders varied from 250 to 750 MBq. The number of transmission events are calculated within a FOV determined by the radius of the cylinder.

3.4.2.1 Extraction of transmission data

The TOF-based extraction process was applied to simulations of type TE_{40} and TE_{60} and results are summarized in figure 3.12. The graphs show the ECR and TRR for different values of τ_1. Emission activity levels of 250,

Annulus radius		30 cm			35 cm	
Activity\Diameter	20 cm	40 cm	60 cm	20 cm	40 cm	60 cm
250 MBq	0.26	0.10	8.36	0.29	0.10	5.09
500 MBq	0.99	0.58	13.59	0.66	0.64	9.11
750 MBq	1.63	0.95	17.62	0.98	0.75	12.61

Table 3.3: Relative error (%) of attenuation coefficient of water (0.097 cm^{-1}) for three cylindrical phantoms of 20-cm, 40-cm, 60-cm-diameter filled with 250 to 750 MBq of FDG. A 30 and 35-cm-radius annulus transmission source was used.

500 and 750 MBq were used.
When a 35-cm-radius annulus source is used and τ_1 is set to 30 cm a ECR of 0.52% and 15.31% is obtained for the 40 and 60-cm-diameter cylinders injected with 750MBq of ^{18}F-FDG. The TRR is below 2%. When the radius of the source is reduced to 30 cm, and $\tau_1 = 30$ cm the ECRs are 0.26% and 14.10% but the TRR increases to 47.48%. Choosing a threshold value τ_1 of 25 cm resulted in an ECR of 49,84% and 2,66% and a TRR of 0.16%.

3.4.2.2 Reconstruction of the attenuation map

Based on all configurations of simulation type TE_{20},TE_{40} and TE_{60}, 18 attenuation maps were reconstructed. The relative percent difference of the reconstructed attenuation coefficient compared to the real attenuation coefficient of water at 511 keV are depicted in table 3.3.

3.4.3 NCAT simulation study

Finally the method was evaluated with a phantom study closer to clinical practice. For this study we also present the influence of the estimated attenuation map on the reconstructed emission image.

3.4.3.1 Extraction of transmission data

Table 3.4 shows the number of events simulated during the simultaneous transmission/emission scans of type TE_{ncat}. The transmission events within a FOV-diameter of 57 cm as well as the total amount of transmission events

Counts collected in TE$_{ncat}$ scan		% of counts after extraction		
		τ_1 = 200	250	300 mm
True TX (57 cm FOV)	25.60 M	99.94	99.85	95.84
True TX	50.38 M	99.97	99.92	97.26
True EX	25.98 M	10.91	1.39	0.52
TX scattered in annulus	3.03 M	99.85	98.82	87.39
EX scattered in annulus	1.19 M	10.91	1.39	0.79
TX scattered in phantom	0.77 M	99.52	99.71	94.57
EX scattered in phantom	8.08 M	19.61	5.23	0.71
Randoms	20.80 M	71.44	60.74	46.95
Delays	21.62 M	71.01	60.42	46.79

Table 3.4: First column : collected trues, randoms, delays, annulus scatter and phantom scatter during a simulation of type TE$_{ncat}$. Second column: percentage of collected counts after extractions. In the first row, only LORs who pass through a FOV of 57 cm are considered.

are counted. The second column shows the fraction of counts that remains after TOF-based extraction of transmission events. This fraction will be used to reconstruct the attenuation map. From these results we measured that for τ_1=30 cm the ECR is 0.55% and the TRR is 4.61%. If the scattered events are also taken into account the ECR reaches 0.72%. We also see that 5.06% of the extracted transmission data are transmission events scattered in the annulus source and 1.38% scattered in the NCAT phantom.

3.4.4 Reconstructed attenuation maps

Six attenuation maps were reconstructed from a simultaneous transmission/emission scan of type TE$_{\mathrm{ncat}}$. An overview is listed in Table 3.5. First a consistency correction factor of $\beta_{\tau_2=325} = 0.9155$ was derived (3.2.3.3). In the first four reconstructions τ_1 was set to 30 cm. The fifth and last map were reconstructed with $\tau_1 = 25$ cm and $\tau_1 = 20$ cm respectively. We included scatter and random events in the second and third dataset to evaluate their effect on the reconstructed attenuation coefficients. Random events were also included in the fourth data set but were compensated by subtracting the delayed events during reconstruction. For each tissue type VOIs of 4 cm^3 were defined: 15 in the lungs, 5 in soft tissue and 5 in bone.

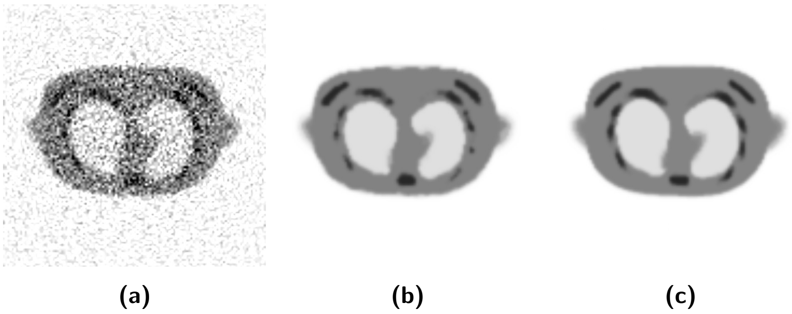

Figure 3.13: Visual comparison of a central slice of the unsegmented (a) and segmented (b) attenuation map derived from a transmission scan of type TE_{ncat} and the correct attenuation map (c).

Mean percentage difference compared to the correct attenuation coefficients were calculated and shown in table 3.5. Figure 3.13 shows a central slice of the unsegmented, segmented and the correct attenuation map.

3.4.5 Reconstructed PET images

The first reconstructed attenuation map was used to evaluate reconstruction of emission data. Two emission data sets were derived and reconstructed from the transmission/emission scan TE_{ncat} and emission scan E_{ncat}. Deadtime correction factors were used in order to correct for coincidence losses in both scans. Attenuation correction was implemented in the forward projector of the ML-EM algorithm. In the first reconstruction an emission map E_1-map was derived using our reconstructed attenuation map for attenua-

τ_1	TX events	Lung	Soft tissue	Bone
300	Trues	1.75	1.74	-3.61
300	Trues + scatter	0.45	-10.62	-16.87
300	Trues + randoms	-25.28	-46.24	-38.84
300	Trues + randoms - delays	1.43	-2.20	3.01
250	Trues	-5.74	-3.27	-3.08
200	Trues	-34.23	-38.88	-25.76

Table 3.5: Percentage mean difference in μ-values (%) in VOIs of different tissues compared to the correct values (table 3.2).

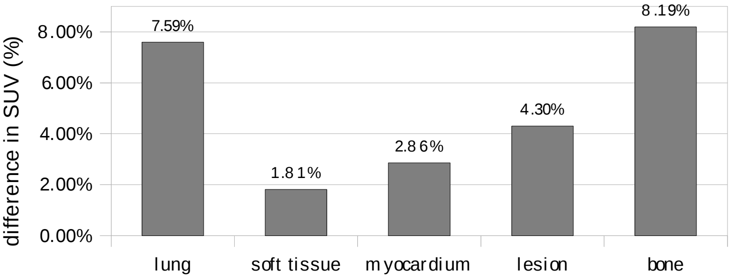

Figure 3.14: Absolute mean percentage difference of reconstructed SUV values of the E_1-map compared to the SUV-values from the E_2-map

tion correction. In the second reconstruction an E_2-map was reconstructed using the correct attenuation map.

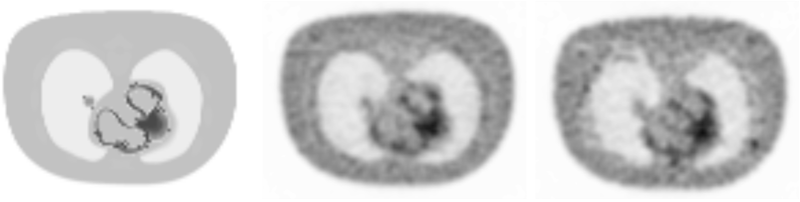

(a) (b) (c)

Figure 3.15: Visual comparison of a central slice of the true tracer distribution (a), reconstructed E_1-map (b) and reconstructed E_2-map (c).

Figure 3.15 shows a central slice of the true tracer distribution, E_1-map and the E_2-map. The absolute mean percentage error ($|\%SUV|$) of the E_1-map compared to the E_2-map is depicted in figure 3.14. The same VOIs as in table 3.5 were used, except for the myocardium and the lesion where new VOIs were defined. When no attenuation correction is applied, errors are above 95% for all tissues.

3.4.6 Estimation of Radiation Dose

Figure 3.16 shows the maximum intensity projection of the tracer distribution and the absorbed dose collected during the first T_{xcat} scan and the emission scan E_{xcat}. The effective doses to particular tissue are depicted in table 3.6. The effective dose was summed over all tissue and a comparison between transmission scans with different source activities and the emission scan is shown in figure 3.17. When an annulus source activity of 18 MBq

Tissue	Transmission scan			Emission scan
	18 MBq	37 MBq	74MBq	
Adipose tissue	3.82e-03	6.26e-03	1.25e-02	9.25e-02
Cartilage	3.97e-03	7.44e-03	1.49e-02	1.10e-01
Intestine	4.44e-03	8.30e-03	1.66e-02	1.09e-01
Lungs	5.15e-03	8.08e-03	1.61e-02	6.89e-02
Liver	1.20e-03	2.22e-03	4.44e-03	4.86e-02
Muscle	4.18e-03	7.68e-03	1.54e-02	9.51e-02
Spine	3.11e-03	6.02e-03	1.21e-02	1.36e-01
Rib	2.61e-04	5.03e-04	1.01e-03	7.81e-03

Table 3.6: Simulated effective dose (mSv) for different tissue types during transmission and emission scanning. During the transmission scans, an annulus transmission source with different activities was used.

was used, the total effective dose is less than 4% of the total effective dose during the emission scan. When the activity inside the source is increased to 74 MBq, the dose increases to 13% of the emission dose. The total effective dose during the emission scan was 0.5 mSv.

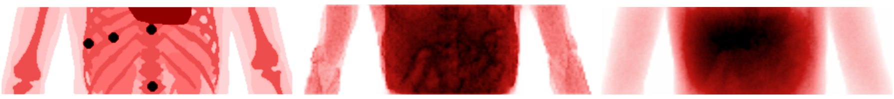
(a) (b) (c)

Figure 3.16: Maximum intensity projection of tracer distribution (a), absorbed dose from transmission scan (b) and absorbed dose from emission scan (c).

3.5 Discussion

An annulus transmission source can be used to measure the transmission of gamma photons through tissue in coincidence mode. In the study presented in this chapter the concept of simultaneous transmission and emission imaging was tested with simulation studies using a digital torso phantom. Without the presence of scatter and random coincidences, the mean absolute error in μ-values was below 2% in the lungs and soft-tissue and below 4% in bone. A mean error of the reconstructed SUV values below 9 % was

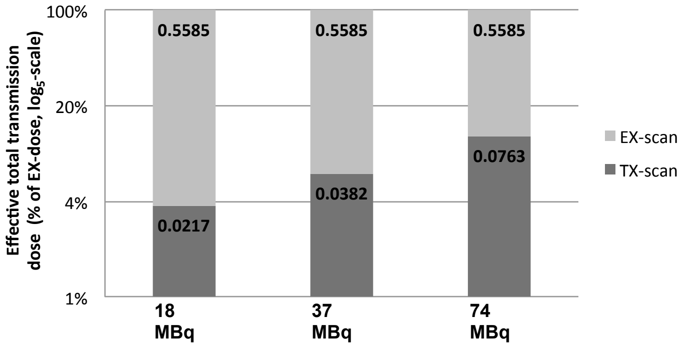

Figure 3.17: Effective total transmission dose as a percentage of the total effective emission dose. A logarithmic scale was used.

obtained in all regions. However, larger errors are found in bone and lung tissue compared to soft tissue.

The presence of randoms, scatter and count-rate effects will increase noise and decrease contrast yielding less accurate attenuation coefficients (table 3.5). In this work randoms were estimated in both blank and transmission scan using a delayed window method. The advantage of this method is that the delayed channel has identical dead-time properties to the prompt channel. Furthermore, the extraction of transmission data can easily be applied to the delayed data, to estimate the extracted randoms. The delayed counts are then subtracted from the prompt signal during reconstruction.

In 3D PET, the amount of scattered events can become substantial. The extracted transmission events derived from a simultaneous transmission/emission scan will contain true and scattered transmission events. The presence of scattered transmission events causes an increase of T_j in eq. 3.9. As a results, attenuation coefficients will be underestimated. Although scatter estimation is currently not implemented in the method described in this chapter, it will be necessary in the future. A possible approach is to first estimate the distribution of the extracted scattered transmission events using a Single Scatter Simulation method. This distribution must be normalized to fit the data. Because the same transmission source is used for each blank scan, the scatter scaling factor can be derived by calibrating the SSS software with GATE simulations. The reader is referred to the next chapter for more details on this approach.

In section 3.2.3.3 we introduced a correction factor (β_{τ_2}) to ensure count-rate consistency between the transmission data and blank data. τ_2 is chosen high enough to avoid contamination of true and scattered emission data. If contamination is still present, β_{τ_2} will be overestimated causing an overestimation of the attenuation coefficients.

Care should be taken when choosing the amount of activity inside the source. In order to provide good statistics, the amount of activity should be high enough. However, increasing the activity decreases the count rate performance of the true emission data due to dead-time effects and random cross-talk. The loss of emission data needs to be limited for accurate quantitative PET imaging. Our results show that a 3 minutes transmission scan using 18 MBq ($\simeq$ .5 mCi) of source activity inside the annulus is adequate to reconstruct an accurate attenuation map. In this case the presence of the source causes the emission true count rate to drop to $\sim$ 86% of its original value (figure 3.11). However, higher activities might be needed when experimental data is acquired as image degrading effects such as scattered coincidences, randoms, detector efficiency will compromise the accuracy of the reconstructed attenuation map. The loss of emission data can be compensated by longer scanning times.

Another parameter that needs to be optimized is the choice of the threshold value τ_1. Table 3.5 shows an underestimation of soft-tissue attenuation when τ_1 is set to 200 mm. For $\tau_1 = 300$ mm less emission will be misclassified and better estimates of attenuation coefficients are obtained. However, higher values for τ_1 would cause more loss of transmission data resulting in low statistics.

Increasing the activity would also increase the dose exposed to the patient. In conventional PET, a typical source strength used for PET transmission scanning in coincidence mode ranges from 370 to 740 MBq and scanning times are in the order of 5-10 min. Studies have been done comparing radiation exposure between CT- and germanium-based techniques with a recent PET scanner [152]. These results showed that the doses in a typical PET transmission scan is negligible compared with the internal radiation doses from a 370 MBq intravenous injection of ^{18}F-FDG. The effective dose from the CT-scan is found to be significantly higher than the dose of the germanium-based technique. The effective dose will be much lower in our case than the typical effective dose in one bed position of the ^{68}Ge transmission scan as both activity and time of exposure are lower. In a simulation study using the XCAT phantom we compared the effective dose during a transmission scan with the dose from a stand-alone emission scan. Even when 74 MBq of ^{18}F-FDG is inserted in the annulus transmission source, the total effective dose was below 0.1 mSv. The dose accumulated during the stand-alone emission scan was 0.5 mSv. Additionally, these simulations only take into account the dose accumulated during the PET acquisition. After the acquisition, only the tracer administered to the patient will cause additional radiation to the patient.

The simulation study provides a proof of concept, illustrating the potential benefit of using an annulus-shaped transmission source for simultaneous transmission and emission imaging. A next step will be to validate our method on the sequential PET/MRI system and compare transmission-based attenuation correction with different MR-based techniques. However, the detector ring of the Gemini TF PET scanner is larger than what we would expect from a simultaneous PET/MRI system. A reduced diameter would affect the PET count rate performance of the simultaneous emission/transmission scan, increase the emission/transmission cross-talk during extraction and increase errors in the reconstructed attenuation/emission. Although this method is compatible with MR, its potential in fully integrated PET/MRI systems also forms a part of future research.

3.6 Conclusion

Attenuation correction remains a major issue when combining PET systems with MRI systems. Most of the current research focuses on segmentation, template and atlas registration techniques using the MRI side of the hybrid imaging technique. These methods have some drawbacks related to bone/lung imaging, inter and intra-patient variability of attenuation coefficients, imaging of flexible MRI coils and truncation of the arms. In this chapter we presented a transmission based technique which could be used to solve most of these issues. An annulus shaped positron emitting source is placed inside the FOV of the PET scanner and transmission data is acquired in coincidence mode. Simultaneous acquisition of transmission and emission data is possible by using the TOF capabilities of current PET detectors. Simulation results show that with a typical commercially available system, accurate attenuation maps can be reconstructed and used in order to obtain quantitative PET images. In the next chapter we will investigate if this conclusion still holds for experimental data.

3.7 Original contributions

The method was first demonstrated with the NCAT simulations at the SNM conference in 2010 [153]. In 2011, more detail was added to the simulation study: PET system simulation, NEMA study and NCAT simulations. Results obtained were published in a A1 journal paper [154]. Later, dosimetry calculations were added as these were necessary to obtain approval for the patient studies presented in chapter 5.

Chapter 4

Phantom experiments

4.1 Introduction

In the previous chapter we proposed a new method for deriving the attenuation map in a TOF-PET system. An annulus shaped transmission source with a limited amount of activity was used. The major advantage of the method compared to standard transmission based techniques is the fact that simultaneous transmission and emission imaging is feasible through the use of TOF technology. In the previous chapter, we have shown how accurate attenuation maps can be derived using simulated data. The main goal of this PhD project is to investigate whether this method is applicable to whole-body patient studies in clinical practice. Therefore experiments with real data are required for further validation.

In this chapter we evaluate the proposed correction technique with phantoms on state-of-the-art TOF PET/CT and TOF PET/MRI systems. This is done before performing patient studies, as phantoms have some advantages over real patient acquisitions. First, phantoms are motionless, rigid structures. This allows easy co-registration and comparison between attenuation maps derived from a stand-alone TX scan with attenuation maps derived from a simultaneously acquired TEX scan of the same object. Second, phantom studies are far easier to organize than patient studies. Furthermore the radiation dose is of no concern. This means that phantoms studies can be repeated as much as needed. Finally, phantom studies can be reproduced which creates the opportunity of using comparable phantoms in different locations, allowing comparison of results obtained by different groups and using different systems.

Contrary to simulation studies, working with experimental data does not

allow any simplification of the PET acquisition process. All image degrading effects such as scatter and random coincidences will be present in the acquired data sets. Hence, in the first part of this chapter we will present the different approaches that were used to compensate for these effects.
In the second part we describe six phantom studies. In each phantom study we try to address specific problems related to attenuation correction such as bone imaging or scatter and emission contamination. At the end of the chapter the results of all phantom studies are discussed and a final conclusion is drawn.

4.2 Data corrections

Working with experimental data requires correction methods for random and scattered coincidences and count rate issues as well as regularization methods which reduce noise in the reconstructed attenuation map. In this section we will introduce different methods that were considered to compensate for these image degrading effects.

4.2.1 Random correction

Random coincidences contaminate the extracted transmission data. If we include random transmission data into eq. 3.13 from chapter 3 we get:

$$\mu_j^{k+1} = \mu_j^k + \alpha \left(1 - \frac{\sum_i c_{ij}(\hat{t}_{i,t} + \hat{t}_{i,r})}{\beta_{T_2} \sum_i c_{ij} a_i^k (\hat{b}_{i,t} + \hat{b}_{i,r})} \right), \tag{4.1}$$

with

$$\begin{aligned} \hat{t}_{i,t} &= \text{ extracted true transmission events on LOR } i \\ \hat{t}_{i,r} &= \text{ extracted random transmission events on LOR } i \\ \hat{b}_{i,t} &= \text{ extracted true blank events on LOR } i \\ \hat{b}_{i,r} &= \text{ extracted random blank events on LOR } i \\ c_{ij} &= \text{ sensitivity of detecting activity from voxel } j \text{ on LOR } i \\ a_i^k &= e^{(-\sum_m L_{im}\mu_m^k)}, \text{ the current estimate of the attenuation on LOR } i \\ L_{im} &= \text{ the intersection length of LOR } i \text{ with voxel } m \end{aligned} \tag{4.2}$$

Because the relation a_i between the true count rates $t_{i,t}$ and $b_{i,t}$ does not hold for the randoms ($t_{i,r}$ and $b_{i,r}$), a correction method is mandatory. In our work, randoms were corrected using the delayed window method described in chapter 2 . The delayed coincidences are subtracted from the prompt data during reconstruction :

$$\mu_j^{k+1} = \mu_j^k + \alpha \left(1 - \frac{\sum_i c_{ij}(\hat{t}_{i,t} + \hat{t}_{i,r}) - \sum_i c_{ij}\hat{t}_{i,d}}{\beta_{T2} \sum_i c_{ij} a_i^k (\hat{b}_{i,t} + \hat{b}_{i,r}) - \beta_{T2} \sum_i c_{ij} a_i^k \hat{b}_{i,d}} \right), \quad (4.3)$$

where $\hat{t}_{i,d}$ and $\hat{b}_{i,d}$ represent the delayed counts on LOR i after the TOF-based extraction of transmission data was applied. The method is easy to implement and allows accurate correction. The disadvantage of this method is that the noise increases due to the subtraction of the delayed coincidences.

4.2.2 Scatter correction

When a transmission scan is acquired, photons originating from the transmission source may scatter in the tissue of the patient. Scattered events contaminate the transmission data and cause an underestimation of the attenuation coefficients and a reduced contrast recovery. If we include scattered transmission data into eq. 4.3 we get:

$$\begin{aligned} \mu_j^{k+1} &= \mu_j^k + \alpha \left(1 - \frac{\sum_i c_{ij}(\hat{t}_{i,p} - \hat{t}_{i,d})}{\beta_{T2} \sum_i c_{ij} a_i^k (\hat{b}_{i,p} - \hat{b}_{i,d})} \right) \\ &= \mu_j^k + \alpha \left(1 - \frac{T_j + S_j}{\beta_{T2} B_j^k} \right) \end{aligned} \quad (4.4)$$

with $\hat{t}_{i,p} = \hat{t}_{i,t} + \hat{t}_{i,r} + \hat{t}_{i,s}$ the number of extracted prompt events (trues, randoms and scatter) on LOR i. The image S_j is produced by back projecting each scattered transmission event into image space. The increase of T_j by S_j will be lead to a lower estimate of the attenuation coefficients during reconstruction. In order to compensate for this error different methods can be used. Two approaches to reduce the influence of the scattered transmission data were implemented during this project: The first approach uses the knowledge that scattered photons have a lower photon energy than unscattered photons, and removes scatter from the data based on the detected photon energy. The second, more complicated, approach determines the scatter distribution using the Klein-Nishina equation and is similar to

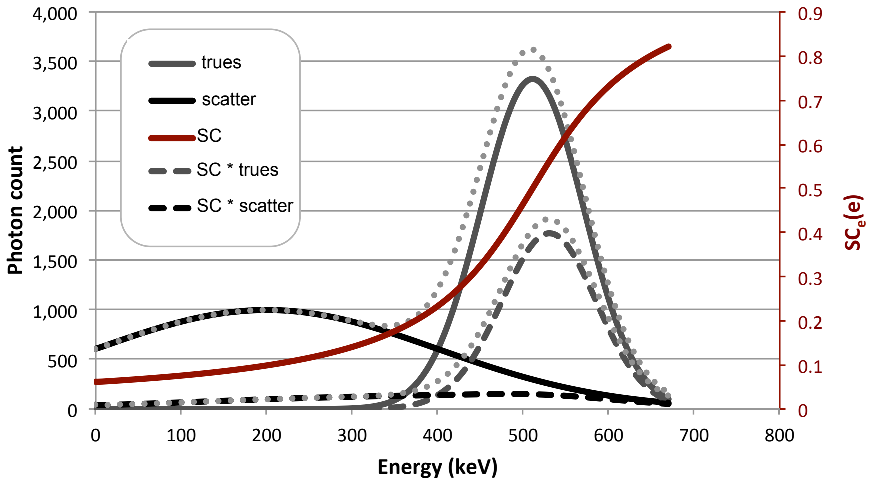

Figure 4.1: Suppression of scattered events using the $SC(\cdot)$ scaling function. Only one factor of the formula in eq. 4.5 is shown. The scaling is applied to both the blank and transmission scan. The method preserves the relation a_i between the true transmission counts $\bar{t}_i$ and true blank scouts $\bar{b}_i$.

Single Scatter Simulation, used in emission reconstruction. The latter was finalized in the last term of this work. Therefore, in some phantom studies, presented in the second part of this chapter, reconstructions were redone to include these modifications.

4.2.2.1 Energy-based methods

When photons interact with matter, they lose energy. Hence, scattered photons are found in the lower end of the energy spectrum. Although most scanners apply an energy window to reject a significant part of the scattered data, due to the finite energy resolution, some scattered coincidences still fall inside the energy window. In the context of our work we assume that the energy distribution of the true blank and true transmission events are identical. Because of the small thickness of the annulus source, the scatter of photons inside the transmission source is neglected. In order the reduce the influence of S_j in eq. 4.4, a scaling function is used to suppress coincidences in which the energies of the detected photons are low compared to a given energy threshold ϵ_t (see figure 4.1):

$$SC_e(\epsilon_1, \epsilon_2) = (0.5 + \frac{\arctan(\gamma \cdot (\epsilon_1 - \epsilon_t))}{\pi}) \cdot (0.5 + \frac{\arctan(\gamma \cdot (\epsilon_2 - \epsilon_t))}{\pi} \tag{4.5}$$

where ϵ_1, ϵ_2 represent the energies of the detected photons of event e. The parameters ϵ_t and γ allow to adapt the scaling function. For high values of γ the arctangent function approximates a step function, where only energies equal or above ϵ_t are accepted. In figure 4.1, γ was set to 0.01 and ϵ_t to 511 keV. It is easily shown that the relation a_i between the true coincidence counts t_i and b_i still holds, when each event is weighted with the factor $SC_e(\epsilon_1, \epsilon_2)$. Suppose $t_i\{\epsilon_1, \epsilon_2\}$ and $b_i\{\epsilon_1, \epsilon_2\}$ represent the number of events with energy pair ϵ_1, ϵ_2 detected on LOR i in the transmission scan and blank scan respectively. The weighted counts $\bar{t_i}$ and $\bar{b_i}$ can be expressed as follows:

$$\begin{aligned} \bar{t_i} &= \sum_{e \in t_i} SC_e\{\epsilon_1, \epsilon_2\} t_i\{\epsilon_1, \epsilon_2\} \\ \bar{b_i} &= \sum_{e \in b_i} SC_e\{\epsilon_1, \epsilon_2\} b_i\{\epsilon_1, \epsilon_2\} \end{aligned}$$

Because t_i and b_i only contain true coincidences and the energy distribution of their photon-pairs are identical, the relation a_i between the true blank and true transmission events still hold when the events are weighted with factor $SC_e(\epsilon_1, \epsilon_2)$:

$$\sum_i \bar{t_i} = \sum_i a_i \bar{b_i} \tag{4.6}$$

4.2.2.2 TX-based Single Scatter Simulation

The results presented in section 4.5 will show that the energy-based method does not allow accurate correction for scattered transmission events contaminating the extracted transmission data. Here we present another approach. In chapter 2 we briefly introduced a simulation method to estimate the single scatter fraction on each LOR of a PET emission scan. For this purpose an estimate of the tracer distribution as well as the attenuation map is required. In this section we describe how this technique can be applied to estimate the amount of transmission events scattered inside the patient during a PET transmission scan. Contrary to conventional SSS, the TX-based SSS uses a model of the transmission source distribution instead of

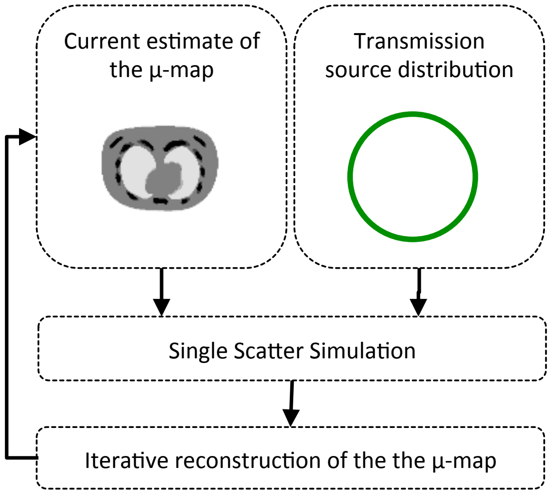
Current estimate of the μ-map
Transmission source distribution
Single Scatter Simulation
Iterative reconstruction of the the μ-map

Figure 4.2: Single Scatter Simulation for transmission scanning in coincidence mode.

the distribution of the tracer administered to the patient. The attenuation map is obtained from the iterative gradient ascent algorithm. Because only an estimate of the attenuation map is available, the SSS method needs to be repeated several times. The process is illustrated in figure 4.2.

The TX-based SSS method involves the following steps:

- Scatter points are defined by random sampling of the current estimate of the attenuation map.
- For each scatter point we calculate the line integrals through the transmission source and the attenuation map, connecting the scattered point which each PET detector.
- On each LOR the fraction of scattered transmission events is estimated using the Klein-Nishina formula.
- The scatter sinogram is scaled and back projected into image S_j which is then included in the iterative reconstruction.

Two major drawbacks limit the accuracy of the TX-based SSS method. First, differences in detector efficiencies and dead-time effects are not accommodated for during the fast simulation. For these reasons, the SSS

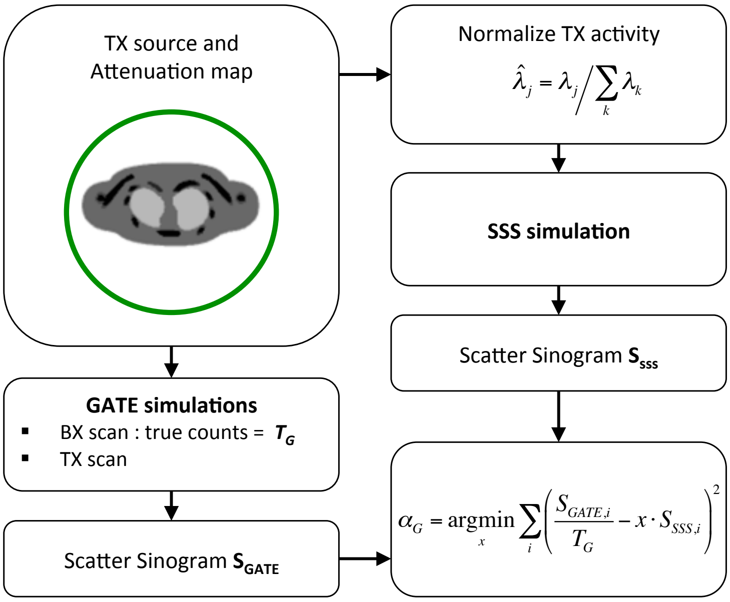
TX source and Attenuation map
Normalize TX activity
$\hat{\lambda}_j = \lambda_j / \sum_k \lambda_k$
SSS simulation
Scatter Sinogram S_{SSS}
GATE simulations
BX scan : true counts = T_G
TX scan
Scatter Sinogram S_{GATE}
$\alpha_G = \underset{x}{\operatorname{argmin}} \sum_i \left(\frac{S_{GATE,i}}{T_G} - x \cdot S_{SSS,i} \right)^2$

Figure 4.3: Calibration of the TX-based SSS algorithm with GATE.

method will only provide a rough estimate of the scatter distribution. Second, photons that scatter multiple times are not simulated. Although multiple scatter may account for 20% of the total scatter, neglecting them is justified by the fact that multiple scatter has little effect on the shape of the spatial distribution of the scatter inside the patient. To achieve a quantitative estimate of the scatter distribution, the SSS scatter sinogram needs to be scaled to fit the measured data. In an emission scan, scaling can be done by fitting the tails of the SSS sinogram which fall outside the contour of the patient with the same tails of the emission sinogram. Tail-fitting assumes that the tails of the emission sinogram only contain scatter. In a transmission scan, this technique can not be used because the tails are contaminated with transmission data. However, because in each transmission study, the same model for the transmission source is used, the TX-based SSS algorithm can be calibrated with GATE (see figure 4.3). For this purpose, an NCAT simulation was used. The scatter derived from the GATE simulation was normalized to the number of true counts collected during the blank scan. A scaling factor α_s was derived by fitting the scatter derived from the SSS simulation with the normalized sinogram from GATE. Hence for each TX study, the SSS sinogram is first scaled with α_s followed by a

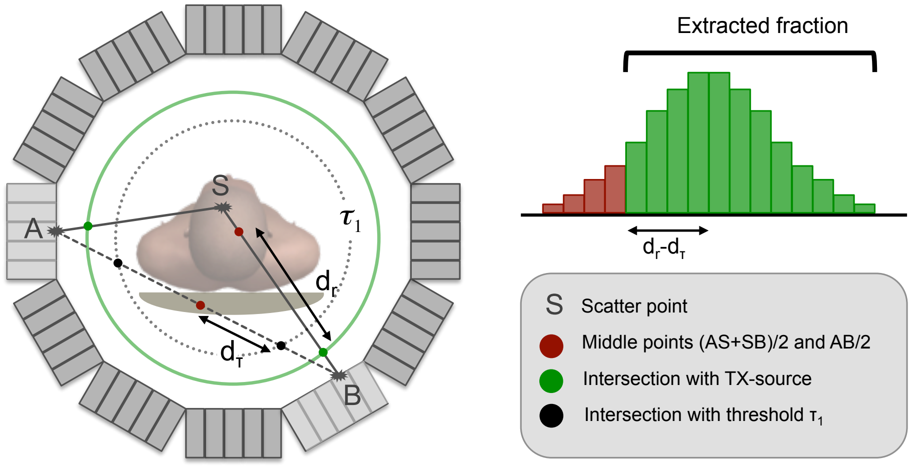
Extracted fraction
S
A
B
τ_1
d_r
d_T
d_r-d_T
S Scatter point
● Middle points (AS+SB)/2 and AB/2
● Intersection with TX-source
● Intersection with threshold τ_1

Figure 4.4: Single Scatter Simulation adapted for the estimation of the TOF-based extracted scattered transmission data.

scaling with the number of prompt counts minus delayed counts collected during the blank scan.

When the transmission and emission data are acquired simultaneously, TOF information will be used to extract the transmission events. As a consequence, some of the scattered transmission events will be rejected. Although this is desired, the Single Scatter Simulation should be adapted to include the TOF-based extraction in order to avoid an overestimation of the scatter fraction. Figure 4.4 illustrates how this works: suppose an annihilation occurred in the transmission source close to detector B and a scattered coincidence is registered on the LOR connecting detector A and B. One of the two photons in coincidence scattered in point S and a time difference of Δt was registered. Given Δt, the estimated annihilation point on LOR AB is located at a distance $\Delta x = \Delta t \cdot c/2$ from the center of line segment $|AB|$. If the TOF-information was exact, Δx would equal the distance d_r from the center of line segment $|AS| + |SB|$ (red dot) to the intersection point of line SB with the transmission source (green dot). However, the TOF-based extraction process will only accept those events for which the distance Δx is greater than the distance d_τ from the center of line segment $|AB|$ (red dot) to the intersection point of line AB with threshold radius τ_1 (black dot). Hence, the fraction of scattered events classified as transmission can be derived from the difference $d_r - d_\tau$.

The method was validated with a simulation study in GATE. A region of

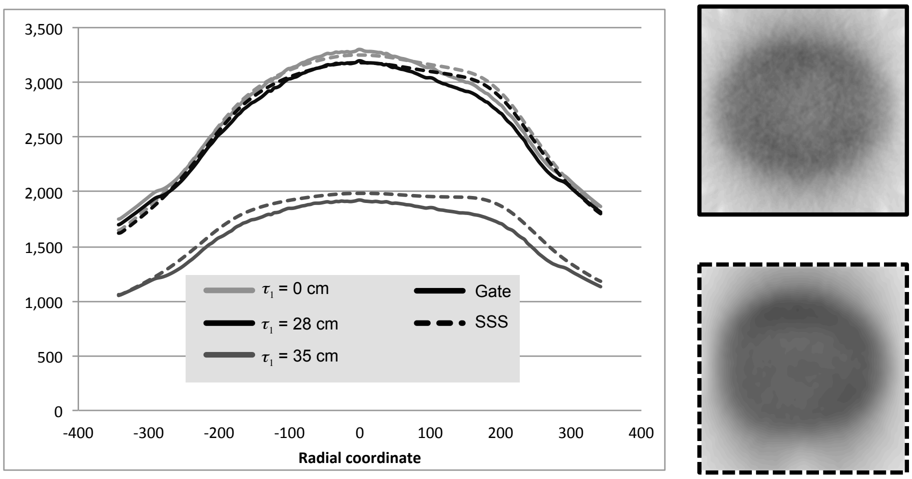

Figure 4.5: Summation over coronal and sagittal direction and central transverse slice of the back projected estimated scatter data into image space. Both GATE and SSS estimated scatter are shown. The profiles were calculated for three different threshold values for τ_1.

the human torso containing soft tissue, bone and lungs was generated using the NCAT software. A 3 minute blank and transmission scan were simulated. The scatter contributions were derived from GATE and estimated using the SSS method for different values of τ_1. The images S_j derived from both simulations were summed in the coronal and sagittal direction into a one-dimensional profile. The profile is shown in Figure 4.5. Visual inspection shows good agreement between the profiles derived from the GATE simulation and the Single Scatter simulation. Subsequently, three attenuation maps were reconstructed. In the first reconstruction no scatter correction was applied. In the second and the third reconstruction, the S_j image was derived from the SSS and the GATE scatter sinogram respectively. Figure 4.6 show the relative difference of the reconstructed attenuation coefficients of the first and the second attenuation map compared to the third attenuation map.

4.2.3 Count rate correction

As discussed in the previous chapter, random cross-talk and dead-time cause a mismatch between the count-rate performance during the blank and transmission scans. This is taken into account by scaling the blank image B_j^k

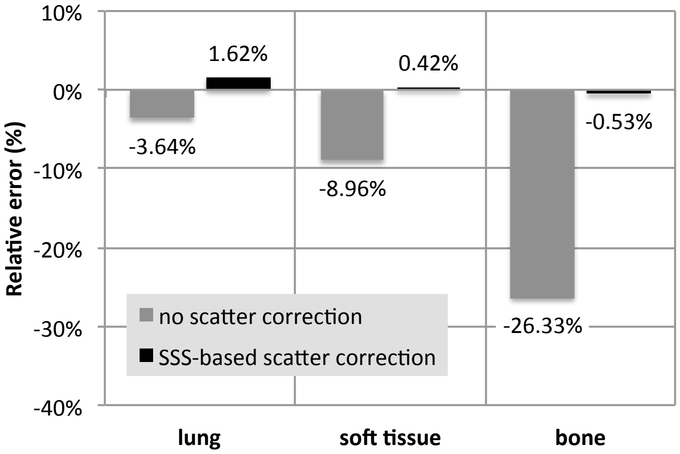

Figure 4.6: Relative error of the reconstructed attenuation coefficients in soft tissue, lungs and bone. The attenuation map without scatter correction and with SSS-based scatter correction were compared with the attenuation map derived from a transmission scan were the scatter was rejected.

with a correction factor β_{τ_2} derived from the ratio of the extracted counts outside a FOV of radius τ_2. Because scattered transmission events may contaminate these tails, β_{τ_2} is recalculated by first subtracting the scatter sinogram from the transmission sinogram when the SSS method is used.

4.2.4 Noise regularization

In the previous chapter we presented a post-processing segmentation algorithm to handle the issue of noise in the reconstructed attenuation maps. Although good results were obtained, the accuracy of the segmentation technique highly depends on the subject studied. For example, the segmentation might fail to classify bone if only a limited amount of bone tissue is present. Additionally, when the attenuation maps are segmented after reconstruction, the acquired transmission data is not used to guide the classification of the voxels. As described in the introduction, Bayesian methods provide a framework to include additional knowledge in the iterative algorithm to restrict the solution space to solutions yielding particular properties. In our situation, edge-preserving smoothing priors can be used to regularize noise during attenuation reconstruction while preserving the sharp edges between different tissue types. The advantage of using this approach has been reported intensively in literature [155–157]. However, the major difficulty lies in modeling the prior knowledge. Prior information is commonly modeled through Gibbs distribution functions using a potential function to penalized unwanted features :

$$P_G(\boldsymbol{\mu}) = \frac{1}{Z}\exp(-\beta U(\boldsymbol{\mu})), \tag{4.7}$$

with

$$U(\boldsymbol{\mu}) = \sum w_{jk} V(\mu_j, \mu_k). \tag{4.8}$$

$V(\mu_j, \mu_k)$ represents the potential function. w_{jk} are weights depending on the distance between two voxels in the image. Mostly w_{jk} is zero for voxels which are not within the same neighborhood. For neighboring voxels the inverse euclidian distance can be chosen. Several prior distributions have been proposed [158–160]. A possible and easy candidate to suppress noise is the quadratic function :

$$V(\mu_j, \mu_k) = (\mu_j - \mu_k)^2 \tag{4.9}$$

In order to preserve the sharp edges between different tissue, the quadratic function can be modified as proposed by Geman and McClure [158]:

$$V_\sigma(\mu_j, \mu_k) = \frac{(\mu_j - \mu_k)^2}{\sigma^2 + (\mu_j - \mu_k)^2} \tag{4.10}$$

Another approach is to use a total variation model as defined in [161]:

$$U(\boldsymbol{\mu}) = \sum \Phi(|\nabla\boldsymbol{\mu}|), \tag{4.11}$$

with $\Phi(\mathbf{s}) = \sqrt{1+\mathbf{s}^2}$.

To include the noise regularization in eq. 4.4 we defined two update steps:

$$\begin{aligned}
\mu_j^{k+\frac{1}{2}} &= \mu_j^k + \alpha\left(1 - \frac{\sum_i c_{ij}(\hat{t}_{i,p} - \hat{t}_{i,d} + \hat{t}_{i,s})}{\sum_i c_{ij} a_i^k (\hat{b}_{i,p} - \hat{b}_{i,d})}\right) \\
\mu_j^{k+1} &= \mu_j^{k+\frac{1}{2}} - \beta\left(\frac{\partial U(\boldsymbol{\mu})/\partial\mu_j}{\partial^2 U(\boldsymbol{\mu})/\partial\mu_j^2}\right)
\end{aligned} \tag{4.12}$$

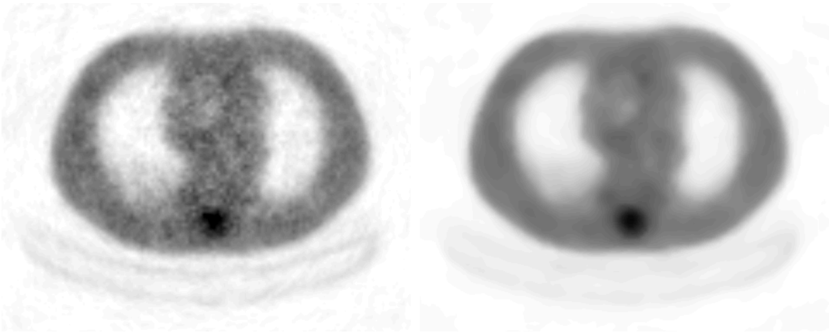

(a) (b)

Figure 4.7: Reconstructed attenuation map of an anthropomorphic torso phantom without (a) and with noise regularization (b).

In the first step the μ-values are updated according to the comparison between the images B_j and T_j. The second step minimizes the potential function after each iteration. In the experimental studies the total variation was used. Figure 4.7 shows a comparison between an attenuation map reconstructed without noise regularization and the same attenuation map, reconstructed with regularization.

4.2.5 μ-value scaling

The correction methods described above only correct the data for randoms, count rate related issues, noise and scattered transmission events. When transmission and emission data are acquired simultaneously, some true and scattered emission events will contaminate the transmission data. So far, no method was presented to compensate for these effects. If inaccurate attenuation coefficients are obtained and predefined information about their value is available, a histogram matching method can be used to scale the μ-values. The method starts with building a training set containing attenuation maps of subjects similar to the subject being studied. For each subject two attenuation maps are determined: an uncorrected TX-based attenuation map and an accurate attenuation map (μ-map) derived from CT-data or other transmission-based methods. Subsequently, a histogram of the attenuation coefficients in both TX-maps and μ-maps is determined. The relevant tissue types appear as peaks in the histograms. Hence, a peak detection algorithm can be used to determine the attenuation coefficients of all relative tissues in each attenuation map. Additionally, the standard

Phantom	Tissues	Scanner	PET	CT/MRI
Water cylinder	Water	Gemini,	TX	CT
Anisotropic torso*	Spine, lung soft tissue	Gemini,	TX, TEX	CT
The Alderson phantom*	Ribs, spine, lungs, soft tissue	Gemini	TX	CT
Pig head	Bone, air, soft tissue	Gemini	TX	CT
Human thorax I	Femur bone, lung, soft tissue	Gemini	TEX, EX	CT
Human thorax II	Spine, lung, soft tissue	Ingenuity Discovery	TEX, EX	CT, MRI

Table 4.1: Overview of phantom studies acquired on the Gemini TF PET/CT scanner and the Ingenuity TF PET/MRI scanner. The type of PET scanning (transmission only TX, simultaneous transmission/emission TEX or emission only EX) is also shown. Additionally, we indicate whether CT or MRI data of the phantom was available.

---

*tissues are simulated using synthetic materials with similar density properties as the human equivalent.

deviation of each tissue is also derived. For this purpose a Gaussian fitting method can be used. Next, the peak values and standard deviations are averaged over all patients for both TX-maps and μ-maps. Given the mean attenuation coefficients and their standard deviation, Gaussian mixture models define the distribution of the attenuation coefficients. Finally, the cumulative distribution functions CDF_{TX} and CDF_{μ} of these models are calculated. The non-linear rescaling function is then defined by

$$\mu'_{\mathrm{TX}} = f(\mu_{\mathrm{TX}}) = \mathrm{CDF}^{-1}_{\mathrm{CT}}(\mathrm{CDF}_{\mathrm{TX}}(\mu_{\mathrm{TX}})) \tag{4.13}$$

4.3 Data acquisition

4.3.1 Phantom studies

Because the proposed method will eventually be used in a clinical setting, the phantoms we have chosen represent different parts of the human body. Consequently, the results obtained will give an indication on how the transmission-based method will perform on patient data. An overview of the experiments is shown in table 4.1. In total 6 phantom studies were done. In the first three studies, phantoms made from synthetic materials were used. Water and plastics are typically used to mimic soft tissue such as skin or muscle while a mixture of water with styrofoam beads can be used to mimic lung tissue. Mostly, these materials have realistic properties comparable to human tissue for transmission imaging. If realistic values are required on MR images as well, this is far more difficult. For such applications, using biological tissue is an option. In the last three experiments listed in table 4.1 tissues recovered from a pig and cow were used. Because biological tissues exhibit realistic values on PET,CT and MRI, the performance of MR and TX-based AC methods can then be compared with a standard CT-based AC method. A major drawback of these phantoms is that they are more difficult to reproduce than synthetic phantoms.

The first 5 datasets were acquired on the sequential Gemini TF PET/CT system (Philips Healthcare, Cleveland, OH, USA) available at UCL (Université Catholique de Louvain), in Brussels. A detailed description of the PET scanner can be found in the previous chapter. The CT system is a Brilliance CT 16-slice scanner (Philips Healthcare). The last dataset was acquired on the Ingenuity TF PET/MRI system (Philips Healthcare) installed at Mount Sinai Hospital, New York, USA. The system combines the Gemini TF PET scanner with the imaging capabilities of a 3.0 T Achieva MRI scanner in a sequential setup. To avoid MRI interference with the PET system and vice versa, the PET and MRI scanners are located at opposite ends of the table, rotating the patient between the two scanners. The experiments on the PET/CT system allows comparison between the transmission based method and CT-based attenuation correction, while a comparison with MR-based techniques can be evaluated on the the PET/MR system. Additionally, a PET/CT scan of the last phantom was acquired on the Discovery PET/CT (GE Medical Systems, Little Chalfont, Buckinghamshire, UK), also available at Mount Sinai Hospital.

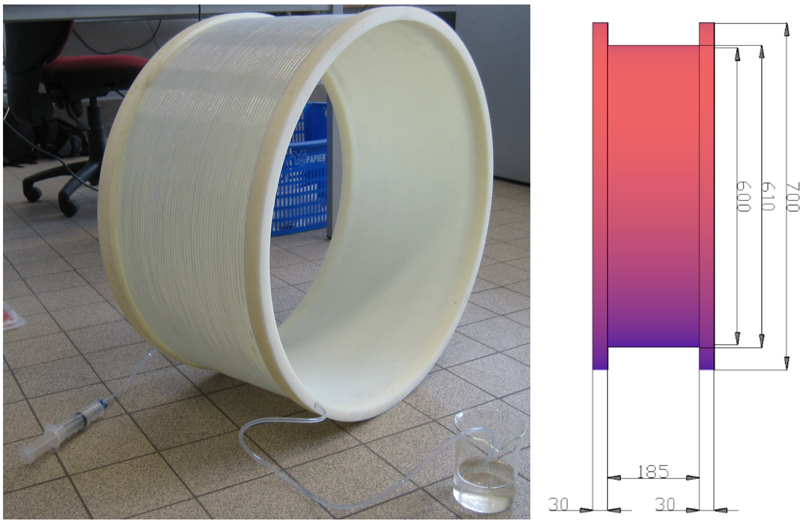

Figure 4.8: Annulus-shaped transmission source

4.3.2 Annulus-shaped transmission source.

The annulus-shaped transmission source, used to acquire the transmission data, was constructed using a polymethyl methacrylate (PMMA) hollow cylinder and an air-tube. The cylinder was fabricated by Vaskon (Oudenaarde, Belgium), acts as a support and has an inner diameter of 60 cm and thickness of 0.5 cm. The tube is 103.7 m long and is wrapped around the surface of the cylinder (figure 4.8). The tube has an inner diameter of 4 mm and an outer diameter of 6 mm. The total volume of the source is 1.3L. In order to fill the tube, one end is put in a beaker of ^{18}F-FDG solution while creating negative pressure at the other side using a syringe. This filling process takes 5 minutes. In our experiments, the transmission source activity ranges from 18 to 74 MBq at the time of acquisition.

4.4 Stand-alone transmission scanning

4.4.1 Cylindrical water phantom and MRI coil imaging

The transmission-based technique was first validated with stand-alone transmission experiments on the Gemini TF PET/CT scanner. Two experiments

Scan type	Phantom	Annulus source	Activity in phantom
BX	-	Yes	-
TX	20-cm cylinder	Yes	No
TX	MR head coil	Yes	No

Table 4.2: Overview of the PET acquisition of the initial experiments on the Gemini TF PET/CT system.

were performed. In the first study a cylindrical phantom was used. The cylinder has a diameter of 20 cm and was filled with water which has an attenuation coefficient of 0.097 cm^{-1} at 511 keV. No activity was injected in the phantom, hence, cross-contamination of transmission and emission data is not present. Because the transmission-based technique is intended to be used for TOF PET/MRI systems we also illustrate the feasibility of imaging MR-coils in a second study.

4.4.2 Data acquisition

An overview of the acquired PET data is shown in table 4.2. The PET protocol included a 5 minutes blank scan followed by a 5 minute TX scan of the 20-cm cylinder. The annulus-shaped source was injected with 110 MBq of ^{18}F-FDG 80 minutes prior to the start of the PET acquisition. No activity was injected in the cylinder. Finally, a 5 minutes TX-scan of an MR-head coil was acquired.

Scan type	Scatter correction	μ-value
TX	-	0.00855
TX	Energy-based	0.00936
TX	SSS	0.00964

Table 4.3: Reconstructed attenuation coefficients (mm^{-1}) of water for cylindrical water phantom.

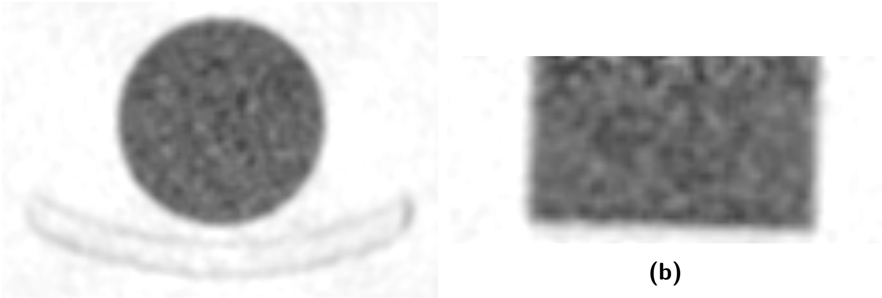

(b)

(a)

Figure 4.9: Central transverse (a) and coronal slice (b) of the reconstructed attenuation map of the cylindrical phantom acquired with a TX-scan on the Gemini TF PET/CT system.

4.4.3 Results

4.4.3.1 Cylindrical water phantom

For the first study, 3 attenuation maps were reconstructed. During the first reconstruction no scatter correction was applied. In the second reconstruction, scattered events were suppressed using the energy-based method while in the third reconstruction the TX-based SSS method was used. All attenuation maps were reconstructed on a 176 x 176 x 40 matrix with a 4-mm isotropic voxel dimension and randoms were compensated using the delayed window method. To ensure consistency between the BX and TX scan, a count rate correction value of 0.95 was derived for $\tau_2 = 28.5$ cm. No iterative noise regularization was applied, but the images were smoothed with a Gaussian filter after reconstruction. A central transverse and coronal slice of the reconstructed attenuation map with SSS-based scatter correction is shown in figure 4.9. Table 4.3 summarizes the reconstructed attenuation coefficients for water. Results show how accurate attenuation coefficients are obtained for both scatter compensation methods. A relative error of 11.8% was obtained when no scatter correction was applied. By using the energy-based method, the relative error decreased to 3.5%. More accurate results are obtained when scatter is estimated using the SSS method (0.6% error).

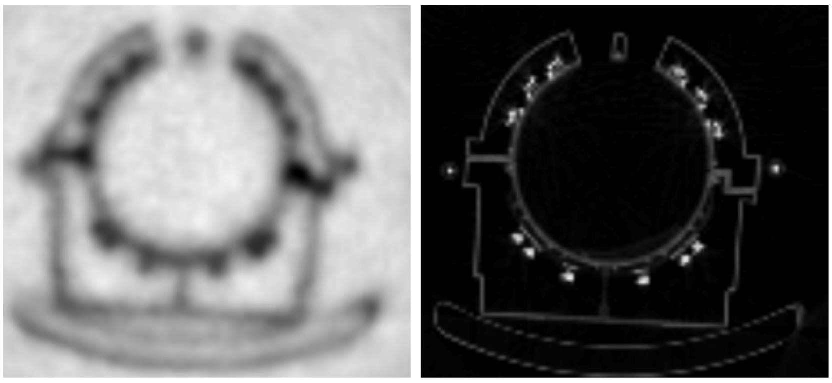

(a) (b)

Figure 4.10: Transverse slice of the TX-based attenuation map (a) and CT image (b) of an MR head coil.

4.4.3.2 MR coil imaging

One of the difficulties in attenuation correction for PET-MR is that the MR coils should also be included in the attenuation map. In MR-based attenuation correction this is difficult, as MR coils are usually designed to be invisible on MRI. Although templates can be used to solve this issue, this is complicated when working with flexible coils. TX-based methods are able to visualize any object inside the FOV. Figure 4.10 shows an attenuation map of an MR coil used for brain imaging. The map was reconstructed on a 176 x 176 x 44 reconstruction matrix. An isotropic voxel size of 4 mm was used. All parts of the MR coil are visible. However, small structures are blurred because of the limited spatial resolution.

4.5 Simultaneous transmission/emission imaging

Because positron emitters are used as a transmission source, and the data are acquired in coincidence mode, the transmission and emission data can be acquired at the same time. In the previous chapter we discussed how the transmission data can be extracted by using the TOF information available for each event. In this section we present a simultaneous transmission/emission study with an anthropomorphic torso phantom.

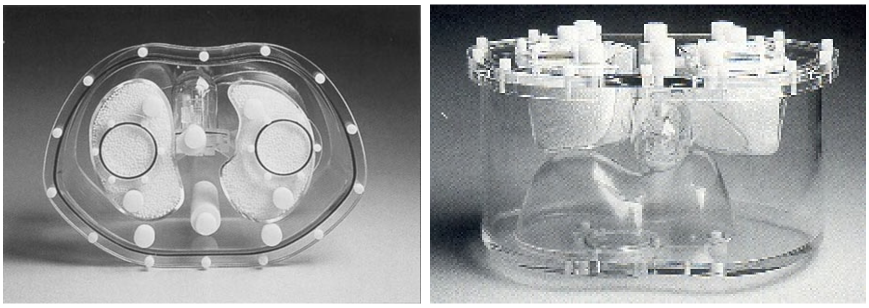

(a) (b)

Figure 4.11: An anthropomorphic torso phantom containing lung and liver compartments and a cardiac and spine insert.

4.5.1 Anthropomorphic torso phantom

The anthropomorphic torso phantom consists of two chambers that are shaped to mimic the lungs, a liver compartment which can be filled separately and a spine insert (see figure 4.11). Optionally, a cardiac insert can be included. The lung-chambers are filled with a mixture of styrofoam beads and water to emulate lung tissue. The container itself has a shape similar to a human torso and can easily be filled with water. In our experiments, water containing 18F-FDG was only added to the container and the cardiac insert. We evaluated the TX-based method with a stand-alone transmission scan as well as a simultaneous transmission/emission scan. For the TEX-scan, the container was filled with approximately 74 MBq of ^{18}F-FDG prior to scanning. The TX-based method was compared to a conventional CT-based attenuation correction method.

Scan type	Annulus	Phantom	Activity in phantom
BX	Yes	-	-
TX	Yes	Torso	No
TEX	Yes	Torso	Yes

Table 4.4: Overview of PET acquisition on the Gemini TF PET/CT system using the anthropomorphic torso phantom.

4.5.1.1 Data acquisition and image reconstruction

An overview of the PET acquisitions is shown in table 4.4. The annulus source was placed inside the FOV and a blank reference scan of 5 minutes was acquired. Subsequently the torso phantom was placed on the table and a PET/CT scan was acquired. The transmission scan had a duration of 5 minutes. Finally, we inserted approximately 74 MBq of ^{18}F-FDG in the phantom and the PET/CT scan was repeated. The annulus shaped transmission source remained in the FOV during both PET/CT acquisitions. The CT data was acquired with following parameters: 120 kVp, 81 mAs, 5 mm slice thickness, 0.853 pixels per mm transverse resolution, and a 512 x 512 x 36 reconstruction matrix.

4.5.1.2 Results

Reconstructed attenuation maps

From both the TX and TEX-scan three attenuation maps were reconstructed. During the first reconstruction no scatter correction was applied. In the second reconstruction the influence of the scattered transmission events was reduced with the energy-based method. Finally, in the third reconstruction, the fraction of scattered transmission events was estimated with the SSS method. τ_1 was set to 28.5 cm in the reconstruction derived from the TEX-scan. The count rate correction factors were 0.94 and 0.83 for the TX and TEX-based reconstructions respectively. Subsequently, CT-based attenuation maps were derived from the two CT data sets. For this purpose bilinear scaling was used (see next chapter). All attenuation maps were reconstructed on a 176 x 176 x 40 matrix with a 4-mm isotropic voxel dimension.

Figure 4.12 shows a central transverse slice of the reconstructed attenuation maps of the anthropomorphic torso phantom. The reconstructed attenuation coefficients for VOIs defined in the lungs, soft tissue and bone are shown in table 4.5. Figure 4.13 and 4.14 show the percentage difference of the reconstructed attenuation coefficients compared to the values obtained from the CT-based attenuation map.

Reconstructed PET images

The TEX data was reconstructed on a 144 x 144 x 40 matrix with 4 mm isotropic voxel size. Three PET images were derived. In the first reconstruction no attenuation correction was implemented. In the second and

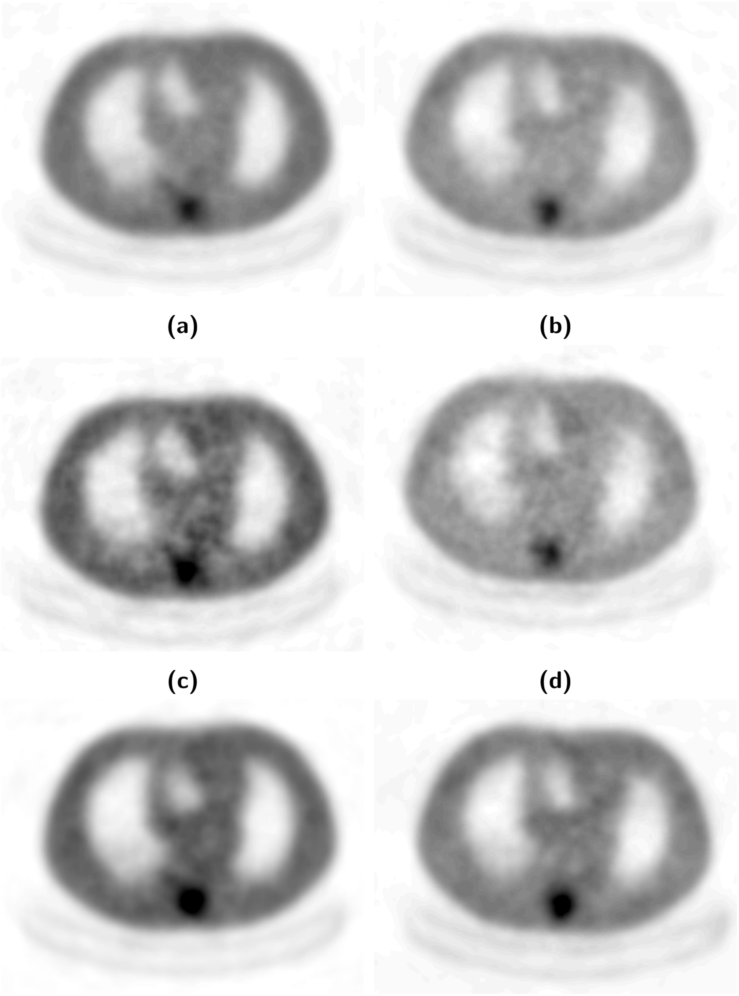

(a) (b)

(c) (d)

(e) (f)

Figure 4.12: Left to right: central transverse slice of the TX-based (a,c,e) and TEX-based (b,d,f) attenuation maps. Top to bottom: reconstructed attenuation maps without scatter correction (a,b), energy-based scatter compensation (c,d) and SSS-based scatter correction (e,f).

Scan type	Scatter correction	Lung	Soft tissue	Bone
CT	-	0.00343	0.00963	0.0147
TX	-	0.00308	0.00833	0.0124
TX	Energy-based	0.00284	0.00890	0.0148
TX	SSS	0.00334	0.00944	0.0146
TEX	-	0.00287	0.00715	0.0120
TEX	Energy-based	0.00286	0.00727	0.0121
TEX	SSS	0.00356	0.00900	0.0146

Table 4.5: Reconstructed attenuation coefficients (mm^{-1}) of lung, soft-tissue and bone in the anthropomorphic torso phantom. The scatter correction method applied is also shown.

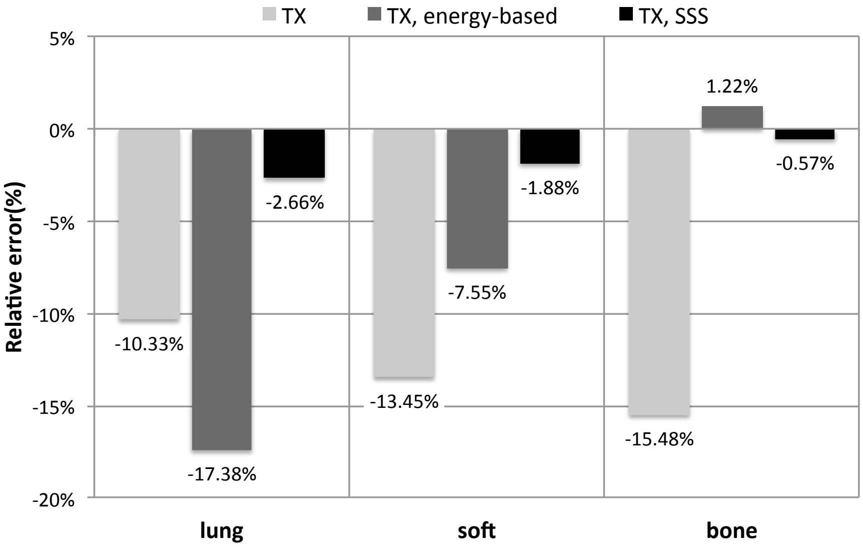

Figure 4.13: Relative percent difference of reconstructed TX-based attenuation maps (see table 4.5) compared to the CT-based attenuation map.

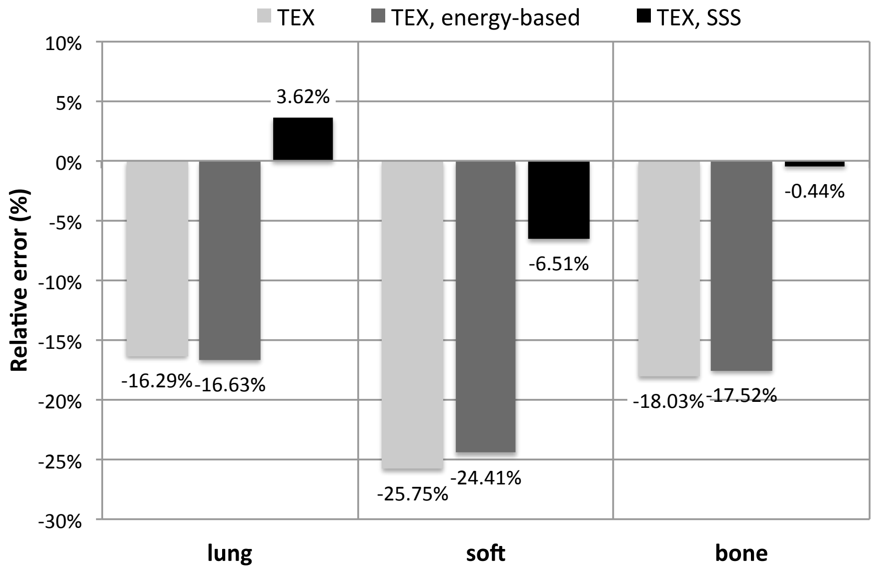

Figure 4.14: Relative percent difference of reconstructed TEX-based attenuation maps (see table 4.5) compared to the CT-based attenuation map.

third reconstruction, attenuation corrections were done using the CT-based and the scatter corrected (using SSS) TEX-based attenuation map respectively. Figure 4.15 shows transverse central slices of the reconstructed PET images as well as the error image illustrating the relative difference between the CT-AC and TEX-AC PET images.

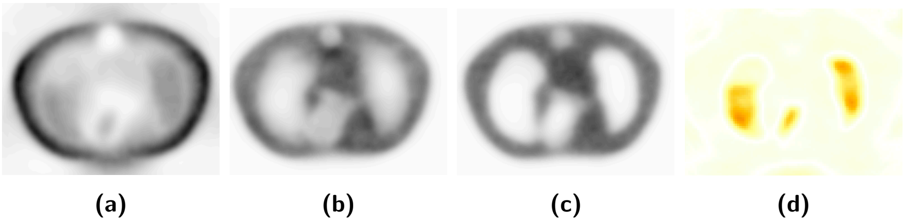
(a) (b) (c) (d)

Figure 4.15: Left to right: central transverse slice of the non attenuation corrected PET image (a), the TEX-based AC PET image (b), the CT-based AC PET image (c) and the difference image between the CT-AC and the TEX-ac PET images (d).

4.6 Bone imaging

In order the derive accurate attenuation correction, imaging of bone structures is mandatory. In this section we will investigate how well the transmission-based technique is able to distinguish bone structures from surrounding tissue in the head and upper torso region. For this purpose two phantom studies were done.

4.6.1 Pig head phantom

In this study we investigated the feasibility to image the head of a pig with short transmission scans in coincidence mode. The head is a rigid structure containing soft-tissue, bone structures (skull, facial bone) and air (nasal cavity, sinuses). The pig head was obtained from a local slaughterhouse and stored in a freezer in between experiments to prevent decomposition.

4.6.1.1 Data acquisition

The annulus-shaped transmission source was positioned in the center of the FOV of the PET scanner and a 15 min blank reference scan was acquired. Subsequently the pig head was placed on the patient table and a CT-scan was acquired followed by a TX scan. There was no activity in the pig head. The acquisition time of the transmission scan was 5 minutes, in the same range as the acquisition time of one bed position in a clinical PET brain protocol.

4.6.1.2 Results

Two TX-based attenuation maps were derived, one without scatter correction and one where scattered events were estimated using the Single Scatter Simulation method. The attenuation maps were reconstructed using the iterative gradient ascent algorithm described in the previous chapter. Random coincidences were corrected using the delayed window method and a count rate correction value β_{T_2} of 0.78 was derived. All attenuation maps were reconstructed on a 176 x 176 x 40 reconstruction matrix with a 4-mm isotropic voxel dimension and noise was regulated with total variation minimization. Figure 4.16 shows central transverse and sagittal slices of the reconstruction transmission-based attenuation map as well as the attenuation map obtained from the CT data. Air cavities and bone structure are clearly visible. For each relevant tissue VOIs of 4 cm^3 were defined: 5 in

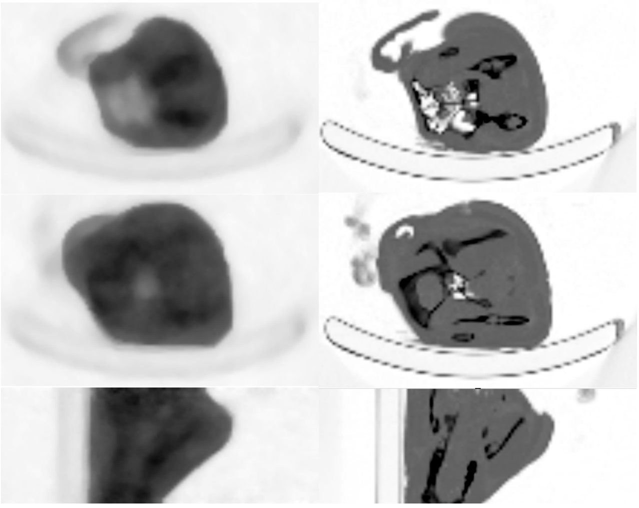

Figure 4.16: Central transverse and sagittal slices of the TX-based (left) and CT-based (right) attenuation map of the pig phantom.

soft tissue, 5 in bone and 2 in the air cavities (see figure 4.17). The mean reconstructed attenuation coefficient for the CT-based, TX-based and scatter corrected TX-based attenuation maps are depicted in table 4.6. A large overestimation in the air cavities was obtained in both TX-based attenuation maps. A significant improvement was observed in bone and soft tissue when scattered transmission events were compensated.

4.6.2 Alderson torso phantom

The previous torso phantom showed how lung, soft-tissue and bone can be distinguished on a TX-based attenuation map. By compensating for scatter, accurate attenuation coefficients comparable to CT-based values

Method	Scatter correction	Air	Soft tissue	Bone
CT-based	-	0.0025	0.0095	0.0126
TX-based	No	0.0066	0.0089	0.0104
TX-based	SSS	0.0066	0.0105	0.0123

Table 4.6: Mean reconstructed attenuation coefficients (mm^{-1}) in VOIs defined in the air cavities, soft tissue and bone of the pig phantom.

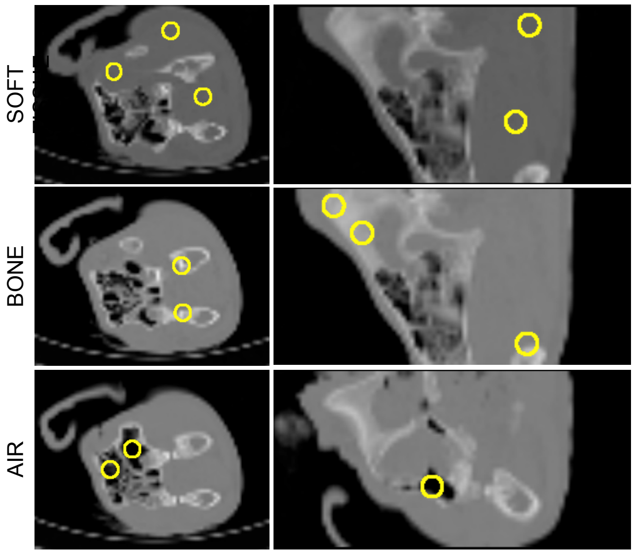

Figure 4.17: VOIs of 4 cm^3 were defined for each tissue: 5 in soft tissue, 5 in the bone structures and 2 in the air cavities.

are obtained. However, the phantom does not contain great detail and the spine insert is relatively large compared to the human spine. Therefore, in this section a more complex phantom is used, the Alderson torso phantom (see figure 4.18). This allows us to evaluate to what extent small bone structures such as the ribs are detectable on the reconstructed attenuation maps using a transmission-based technique.

4.6.2.1 Data acquisition

The Alderson torso experiment was conducted at the same time of the pig head acquisitions. The same 15 minute blank scan was used for the reconstruction of the attenuation map. The transmission data was acquired with a 5 minute TX-scan. No activity was injected in the phantom. Hence all acquired data was used to reconstruct the attenuation map. Additionally, a CT image of the torso was acquired with the following parameters: 120 kVp, 81 mAs, 5 mm slice thickness, 0.853 pixels per mm transverse resolution, and a 512 x 512 x 36 reconstruction matrix.

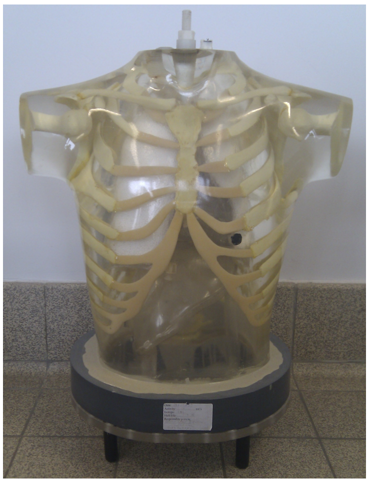

Figure 4.18: the Alderson torso phantom.

4.6.2.2 Results

Two attenuation maps were derived. The first map was reconstructed from the TX-scan and corrected for scatter using the SSS method. The second attenuation map was obtained from the CT data using bilinear scaling. All reconstructions were done using a matrix of 176 x 176 x 40 with an isotropic voxel size of 4 mm. Figure 4.19 shows central coronal and sagittal slices of the reconstructed CT-based and TX-based attenuation maps. The humerus is visible on Figure 4.19 and figure 4.20 indicates an increased attenuation coefficient close to the spine and the sternum. In order to evaluate the accuracy of the reconstructed attenuation coefficients in different tissues we defined 2D isocontours on the CT-image for the bone: 2 in the humerus, 5 in the ribs, 1 in the spine and 1 in the sternum. Additionally, 3 VOIs of 27 cm^3 were defined in soft tissue and 3 VOIs of 8 cm^3 in the lungs. The relative difference of the reconstructed attenuation coefficients compared to the CT-based attenuation coefficients are shown in figure 4.21.

4.7 Thoracic imaging

PET imaging of the thorax is commonly used in cardiology and oncology. In this section we will give an overview of the phantoms we used to mimic human thoracic imaging. For the purpose of attenuation correction, the

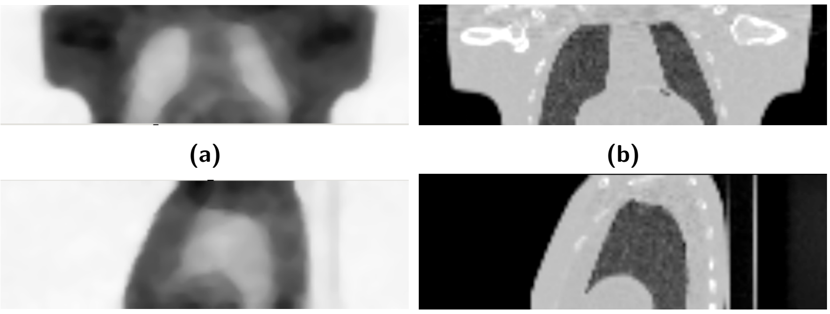

(a) (b)

(c) (d)

Figure 4.19: Coronal (a,b) and sagittal (c,d) slice of the reconstructed TX-based (a,c) and CT-based (b,d) attenuation map of the Alderson torso phantom.

most important tissue types are: the lungs, bone and soft tissue. All three tissue types are included in each phantom.

4.7.1 Thorax phantom I

So far we have validated our transmission based technique on torso phantoms composed out of synthetic materials. These materials posses density properties similar to human tissue which allows comparing CT-based and TX-based reconstruction methods in thoracic imaging. Parallel to our research, much work is also done to investigate the feasibly of obtaining the

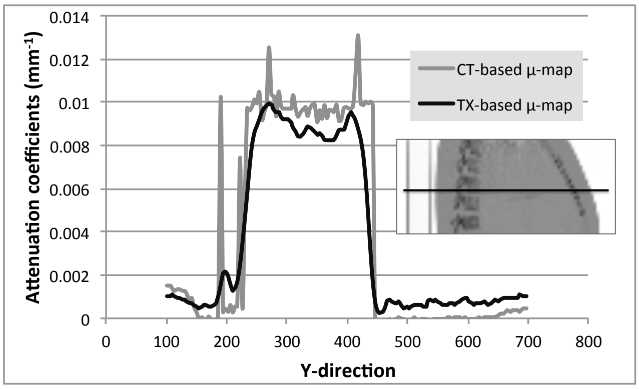

Figure 4.20: Profile in a slice of the TX-based and CT-based attenuation map showing an increased μ-value close to the ribs and sternum.

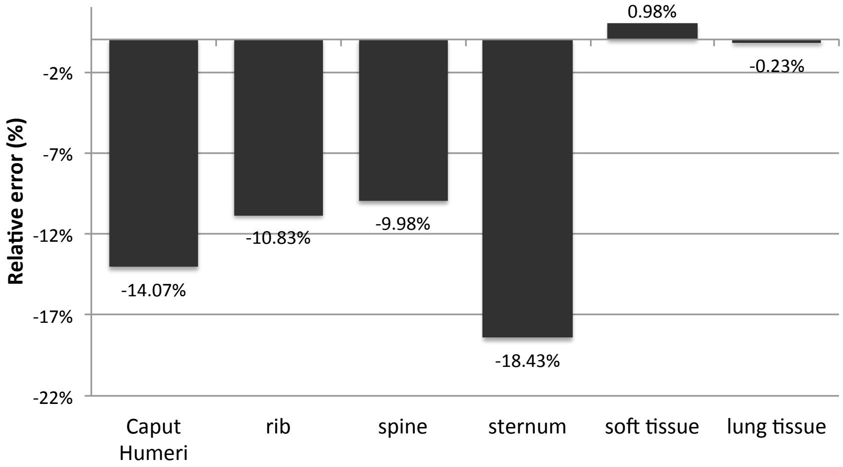

Figure 4.21: Relative difference of the reconstructed TX-based attenuation map compared to the CT-based attenuation maps in VOIs defined in the humerus, rib, spine, sternum, soft tissue and lung tissue.

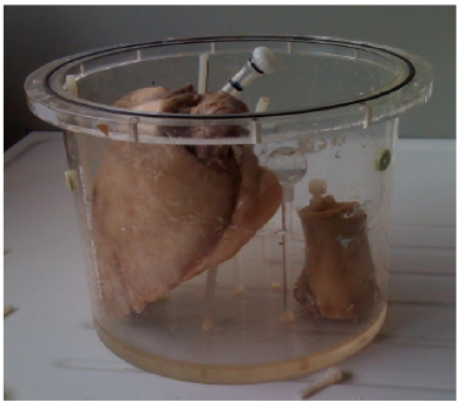

Figure 4.22: A thorax phantom contains one lobe of a pig lung and a bovine bone.

attenuation maps from the MRI images. As discussed in the introduction, MR-based attenuation correction has some drawbacks. The most important issue is related to the fact the some tissues such as lung and bone show very low signal intensity in conventional MRI. Because it is very hard to find synthetic materials that mimic the behavior of protons in tissue with special relaxation properties while preserving similar electron densities to the human equivalent tissue, we designed a torso phantom containing real tissue from animals. As real tissue is used, it inherently mimics the MR as well as the density properties of the different tissue types. A Jaszczak cylindrical phantom was chosen as a container to position an inflated lobe of a pig lung and a part of a bovine femur bone (see figure 4.22). The PMMA cylinder has a diameter of 22 cm and height of 20 cm. The lung was obtained from a female pig which was sacrificed after cardiac surgery experiment. Because of the negative pressure within the chest cavity, the lung remained open inside the body. Once it was exposed to atmospheric pressure the lung collapsed and had to be reinflated. For this purpose a cannula was inserted into the main bronchus, fixed air-tight and the lobe was inflated using a ventilator available in the lab. The bone was obtained from a local slaughter house. It has a thick cortical layer ($\approx$ 1cm) and a center filled yellow bone marrow, which has similar density properties to adipose tissue. Because of its shape, the bone could be used to mimic the spine, which is the most important bone structure in thoracic imaging. To allow long term storage of the biological tissue, both the femur bone and the inflated lung were submersed in a 4% formaldehyde solution.

4.7.1.1 Data acquisition and processing

The Jaszczak container was filled with water containing ^{18}F-FDG and two hot spheres with a 8:1 foreground to background activity ratio were inserted. A cold sphere was also inserted. The total activity in the phantom was approximately 74 MBq. First a blank reference scan was acquired. Then a simultaneous transmission/emission scan of the torso phantom was acquired. Finally the transmission source was removed and an emission scan of the torso phantom was acquired. All scans had a duration of 5 minutes. An overview is shown in table 4.7 and 4.8. Additionally, a CT image was acquired with the following parameters: 120 kVp, 81 mAs, 5 mm slice thickness, 0.853 pixels per mm transverse resolution, and a 512 x 512 x 36 reconstruction matrix.

Scan type	Annulus	Phantom	Activity in phantom
BX	Yes	-	-
TEX	Yes	Cylinder	Yes
EX	No	Cylinder	Yes

Table 4.7: Overview of measurements on the Gemini TF PET/CT.

4.7.1.2 Results

Reconstructed attenuation maps

An attenuation map was reconstructed from the blank scan and transmission scan. τ_1 was set to 28.5 cm and a count rate correction factor for $\tau_2 =$ 30 cm of 0.77 was derived. No scatter correction was applied. A transverse and sagittal slice of the reconstructed attenuation map of the human thorax phantom is depicted in figure 4.23. An underestimation of the attenuation coefficients was noticed in areas of high PET uptake such as in the hot lesions (see figure 4.24). Table 4.9 shows the mean reconstructed attenuation coefficients in VOIs defined in the lungs, soft tissue and bone. The attenuation coefficients derived from the CT-image are also shown.

Reconstructed PET image

Emission data set EX and TEX were reconstructed using 50 iterations of the ML-EM algorithm. Attenuation correction was done using a CT-based attenuation map for the first reconstruction (EX) and the TX-based attenuation map for the reconstruction of the TEX-data. The reconstructed PET images were evaluated by calculating Contrast Recovery Coefficients (CRC) of the two hot spheres versus background intensity. When using the CT-based attenuation map CRCs of 94% and 85% were found. For the TX-based reconstruction CRCs of 73% and 62% were obtained. Additionally, we noticed a higher uptake in the lungs and a lower uptake in soft tissue. This results reflects the underestimation of the soft tissue attenua-

Scan type	Total activity (MBq)	Prompts (Mcts)	Delays (Mcts)
BX	75	245.3	67.5
TEX	125	254.4	84.3
EX	71	110.3	18.5

Table 4.8: Overview of the total counts and total activity of the acquisitions listed in table 4.7

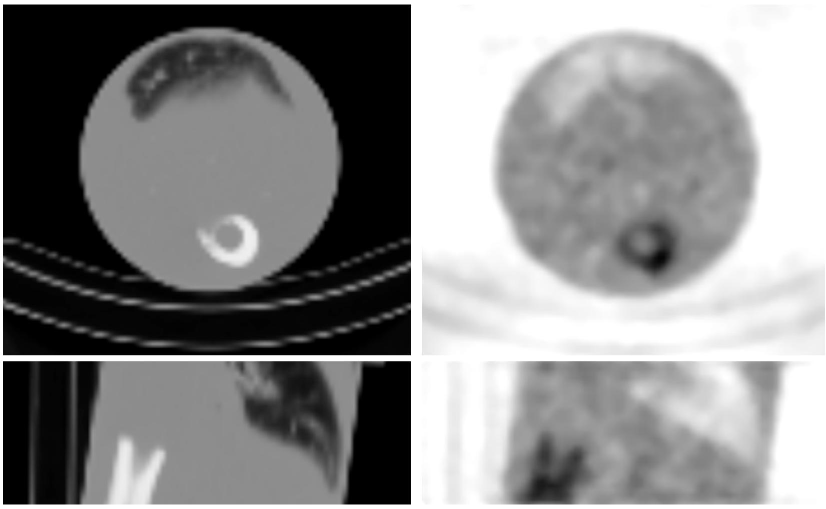

Figure 4.23: Transverse and sagittal slice of the reconstructed CT-based (a) and TEX-based (b) attenuation map.

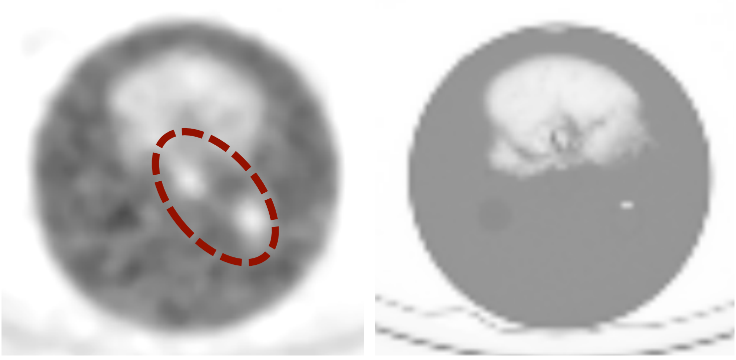

Figure 4.24: Transverse slice of the reconstructed TEX-based (a) and CT-based (b) attenuation map. The underestimated attenuation coefficients in the hot lesions are indicated in red.

	Lung	Water	Bone
CT-based	0.00142	0.00953	0.0172
TEX-based	0.00202	0.00711	0.0121

Table 4.9: Mean reconstructed attenuation coefficients (mm^{-1}) for VOIs defined in the pig lungs, bovine bone and water container.

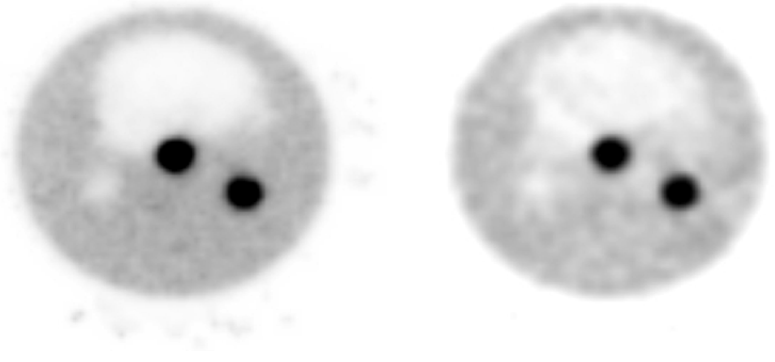

(a) (b)

Figure 4.25: Transverse slice of the reconstructed PET image with CT-based (a) and TEX-based (b) attenuation correction respectively. Compared to the CT-based AC PET image, a higher uptake in the lungs and a lower uptake in the soft tissue was noticed.

tion coefficients and the overestimation of the lung attenuation coefficient. A transverse slice of the reconstructed emission is depicted in figure 4.25.

4.7.2 Thorax phantom II

In the previous thorax study one lobe of pig lung and a bovine femur bone were inserted in a cylindrical phantom with an diameter of 20 cm. Three concerns have led to the creation of a second, more realistic phantom. First,

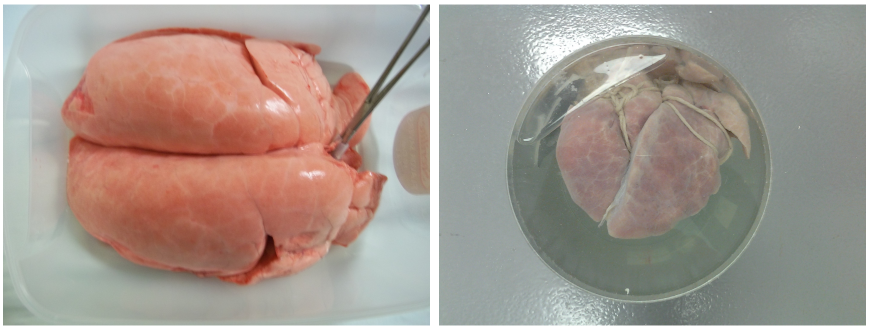

(a) (b)

Figure 4.26: Thorax II phantom: inflated pig lungs (a) and top view of the phantom (b).

only one lobe of a pig lung was used. However, the MR-based segmentation method installed on the Ingenuity scanners uses predefined information about the anatomy of the human body, i.e. that it contains two separate lungs, in order to segment lung tissue. Because we are interested in comparing our method with the MR-based method, we inflated a new pair of lungs obtained from a piglet who was sacrificed after surgery. The lungs were inflated, sealed air-tight and submersed in formaldehyde to preserve the biological tissue. Figure 4.26 shows the inflated pig lungs and a top view of the phantom. Secondly, the bovine femur bone has a thick cortical layer with a relatively high attenuation coefficient compared to a human spine. More realism was added by including the spine of the pig instead of the bovine bone. The spine was also submersed in formaldehyde and inserted in a cylindrical container together with the lungs. Finally, to increase the lateral outside dimension two bottles of water were added to mimic the arms of the patient.

4.7.2.1 Data acquisition

Similar to the previous phantom we acquired a blank, a simultaneous transmission/emission scan and a stand-alone emission scan. For this purpose the phantom was filled with 74 MBq of ^{18}F-FDG prior to the transmission scanning. A similar amount of activity was inserted in the transmission source. The PET/MRI protocol included a conventional T1-weighted MRI acquisition for the purpose of attenuation correction. The MR image was reconstruction on a 320 x 320 x 56 matrix with voxel dimension 1.88 x 1.88 x 6.00 mm^3. Additionally, a PET/CT-image of the thorax phantom was acquired on the Discovery PET/CT (Ge Medical Systems). The CT was acquired with the following parameters: 140 kVp, transverse resolution of 1.463 pixels per mm, slice thickness of 6 mm and a 878 x 878 x 56 reconstruction matrix.

4.7.2.2 Results

Reconstructed attenuation maps

Figure 4.27 shows a profile of the TEX and the EX scan. The images were obtained by calculating the annihilations points from the TOF information. In total three attenuation maps were derived: a CT-based map using bilinear scaling, an MR-based map derived from the software available on the Ingenuity TF PET/MR system and TEX-based attenuation map

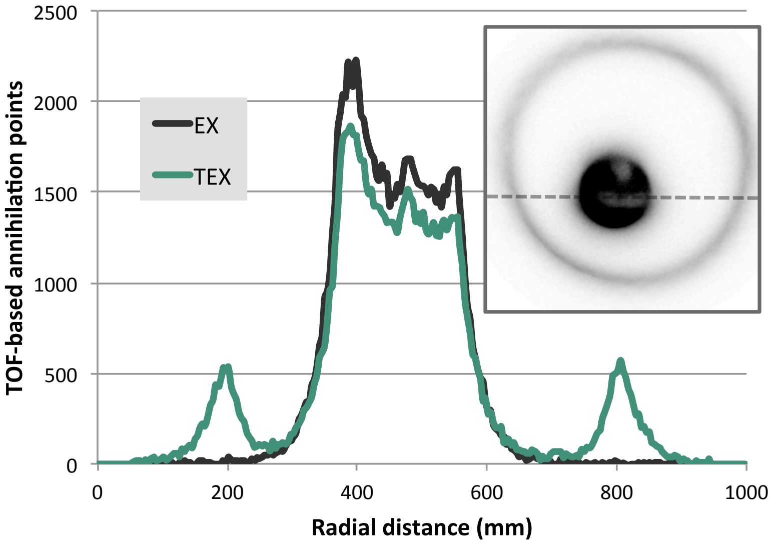

Figure 4.27: Profile of the TEX and EX scan. For each event the location of the annihilations was estimated using the TOF information.

derived from the TEX scan. During the last reconstruction scatter transmission events were compensated using the SSS method. All attenuation maps were reconstructed on a 176 x 176 x 40 matrix with a 4-mm isotropic voxel dimension. Unfortunately, the MR-based reconstruction failed to segment the lungs. Figure 4.28 shows a central slice of three reconstructed attenuation maps : a CT-based attenuation map, a TEX-based attenuation map without scatter compensation and the MR-based contour map without lung segmentation. The reconstructed attenuation coefficients of the three important tissue types are depicted in table 4.10.

Reconstructed PET images

	Lungs	Soft tissue	Spine	Arms
CT-based	0.0052	0.0097	0.0111	0.0097
MR-based	0.0022	0.0097	0.0097	0.0097
TX-based	0.0056	0.0070	0.0105	0.0090

Table 4.10: Reconstructed attenuation coefficients (mm^{-1}) of water for cylindrical water phantom.

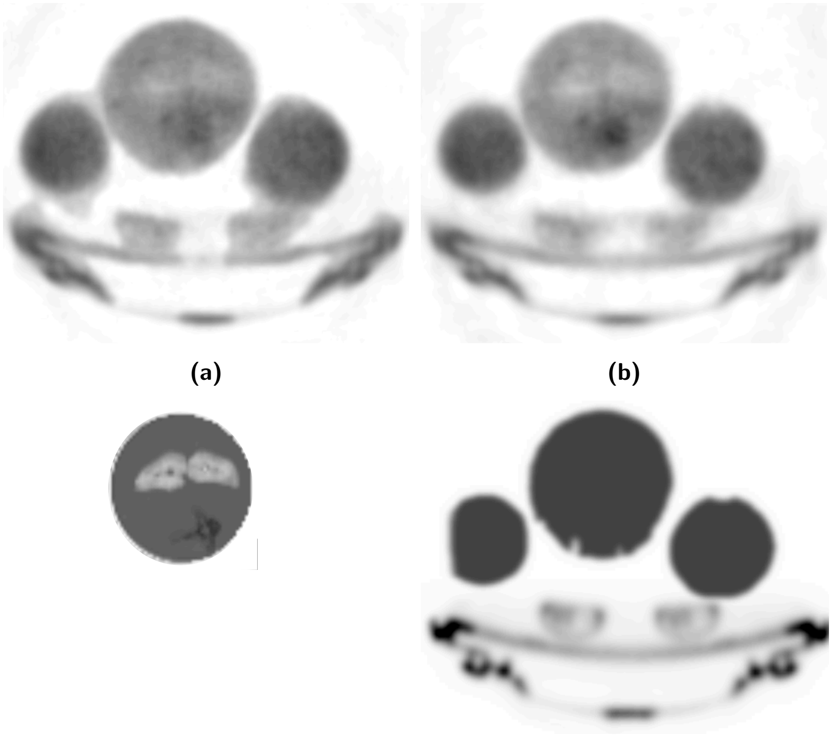

(a) (b)

(c) (d)

Figure 4.28: Transverse slice of the TX-based attenuation map without scatter correction (a), the TX-based attenuation map with SSS scatter correction (b), the CT-based attenuation map and the MR-based attenuation map (d). Remark: the MR-based attenuation map failed to segment the lungs, because of a lack of similarity with human data.

In total four PET images were derived (see table 4.11). The first and the second PET images were derived from the TEX and the EX scan respectively. Both reconstructions were performed with our in house software using the TEX-based attenuation map for attenuation correction. The third and the fourth PET image was obtained from the Ingenuity TF PET/MRI and the Discovery PET/CT respectively. A central transverse slice of PET images $\mathrm{TEX}_{\mathrm{TX}}$, $\mathrm{EX}_{\mathrm{MR}}$ and $\mathrm{EX}_{\mathrm{CT}}$ is shown in Figure 4.29. Subsequently, we calculated the contrast recovery of the PET image intensity values in the lungs and bone compared to soft tissue for one slice of images $\mathrm{EX}_{\mathrm{TX}}$, $\mathrm{EX}_{\mathrm{MR}}$ and $\mathrm{EX}_{\mathrm{CT}}$. For this purpose the following CRCs was used:

PET image	System	PET reconstruction	Attenuation map
$\mathrm{TEX}_{\mathrm{TX}}$	Ingenuity	In house	TEX
$\mathrm{EX}_{\mathrm{TX}}$	Ingenuity	In house	TEX
$\mathrm{EX}_{\mathrm{MR}}$	Ingenuity	Manufacturer	MR
$\mathrm{EX}_{\mathrm{CT}}$	Discovery	Manufacturer	CT

Table 4.11: Overview of reconstructed PET images. For the first two reconstructions our in house reconstruction software was used. The last two PET images were obtained from the Ingenuity PET/MRI scanner and the Discovery PET/CT.

$$\mathrm{CRC}_x^{\mathrm{tissue}} = \frac{1 - \lambda_x^{\mathrm{tissue}} / \lambda_x^{soft}}{1 - \lambda_{\mathrm{CT}}^{\mathrm{tissue}} / \lambda_{\mathrm{CT}}^{soft}} \tag{4.14}$$

The contrast recovery coefficients (see figure 4.30) $\mathrm{CRC}_{\mathrm{TEX}}^{\mathrm{bone}}$ and $\mathrm{CRC}_{\mathrm{TEX}}^{\mathrm{lung}}$ were obtained by comparing PET images $\mathrm{EX}_{\mathrm{TX}}$ and $\mathrm{EX}_{\mathrm{CT}}$ and the $\mathrm{CRC}_{\mathrm{MR}}^{\mathrm{bone}}$ and $\mathrm{CRC}_{\mathrm{MR}}^{\mathrm{lung}}$ were derived from a comparison between the $\mathrm{EX}_{\mathrm{MR}}$ and the $\mathrm{EX}_{\mathrm{CT}}$ images. Although better contrast recovery is obtained with the MR-based AC, the $\mathrm{CRC}_{\mathrm{MR}}^{\mathrm{bone}}$ and $\mathrm{CRC}_{\mathrm{MR}}^{\mathrm{lung}}$ values differ by 22%. For the TEX-based AC PET images, this difference ($\mathrm{CRC}_{\mathrm{TEX}}^{\mathrm{bone}} - \mathrm{CRC}_{\mathrm{TEX}}^{\mathrm{lung}}$) is 7%. This can be explained by the fact that the MR-based method misclassified bone and lung tissue as soft tissue. It is also important to mention that no scatter correction was applied during the reconstruction of the PET images with the in-house software.

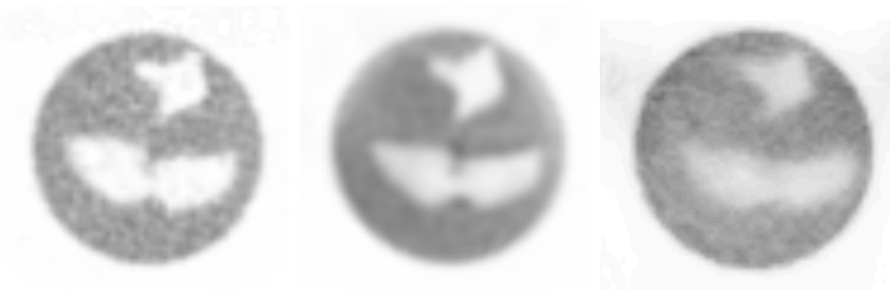
(a) (b) (c)

Figure 4.29: Transverse slice of the reconstructed PET images from the PET/CT scan ($\mathrm{EX}_{\mathrm{CT}}$) (a), the Ingenuity PET/MR with MR-based attenuation correction ($\mathrm{EX}_{\mathrm{MR}}$) (b) and the TEX-based attenuation corrected PET image ($\mathrm{TEX}_{\mathrm{TX}}$) (c).

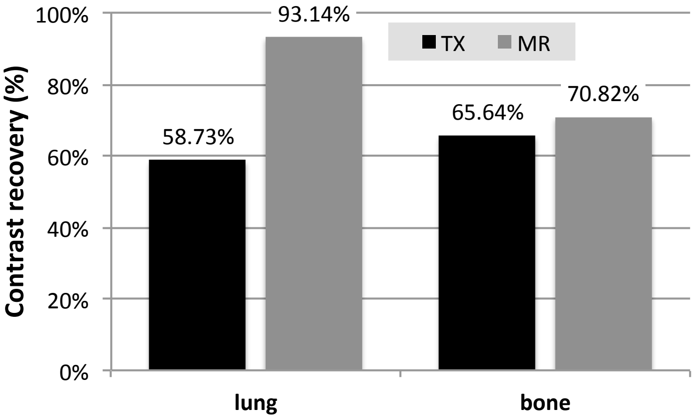

Figure 4.30: Contrast recovery of PET image intensity compared to the PET images derived from the PET/CT scan.

4.8 Discussion and conclusion

In this chapter, we have presented six phantom studies to illustrate the feasibility of reconstructing the attenuation map with a transmission-based technique in a clinical TOF PET system. Four major conclusions can be drawn from the results presented in this chapter. First, in order to obtain accurate attenuation coefficients at 511 keV, the transmission data needs to be corrected for image degrading effects such as random coincidences, noise, count rate related issues and scattered coincidences. In all phantom studies, random coincidences were compensated using the delayed window method. This was done by subtracting the delayed channel from the prompt channel during reconstruction. The influence of noise was regulated by decreasing the total variation after each iteration in the gradient ascent algorithm. Additionally, the count rate performance mismatch between the blank and transmission scan was compensated by estimating a global correction factor β_{T_2}. Finally, we also introduced two methods to compensate for scattered transmission events: an energy-based scaling method and the TX-based Single Scatter Simulation (SSS) method. In all phantom studies, the SSS method yielded the best results. We illustrated this finding with the results obtained from the TX-scan of the anthropomorphic torso. When scattered transmission events were compensated using the energy-based method a quantification error of -7.55% for the attenuation coefficient of soft tissue was obtained while an error of only -1.88% was obtained when the SSS method was applied.

Secondly, when the transmission data and emission data are acquired simultaneously, a TOF-based extraction method is applied to extract the transmission events. Because of the limited TOF resolution, true and scattered emission data might still contaminate the extracted transmission data, especially when the activity inside the transmission source is low compared to the activity injected in the phantom. This could lead to an underestimation of attenuation coefficients in areas of high emission uptake. This was illustrated with the two thorax studies. An underestimation of the soft tissue attenuation coefficient was obtained in the hot lesions of the thorax I phantom. In the second thorax study a significant difference of the soft tissue attenuation coefficient was obtained in the center hot water cylinder compared to the cold water bottles. The influence of the emission data can be decreased by increasing the activity inside the transmission source at a cost of additional radiation dose to the patient, or by increasing threshold value τ_1 at the cost of more noise in the reconstructed attenuation map.

Thirdly, during a PET scan, any object inside the FOV will cause attenuation of the gamma rays. When combining PET with MRI, conventional MR-imaging will generally not be able to visualize MR-coils or the patient table. Hence, most MR-based attenuation correction techniques use templates derived from CT or transmission images. In the initial phantom studies we have demonstrated that the MRI-coils and the patient table can easily be reconstructed and visualized in the attenuation map obtained from the TX data.

Finally, to achieve absolute PET quantification, correcting for the attenuation of gamma rays in bone tissue is mandatory. The phantom studies illustrate how the TX-based method is able to visualize large bone structures such as the jaws of the pig, the humerus in the Alderson torso phantom, the spine insert in the anthropomorphic torso phantom and the bovine femur bone. However, smaller bone structures or spongious bone tissue characterized by a smaller attenuation coefficient are more difficult to distinguish from the surrounding tissue. Typically, a mixture of tissue attenuation coefficients is found. In the pig head study, the attenuation coefficients in the air cavities are more than doubled compared to the CT-based attenuation coefficients. This can be explained by the presence of the nasal and ethmoid bones close to the nasal cavities. Additionally, in the Alderson torso phantom, the ribs and the spine are almost not visible in the reconstructed images. In these tissues a mixture of soft tissue attenuation and bone attenuation was obtained. Similar for the humerus, a lower attenuation coefficient compared to the CT-based attenuation was found. Hence, the TX-based method performs well in distinguishing large structures from surrounding tissue but the performance in detecting smaller bone structures within the body is limited. Improvement can be made by increasing the activity inside the transmission source or prolonging the acquisition times.

In conclusion, the phantom studies have allowed us to validate the transmission-based attenuation correction technique in an experimental environment. When the TX data is corrected for random and scattered transmission events and count rate related issues, stand-alone transmission scanning yielded acceptable accuracy of the attenuation coefficients at 511 keV in thoracic and head imaging. Additionally, we have illustrated how simultaneous transmission/emission scanning is feasible with state-of-the art TOF PET systems. These results show that the presence of the emission data significantly influences the accuracy of the reconstructed attenuation map in areas of high emission uptake. In these situations μ-value scaling might be the method of choice to improve PET quantification.

4.9 Original contributions

The first experiments and the pig head study were presented at the SNM conference in 2010 [153]. In the same year, the Single Scatter Simulation method was first illustrated with the NCAT simulation study at the PET/MR workshop at the MIC conference [162]. One year later, the first thorax study was presented at the same conference. Other studies such as the torso phantom studies and the TF PET/MRI thorax study have not been published. The energy-based scatter correction and μ-value scaling technique were introduced in a patient study accepted for publication in JNM [163] (see next chapter). The modification of the SSS algorithm to include the TOF-based extraction was implemented in the final year of this PhD project. Some phantom studies were redone to include this scatter correction technique.

Chapter 5

Clinical imaging experiments

5.1 Introduction

In the previous chapter we demonstrated the transmission-based attenuation correction technique with six phantom studies on the Gemini TF PET/CT and the Ingenuity TF PET/MRI system. In this chapter we will investigate whether our attenuation correction method can be used in patient studies acquired on a TOF PET/MRI scanner. The Ingenuity TF PET/MRI is currently the only FDA-approved system that is equipped with TOF PET detectors. Eventually, this system will evolve into clinical practice for the diagnosis and follow up of various diseases. In clinical applications, PET quantification is very important. Hence the attenuation correction technique must fulfill some requirements. Although most of these requirements were discussed in the previous chapters, we will give a summary in this introduction. First, the reconstructed attenuation maps should be free of artifacts. Three major sources of artifacts are noticed in the attenuation maps derived with methods that exist today: artifacts caused by segmentation errors and noise [164], truncation artifacts caused by a limited FOV and artifacts that arise because of characteristics of the materials inside the FOV (metal implants in CT, magnet susceptibility in MRI). Second, the use of predefined knowledge about the anatomy of the patient or the attenuation coefficients of tissues should be limited. In literature, a high inter- and intra-patient variability of attenuation coefficients of lung tissue is reported [165]. Assigning predefined attenuation coefficients in these tissues is not advisable. Additionally, atlas-based methods might fail when the patient exhibits severely damaged organs or anatomical abnormalities. Thirdly, the method should be able to visualize any object inside the FOV.

MRI protocols require the use of MRI coils which are inside the FOV of the PET scanner. These materials significantly attenuate gamma radiation and should be considered when correcting for attenuation. Additionally, the patient bed should be included in the reconstructed attenuation map. Although when working with MR-based methods, templates can be used for the patient table and fixed coils, special care is needed when working with flexible coils. Finally, because in clinical practice, standard protocols are used and acquisition times are often limited, a robust technique which does not require additional acquisition time from the PET or MRI scanner and which can be fully automated is preferred to maintain a high throughput.

The TEX-based attenuation correction method, described in the previous chapters, attempts to derive the attenuation map with a transmission scan by inserting an annulus shaped positron emitting source inside the FOV of the PET scanner. The method fulfills most of the requirements described above. The FOV is typically much larger than the FOV used in a CT or MRI scan and any object inside can be visualized. Additionally, the method does not depend on any CT or MRI atlases, nor does it require additional acquisition time from the MRI or the PET system. However, some issues remain. Deriving accurate attenuation coefficients is a challenging task, because of the presence of random and scattered coincidences and count rate issues related to the PET system. The reader is referred to the previous chapters on how these image degrading effects were corrected. In this chapter, the attenuation correction method was applied to patient data. As PET/MRI systems will probably be used in clinic for neurology, cardiology and oncology, we investigated how well our method would perform in brain and thoracic imaging. The clinical study involved 6 patients, one brain study and 5 studies of the head/neck and torso region. The goal of this work is to compare our TEX-based method with the MR-based method currently available on the sequential TF PET/MRI and the gold standard CT-based attenuation correction.

5.2 Materials and methods

First we give an overview of the TOF-PET/MRI and CT acquisition protocols used in the brain and thoracic study. Second, we describe how the TEX-, MR- and CT-based attenuation maps were obtained. Finally, we present how the reconstructed PET images were evaluated. If needed, a distinction is made between the brain and the thoracic study.

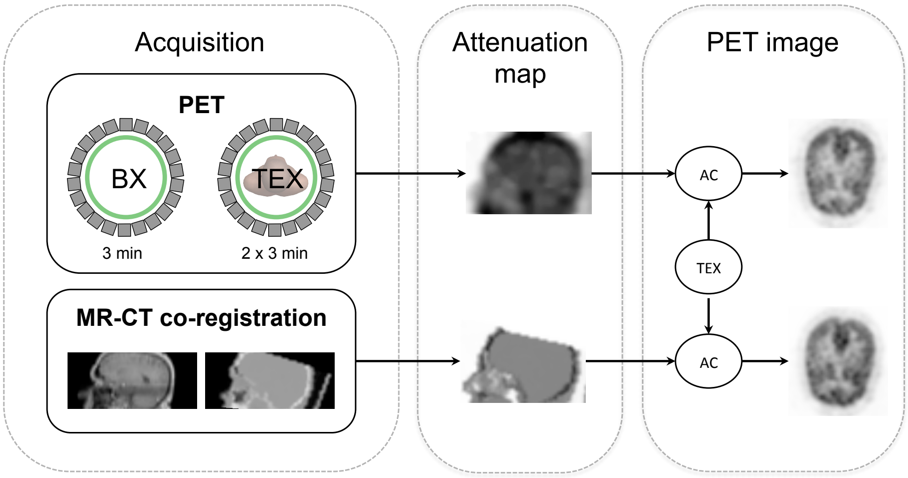

Figure 5.1: Acquisition and image-processing workflow of brain study. From left to right : PET/MRI and CT acquisition and co-registration, derivation of the CT-based and TEX-based attenuation maps and reconstruction of the PET images using the CT-based and TEX-based attenuation map for attenuation correction.

5.2.1 PET/MRI and CT Acquisition protocols

All PET and MRI data were acquired with the Ingenuity sequential TOF PET/MRI scanner (Philips Healthcare, Cleveland, OH, USA) installed at Mount Sinai Hospital in New York. The system combines state-of-the-art TOF PET technology (500-600 ps TOF resolution) with the imaging capabilities of a clinical 3.0T MRI system. The CT data was acquired on the Philips Brilliance iCT (Philips Healthcare, Cleveland, OH) which is installed in the room next to the PET/MRI site. All acquisition protocols were approved by the Icahn School of Medicine at Mount Sinai institutional review board (IRB) and all subjects signed written informed consent.

5.2.1.1 Brain imaging

In the first patient study, the accuracy of the attenuation correction method in human brain imaging was examined with a TOF-PET/MRI and CT study. An overview of the complete workflow is given in figure 5.1. First a CT image of the head and torso was acquired. The CT was acquired with a tube voltage and current of respectively 120 kVp and 78 mAs. The CT image was reconstructed on a 512 x 512 x 62 matrix with a 0.6 x 0.6 x 5

Patient	Weight(kg)	Activity (MBq)	Bed positions
1	96	200	2 (head)
2	92	363	3 (neck, torso)
3	129.3	407	3 (neck, torso)
4	73.5	498	3 (neck, torso)
5	65	364	2 (torso)
6	84	555	2 (neck, upper torso)

Table 5.1: Patient weight (kg), injected activity (MBq) 80-90 minutes prior to PET/MRI acquisition and acquired bed positions during PET/MRI acquisition.

mm^3 voxel size. Next, the patient was asked to take place on the table of the TOF-PET/MRI system. First, a T1-weighted MRI was acquired and reconstructed on a 320 x 320 x 92 matrix with 1.88 x 1.88 x 6 mm^3 voxel dimensions. The MR image was later used to co-register the PET/MRI and CT data. Unfortunately, the MR-based attenuation map was unavailable. On the PET side, two scans were acquired: a blank reference scan (BX-scan) and a simultaneous transmission/emission scan (TEX-scan). During both scans the annulus shaped source was inserted into the FOV. All scans had a duration of 3 minutes. The patient was injected with 200 MBq of ^{18}F-FDG, 90 minutes prior to the TEX-scan (see table 5.1). No stand-alone emission scan was acquired.

5.2.1.2 Body imaging

Five patients with risk factors for development of atherosclerotic plaques in the aorta (chest/whole body scans) and carotid (head/neck scans) were investigated with the sequential TOF PET/MRI system. An overview of the complete workflow per patient is given in figure 5.2. Each patient was examined with the same PET/MRI and CT protocols. The MRI acquisition protocol included a conventional T1-weighted image with a FOV of 57cm for the purpose of attenuation correction [166]. The MR image was reconstructed to a 320 x 320 x 90 voxel matrix, with 1.88 x 1.88 x 6.00 mm^3 voxel dimensions. The PET protocol included three types of scans : a BX-scan, a TEX-scan and an EX-scan. First an annulus shaped source was placed inside the FOV of the PET scanner and a 5 minute blank scan was acquired. Then the patient was asked to take place on the table and

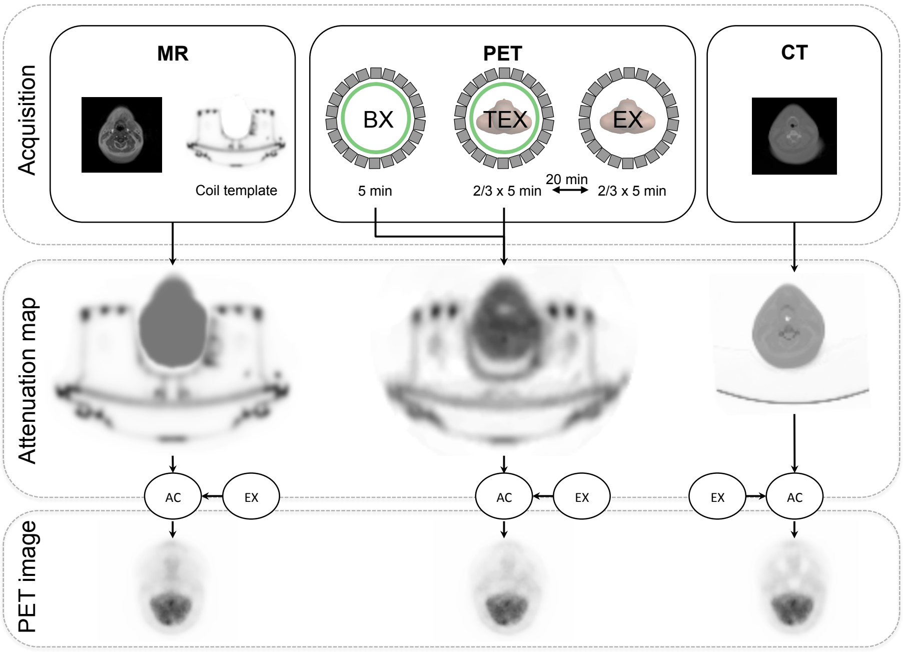

Figure 5.2: Acquisition and image-processing workflow of thoracic study. From top to bottom : PET/MRI and CT acquisition, derivation of the CT-based, MR-based and TEX-based attenuation maps and reconstruction of the PET images using the CT-based, MR-based and TEX-based attenuation map for attenuation correction.

was moved inside the PET scanner followed by a simultaneous transmission/emission scan of 5 minutes per bed position. Finally the transmission source was removed and the previous PET scan was repeated measuring only emission data. Each patient received an ^{18}F-FDG injection of 370 to 550 MBq 80-90 minutes prior to scanning. An overview of the acquired bed positions and injected activity of all patients is given in table 5.1. Additionally, for each patient, a CT was acquired on the Philips Brilliance iCT using the following parameters: 140 kVp, 79 mAs, 0.9-mm slice thickness, in-plane resolution of 0.45 mm and a reconstructed FOV of 40 cm.

5.2.2 PET/MRI and CT co-registration

The co-registration of the CT images with the PET/MRI images was performed automatically using rigid registration in the Philips DICOM viewer.

For this purpose normalized mutual information was used. Manual fine adjustments were performed by visual inspection using the patient spine as an anatomical landmark, as it is least susceptible to breathing artifacts. Visual inspection was performed to check for gross misalignments in lungs, heart, rib cage, and head/neck anatomical structures. We found the spatial error to be less than 4mm, which is acceptable considering the resolution of the PET scanner.

5.2.3 Derivation of the attenuation maps

In this section we will describe how the attenuation maps are derived. All attenuation maps were resampled to a 176 x 176 x 40 voxel matrix, with a 4-mm isotropic voxel dimension, the same matrix as we used for the reconstruction of the PET images. For the brain study, only a TEX-based and a CT-based attenuation map was derived. For the neck and torso studies, attenuation maps were derived from all three modalities.

5.2.3.1 CT-based attenuation map

CT-images are related to electron density and can therefore easily be converted into an attenuation map at 511 keV. In this work, CT-based μ-values were obtained from the CT Hounsfield Units (HU) using a bilinear scaling function as reported in [167]. In both the brain and whole body experiments, the CT-based attenuation map was used as a reference for comparison with the MR and/or TEX-based attenuation maps. For Hounsfield Units (HU) lower than or equal to 0 the following scaling was applied:

$$\mu = \mu_{\mathrm{H_2O}} \cdot \frac{HU + 1000}{1000} \tag{5.1}$$

For $HU > 0$:

$$\mu = \mu_{\mathrm{H_2O}} + (HU) \cdot \frac{\mu^{\mathrm{CT}}_{\mathrm{H_2O}}}{1000} \cdot \frac{(\mu_{\mathrm{bone}} - \mu_{\mathrm{H_2O}})}{(\mu^{\mathrm{CT}}_{\mathrm{bone}} - \mu^{\mathrm{CT}}_{\mathrm{H_2O}})} \tag{5.2}$$

with

$$\begin{aligned} \mu_{\mathrm{H_2O}} &= 0.096\ \mathrm{cm}^{-1}, & \mu_{\mathrm{bone}} &= 0.172\ \mathrm{cm}^{-1} \\ \mu^{\mathrm{CT}}_{\mathrm{H_2O}} &= 0.184\ \mathrm{cm}^{-1}, & \mu^{\mathrm{CT}}_{\mathrm{bone}} &= 0.428\ \mathrm{cm}^{-1} \end{aligned}$$

5.2.3.2 MR-based attenuation map

The whole body MR-based attenuation map was obtained using the software available on the scanner [129, 168, 169]. The process consists of MR acquisition, segmentation, μ-value assignment and inclusion of the patient bed and fixed RF coils using templates.

MR images suitable for deriving the attenuation map are acquired with a 3D multi-station spoiled gradient echo sequence with a flip angle of 10 degrees, TE 2.3 ms, TR 4ms, 53 cm transverse FOV with a 3D slab thickness of 60 mm, voxel size 3x3x6 mm^3, and 6 mm overlap between adjacent stations.

The segmentation algorithm attempts to distinguish air and 2 types of tissue : lung tissue and soft tissue. Special care is taken when segmenting the lungs: a deformable shape model was derived from manual segmentation of 20 high-resolution CT datasets [169]. The algorithm works in two phases: first the patients contour and orientation is derived. In the second phase intensity-based region growing is used in combination with the deformable shape model to segment the lungs. This avoids 'leakage' of lung segmentation into the stomach and bowel. Although MRI data was acquired for the brain study, no MR-based attenuation map was available.

5.2.3.3 Transmission-based attenuation map

Given a BX and TEX-scan, the attenuation map can be reconstructed. The transmission data is extracted from the TEX dataset using the TOF information. After extraction, the estimated TX data is used to reconstruct the attenuation map using an list-mode based iterative gradient ascent algorithm derived from eq. 4.4 :

$$\mu_j^{k+1} = \mu_j^k + \alpha \left(1 - \frac{\sum\limits_{e \in \hat{TX}} c_{i_e j} w_e SC_e(\epsilon_1, \epsilon_2)}{\beta_{\tau_2} \sum\limits_{e \in \hat{BX}} c_{i_e j} w_e a_i^k SC_e(\epsilon_1, \epsilon_2)} \right) \tag{5.3}$$

with

$e =$ list-mode event index

$i_e =$ LOR or crystal pair index of list-mode event e

$SC_e(\epsilon_1,\epsilon_2)$ = energy-based scaling factor to suppress scattered events
c_{ej} = probability that an event e generated in voxel j is detected along LOR i_e
$w_e = -1$ if event e is marked as a delayed event and 1 otherwise

Because of the limited TOF resolution of the PET scanner ($\approx$ 600 ps), the measured source position (x_s, y_s, z_s) might fall outside the cylinder radius τ_1, hence, not all transmission data will be separated from the emission data. Secondly, emission events originated at locations close to the radius τ_1 could be misclassified. In chapter 3 we evaluated these classification errors using the Transmission Rejection Rate (TRR) and the Emission Contamination Rate (ECR):

$$\mathrm{TRR} = \frac{\#\text{rejected true transmission events}}{\#\text{total true transmission events}}$$

$$\mathrm{ECR} = \frac{\#\text{misclassified emission events}}{\#\text{extracted transmission events}}$$

Here, the exact amount of true transmission events and true emission events are unknown. Therefore the blank scan and the stand alone emission scans are used in stead:

$$\mathrm{TRR} = \frac{\#\text{rejected BX events}}{\#\text{BX events}}$$

$$\mathrm{ECR} = \frac{\#\text{misclassified EX events}}{\#\text{extracted TX events}}$$

For this purpose, the TOF separation method is applied on the BX, EX and TEX data. Although, a different definition for TRR than the theoretical TRR defined in chapter 3 is used, the metric still gives an idea of the amount of transmission data that will be rejected in the TEX scan.

μ-value scaling

Although PET image degrading effects caused by scatter can be reduced using the energy based corrections described above, the method does not yield exact absolute values for the attenuation coefficients at 511 keV because of the limited energy resolution. More accurate values were obtained by scaling the attenuation coefficients in the TEX-maps. For the brain study, the attenuation coefficient of water (0.097 cm^{-1}) was used as a reference for soft tissue. For this purpose the mean attenuation coefficient for soft brain tissue was derived from the histogram of the TEX-based attenuation coefficients. A linear scaling was applied:

$$\mu = \mu_{\mathrm{H_2O}} \cdot \frac{\mu^*}{\mu^*_{\mathrm{soft}}} \tag{5.4}$$

Where * indicates the unscaled attenuation coefficients.

For the thoracic study, a histogram matching technique, using all 5 patients was used. The method is described in the previous chapter. Mean CT and TEX-based μ-values as well as the intra-patient variability for lung and soft-tissue were derived from the histograms of the attenuation maps of all five patients using a peak detection algorithm. Given the peak values for both tissues in each patient, the standard deviation is derived by locally fitting a Gaussian distribution to the histograms. Subsequently, the peak values and standard deviations are averaged over all patients. A histogram model was defined for each modality as the sum of two Gaussian distributions. As the number of lung and soft-tissue voxels is unknown, the mixture weights of the two Gaussians were set to 0.5. Finally, the cumulative distribution functions $\mathrm{CDF_{TX}}$ and $\mathrm{CDF_{CT}}$ were calculated from the two mixture models. The TEX-based μ-values were rescaled as follows (see figure 5.3):

$$\mu^{'}_{\mathrm{TEX}} = f(\mu_{\mathrm{TEX}}) = \mathrm{CDF}^{-1}_{\mathrm{CT}}(\mathrm{CDF_{TX}}(\mu_{\mathrm{TEX}})) \tag{5.5}$$

5.2.3.4 Truncated TEX/MR-based attenuation map

The discrepancy between the field of view (FOV) of the PET/MRI and CT scanner may influence the reconstructed PET images [170, 171]. To allow quantitative comparison with the CT-based attenuation map, truncated attenuation maps were derived from the TEX- and MR-maps. All voxels outside of the FOV of the CT scanner in both TEX- and MR-based attenuation maps were set to zero. Additionally we decided to remove the patient bed from these attenuation maps as the CT was acquired on a different bed. For the remainder of this work we will refer to these truncated maps as the $\mathrm{TEX_{tr}}$ and the $\mathrm{MR_{tr}}$-map. An overview of reconstructed attenuation maps is given in table 5.2.

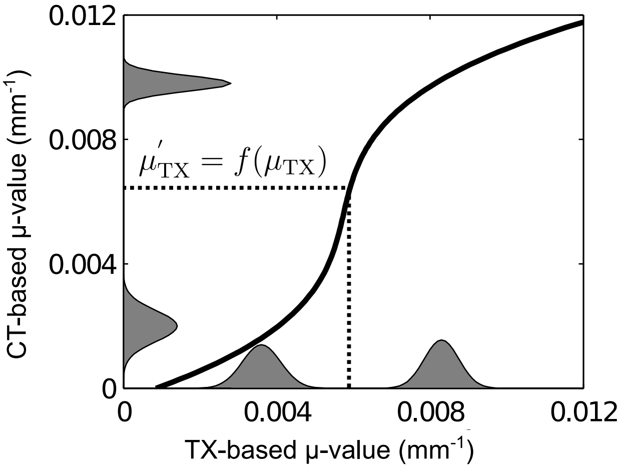

Figure 5.3: Black line represents the scaling function. The histogram model of the CT and TEX-based attenuation coefficients is also shown.

5.2.4 Reconstruction of the PET images

All PET images were reconstructed using 50 to 100 iterations of the standard ML-EM algorithm. Attenuation correction was applied in the forward projection. Random coincidences were estimated using the delayed window method with standard settings of the scanner. Scatter correction was not implemented. The PET images were reconstructed using a 176 x 176 x 40 voxel matrix with a 4 mm-section isotropic voxel.

Attenuation map	FOV	Patient bed
CT	CT	No
TEX	PET	Yes
TEX$_{\mathrm{tr}}$	CT	No
MR	MR	Yes
MR$_{\mathrm{tr}}$	CT	No

Table 5.2: TEX- MR- and CT-based reconstructed attenuation maps.

5.2.4.1 Brain study

In the brain study, the emission data obtained from the TEX scan was reconstructed using three different maps: a wide FOV TEX-based attenuation map, a CT-based attenuation map and a rescaled truncated TEX-based attenuation map (TEX_{tr}-map). No stand-alone emission data was acquired.

5.2.4.2 Thoracic study

For each patient in the thoracic study, the PET data of the stand-alone emission scans were reconstructed using the 5 different μ-maps listed in table 5.2. Additionally, the PET data obtained from the simultaneous TEX scan was reconstructed with the TEX-maps derived from the same dataset.

5.2.4.3 Evaluation of the images

In order to evaluate the effect of the different attenuation maps on the reconstructed PET images, the PET images were compared using a similarity measure. For this purpose the **normalized root mean square deviation (NRMSD)** was chosen because this metric requires the two images to have intensity values of the same range :

$$NRMSD(x,y) = \frac{1}{R_{xy}} \sqrt{\sum_{i=1}^{N} (x_i - y_i)^2} \tag{5.6}$$

with

$$R_{xy} = \sqrt{N} \cdot (\max(x,y) - \min(x,y)) \tag{5.7}$$

The similarity is then given by :

$$\text{SIM}(x,y) = 1 - \text{NRMSD}(x,y) \tag{5.8}$$

Additionally, a quantitative evaluation was performed for both the brain and thoracic study. For the brain study, VOIs of variable size were defined in the frontal lobe, occipital lobe, white matter, the thalamus and the cerebellum. The relative error of the TEX_{tr}-based AC PET images with the CT-based AC PET images was measured.

A comparison between the thoracic MR_{tr}, TEX_{tr} and CT-based attenuation

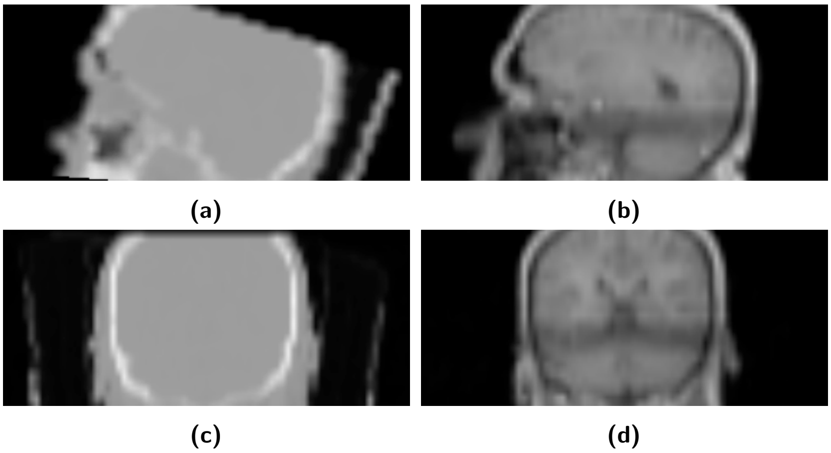

Figure 5.4: Central sagittal (a,b) and coronal slice (c,d) of the co-registered CT (left) and MRI (right) image of the brain study.

corrected PET images is reported by measuring the mean percentage difference in reconstructed PET FDG-uptake in three relevant tissue types (lungs, bone and soft-tissue). For this purpose 20 Volumes-Of-Interest (VOIs) of 8 cm^3 were defined in each region. Special care was taken in selecting the VOIs in order to avoid co-registration errors caused by the misalignment of the PET/MRI and CT data.

5.3 Results

5.3.1 Brain imaging

5.3.1.1 PET/MRI and CT co-registration

A central sagittal and coronal slice of the co-registered brain CT and MRI images is shown in figure 5.4. During the CT protocol, the head of the patient was positioned in a different way than during the PET/MRI acquisition. Hence, part of the head was truncated in the CT image.

5.3.1.2 Extraction of transmission data

For each event in the TEX-scan, the estimated annihilation point was derived from the TOF information and reconstructed on a 250 x 250 x 50 matrix with a 4-mm isotropic voxel dimension. A central transverse slice is

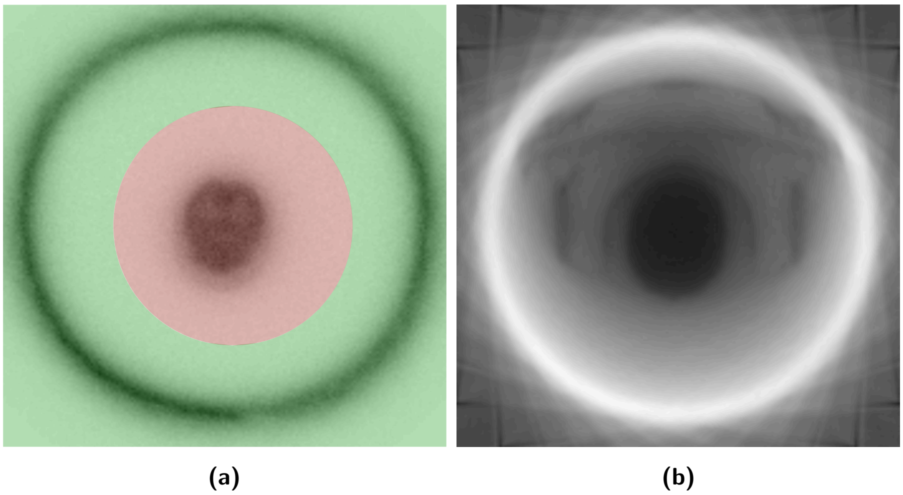
(a) (b)

Figure 5.5: Transverse slice of the estimated annihilation points derived from the TOF information (a). Source positions above the threshold value $\tau_1 = 22$ cm are indicated in green, the source positions that fall within a cylinder of radius $\tau_1 = 22$ cm are indicated in red. The back-projection of the extracted transmission events is also shown (b).

shown in figure 5.5a. Visual inspection shows that for the brain, the transmission and emission data can easily be separated. In this study a threshold value $\tau_1 = 22$ cm was used and an TRR of 6.92% was obtained. Because we did not acquire a standalone EX-scan, the ECR could not be estimated. 5.5b shows a central transverse slice of the back-projected image obtained from the extracted transmission data.

5.3.1.3 Reconstructed attenuation map

Figure 5.6 shows central slices of the reconstructed CT- and TEX-based attenuation maps of the brain. Table 5.3 summarizes the reconstructed attenuation coefficients for different tissues inside the brain. In this table, the unscaled $\text{TEX}_{\text{tr}}^{**}$ map without scatter compensation, the unscaled $\text{TEX}_{\text{tr}}^{*}$ map with scatter compensation and the scaled TEX_{tr} map with scatter compensation are compared to the attenuation map derived from the bilinear scaling of the CT-map for soft tissue and bone. For this purpose, soft tissue and bone regions were defined from the segmented CT image using a thresholding technique.

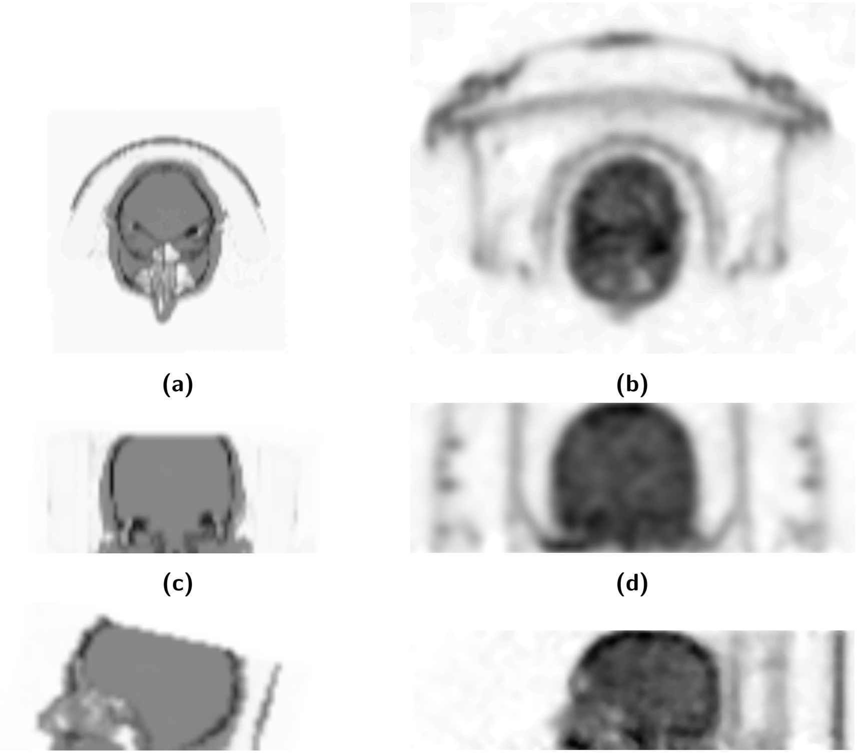

(a) (b) (c) (d) (e) (f)

Figure 5.6: Visual comparison of the TEX-based (right) and CT-based (left) attenuation map of the brain. Central transverse (a,b), coronal (c,d) and sagittal slices (e,f) are shown.

μ-values (mm^{-1})	White/grey matter	Skull
CT	0.0099	0.0116
TEX_{tr}^{**}	0.0077	0.0085
TEX_{tr}^{*}	0.0081	0.0091
TEX_{tr}	0.0093	0.0103

Table 5.3: Mean reconstructed μ-values (mm^{-1}) in VOIs defined in white/grey matter, bone structures and air cavities. (**) indicates that the attenuation map was neither scaled nor compensated for scatter. For The TEX_{tr}^{*} scatter compensation was implemented. For the TEX_{tr}-map both μ-value scaling and scatter compensation were applied.

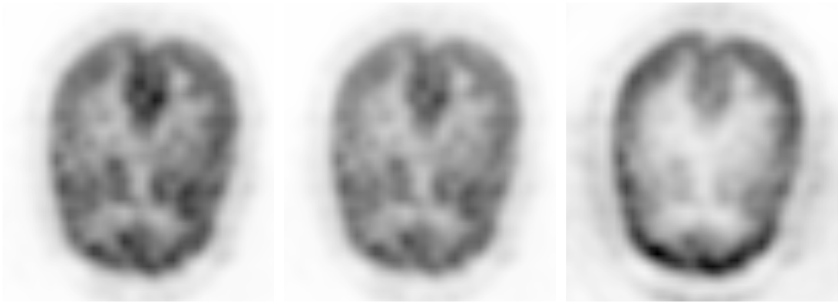

(a) **(b)** **(c)**

Figure 5.7: From left to right: transverse slice of the CT-based (a), TEX_{tr}-based (b) and non attenuation corrected (c) PET image of the brain. For the CT-based and TEX_{tr}-based AC PET images, the same thresholds for the color scaling were used. For the non attenuation corrected image the upper threshold was 4 times lower.

5.3.1.4 Reconstructed PET image

Figure 5.7 shows a transverse slice of the CT-based, TEX_{tr}-based and non-attenuation corrected PET image. A central coronal and sagittal slice of the PET/MRI image reconstructed with the non-truncated TEX-map for attenuation correction is shown in figure 5.8. A similarity above 99% was obtained for both the $\text{TEX}^{*}_{\text{tr}}$-based and TEX_{tr}-based AC PET images. A more detailed quantitative analysis is depicted in figure 5.9, where the relative error of the $\text{TEX}^{**}_{\text{tr}}$-based, $\text{TEX}^{*}_{\text{tr}}$-based and TEX_{tr}-based AC PET images compared with the CT-based AC PET image is shown.

5.3.2 Body imaging

5.3.2.1 PET/MRI and CT co-registration

Figure 5.10 shows a central transverse and coronal slice of the co-registered CT and MRI images of a thoracic study (patient 6).

5.3.2.2 Extraction of transmission data

Figure 5.11 shows a transverse slice of the estimated annihilation points derived from the TOF information. The threshold value τ_1 was set to 28.5 cm and covers a FOV marked in red. Annihilations points that occurred in the green area, were classified as transmission data. Additionally, for each

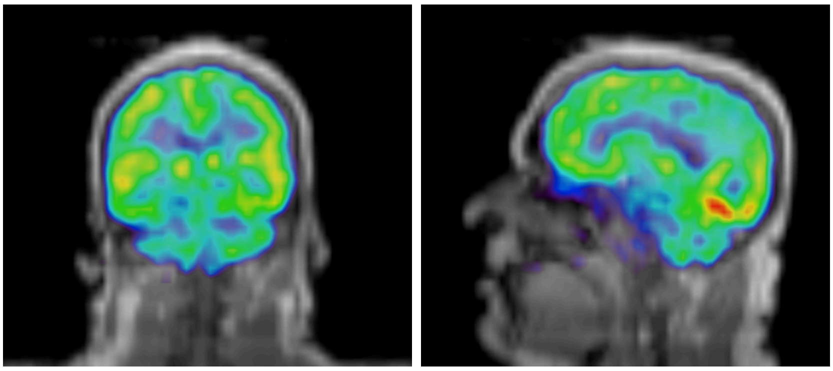

(a) (b)

Figure 5.8: Coronal (a) and sagittal (b) slice of the fused PETMRI image using the non-truncated TEX-based attenuation map for attenuation correction.

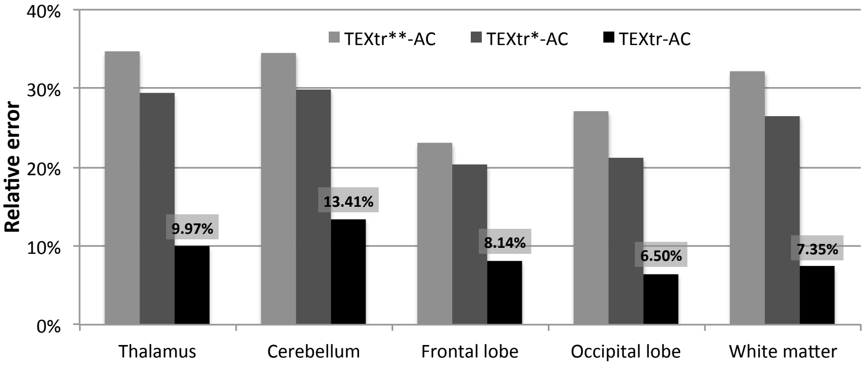

Figure 5.9: Relative comparison between the TEX-AC and CT-AC PET images for different VOIs in the brain. The unscaled $\text{TEX}_{\text{tr}}^{**}$ map, unscaled, scatter compensated $\text{TEX}_{\text{tr}}^{*}$ map and scaled TEX_{tr} map were evaluated.

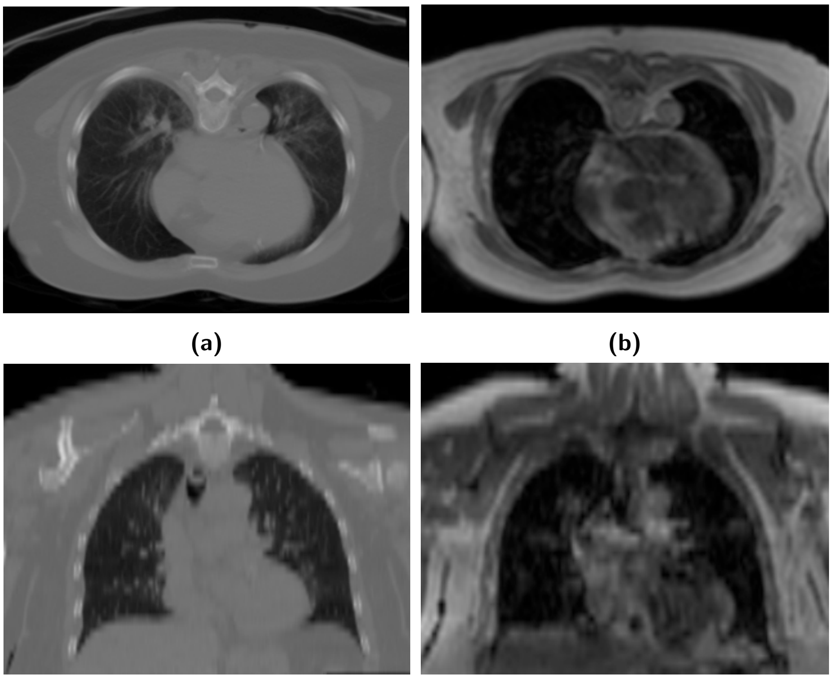

(c) (d)

Figure 5.10: Central transverse (a,b) and coronal slice (c,d) of the co-registered CT (left) and MRI (right) image of the torso of the 6th patient.

patient the TRR and ECR were measured. An overview is given in table 5.4.

Patient	TRR (%)	ECR (%)
1	8.70	0.23
2	9.20	0.58
3	9.26	0.31
4	9.25	0.44
5	9.25	0.46

Table 5.4: Transmission rejection rate (%) and emission contamination rate (%) for 5 patients. Rates are averaged over all bed positions.

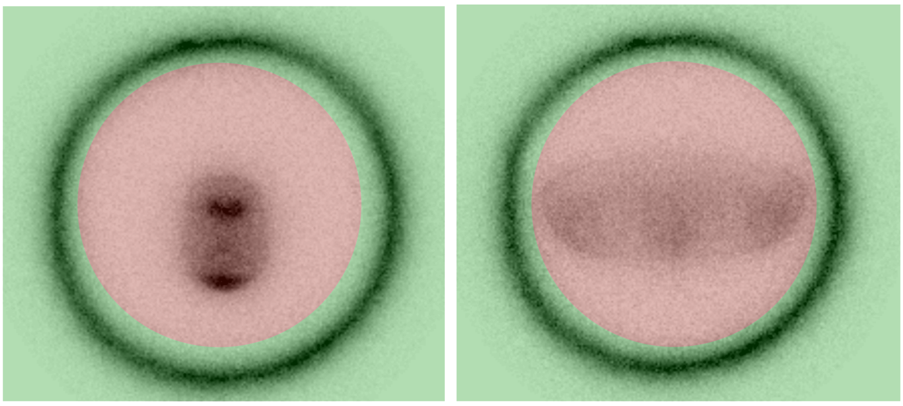
(a) (b)

Figure 5.11: Transverse slice of the estimated annihilation points derived from the TOF information. The head (a) and torso (b) region are shown. The threshold value τ_1 is also indicated.

5.3.2.3 Reconstructed attenuation maps

The mean μ-values as well as the mean intra-patient variation for lung and soft-tissue used in the Gaussian mixture models are listed in table 5.5. The effect of the scaling method is illustrated in figure 5.12, where the histograms of the unscaled (TEX*) and the scaled TEX-based attenuation maps of one patient are shown.

Joint histograms were derived by voxelwise comparison between the TEX$_{tr}$- and CT-map (figure 5.13c) and between the MR$_{tr}$ and the CT-

Modality	Lung		Soft-tissue	
	Mean	Std	Mean	Std
CT	0.0018	0.00052	0.0098	0.00023
TEX*	0.0036	0.00051	0.0083	0.00043
TEX	0.0019	0.00044	0.0098	0.00024
MR	0.0022	-	0.0096	-

Table 5.5: Mean and mean standard deviation of reconstructed μ-values (mm^{-1}) in lung and soft-tissue for CT, unscaled and scaled TEX-based attenuation map for all patients. Predefined μ-values assigned in the MR-based method are also shown.

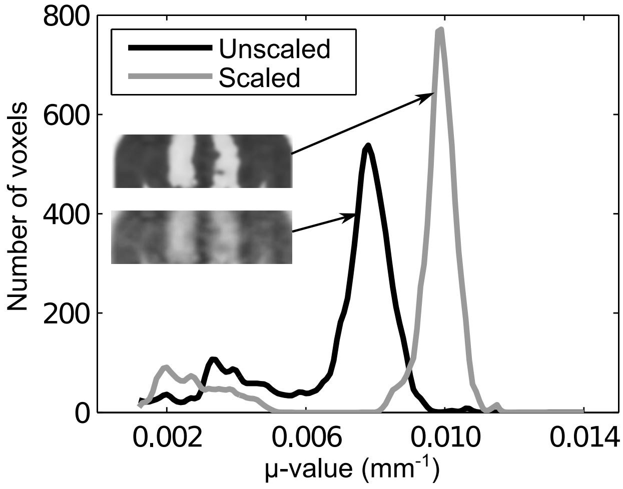

Figure 5.12: Unscaled and scaled TEX-based attenuation map and μ-value distribution using histogram matching with predefined distributions for lung and soft-tissue μ-values in both TEX and CT-based attenuation maps for one patient.

map (figure 5.13d) for all patients combined. Figure 5.13a and 5.13b show the histograms of the reconstructed $\mathrm{TEX}_{\mathrm{tr}}$ and $\mathrm{MR}_{\mathrm{tr}}$-maps, respectively. In the joint histograms, as well as in the histograms, voxels in which the CT-based attenuation coefficient was less than (0.5×10^{-4} mm^{-1}) were excluded. Finally, figure 5.14 shows a central slice of the TEX- and MR-based attenuation maps of 3 different patients.

5.3.2.4 Reconstructed PET images

An overview of the similarity between different PET images using the CT and truncated TEX or MR-based attenuation maps is listed in table 5.6. Table 5.6 also shows the similarity between the non-truncated TEX and MR-based AC PET images. Additionally, for both TEX and MRI, the similarity between the PET images reconstructed with the truncated and non-truncated attenuation maps is shown.

Next we evaluated the similarity between the CT-based attenuation corrected (AC) PET image and the PET images reconstructed using the $\mathrm{TEX}_{\mathrm{tr}}$ and $\mathrm{MR}_{\mathrm{tr}}$-maps for attenuation correction. The scatter plots in figure 5.15a-5.15e give an indication of the correlation between the reconstructed CT-based AC emission values and the $\mathrm{TEX}_{\mathrm{tr}}$ or $\mathrm{MR}_{\mathrm{tr}}$-based AC emission values.

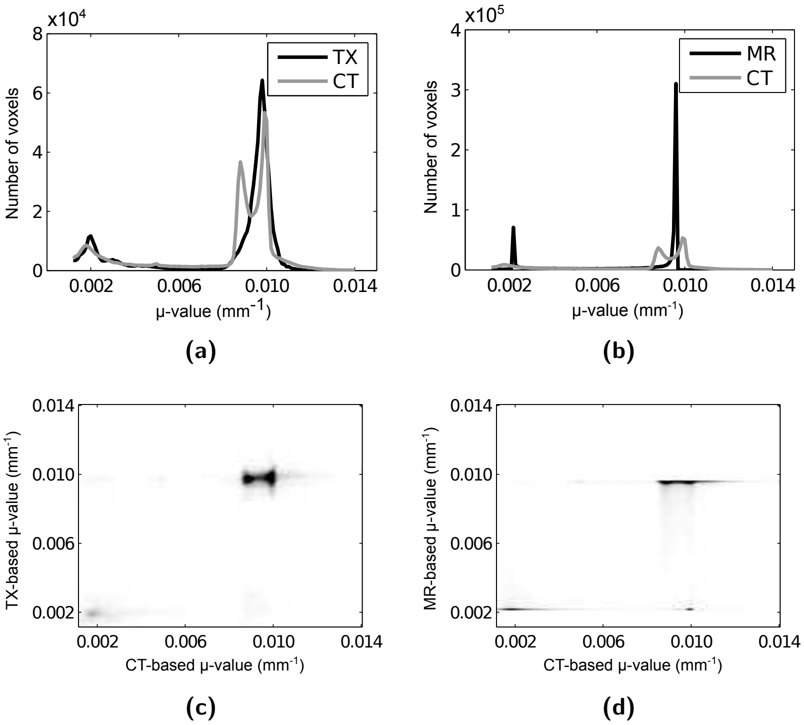

Figure 5.13: Histograms (a,b) and joint histograms (c,d) of the CT- vs TEX_{tr}-map (a,c) and CT- vs MR_{tr}-map (b,d). The joint histograms and histograms were obtained from all patient data combined.

Figure 5.15f depicts the mean percentage difference of the TEX_{tr} and MR_{tr}-based AC PET image compared to the CT-based AC PET image in VOIs in lung, soft tissue and bone.

5.4 Discussion

5.4.1 Brain imaging

Results show that the annulus-shaped transmission source can be used to obtain an attenuation map of the brain with acceptable accuracy. The method clearly distinguishes bone, air and soft tissue. Additionally, MR brain coils can be visualized and hence, the PET image can be corrected for coils attenuating the gamma radiation. Although scatter compensation

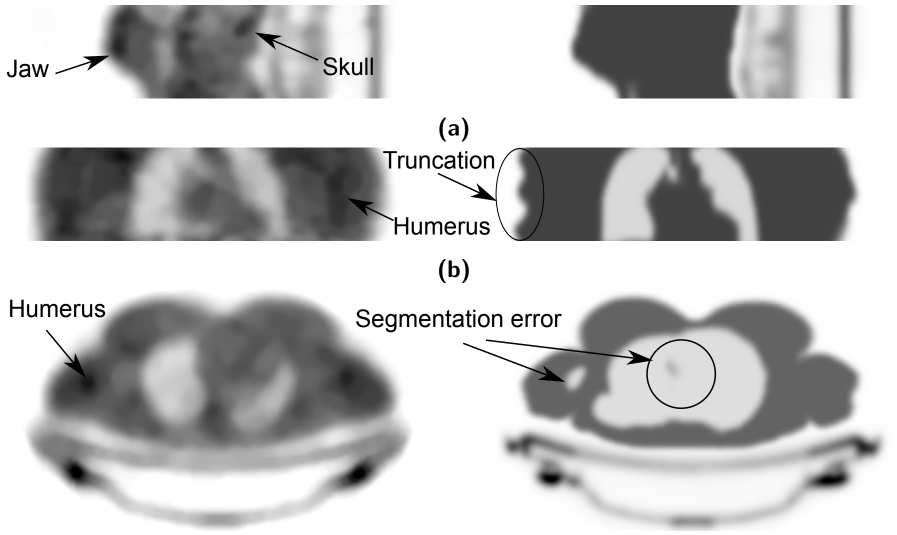

(a)

(b)

(c)

Figure 5.14: Visual comparison of the TEX-based (left) and MR-based (right) attenuation maps of 3 patients. (a) Central sagittal slice from the lower head/jaw, showing better recovery of the jaw and skull with the TEX-based method. (b) Coronal slice of the torso only shows part of the humerus in the TEX-based attenuation map while the MR-based attenuation map clearly shows truncation artifacts in the arms. (c) Transverse slice of torso indicating segmentation error in the lungs and right humerus with the MR-based method.

and μ-value scaling significantly improve the accuracy of the attenuation coefficients, absolute quantification was not obtained. For brain imaging, the accuracy is dominated by the presence of the skull. An underestimation of the attenuation coefficient was noticed in bone tissue. As a consequence, a PET quantification error between 10 and 15% was obtained for different regions inside the brain. Although CT-based attenuation correction was used as a gold standard in this work, it is not clear if the bilinear scaling causes an overestimation of CT-based attenuation coefficient of bone.

Because brain imaging typically requires a smaller FOV, the threshold value τ_1 can be lowered significantly allowing more transmission data to be extracted. A TRR of 6.9% was obtained for $\tau_1 = 22$ cm. the TRR would increase to 9.92% if τ_1 was set to 28.5 cm, the threshold used for the thoracic study.

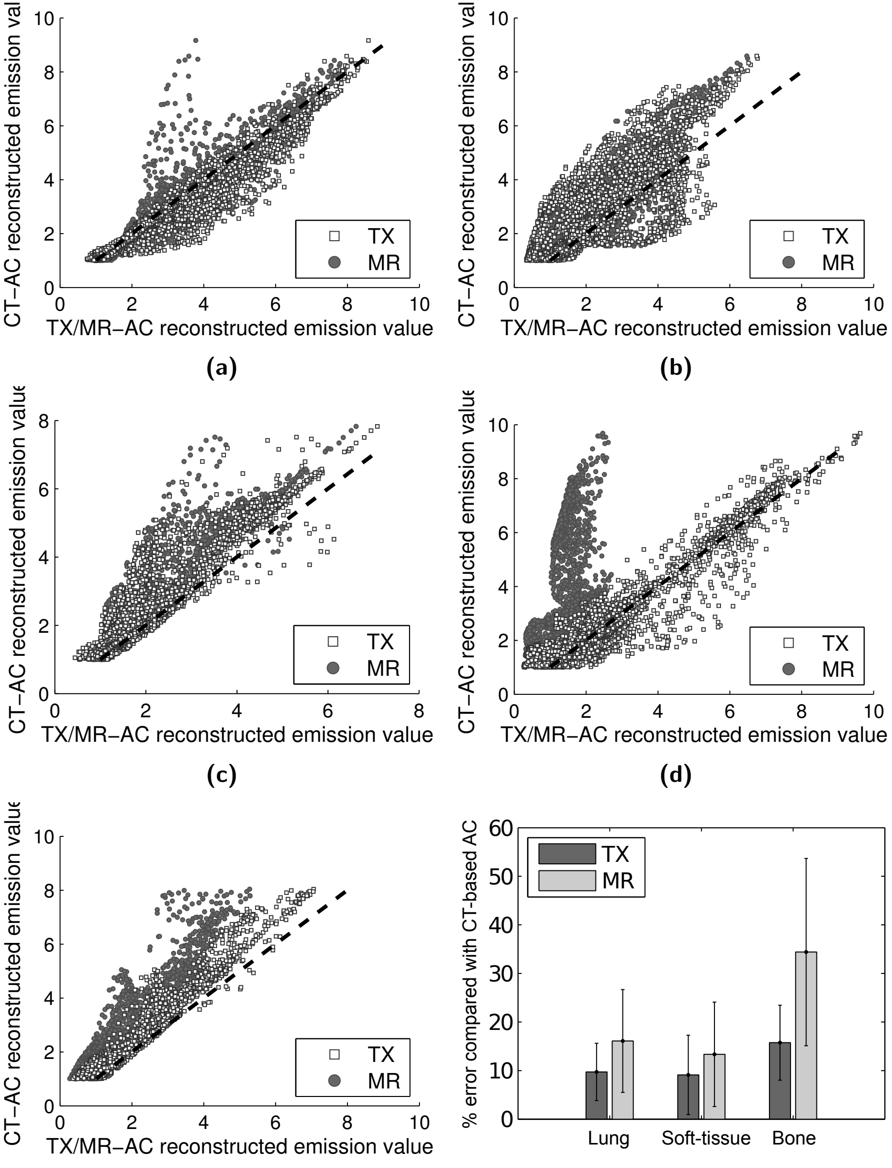

(a) **(b)**

(c) **(d)**

(e) **(f)**

Figure 5.15: Scatter plot of the CT-based attenuation corrected (AC) PET image vs TEX_{tr}-based AC and MR_{tr}-based AC PET image for patient 2-6 (a-e), Absolute mean percentage difference of reconstructed emission values of the TEX_{tr} and MR_{tr}-based AC PET image compared to the CT-based AC map (f).

PET image x	PET image y	SIM
TEX_{tr}-based AC	CT-based AC	93.01
MR_{tr}-based AC	CT-based AC	90.43
TEX_{tr}-based AC	MR_{tr}-based AC	92.23
TEX-based AC	MR-based AC	82.86
TEX-based AC	TEX_{tr}-based AC	78.78
MR-based AC	MR_{tr}-based AC	87.13

Table 5.6: First three rows: mean normalized similarity (%) between reconstructed PET images of 5 patients using 3 different truncated attenuation maps (CT-map, TEX_{tr}-map, MR_{tr}-map). Last three rows: mean normalized similarity (%) between TEX- and MR-based AC PET images and similarity between PET images reconstructed using the non-truncated (TEX-map, MR-map) and truncated (TEX_{tr}-map, MR_{tr}-map) attenuation maps. Similarities were measured over all patient data combined.

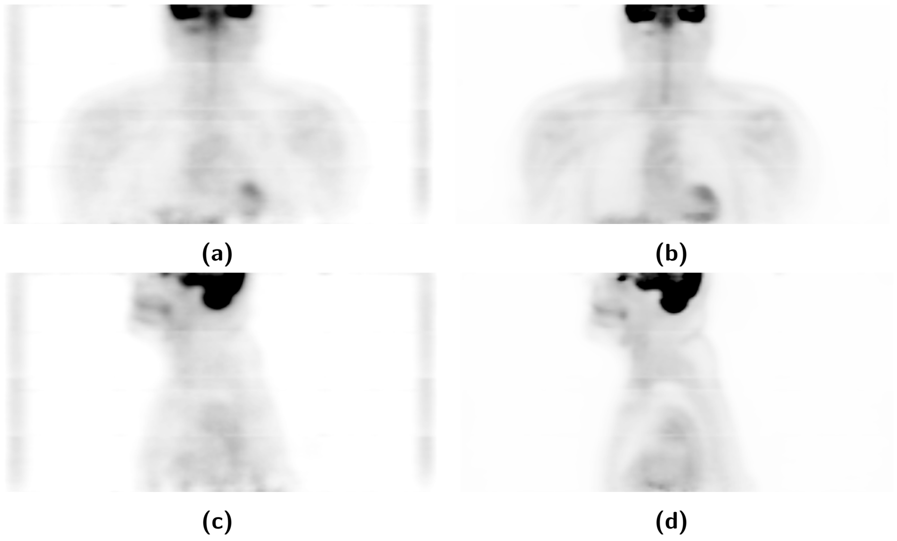

(a) (b) (c) (d)

Figure 5.16: Central coronal (a,b) and sagittal slice (c,d) of the reconstruction emission data from TEX scan using TEX-based attenuation correction (a,c), from EX scan using MR-based attenuation correction (b,d).

5.4.2 Body imaging

The results presented above demonstrate that the proposed method can be used to derive attenuation coefficients at 511 keV in thoracic imaging. The similarity measurements listed in table 5.6 and the mean percentage differences depicted in figure 5.15f indicate that the $\mathrm{TEX}_{\mathrm{tr}}$-based AC outperforms the $\mathrm{MR}_{\mathrm{tr}}$-based AC compared to CT, for all tissue-types. In bone tissue 18.7% less error is reported when using $\mathrm{TEX}_{\mathrm{tr}}$-based AC compared to $\mathrm{MR}_{\mathrm{tr}}$-based AC, while 6.2% and 2.4% less error is obtained in soft-tissue and the lung, respectively (see figure 5.15f). The absolute percentage difference between the $\mathrm{TEX}_{\mathrm{tr}}$- and CT-based AC PET images in regions of normal tracer update are in the same range of the errors reported in [139].

Figure 5.14c illustrates severe segmentation errors of lung-tissue in the areas close to the heart as well as a misclassification of the right humerus in the MR-based attenuation map of patient 4. Segmentation errors decrease correlation of the reconstructed emission value to the CT-based AC emission values as depicted in the scatter plots (see figures 5.15a-e). These errors do not occur with the TEX-based technique. Additionally, bone structures such as the skull, humerus and jawbone can be discriminated on the TEX-based attenuation maps (see figure 5.14).

The presence of MR coils during a PET acquisition can cause significant quantifications errors. Although attenuation coefficients of fixed coils can be included in the attenuation map using a template derived from a transmission or CT scan, difficulties remain when working with flexible coils. The transmission based technique described in this work can measure the attenuation coefficients for any object inside the FOV, even flexible coils. This also applies to metallic implants, which can cause streak artifacts in CT-based attenuation maps.

In clinical practice, patients usually extend beyond the FOV of the MRI scanner causing truncation artifacts in the MR-based attenuation map (see figure 5.14b) and an underestimation of the reconstructed PET uptake. This causes significant image bias near the arms. The transmission based technique does not have these issues. As shown in table 5.6 the high error between the TEX and $\mathrm{TEX}_{\mathrm{tr}}$ indicates the significant effect of truncation of the FOV on the reconstructed PET images. Additionally, as the FOV of the CT acquisitions is smaller than the FOV of the MRI, a significant error is reported between $\mathrm{MR}_{\mathrm{tr}}$- and MR-based AC PET images.

Table 5.5 shows an underestimation of the attenuation coefficient of soft tissue and an overestimation for lung tissue for the TEX-based attenuation correction compared to the predefined values used for the MR-based attenuation correction as well as the mean μ-values in the bilinearly scaled CT-based attenuation maps. An underestimation is probably caused by scatter and misclassified emission data contaminating the extracted transmission data. It is not clear at this point which effect causes an overestimation of the attenuation coefficient of lung tissue. This is possibly due to inaccuracies in the global count rate correction method used in eq. 5.3. As explained in [154], the correction factor β_{τ_2} is derived from the count rate on LORs which fall outside a FOV defined by the radius τ_2. These LORs are selected because the correction method was designed to handle count rate mismatches between the transmission and blank scan. The count rates are typically higher during the simultaneous transmission and emission scan causing more dead-time effects, leading to a loss of counts relative to the blank scan. This is however a global correction technique. The count rate decreases for LORs that pass through the patient and experience high attenuation. Therefore the correction factor β_{τ_2} might be overestimated on these LORs. As most of these LORs pass through the lungs, the multiplication by β_{τ_2} in (5.3) could cause an overestimation of the attenuation coefficient of lung tissue.

This issue is solved by applying the scaling method (see figure 5.3), which ensures that the mean TEX-based lung and soft-tissue μ-values are translated into the mean attenuation coefficients derived from the CT database composed out of 5 patients. Additionally, the scaling process reduces the noise and improves the contrast between different tissues (see figure 5.12). One of the major limitations of the scaling method is that only 5 patients were used in this study. More appropriate models could be derived using a larger database other that the 5 patients examined.

The distribution of the CT-based attenuation coefficients shown in Figures 5.13a and 5.13b clearly indicate two peaks in the soft-tissue region. Although the difference is small, classifying adipose tissue improves the accuracy of the attenuation correction [133, 172]. The distinction between fat and soft tissue is not visible in the transmission based methods (see figure 5.13a). However, the broad distribution of the TEX-based attenuation coefficients around soft tissue compensates for that.

The TRR and ECR reported in table 5.4 indicate that the amount of misclassification during the extraction of transmission data is limited. However, a slightly higher ECR value for a larger patient (patient 2) explains a local underestimation of the attenuation coefficients in regions close to the transmission source (shoulder and arms) compared to the other smaller patients. This effect will be more noticeable when the diameter of the source is reduced to fit the bore of a fully integrated PET/MRI system. These issues can be solved when more complex algorithms are used allowing the simultaneous reconstruction of emission and transmission data. Another approach is to consider alternative geometries for the transmission source such as multiple line sources (see next chapter) or partial rings.

5.5 Conclusions

In this work we have demonstrated that an annulus shaped transmission source can be used to estimate the attenuation map at 511 keV in a sequential TOF-PET/MRI system. Our results show the advantages of our method over the MRI-based two-tissue segmentation method available on the system. An average improvement in PET quantification of 6.4%, 2.4% and 18.7% was obtained in lung tissue, soft-tissue and bone tissue, respectively. Both in brain and thoracic imaging, the relative error of the transmission based technique compared to CT-based attenuation correction PET images show the highest errors in regions containing bone tissue. Hence, obtaining absolute quantification remains a challenging task.

5.6 Original contributions

The 5 thoracic studies were recently published online in the Journal of Nuclear Medicine[163]. Additionally, all patient studies, including the brain study, were presented at the PSMR conference in Elba, Italy in May 2012 [173].

Chapter 6

Transmission scanning using fixed line sources

6.1 Introduction

In the previous chapters we proposed and evaluated a technique to derive the attenuation map from a PET transmission scan using an annulus shaped phantom containing a positron emitting source. Results look promising and show how simultaneous emission and transmission imaging is possible through the use of Time-Of-Flight information. Additionally, the approach is MR-compatible and could be used in future TOF PET/MRI systems, avoiding the use of the MR system to derive the attenuation map. However, difficulties arise when accurate attenuation coefficients need to be determined. Scattered events, contamination of the misclassified emission data and count rate issues compromise the quality of the PET transmission data and inaccurate attenuation coefficients are obtained. Scattered data and emission contamination cause an underestimation of the attenuation coefficients while the use of a global count rate correction factor might cause an overestimation of attenuation coefficients as explained in the discussion of the previous chapter. Complicated correction methods are needed to compensate for these errors. In this chapter we propose to limit the influence of scatter and emission contamination by replacing the annulus shaped source with a fixed number of stationary line sources. First we will give a detailed description of the technique and how the transmission data can be extracted from a simultaneously acquired transmission/emission dataset. Next we will show how the optimal configuration and number of line sources was determined using simulated data. Finally, the method is evaluated with a simulation study close to clinical practice as well as with experimental data acquired on the $LaBr_3$ TOF PET scanner (LaPET) installed at the Radiology department of the University of Pennsylvania (UPENN), Philadelphia.

6.2 Materials and methods

6.2.1 Transmission source

A fixed number of stationary line sources are placed inside the FOV of the PET scanner close to the detectors. In order to acquire transmission data covering the whole axial FOV of the scanner, the length of line sources equals the axial length of the scanner. The gamma rays, originated from annihilations in the line sources will travel through the subject and hit the PET detectors. The attenuation coefficients can be determined by comparing the measured transmission data with the signal that is measured during a blank reference scan. Depending on whether the patient was scanned before or after injection the transmission scan is called a cold transmission scan (TX-scan) or a hot simultaneous transmission/emission scan (TEX-scan). The position, amount of activity and number of stationary line sources should be optimized to maximize the amount of transmission data passing through the subject. However, to limit the dose delivered to patients and to limit the count rate, the activity should not exceed what was commonly used with the annulus shaped transmission source. A possible configuration is shown in figure 6.1. As we will see later, the use of line sources improves the selection of the transmission data, hereby removing a significant fraction of scattered and/or emission data. A major difficulty with the use of stationary line sources is that not all voxels within the reconstruction matrix will be equally sampled. Insufficient sampling can lead to artifacts which requires special treatment. Later in this chapter we will see how these artifacts can be removed to ensure similar quality compared to the annulus-based technique.

6.2.2 Extraction of transmission data

Before the attenuation map can be derived, the transmission data need to be extracted from the simultaneous transmission/emission dataset. As proposed previously, TOF information can be used. However, when the transmission data is acquired with a fixed number of stationary line sources

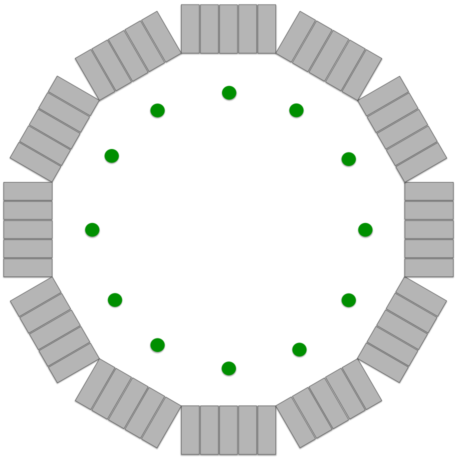

Figure 6.1: 12 Stationary line sources positioned inside the FOV of a PET scanner. In this situation a line source is placed in front of each detector block. The activity, location and number of line sources should be optimized to ensure accurate attenuation coefficients are obtained.

the extraction process can be improved by also ignoring all events which do not pass close to any line source (see figure 6.2). Because the length of the line sources equals the axial length of the scanner and they are parallel with

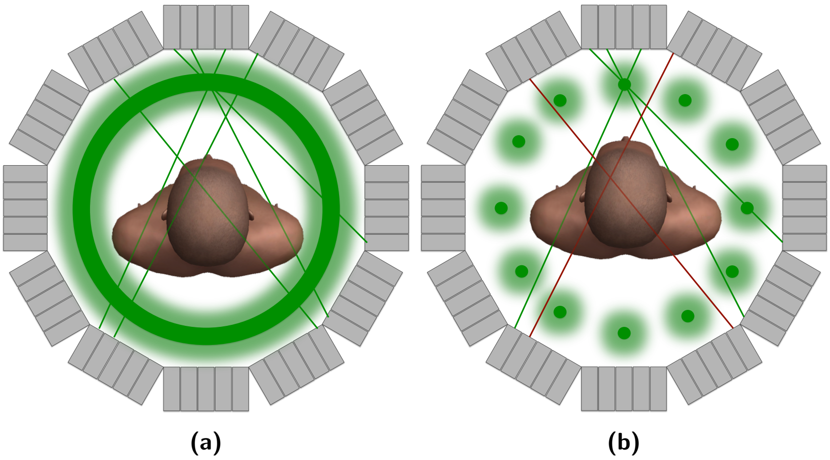

Figure 6.2: The previously defined TOF-based extraction accepts all events whose estimated annihilation point falls outside a cylinder with radius τ_1 (a). LOR-based selection improves the extraction by ignoring the events marked in red (b).

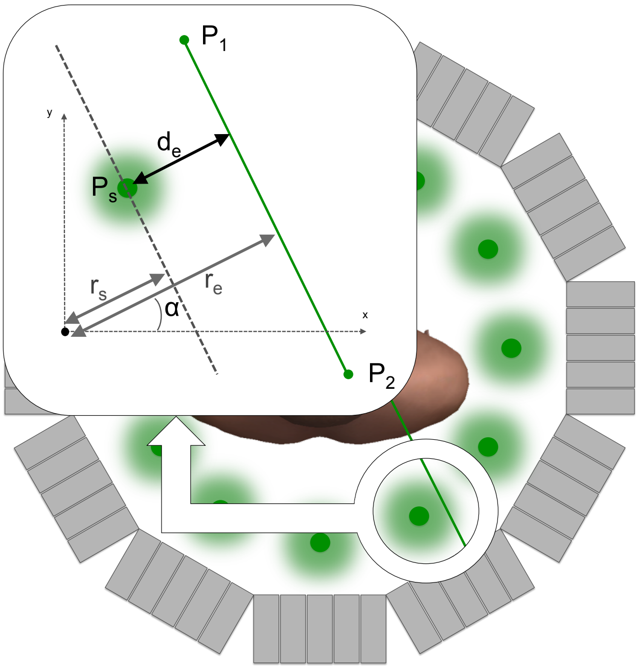

Figure 6.3: Distance d_e between event $\{P_1, P_2\}$ and closest line source.

the central axis, each line source can be determined by its coordinates in the XY-plane. For each event e the distance d_e to the closest line source (x_s, y_s) is determined (see figure 6.3) :

$$d_e = |r_s - r_e|, \tag{6.1}$$

with

$$\begin{aligned} r_s &= x_s \cos\alpha + y_s \sin\alpha \\ r_e &= x_1 \cos\alpha + y_1 \sin\alpha \\ \alpha &= \arctan -\frac{x_2 - x_1}{y_2 - y_1} \end{aligned} \tag{6.2}$$

$$\tag{6.3}$$

and (x_1, y_1) and (x_2, y_2) the crystal coordinates of the event in the XY-plane.

An event is classified as transmission data if the distance d_e is smaller

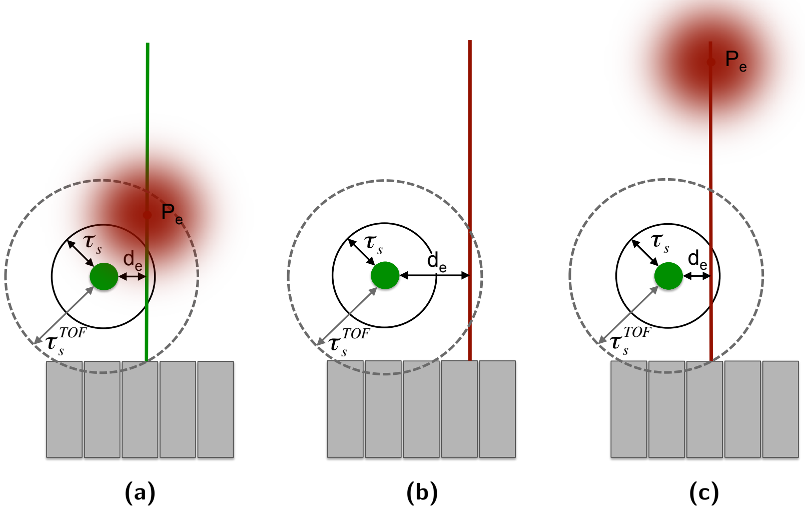

Figure 6.4: Three situations to clarify the extraction process : Event (a) is classified as transmission data because the distance d_e to the closest line source is smaller than τ_s and the estimated emission point P_s is close to the line source. Event (b) is rejected because d_e is too large. Event (c) is rejected because no line source closer than d_e is found in the direct neighborhood (cylinder with radius τ_s^{TOF}) of the estimated emission point P_e.

than a given threshold τ_s. When TOF-information is available, a TOF-based extraction as described in chapter 3 is also applied. Additionally, TOF-information is used to confirm that the emission originated closer than distance τ_s^{TOF} to the selected line source. If not, the event is only accepted if another line source at a distance closer than τ_s from the event is found. Both TOF and LOR-based extraction methods are complementary and improve the classification when combined. Figure 6.4 shows one situation where the event is classified as transmission data and two situations in which an event is rejected.

Three thresholds need to be determined: τ_1 for the TOF-based extraction, τ_s and τ_s^{TOF} for the LOR-based extraction of transmission data. Similar to the annulus-based method, we evaluated the classification error using the Transmission Rejection Rate and the Emission Contamination Rate. Emission events originating close to the threshold radius τ_1 will only be classified as transmission if the event also passes closer than τ_s for at least one line source. τ_s should be chosen large enough to allow acceptance of true events which suffered from parallax errors or acollinearity. However, larger values for τ_s will increase the contamination of scattered or emission events in the transmission data. τ_s^{TOF} depends on the timing resolution of the scanner and should be small enough to determine the line source in which the annihilation occurred if the LOR passes close to at least two line sources.

6.2.3 Derivation of the attenuation map

Similar to the case where an annulus shaped transmission source was used, the attenuation map can be derived using the gradient descent algorithm proposed in chapter 3:

$$\mu_j^{k+1} = \mu_j^k + \alpha\left(1 - \frac{\sum\limits_{e \in \widehat{\mathrm{TX}}} c_{i_e j} w_e}{\beta_{\tau_2} \sum\limits_{e \in \widehat{\mathrm{BX}}} c_{e_i j} a_i^k w_e}\right) \tag{6.4}$$

Where $\widehat{\mathrm{BX}}$ and $\widehat{\mathrm{TX}}$ represent the blank and transmission data extracted from the acquired PET data using both LOR and TOF-based extraction rules.

6.3 Simulation study

The transmission-based technique was evaluated with simulation studies in GATE and compared with the transmission-based technique using an annulus shaped source. For the PET scanner, we have chosen to use a model of the LaPET scanner installed at the radiology department at UPENN, Philadelphia. This scanner was later used to acquire experimental data for further validation. The simulations allow us to derive the optimal number of stationary line sources, their configuration and the amount of activity needed. Subsequently, the performance of the LOR and TOF-based extraction process was evaluated and compared with the annulus-based approach. Finally, the method was illustrated with a simulation study using the digital NCAT phantom. An overview of the GATE simulations can be found in table 6.1. Notice that similar simulations were performed in chapter 3 for the validation of the annulus-shaped transmission-based method.

Scan type	Transmission source	Phantom (type, total activity)
E_{Nema}	-	NEMA cylinder, 50-1050 MBq
B	0-148 MBq 30-35 cm radius 6-24 line sources	-
TE_{Nema}	0-74 MBq 30-35 cm radius 6-24 line sources	NEMA cylinder, 500 MBq
T_{ncat}	18 MBq, 35 cm radius 6-24 line sources	NCAT phantom, 0 MBq
TE_{ncat}	18 MBq 35 cm radius 24 line sources	NCAT phantom, 44.5 MBq
TE_{ncat2}	18 MBq 35 cm radius Annulus source	NCAT phantom, 44.5 MBq

Table 6.1: Blank scans (B_x), simultaneous transmission/emission scans (TE_x) and emission scans (E_x) using GATE. All scans had an acquisition time of 3 minutes.

6.3.1 PET count rate performance

The LaPET scanner comprises a full ring of 24 blocks of detectors. The radius is 93.3 cm and each block contains a 27x60 array of 4x4x30 mm^3 $LaBr_3$ (5% Ce) crystals. To compensate for the lower stopping power compared to the Gemini TF PET scanner, the $LaBr_3$ system has a longer FOV (25 cm) and longer crystals (30 mm). The crystals are coupled via a continuous light guide to a hexagonal array of PMTs in the same way as in the Gemini TOF PET system, however high light output and fast decay allowed the use of the larger 51mm-PMTs. Studies show that with this setup a timing resolution of 313 ps FWHM and an average energy resolution at 511 keV of 5.1% FWHM can be achieved [174]. Additionally, an integration time on photon detection of 50 ns is reported [174, 175], which was modeled in GATE with a paralysable dead-time of 50 ns on the singles chain. A paralysable coincidence dead-time of 120 ns was included. GATE simulations of type E_{Nema} were done in accordance with the NEMA NU 2-2001 protocols [149]: A 20 x 70-cm cylindrical phantom containing a 70 cm long line source at 4.5 mm of center was modeled in GATE. Injected activities range from 50 to 1050 MBq.

6.3.2 Transmission source

The presence of the line sources inside the FOV of the PET scanner is expected to influence the count rate performance of the system. Different parameters should be determined to minimize this influence without losing sufficient transmission data. These parameters include the number of sources, their location relative to the detector, the radius at which to place the sources and the amount of activity inside the sources. The count rate performance of the system during a blank scan and simultaneous emission/transmission scans of type TE_{Nema} were evaluated in function of the different design parameters. Similar to the E_{Nema} simulations, a 20-cm-diameter cylindrical phantom containing an off-center line source was used.

6.3.3 NCAT phantom study

Finally, the method was validated with a simulation study using the digital NCAT phantom (TE_{ncat}, TE_{ncat2}) [2]. Thirty-two 4 mm slices of the torso were segmented into different tissue types. The phantom was filled with 6.5 MBq/kg of ^{18}F-FDG, 60 minutes prior to scanning.Table 3.2 shows the FDG-PET uptake values (SUV) and attenuation coefficients assigned to each tissue. A central slice of the tracer distribution and attenuation map is shown in figure 6.6. The NCAT phantom has a maximum lateral outside dimension of 57 cm and weighs 10 kg.

6.4 Experimental study

Experiments were performed on the $LaBr_3$ prototype scanner. The system has excellent timing properties and is equipped with a rotation device which can be used to acquire accurate transmission maps with a rotating ^{137}Cs source. 24 line sources were mounted on a wooden template as shown in figure 6.5. The template is then fixated to the rotating device. This allows us to change the angular position of the line source relatively to the PET detectors. The sources were positioned at a 32-cm of center radius. First a blank reference scan was acquired. For this purpose the patient bed was moved outside the FOV of the PET scanner. Subsequently, an

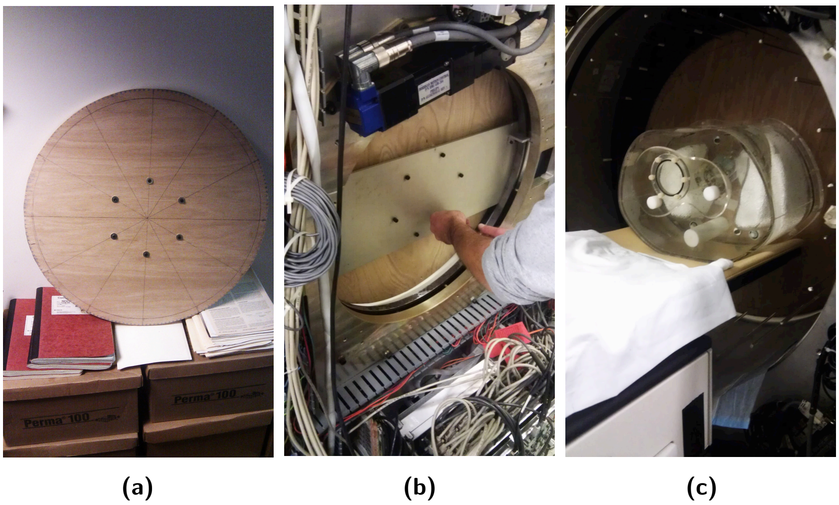

Figure 6.5: Positioning of the line sources inside the FOV of the LaPET scanner. First, 24 holes were drilled in a wooden template at 32 cm off-center radius (a). Next, the template was mounted on the rotating device of the LaPET scanner (b). Finally, the line sources can be fixated in the holes of the wooden template.

anthropomorphic phantom (see figure 4.11), filled with water was placed on the patient table and moved inside the PET bore. A stand-alone TX scan was acquired. Finally, the phantom was injected with approximately 128 MBq of ^{18}F-FDG and a simultaneous TEX scan was acquired. All acquisitions had a duration of 15 minutes.

6.5 Results

6.5.1 Simulation study

6.5.1.1 PET count rate performance

Figure 6.7 summarizes the results from the count rate simulations for a 20 x 70-cm cylindrical NEMA phantom. The NEC curve shows a peak value of 83.3 kcps which occurs at an activity of 15.92 KBq/ml. No studies in literature have been found to confirm these results. However, similar performance was obtained with the Gemini TF PET system reported in chapter 3. We believe this model represents a typical clinical PET system with realistic count rate performance and can therefore be used to prove the feasibility of this transmission-based technique with simulation studies.

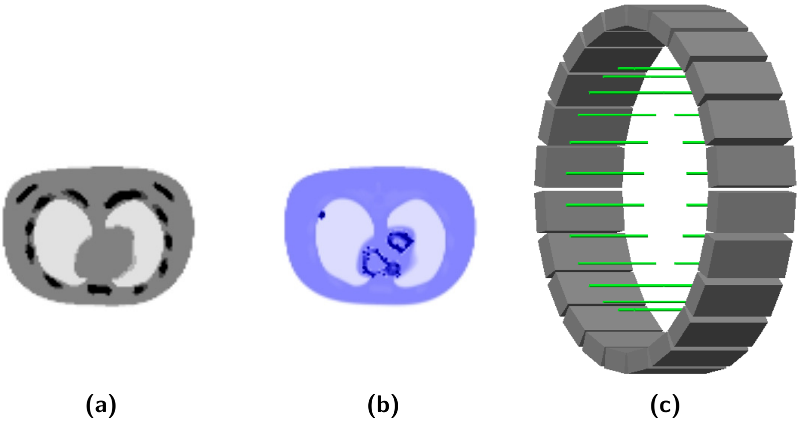

Figure 6.6: Transverse slice of the NCAT attenuation (a) and emission distribution (b). 24 line sources positioned inside the FOV of a PET Scanner based on the $LaBr_3$ PET design (c).

6.5.1.2 Transmission source

Figure 6.8 shows the true count rate performance of the blank reference scan for different configurations. Changing the position of the line sources

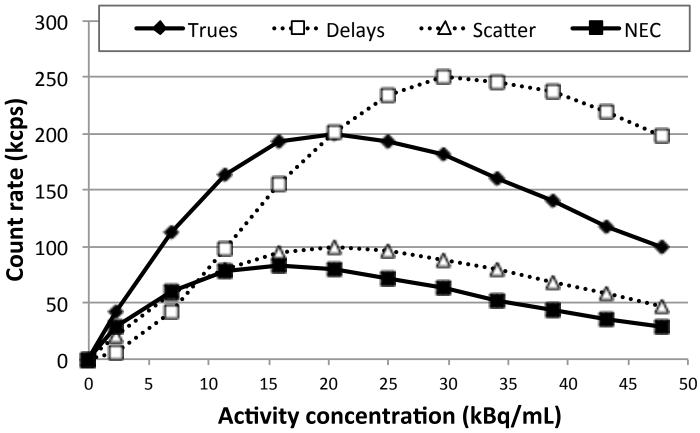

Figure 6.7: True, scattered and random count rate performance of GATE $LaBr_3$ PET model using the NEMA protocol.

μ-map	Scan type	TX-source parameters	TX extraction method
M_1	$\mathrm{T_{ncat}}$	6 line sources	-
M_2	$\mathrm{T_{ncat}}$	12 line sources	-
M_3	$\mathrm{T_{ncat}}$	24 line sources	-
M_4	$\mathrm{TE_{ncat2}}$	Annulus source	TOF
M_5	$\mathrm{TE_{ncat}}$	24 line sources	TOF
M_6	$\mathrm{TE_{ncat}}$	24 line sources	TOF + LOR selection

Table 6.2: 6 attenuation maps reconstructed from the $\mathrm{T_{ncat}}$,$\mathrm{TE_{ncat2}}$,$\mathrm{TE_{ncat}}$ data sets.

relative to the center of the FOV, as well as the number of line sources does not have a significant influence on the amount of true coincidences acquired. However, as we describe later in this chapter, increasing the number of line sources is desirable to improve the sampling. Additionally, the position of the line sources will also influence the sampling and the accuracy of the extraction of transmission data. The influence of the presence of the line sources on the true count-rate performance during a simultaneous transmission/emission scans of type $\mathrm{TE_{Nema}}$ is shown in figure 6.9. Increasing the transmission (TX) activity in a simultaneous transmission/emission scan will influence the count rate performance of the emission. In our work the total activity was 18 MBq of FDG. The emission count rate drops to 84% of the count rate obtained without the transmission source.

6.5.1.3 NCAT phantom study

In this section we present the results obtained from a simulation study using NCAT digital phantom. First we evaluated the influence of the number of line sources on the accuracy of the reconstructed attenuation maps using only a cold transmission scan of type $\mathrm{T_{ncat}}$. In a second part, the TOF and LOR based extraction of the transmission data was evaluated and compared with the annulus-shaped method. For this purpose simulations of type $\mathrm{TE_{ncat}}$ and $\mathrm{TE_{ncat2}}$ were done. In total 6 attenuation maps were derived which are summarized in table 6.2. No noise regularization was applied.

Transmission scanning

For the first three attenuation maps, transmission scans of type $\mathrm{T_{ncat}}$ were acquired (see table 6.2). No TX extraction method is required as only transmission data is acquired. The accuracy of the reconstructed attenua-

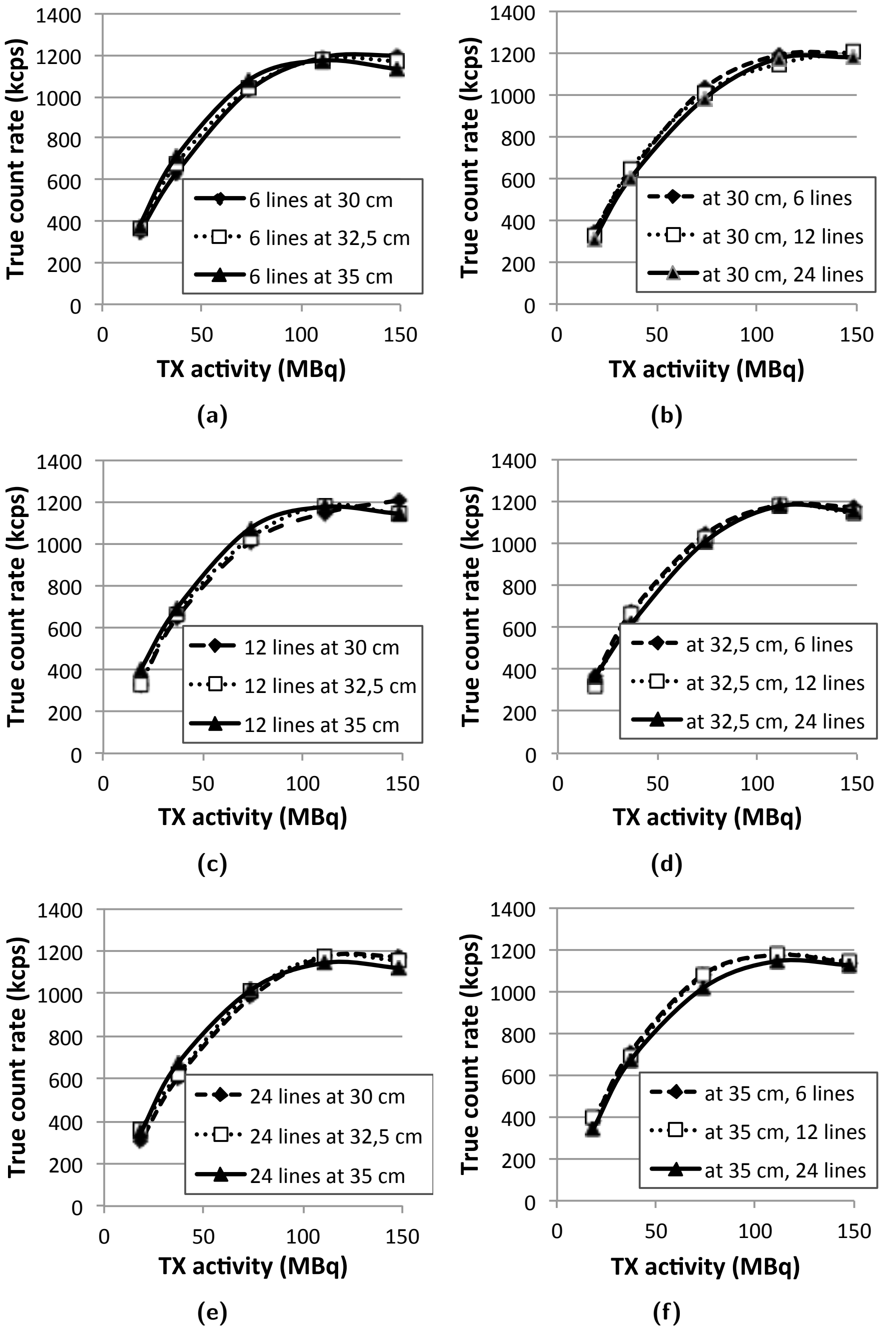

(a) (b)

(c) (d)

(e) (f)

Figure 6.8: True count rate performance of the blank reference scan for different configurations. In the left images, the number of line sources was fixed (6 in (a), 12 in (c) and 24 in (e)) and the position of the line sources varied from 30 to 35 cm. In the right images the position of the line sources was fixed (30 cm in (b), 32.5 cm in (d) and 35 cm in (f)) and the influence of the number of line sources on the true count rate in each configuration was determined.

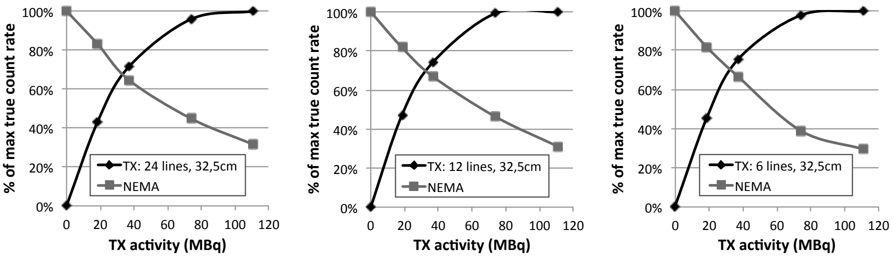

(a) (b) (c)

Figure 6.9: True NEMA emission count rate and true transmission count rate in function of the transmission activity level during a TE_{Nema} scan for a different number of line sources. The transmission count rate was normalized to the count rate simulated at a TX activity level of 100 MBq. The NEMA emission count rate was normalized to the count rate simulated during an E_{Nema}-scan with an activity level of 500 MBq.

tion coefficients was evaluated for transmission scans with 6, 12 and 24 line sources respectively (see figure 6.10 and 6.11). For this purpose VOIs of 4 cm^3 were defined for each relevant tissue type.

Simultaneous transmission and emission imaging

Simultaneous transmission and emission data was acquired using both the annulus-shaped transmission source (TE_{ncat2}) and the line sources (TE_{ncat}). First, we evaluated the different approaches to extract the transmission data from the dataset. Figure 6.12 shows the fraction of emission and scattered

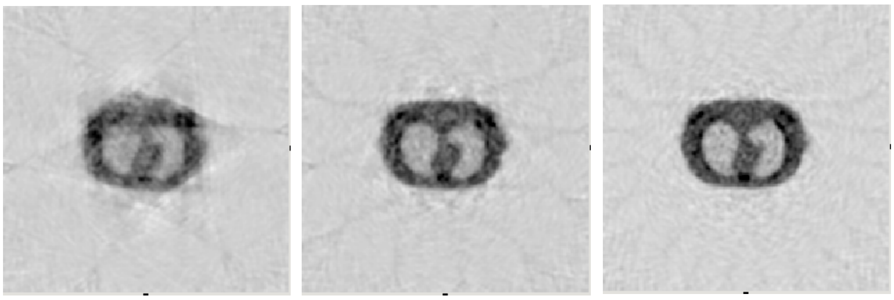

(a) (b) (c)

Figure 6.10: Transverse slices of the reconstructed attenuation maps M_1, M_2 and M_3. The transmission data was acquired with a T_{ncat} scan using 6 (a), 12 (b) and 24 (c) line sources respectively.

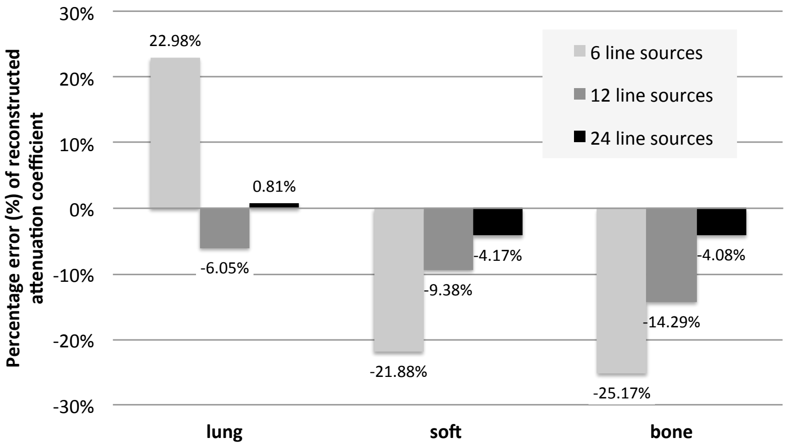

Figure 6.11: Error (%) of reconstructed attenuation coefficients compared to the real values for three tissue types.

data falsely classified as transmission data. Both the influence of the design of the transmission source as well as the extraction process are indicated. Additionally, an ERC of 1.13% and TRR= 0.98% was obtained when only TOF information was used for the extraction of the transmission data. When LOR-based information was included, the ECR improved to 0.45% while the TRR increased to 3.61%.

Finally, three attenuation maps M_4,M_5 and M_6 were reconstructed (see table 6.2). Mean percentage differences compared to the correct attenuation coefficients were calculated an are depicted in figure 6.13. A transverse slice of attenuation maps M_3, M_5 and M_6 is shown in figure 6.14.

6.5.2 Experimental study

In total four attenuation maps were reconstructed from the data acquired on the LaBr_3 PET scanner. Table 6.3 gives an overview. In all attenuation maps noise regularization was applied. The first two maps were derived from the stand alone TX scan using respectively all data and the transmission data extracted using the LOR-based method. The third and the fourth map were derived from the simultaneous transmission and emission scan. For the third map, the transmission data was extracted using the TOF-based method. In the fourth reconstruction the transmission data was extracted

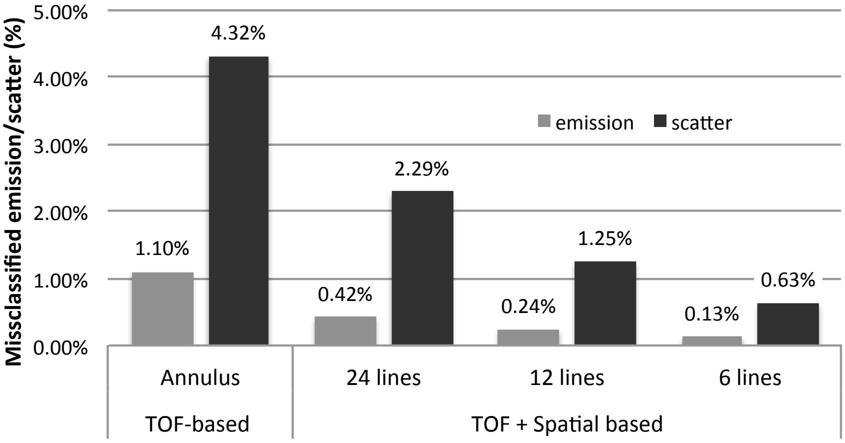

Figure 6.12: Percentage of emission and scattered events classified as transmission data.

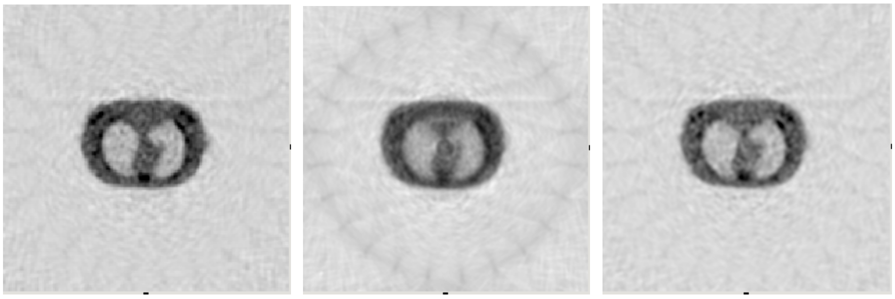
(a) (b) (c)

Figure 6.13: Transverse slices of the reconstructed attenuation maps M_3, M_5 and M_6 using 24 line sources: a T_{ncat} scan containing only transmission data (gold standard)(a) ; a TE_{ncat} scan where the TX data was extracted using only TOF information (b);TE_{ncat} scan where the TX data was extracted using both TOF as LOR information (c).

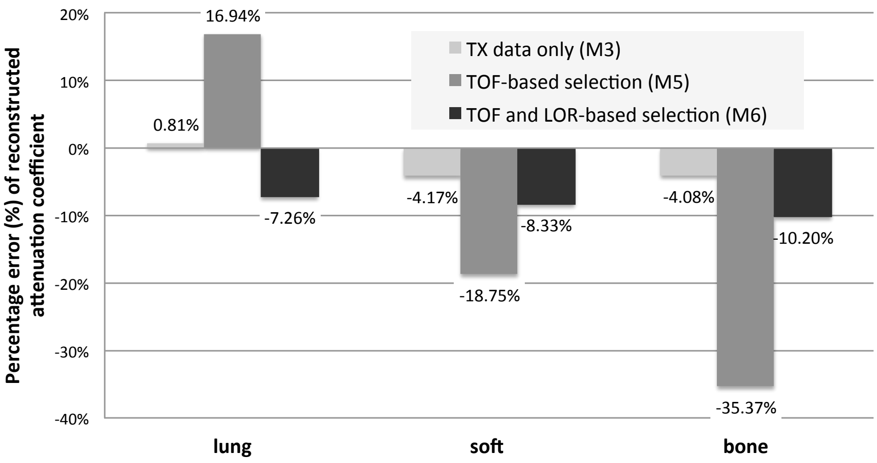

Figure 6.14: Percentage error of reconstructed attenuation coefficients compared to the real values for three tissue types.

using both TOF and LOR-based information.

6.5.2.1 Reconstructed attenuation maps

Central transverse slices of the reconstructed attenuation maps are shown in figure 6.15. Notice the ringing artifacts that arise in images 6.15a and 6.15c. In the simulation study, similar artifacts are noticed in figure 6.13b. Contrary to the annulus-based method, a non-uniform sampling of the FOV occurs when line sources are used. These uniformities will become visible when $\hat{t}_i$ and $\hat{b}_i$ differ more than just attenuation. Therefore, these rings disappear almost completely when the LOR-based extraction of transmission

μ-map	Scan type	TX extraction method
M_7	TX	No extraction
M_8	TX	LOR-based
M_9	TEX	TOF-based
M_{10}	TEX	TOF + LOR-based

Table 6.3: 4 attenuation maps reconstructed from the TX and TEX data acquired on the LaPET scanner.

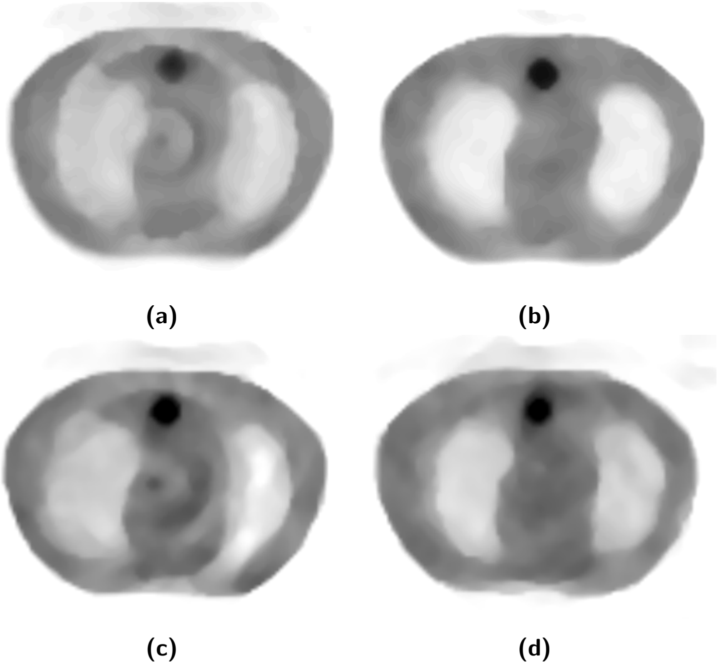

Figure 6.15: Central transverse slice of the reconstructed attenuation maps from table 6.3: M_7: TX-based without LOR-based extraction (a), M_8: TX-based with LOR-based extraction (b), M_9: TEX-based with TOF-based extraction only (c) and M_{10}: TEX-based with both TOF and LOR-based extraction (d).

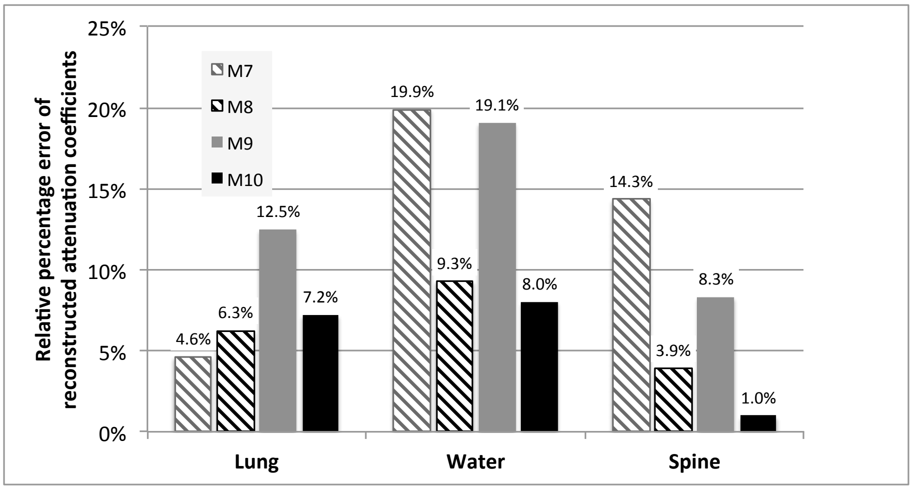

Figure 6.16: Error (%) of reconstructed attenuation coefficients for the M_7, M_8, M_9 and M_{10} maps from table 6.3.

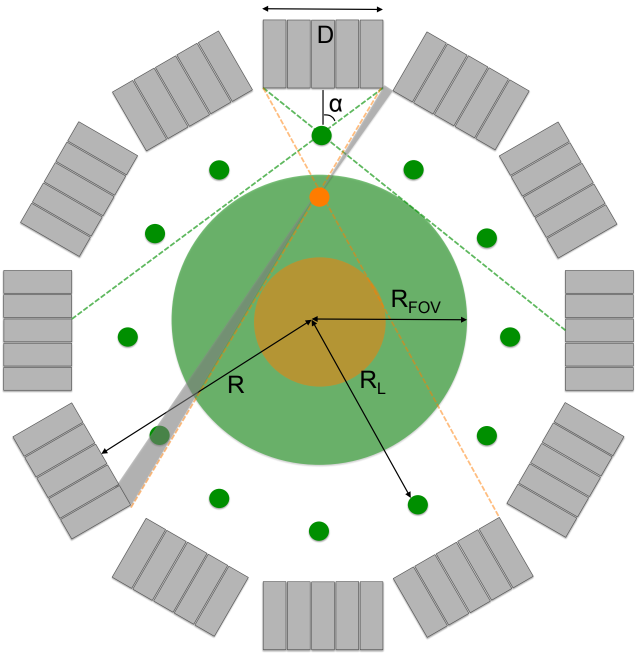

Figure 6.17: Maximum FOV for given line source positions (orange or green) with sampling artifacts caused by the gaps between the detectors (gray area). If the line sources are positioned at the orange spot, a relatively large under-sampled area (gray zone) will cause artifacts in the reconstructed attenuation map. These can be avoided by placing the line source closer to the detector (green spot).

events is applied. The reconstructed attenuation maps were evaluated in VOIs defined in the lungs, water container and the spine insert. Figure 6.16 shows the relative error of the reconstructed attenuation coefficients compared to the attenuation coefficients derived from a CT scan.

Correction for under-sampled voxels

Due to the gaps in between the detector blocks each line source will not sample the whole FOV of the scanner. The gaps are magnified when back projected in image space and cause an under-sampled area in the image space as shown in figure 6.17. Although each voxel is sampled by at least half the number of line sources, sampling artifacts might be noticeable and disturb the image quality if the statistics in both the blank and the transmission scan are low.

Given the length D of the detector blocks, the position of the line sources

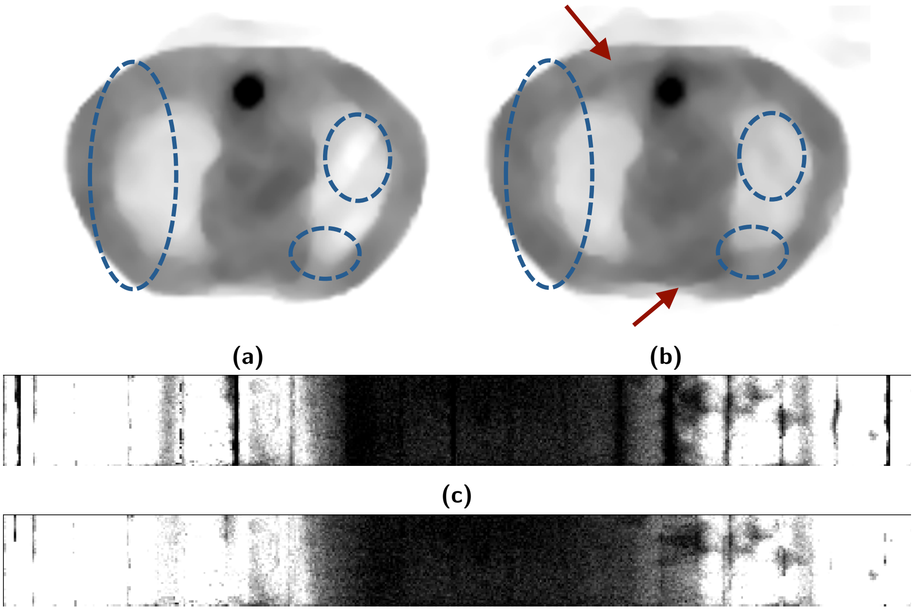

(a) (b)

(c)

(d)

Figure 6.18: Top: reconstructed attenuation map M_{10} without interpolation (a) and reconstructed attenuation map M_{10} with interpolation (b). The erroneous regions due to the under sampling are indicated with blue spheres. The errors introduced by the interpolation are indicated with the red arrows. Bottom: detected counts from line source 0: matrix representation of detections before interpolation (c), matrix representation after interpolation (d).

R_L and the radius R of the scanner, the maximum FOV which is unaffected by artifacts caused by under sampling can be derived as follows:

$$R_{\text{FOV}} = \frac{D \cdot R_L \cdot \cos(\alpha)}{2(R - R_L)} \tag{6.5}$$

The artifact worsens when the detectors at the border of the PET modules have a decreased detection efficiency. In order to remove the artifact, the data was first reorganized as follows: for each line source a matrix is defined. In this matrix all the projections through the line source are stored. Each projection bin of the matrix is defined by 3 parameters: c_1, r_1 and r_2, where c_1 and r_1 are the crystal number and ring number of the photon hit farthest away from the line source and r_2 the ring number of the photon hit closest to the line source. Because the location of the line source is known, c_2 is not required. All events that pass through the line source are stored in this matrix. Second, for each matrix the under-sampled areas are detected using a thresholding technique. The missing data is then obtained from the bins surrounding the under-sampled areas. When analyzing this neighborhood, we gather statistics such as the fraction of non-zeros elements and the mean and standard deviation of the non-zeros. From these statistics, each bin within the under-sampled area is resampled. Figure 6.18 shows the matrix for line source 0 before and after interpolation as well as the corresponding reconstructed attenuation maps.

6.6 Discussion and conclusion

The use of a positron emitting transmission source allows to estimate the attenuation map and correct for attenuation in TOF PET systems. However, some major drawbacks remain. Scattered and emission data contaminate the transmission data and inaccurate attenuation coefficients are obtained. While correction methods were used for the annulus-shaped method, in this chapter we illustrated how a significant part of the image degrading effects can be reduced by using a fixed number of stationary line sources. A simulation study of a simultaneous transmission/emission scan using 24 line sources and a digital torso phantom illustrates that the fraction of scatter, contaminating the transmission data, is 46.9% less compared to the annulus-shaped method, where only TOF-information is used to extract the transmission data. Additionally, while 1.1% of the emission data is misclassified in the annulus-based method, only 0.42% is misclassified when line sources are used and the TOF-based extraction is improved with the LOR-based extraction procedure. Results also show how the accuracy of the reconstructed attenuation coefficients improves with the proposed LOR-based extraction method. Visual inspection of the attenuation maps in figure 6.10 demonstrate that 24 line sources are required to obtain good image quality. A more quantitative investigation is illustrated in figure 6.11 were the relative errors of the attenuation coefficients in the lungs, bone and soft tissue are high ($> 20\%$) when 6 line sources are used and relatively high ($> 5\%$) when 12 line sources are used.

The results obtained from the experimental data also illustrate how the LOR-based extraction of transmission events improves the accuracy of the reconstructed attenuation maps. However, it is important to mention that better results were obtained for stand-alone annulus-based TX scanning when the data was corrected for scattered transmission events using the SSS method. Compared to the annulus-based method, the use of line sources is therefore more interesting when the transmission data and emission data are acquired simultaneously. In this case the effect of emission contaminating the transmission data can be reduced significantly using the LOR-based extraction.

All data acquisitions of the phantom study had a duration of 15 minutes. This is three times more than the acquisition time commonly used during our annulus-based phantom experiments. The acquisition time should be limited in clinical practice. This can be done by increasing the activity. However, care should be taken when increasing the activity as dead time effects will occur more often.

The reconstructed attenuation maps depicted in figure 6.13b, 6.15a and 6.15c show how ringing artifacts arise caused by the non-uniform sampling of the image space when line sources are used. Although the presence of these artifacts are significantly reduced when the LOR-based extraction is applied, some additional artifacts arise due to insufficient data collection at the border of the PET detector modules as well as the presence of the gaps limiting the FOV of the method. These artifacts might cause diagnostic problems when interpreting the final PET images. We showed how the reconstruction can be improved by reorganizing the data and perform interpolation prior to the reconstruction. However, some distortions remain or the interpolation might introduce additional artifacts. We suggest to improve the sampling by placing the line sources closer to the detectors to enlarge the FOV of the transmission-based technique.

In conclusion, improvement in accuracy of the attenuation coefficients was obtained by replacing the annulus shaped transmission source with a fixed number of line sources. Further research is needed to avoid sampling artifacts degrading the image quality and the final PET quantification.

6.7 Original contributions

The simulation study as well as preliminary results from the phantom study were presented at the PSMR PET/MR workshop in Aachen, Germany [176].

Chapter 7

General conclusion

In this chapter we give a general overview of each chapter and the most important results obtained during this work. For some remaining issues a strategy for future research will be presented. We will close this chapter with a final conclusion.

7.1 Summary

In chapter 2 we gave an overview of the imaging techniques relevant for this work. In the first part, Positron Emission Tomography (PET) was introduced. PET imaging is based on the tracer principle, which states that an atom in a molecule which participates in an organism's physiological processes can be replaced by one of its radioactive isotopes. For this purpose positron emitting sources are used. Eventually two gamma photons are produced and detected by a polygonal ring of detectors surrounding the patient. Next, we presented the basics of the PET detector technology including gamma detection, coincidence detection and Time-Of-Flight (TOF) PET. Subsequently, the effects that degrade PET image quality and accuracy were discussed. These effects were grouped into three categories: effects related to positron emission physics, effects related to the limitations of the detector technology and subject dependent effects. Next, the basic concepts of Monte Carlo (MC) simulation in emission tomography were discussed. As an example we presented the GATE simulator, a MC software package which was extensively used in this work. Finally, we summarized the applications of PET in oncology, cardiology and neurology for the diagnosis and follow-up of a wide range of diseases.

In the second part, we described how PET imaging evolved into hybrid imaging techniques such as combined PET/CT and PET/MRI. Special attention was devoted to TOF PET/MRI systems because these are the systems for which the imaging techniques presented in this dissertation were developed. We discussed how PET technology was adapted to become MR-compatible and gave a short overview of the prototypes and clinical systems available today.

PET image reconstruction was introduced in the third part of chapter 2. First the acquired PET data is stored in a sinogram or list-mode format. The data is then reconstructed into image space using an analytical or an iterative algorithm. Iterative PET reconstruction is favorable over analytical reconstruction because it allows more accurate modeling and regularization. For example, we illustrated how the iterative ML-EM reconstruction method can easily be adapted to include TOF information and random and scatter compensation.

Because this research concerns attenuation correction for TOF PET/MRI, the last part of chapter 2 was devoted to this topic. Three approaches were discussed: emission-based, MR-based and transmission-based techniques. The emission-based techniques try to derive the attenuation map from the emission data itself. These techniques can be divided into two methods: the first method attempts to simultaneously reconstruct the activity and density distribution in an iterative algorithm. The second method uses consistency conditions criteria to guide the reconstruction. The MR-based attenuation correction techniques include segmentation techniques, template or atlas-based techniques. In all three approaches predefined information about the attenuation coefficients is used. The template and atlas-based approaches also use anatomical priors. Finally, we also presented the work of Salamon et al [7], in which the authors try to use an MR-based image as a guide in the simultaneous reconstruction of the activity and emission distribution.

In chapter 3 we presented a MR-compatible transmission-based technique to solve the issue of attenuation correction in TOF PET systems. In the first part, the method is described in detail. An annulus shaped transmission source is filled with a positron emitter and inserted inside the Field Of View (FOV) of the TOF PET scanner. First a blank reference scan is acquired. Subsequently, the patient is positioned inside the FOV and a transmission scan is acquired. A distinction is made between a transmission scan (TX-scan) and a simultaneous transmission and emission scan (TEX-scan), depending on whether a tracer was administered to the patient prior or after transmission scanning. Next, we discussed how the transmission data can be extracted from the PET data if a TEX-scan was acquired. For this purpose the TOF information of each event is used. From this timing information, the source position of the annihilation is estimated. If this position falls outside a cylinder of radius r_1, the data is classified as transmission data, else, the data is not used for deriving the attenuation map. Finally, we presented a gradient ascent algorithm that was used to derive the attenuation map. In each iteration of the algorithm, a current estimate of the attenuation map is used to back-project the blank data and compare with the back-projection of the transmission data. An update of the attenuation map is derived from the difference image. Because the reconstructed attenuation maps typically contain a lot of noise, a post processing segmentation technique was also presented. Additionally, we described how the reconstructed attenuation map is used to correct for attenuation during the reconstruction of the PET image.

In the second part, the method was validated with a simulation study in GATE. For this purpose a model of the Gemini TF PET scanner was constructed. The count rate performance of the model was compared with experimental results found in literature. Next, we evaluated how this count rate performance is influenced by the presence of an annulus-shaped transmission source inside the FOV of the PET scanner. Finally, the transmission-based method was evaluated with a TEX-scan of a digital torso phantom obtained from the NCAT software. Additionally, we calculated the effective radiation dose absorbed by the patient during the transmission scan.

The results of the simulation studies were presented in the fourth part and discussed in the final part of chapter 3. In ideal circumstances, without the presence of scatter and random coincidences contaminating the transmission data, accurate attenuation coefficients at 511 keV of the torso region can be obtained from a 3 minute simultaneous transmission emission scan using an annulus shaped transmission source filled with 18 MBq of ^{18}F-FDG. The percentage mean difference in μ-values in VOIs defined in the most relevant tissues, was below 2% for soft tissue and the lungs and below 4% for bone tissue. However, because of the presence of additional activity inside the FOV a drop of the true emission count of approximately 14% is obtained, which can be compensated by prolonging the transmission scan. The error in PET quantification was found to be less then 9% in VOIs inside the lungs, soft tissue and bone tissue. Additionally, the total effective transmission dose delivered to the patient is less then 14% of the effective dose caused by the tracer administered to the patient during the PET acquisition.

Further validation of the transmission-based method was presented in chapter 4. In the first part of this chapter we gave an overview of the data correction methods that are needed to compensate for image degrading effects such as random coincidences, count rate related issues, noise and scatter. In all studies random coincidences were compensated with the delayed window method. The count rate performance of the blank and transmission scan were matched by calculating a global count rate correction factor β_{T2} in each study and the influence of noise was reduced with noise regularization implemented in the iterative reconstruction. To compensate for the scattered transmission events, two methods were proposed. The first method is based on the fact that scattered coincidences are found in the lower end of the energy spectrum. A scaling function is applied to suppress events in which the energies of the photons are low compared to a given threshold ϵ_t. In the second approach, the amount of scatter on each Line-Of-Response (LOR) is estimated with a fast simulation technique called Single Scatter Simulation (SSS). The results obtained from the phantom studies showed that the SSS method yielded more accurate attenuation coefficients at 511 keV than the energy-based method. Finally, we also introduced a μ-value histogram scaling method which can be used to compensate for the scattered and true emission events contaminating the transmission data. For this method predefined information about the attenuation coefficients of the subject are required.

In the second part of chapter 4 we gave an overview of the phantom studies. In total six phantom studies were performed on state-of-the-art TOF PET/CT and TOF PET/MRI scanners. The first 5 experiments were performed on the Gemini TF PET/CT scanner available at UCL (Université Catholique Louvain), in Brussels, Belgium. The last study was performed on the Ingenuity TOF PET/MRI and the Discovery PET/CT at Mount Sinai Hospital, New York, USA. The studies were divided into four groups: stand-alone TX scanning, simultaneous TEX scanning, bone imaging and thoracic imaging. In the first group, two phantom studies were done: a TX scan of a cylindrical water phantom and a TX-scan of a MRI-coil. For the second group an anthropomorphic torso phantom was used. We made a comparison between the attenuation maps derived from a stand-alone TX-scan and a simultaneous TEX-scan. The possibility of visualizing bone was investigated with TX-scans of the head of a pig and the Alderson phantom in the third group. Finally, two thorax phantoms containing real tissues obtained from a cow and pig were presented.

In the last part of chapter 4 we gave a general discussion of the results obtained from the phantom studies. Four major conclusions were drawn. First, in order to obtain accurate PET image, data corrections for random coincidences, count rate related issues and scattered transmission events are mandatory. Second, in a TEX-scan, the transmission and emission data are acquired simultaneously. In each TEX study the transmission data was extracted using the TOF information. Because of the limited TOF resolution of current PET scanners, scattered and true emission data will contaminate the extracted transmission data and inaccurate attenuation coefficients are obtained. In regions characterized by a higher tracer uptake an underestimation of the attenuation coefficients was noticed. Thirdly, the phantom studies illustrate that our method is able to visualize any object inside the FOV. Both the MR coils and patient table can be reconstructed and there is no need to include templates derived from CT data or other transmission-based methods. Finally, absolute PET quantification can only be obtained when the PET data is corrected for the attenuation of 511 keV photons in bone tissue. The TX-based method is able to recover large bone structures. However, the contrast with the surrounding tissue is low. Additionally, smaller bone structures or soft bone tissue characterized by a lower attenuation coefficient are harder to discriminate from soft tissue, lung tissue or air. Improvement can be made by increasing the activity inside the transmission source or prolonging the acquisition time of the transmission scan.

Subsequently, we evaluated the transmission-based attenuation correction method in a clinical setting by performing a patient study on the Ingenuity TF PET/MRI and Brilliance CT available at Mount Sinai Hospital, New York, USA. In total 6 patients were investigated: one brain study and five studies of the head/neck and chest region. μ-value scaling was used to correct for the influence of scatter and emission data contaminating the transmission data. In the brain study, a linear scaling method based on the attenuation coefficient of soft tissue was applied. For the experiments of the upper torso, all 5 patients were used as a training set to derive a scaling function. Finally, we presented how the attenuation maps were used to correction the PET data for attenuation and how the PET quantification was measured. When relevant, a distinction was made between the brain and thorax studies.

The results were presented in the second part of chapter 5. For both the brain and the whole body studies the following criteria were evaluated : the MR/PET and CT co-registration, the extraction of transmission data, the reconstruction of the attenuation map and the reconstruction of the PET images. The extraction of transmission data was evaluated with the TRR and ECR metrics presented in chapter 3. The reconstructed attenuation maps were evaluated by comparing the reconstructed attenuation coefficients with the CT-based attenuation coefficients for the brain study and the CT- and MR-based attenuation coefficients for the thoracic studies. The discrepancy between the CT-based, TEX-based and MR-based attenuation maps were evaluated with joint histograms. Finally, the PET data were reconstructed using the attenuation maps derived from the different modalities. For the brain study, a quantitative comparison was done by evaluating the reconstructed PET intensity in different regions inside the brain. For the whole-body experiments, similarity measures and scatter plots were used.

In the third and last part of this chapter the results were discussed. The most important result obtained from the brain study is the fact that an underestimation of the attenuation coefficient of bone has an significant influence on the reconstructed PET images. Compared to the CT-based AC PET image, a quantitative error between 10% and 15% for different regions inside the brain was obtained. A major advantage of brain studies is that the threshold value τ_1 can be lowered significantly allowing more transmission data to be extracted. The results obtained from the thoracic studies yielded better results with the TEX-based AC compared to the MR-based AC: an average difference in PET quantification of 6.4%, 2.4% and 18.7% was obtained in lung tissue, soft tissue and bone respectively. The scatter plots and the reconstructed attenuation maps clearly show the segmentation artifacts in the MR-based attenuation maps compared to the CT and TEX-based maps. However, the TEX-based maps fail to classify soft tissue and adipose tissue as separate tissue classes and the accuracy of the reconstructed attenuation coefficients highly depends on the μ-value scaling technique applied.

In chapters 2 to 5 we evaluated the transmission-based technique using an annulus shaped transmission source. Experimental results show how difficulties arise in obtaining accurate attenuation coefficients due to scatter and emission contaminating the transmission data. In the sixth chapter we proposed an alternative approach in which the annulus shaped source is replaced by multiple fixed line sources covering the complete axial FOV of the scanner. In the first part of the chapter we discussed how the TOF-based extraction of transmission data can be improved when line-sources are used, hereby reducing the influence of scatter and emission data contaminating the transmission data. By rejecting those LORs which do not pass close to at least one line source and additionally reject events based on the TOF information the TRR and ECR can be reduced significantly.

The concept was illustrated with a simulation study using GATE in the second part of chapter 6. First we built a model of the $LaBr_3$ PET scanner, as this scanner was later used for the experimental evaluation. Next a model of the line sources and a digital torso were generated. The TX and TEX-based methods were evaluated for different configurations of the line sources. From these results the best configuration was selected. The LOR-based extraction of transmission data reduced the effect of the emission and scatter contamination on the reconstructed attenuation coefficients.

Finally, in the third part of the chapter we evaluated the method with a phantom study on the $LaBr_3$ PET system available at the radiology department of the University of Pennsylvania (UPENN), Philadelphia, USA. For this purpose an anthropomorphic torso phantom was used. The attenuation maps derived from a TX and TEX scan were evaluated. Compared to the CT-based μ-values, a relative difference of the attenuation coefficients below 10% was obtained for all tissues in both methods. For bone, the error was below 5%.

7.2 Future research

The transmission-based technique addresses most issues related to MR-based attenuation correction. However, some major drawbacks remain. First, the technique is limited by the poor resolution of the PET system. Small bone structures are hard to distinguish from surrounding tissues and consequently a mixture of multiple attenuation coefficients is found in voxels close to small structures. A way to improve the resolution is to include the MR-images as a guide in the reconstruction of the TX-based attenuation map. A segmented MR-image is used as a first estimate, while the TX-data can be used to estimate the attenuation coefficient in each region. TX-data might also be used to merge or divide existing regions depending on the inter- and intra-region variance of the attenuation coefficients. Secondly, although μ-value scaling or an alternative transmission source configuration reduce the influence of scatter and emission contamination, in order to obtain absolute quantification other approaches should also be considered. For example, simultaneous reconstruction of activity and emission does not require the extraction of transmission data. It has been shown in literature that in a TOF PET system, attenuation coefficients can be determined up to a scaling factor [6]. Hence, combining transmission and emission data could help to improve the accuracy of the attenuation coefficients. Finally, the method was validated with phantom studies and a clinical study including 6 patients. More studies are required to validate the method in clinical practice.

7.3 Final conclusion

Future and current TOF PET/MRI systems require a robust and accurate technique to correct the PET image for attenuation. Many research groups focus on deriving the attenuation map from the MR data. MR-based segmentation and atlas-registration techniques are commonly used for this purpose. However, these approaches show some major difficulties. In this dissertation we have introduced a method to derive the attenuation map from a transmission scan by inserting a positron emitting source inside the FOV of the PET scanner. By using TOF-information one can acquire transmission data simultaneously with the emission data. Hence, no acquisition time is lost on the MR and the PET system for the purpose of attenuation correction. Further improvements are possible by choosing the appropriate geometry for the transmission source. The transmission-based technique solves most issues related to MR-based attenuation correction. However, some difficulties remain which need to be addressed in future research, we believe this method is a potential candidate solution for attenuation correction in clinical PET/MRI, especially in whole-body or thoracic imaging.

References

[1] J. S. Karp, S. Surti, M. E. Daube-Witherspoon, and G. Muehllehner, "Benefit of time-of-flight in PET: experimental and clinical results," *Journal of Nuclear Medicine*, vol. 49, pp. 462–470, Mar. 2008.

[2] W. P. Segars, *Development of a new dynamic NURBS-based cardiac-torso (NCAT) phantom*. PhD thesis, The University of North Carolina, may 2001.

[3] E. M. Rohren, T. G. Turkington, and R. E. Coleman, "Clinical Applications of PET in Oncology1," *Radiology*, vol. 231, no. 2, pp. 305–332, 2004.

[4] C. Buchbender, T. A. Heusner, T. C. Lauenstein, A. Bockisch, and G. Antoch, "Oncologic PET/MRI, part 2: bone tumors, soft-tissue tumors, melanoma, and lymphoma," *Journal of Nuclear Medicine*, vol. 53, no. 8, pp. 1244–1252, 2012.

[5] J. Nuyts, P. Dupont, S. Stroobants, R. Benninck, L. Mortelmans, and P. Suetens, "Simultaneous maximum a posteriori reconstruction of attenuation and activity distributions from emission sinograms," *Medical Imaging, IEEE Transactions on*, vol. 18, pp. 393–403, may 1999.

[6] M. Defrise, A. Rezaei, and J. Nuyts, "Time-of-flight PET data determine the atttenuation sinogram up to a constant," *Physics in Medicine and Biology*, vol. 57, pp. 885–99, Feb 2012.

[7] A. Salomon, A. Goedicke, B. Schweizer, T. Aach, and V. Schulz, "Simultaneous reconstruction of activity and attenuation for PET/MR," *IEEE Trans Med Imaging*, vol. 30, pp. 804–13, Mar 2011.

[8] R. Raylman, B. E. Hammer, and N. Christensen, "Combined MRI-PET scanner: a Monte Carlo evaluation of the improvements in PET

resolution due to the effects of a static homogeneous magnetic field," *Nuclear Science, IEEE Transactions on*, vol. 43, no. 4, pp. 2406–2412, 1996.

[9] D. L. Bailey, *Quantification in 3D Positron Emission Tomography PhD Thesis*. PhD thesis, University of Surrey, United Kingdom, 1996.

[10] G. Hevesy, *Radioactive indicators: their application in biochemistry, animal physiology and pathology*. Interscience New York, 1948.

[11] E. O. Lawrence and M. S. Livingston, "The production of high speed light ions without the use of high voltages," *Physical Review*, vol. 40, no. 1, p. 19, 1932.

[12] B. Cassen, L. Curtis, and C. W. Reed, "A sensitive directional gamma ray detector," tech. rep., 1949.

[13] H. O. Anger, "Scintillation camera," *Review of scientific instruments*, vol. 29, no. 1, pp. 27–33, 1958.

[14] H. O. Anger and D. J. Rosenthal, "Scintillation camera and positron camera," *In: Medical Radioisotope Imaging. Vienna. Austria: International Atomic Energy Agency*, pp. 59–82, 1959.

[15] M. Phelps, E. Hoffman, N. A. Mullani, C. S. Higgins, and M. M. T. Pogossian, "Design Considerations for a Positron Emission Transaxial Tomograph (PETT III)," *Nuclear Science, IEEE Transactions on*, vol. 23, no. 1, pp. 516–522, 1976.

[16] T. Ido, C.-N. Wan, V. Casella, J. Fowler, A. Wolf, M. Reivich, and D. Kuhl, "Labeled 2-deoxy-D-glucose analogs. 18F-labeled 2-deoxy-2-fluoro-D-glucose, 2-deoxy-2-fluoro-D-mannose and 14C-2-deoxy-2-fluoro-D-glucose," *Journal of Labelled Compounds and Radiopharmaceuticals*, vol. 14, no. 2, pp. 175–183, 1978.

[17] M. Moszynski, M. Kapusta, D. Wolski, M. Szawlowski, and W. Klamra, "Energy resolution of scintillation detectors readout with large area avalanche photodiodes and photomultipliers," *Nuclear Science, IEEE Transactions on*, vol. 45, no. 3, pp. 472–477, 1998.

[18] C. W. Van Eijk *et al.*, "Inorganic scintillators in medical imaging," *Physics in medicine and biology*, vol. 47, no. 8, pp. R85–R106, 2002.

[19] R. M. Gray and A. Macovski, "Maximum a posteriori estimation of position in scintillation cameras," *Nuclear Science, IEEE Transactions on*, vol. 23, no. 1, pp. 849–852, 1976.

[20] N. H. Clinthorne, W. L. Rogers, L. Shao, and K. F. Koral, "A hybrid maximum likelihood position computer for scintillation cameras," *Nuclear Science, IEEE Transactions on*, vol. 34, no. 1, pp. 97–101, 1987.

[21] J. Joung, R. S. Miyaoka, S. Kohlmyer, and T. K. Lewellen, "Implementation of ML based positioning algorithms for scintillation cameras," *Nuclear Science, IEEE Transactions on*, vol. 47, no. 3, pp. 1104–1111, 2000.

[22] V. Saveliev, "The recent development and study of silicon photomultiplier," *Nuclear Instruments and Methods in Physics Research Section A: Accelerators, Spectrometers, Detectors and Associated Equipment*, vol. 535, no. 1, pp. 528–532, 2004.

[23] D. Renker, "New trends on photodetectors," *Nuclear Instruments and Methods in Physics Research Section A: Accelerators, Spectrometers, Detectors and Associated Equipment*, vol. 571, no. 1, pp. 1–6, 2007.

[24] J. Ninković, "Recent developments in silicon photomultipliers," *Nuclear Instruments and Methods in Physics Research Section A: Accelerators, Spectrometers, Detectors and Associated Equipment*, vol. 580, no. 2, pp. 1020–1022, 2007.

[25] D. Herbert, S. Moehrs, N. Díascenzo, N. Belcari, A. Del Guerra, F. Morsani, and V. Saveliev, "The silicon photomultiplier for application to high-resolution positron emission tomography," *Nuclear Instruments and Methods in Physics Research Section A: Accelerators, Spectrometers, Detectors and Associated Equipment*, vol. 573, no. 1, pp. 84–87, 2007.

[26] I. Britvitch, I. Johnson, D. Renker, A. Stoykov, and E. Lorenz, "Characterisation of Geiger-mode avalanche photodiodes for medical imaging applications," *Nuclear Instruments and Methods in Physics Research Section A: Accelerators, Spectrometers, Detectors and Associated Equipment*, vol. 571, no. 1, pp. 308–311, 2007.

[27] D. P. McElroy, V. Saveliev, A. Reznik, and J. A. Rowlands, "Evaluation of silicon photomultipliers: a promising new detector for MR

compatible PET," *Nuclear Instruments and Methods in Physics Research Section A: Accelerators, Spectrometers, Detectors and Associated Equipment*, vol. 571, no. 1, pp. 106–109, 2007.

[28] T. K. Lewellen, "Recent developments in PET detector technology," *Physics in medicine and biology*, vol. 53, no. 17, p. R287, 2008.

[29] T. F. Budinger, "Instrumentation trends in nuclear medicine," in *Seminars in nuclear medicine*, vol. 7, pp. 285–297, Elsevier, 1977.

[30] N. A. Mullani, J. Markham, and M. M. Ter-Pogossian, "Feasibility of time-of-flight reconstruction in positron emission tomography," *Journal of nuclear medicine: official publication, Society of Nuclear Medicine*, vol. 21, no. 11, pp. 1095–1097, 1980.

[31] R. Allemand, C. Gresset, and J. Vacher, "Potential advantages of a cesium fluoride scintillator for a time-of-flight positron camera," *J Nucl Med*, vol. 21, pp. 153–155, Feb. 1980.

[32] W. W. Moses and S. Derenzo, "Prospects for time-of-flight PET using LSO scintillator," *IEEE Trans. Nucl. Sci.*, vol. 46, pp. 474 –478, June 1999. New Developments In Photodetection NDIP08, Proceedings of the Fifth International Conference on New Developments in Photodetection.

[33] T. K. Lewellen, "Time-of-flight PET," in *Seminars in nuclear medicine*, vol. 28, pp. 268–275, Elsevier, 1998.

[34] S. Surti, A. Kuhn, M. E. Werner, A. E. Perkins, J. Kolthammer, and J. S. Karp1, "Performance of Philips Gemini TF PET/CT Scanner with Special Consideration for Its Time-of-Flight Imaging Capabilities," *Journal of Nuclear Medicine*, vol. 48, no. 3, pp. 471–480, 2007.

[35] E. Van Loef, P. Dorenbos, C. Van Eijk, K. Kramer, and H. Gudel, "High-energy-resolution scintillator: Ce3+ activated LaCl3," *Appl Phys Lett*, vol. 79, no. 10, pp. 1573–1575, 2001.

[36] S. Surti, J. Karp, G. Muehllehner, and P. Raby, "Investigation of lanthanum scintillators for 3D PET," in *Nuclear Science Symposium Conference Record, 2002 IEEE*, vol. 2, pp. 1177–1181, IEEE, 2002.

[37] J. Karp, A. Kuhn, A. Perkins, S. Surti, M. Werner, M. Daube-Witherspoon, L. Popescu, S. Vandenberghe, and G. Muehllehner,

"Characterization of a time-of-flight PET scanner based on lanthanum bromide," in *Nuclear Science Symposium Conference Record, 2005 IEEE*, vol. 4, pp. 5–pp, IEEE, 2005.

[38] M. Conti, B. Bendriem, M. Casey, M. Chen, F. Kehren, C. Michel, and V. Panin, "First experimental results of time-of-flight reconstruction on an LSO PET scanner," *Physics in medicine and biology*, vol. 50, no. 19, p. 4507, 2005.

[39] G. El Fakhri, S. Surti, C. M. Trott, J. Scheuermann, and J. S. Karp, "Improvement in lesion detection with whole-body oncologic time-of-flight PET," *Journal of Nuclear Medicine*, vol. 52, no. 3, pp. 347–353, 2011.

[40] D. L. Snyder, *Random point processes*. Wiley New York, 1975.

[41] P. Razifar, M. Sandström, H. Schnieder, B. Långström, E. Maripuu, E. Bengtsson, and M. Bergström, "Noise correlation in PET, CT, SPECT and PET/CT data evaluated using autocorrelation function: a phantom study on data, reconstructed using FBP and OSEM," *BMC medical imaging*, vol. 5, no. 1, p. 5, 2005.

[42] D. Brasse, P. E. Kinahan, C. Lartizien, C. Comtat, M. Casey, and C. Michel, "Correction Methods for Random Coincidences in Fully 3D Whole-Body PET: Impact on Data and Image Quality," *Journal of Nuclear Medicine*, vol. 46, no. 5, pp. 859–867, 2005.

[43] O. Klein and T. Nishina, "Über die Streuung von Strahlung durch freie Elektronen nach der neuen relativistischen Quantendynamik von Dirac. (German) [On the scattering of radiation by free electrons according to the new relativistic quantum dynamics of Dirac]," *Zeitschrift für Physik*, vol. 52, pp. 853–868, Nov. 1929. This paper introduces the Klein–Nishina distribution of random numbes.

[44] Y. Picard and C. J. Thompson, "Motion correction of PET images using multiple acquisition frames," *Medical Imaging, IEEE Transactions on*, vol. 16, no. 2, pp. 137–144, 1997.

[45] L. Livieratos, K. Rajappan, L. Stegger, K. Schafers, D. L. Bailey, and P. G. Camici, "Respiratory gating of cardiac PET data in list-mode acquisition," *European journal of nuclear medicine and molecular imaging*, vol. 33, no. 5, pp. 584–588, 2006.

[46] L. Boucher, S. Rodrigue, R. Lecomte, and F. Bénard, "Respiratory gating for 3-dimensional PET of the thorax: feasibility and initial results," *Journal of Nuclear Medicine*, vol. 45, no. 2, pp. 214–219, 2004.

[47] B. Lopresti, A. Russo, W. Jones, T. Fisher, D. Crouch, D. Altenburger, and D. Townsend, "Implementation and performance of an optical motion tracking system for high resolution brain PET imaging," *Nuclear Science, IEEE Transactions on*, vol. 46, no. 6, pp. 2059–2067, 1999.

[48] S. U. N. Metropolis, "The monte carlo method," *Journal of American Statistical Association*, vol. 44, pp. 335–341, Sep. 1949.

[49] H. O. Anger, "A new instrument for mapping gamma-ray emitters," *Biology and Medicine Quartly Report UCRL*, vol. 3653, p. 38, January 1957.

[50] S. Jan, G. Santin, D. Strul, S. Staelens, K. Assié, D. Autret, S. Avner, R. Barbier, M. Bardiès, P. M. Bloomfield, D. Brasse, V. Breton, P. Bruyndonckx, I. Buvat, A. F. Chatziioannou, Y. Choi, Y. H. Chung, C. Comtat, D. Donnarieix, L. Ferrer, S. J. Glick, C. J. Groiselle, D. Guez, P. F. Honore, S. Kerhoas-Cavata, A. S. Kirov, V. Kohli, M. Koole, M. Krieguer, D. J. van der Laan, F. Lamare, G. Largeron, C. Lartizien, D. Lazaro, M. C. Maas, L. Maigne, F. Mayet, F. Melot, C. Merheb, E. Pennacchio, J. Perez, U. Pietrzyk, F. R. Rannou, M. Rey, D. R. Schaart, C. R. Schmidtlein, L. Simon, T. Y. Song, J. M. Vieira, D. Visvikis, R. V. de Walle, E. Wieërs, and C. Morel, "GATE: a simulation toolkit for PET and SPECT," *Phys Med Biol*, vol. 49, pp. 4543–4561, Oct. 2004.

[51] J. De Beenhouwer, S. Staelens, D. Kruecker, L. Ferrer, Y. DíAsseler, I. Lemahieu, and F. R. Rannou, "Cluster computing software for GATE simulations," *Medical physics*, vol. 34, p. 1926, 2007.

[52] I. G. Zubal, C. R. Harrell, E. O. Smith, Z. Rattner, G. Gindi, P. B. Hoffer, *et al.*, "Computerized three-dimensional segmented human anatomy," *Medical physics*, vol. 21, pp. 299–302, Feb. 1994.

[53] W. P. Segars, D. S. Lalush, and B. M. Tsui, "Modeling respiratory mechanics in the MCAT and spline-based MCAT phantoms," *Nuclear Science, IEEE Transactions on*, vol. 48, no. 1, pp. 89–97, 2001.

[54] W. P. Segars and B. Tsui, "MCAT to XCAT: The evolution of 4-D computerized phantoms for imaging research," *Proceedings of the IEEE*, vol. 97, no. 12, pp. 1954–1968, 2009.

[55] S. L. Kitson, V. Cuccurullo, A. Ciarmiello, D. Salvo, and L. Mansi, "Clinical Applications of Positron Emission Tomography (PET) Imaging in Medicine: Oncology, Brain Diseases and Cardiology," *Curr Radiopharm*, vol. 2, pp. 224–53, 2009.

[56] E. Lopci, C. Nanni, P. Castellucci, G. C. Montini, V. Allegri, D. Rubello, F. Chierichetti, V. Ambrosini, and S. Fanti, "Imaging with non-FDG PET tracers: outlook for current clinical applications," *Insights into imaging*, vol. 1, no. 5-6, pp. 373–385, 2010.

[57] J. Czernin, "Clinical Applications of FDG-PET in Oncology," *Acta Medica Austriaca*, vol. 29, no. 5, pp. 162–170, 2002.

[58] F. Keng, "Clinical applications of positron emission tomography in cardiology: a review," *Annals-Academy of Medicine Singapore*, vol. 33, no. 2, pp. 175–182, 2004.

[59] A. Venneri, "Imaging treatment effects in Alzheimer's disease," *Magnetic resonance imaging*, vol. 25, no. 6, pp. 953–968, 2007.

[60] M. Hayden, W. Martin, A. Stoessl, C. Clark, S. Hollenberg, M. Adam, W. Ammann, R. Harrop, J. Rogers, T. Ruth, *et al.*, "Positron emission tomography in the early diagnosis of Huntington's disease," *Neurology*, vol. 36, no. 7, pp. 888–888, 1986.

[61] T. Beyer, D. W. Townsend, T. Brun, P. E. Kinahan, M. Charron, R. Roddy, J. Jerin, J. Young, L. Byars, and R. Nutt, "A combined PET/CT scanner for clinical oncology," *Journal of Nuclear Medicine*, vol. 41, pp. 1369–79, August 2000.

[62] O. Israel, Z. Keidar, G. Iosilevsky, L. Bettman, J. Sachs, and A. Frenkel, "The fusion of anatomic and physiologic imaging in the management of patients with cancer," in *Seminars in nuclear medicine*, vol. 31, pp. 191–205, Elsevier, 2001.

[63] O. Israel, M. Mor, D. Gaitini, Z. Keidar, L. Guralnik, A. Engel, A. Frenkel, R. Bar-Shalom, and A. Kuten, "Combined functional and structural evaluation of cancer patients with a hybrid camera-based PET/CT system using 18F-FDG," *Journal of Nuclear Medicine*, vol. 43, no. 9, pp. 1129–1136, 2002.

[64] R. Bar-Shalom, N. Yefremov, L. Guralnik, D. Gaitini, A. Frenkel, A. Kuten, H. Altman, Z. Keidar, and O. Israel, "Clinical performance of PET/CT in evaluation of cancer: additional value for diagnostic imaging and patient management," *Journal of nuclear medicine*, vol. 44, no. 8, pp. 1200–1209, 2003.

[65] D. J. Wagenaar, M. Kapusta, L. JUNQIANG, and B. E. Patt, "Rationale for the combination of nuclear medicine with magnetic resonance for pre-clinical imaging," *Technology in cancer research & treatment*, vol. 5, no. 4, pp. 343–350, 2006.

[66] H.-P. Schlemmer, B. J. Pichler, R. Krieg, and W.-D. Heiss, "An integrated MR/PET system: prospective applications," *Abdominal imaging*, vol. 34, no. 6, pp. 668–674, 2009.

[67] B. J. Pichler, A. Kolb, T. Nägele, and H.-P. Schlemmer, "PET/MRI: paving the way for the next generation of clinical multimodality imaging applications," *Journal of Nuclear Medicine*, vol. 51, no. 3, pp. 333–336, 2010.

[68] H. Zaidi, M.-L. Montandon, and A. Alavi, "The clinical role of fusion imaging using PET, CT, and MR imaging," *PET Clinics*, vol. 3, no. 3, pp. 275–291, 2008.

[69] G. Antoch and A. Bockisch, "Combined PET/MRI: a new dimension in whole-body oncology imaging?," *Eur. J. Nucl. Med. Mol. Imag.*, vol. 36 Suppl 1, pp. S113–S120, Mar. 2009.

[70] G. K. von Schulthess and H.-P. W. Schlemmer, "A look ahead: PET/MR versus PET/CT," *European journal of nuclear medicine and molecular imaging*, vol. 36, no. 1, pp. 3–9, 2009.

[71] M. S. Judenhofer, H. F. Wehrl, D. F. Newport, C. Catana, S. B. Siegel, M. Becker, A. Thielscher, M. Kneilling, M. P. Lichy, M. Eichner, K. Klingel, G. Reischl, S. Widmaier, M. Röcken, R. E. Nutt, H.-J. Machulla, K. Uludag, S. R. Cherry, C. D. Claussen, and B. J. Pichler, "Simultaneous PET-MRI: a new approach for functional and morphological imaging," *Nat Med*, vol. 14, pp. 459–465, Apr. 2008.

[72] Y. Shao, S. R. Cherry, K. Farahani, K. Meadors, S. Siegel, R. W. Silverman, and P. K. Marsden, "Simultaneous PET and MR imaging," *Physics in medicine and biology*, vol. 42, no. 10, p. 1965, 1997.

[73] P. K. Marsden, D. Strul, S. F. Keevil, S. C. Williams, and D. Cash, "Simultaneous PET and NMR," *British journal of radiology*, vol. 75, no. suppl 9, pp. S53–S59, 2002.

[74] A. J. Chaudhari, A. A. Joshi, Y. Wu, R. M. Leahy, S. R. Cherry, and R. D. Badawi, "Spatial distortion correction and crystal identification for MRI-compatible position-sensitive avalanche photodiode-based PET scanners," *Nuclear Science, IEEE Transactions on*, vol. 56, no. 3, pp. 549–556, 2009.

[75] R. Hawkes, A. Lucas, S. Siegel, R. Nutt, T. Fryer, R. Ansorge, J. Clark, and T. Carpenter, "Development of a combined microPET®/MR system," in *16th ISMRM Scientific Meeting, Toronto*, 2008.

[76] H. F. Wehrl, M. S. Judenhofer, S. Wiehr, and B. J. Pichler, "Pre-clinical PET/MR: technological advances and new perspectives in biomedical research," *European journal of nuclear medicine and molecular imaging*, vol. 36, no. 1, pp. 56–68, 2009.

[77] V. Spanoudaki, A. Mann, A. Otte, I. Konorov, I. Torres-Espallardo, S. Paul, and S. Ziegler, "Use of single photon counting detector arrays in combined PET/MR: Characterization of LYSO-SiPM detector modules and comparison with a LSO-APD detector," *Journal of Instrumentation*, vol. 2, no. 12, p. P12002, 2007.

[78] G. Delso and S. Ziegler, "PET/MRI system design," *Eur J Nucl Med Mol Imaging*, vol. 36, no. 1, pp. 86–92, 2009.

[79] G. Delso, S. Fürst, B. Jakoby, R. Ladebeck, C. Ganter, S. G. Nekolla, M. Schwaiger, and S. I. Ziegler, "Performance measurements of the Siemens mMR integrated whole-body PET/MR scanner," *Journal of Nuclear Medicine*, vol. 52, no. 12, pp. 1914–1922, 2011.

[80] S. Yamamoto, K. Kuroda, and M. Senda, "Scintillator selection for MR-compatible gamma detectors," *Nuclear Science, IEEE Transactions on*, vol. 50, no. 5, pp. 1683–1685, 2003.

[81] Y. Shao, S. Cherry, K. Farahani, R. Slates, R. Silverman, K. Meadors, A. Bowery, S. Siegel, P. Marsden, and P. Garlick, "Development of a PET detector system compatible with MRI/NMR systems," *Nuclear Science, IEEE Transactions on*, vol. 44, no. 3, pp. 1167–1171, 1997.

[82] R. E. Carson, P. Herscovitch, and M. E. Daube-Witherspoon, *Quantitative functional brain imaging with positron emission tomography*. Access Online via Elsevier, 1998.

[83] R. R. Raylman, S. Majewski, S. K. Lemieux, S. S. Velan, B. Kross, V. Popov, M. F. Smith, A. G. Weisenberger, C. Zorn, and G. D. Marano, "Simultaneous MRI and PET imaging of a rat brain," *Physics in medicine and biology*, vol. 51, no. 24, p. 6371, 2006.

[84] P. K. Marsden, D. Strul, S. F. Keevil, S. C. R. Williams, and D. Cash, "Simultaneous PET and NMR," *British Journal of Radiology*, vol. 75 Spec No, pp. S53–S59, Nov 2002.

[85] C. Catana, Y. Wu, M. S. Judenhofer, J. Qi, B. J. Pichler, and S. R. Cherry, "Simultaneous Acquisition of Multislice PET and MR Images: Initial Results with a MR-Compatible PET Scanner," *Journal of Nuclear Medicine*, vol. 47, no. 12, pp. 1968–1976, 2006.

[86] B. J. Pichler, M. S. Judenhofer, C. Catana, J. H. Walton, M. Kneilling, R. E. Nutt, S. B. Siegel, C. D. Claussen, and S. R. Cherry, "Performance test of an LSO-APD detector in a 7-T MRI scanner for simultaneous PET/MRI," *J Nucl Med*, vol. 47, pp. 639–647, Apr 2006.

[87] D. Schlyer, P. Vaska, D. Tomasi, C. Woody, S.-H. Maramraju, S. Southekal, J.-F. Pratte, S. Junnarkar, S. Solis-Najera, S. Krishnamoorthy, *et al.*, "A simultaneous PET/MRI scanner based on RatCAP in small animals," in *Nuclear Science Symposium Conference Record, 2007. NSS'07. IEEE*, vol. 5, pp. 3256–3259, IEEE, 2007.

[88] W. Handler, B. Chronik, T. Scholl, K. Gilbert, and H. Peng, "Combining field-cycled magnetic resonance imaging with positron emission tomography," *J NUCL MED MEETING ABSTRACTS*, vol. 48, pp. 89P–a, 2007.

[89] M. Schmand, Z. Burbar, J. Corbeil, N. Zhang, C. Michael, L. Byars, *et al.*, "BrainPET: first human tomograph for simultaneous (functional) PET and MR imaging," *J Nucl Med*, vol. 48, no. 6, p. 45P, 2007.

[90] H. Schlemmer, B. Pichler, K. Wienhard, M. Schmand, C. Nahmias, D. Townsend, W. Heiss, and C. Claussen, "Simultaneous MR/PET for brain imaging: First patient scans," *Journal of Nuclear Medicine*, vol. 48, no. Supplement 2, p. 45P, 2007.

[91] A. Drzezga, M. Souvatzoglou, M. Eiber, A. J. Beer, S. Fürst, A. Martinez-Möller, S. G. Nekolla, S. Ziegler, C. Ganter, E. J. Rummeny, *et al.*, "First clinical experience with integrated whole-body PET/MR: comparison to PET/CT in patients with oncologic diagnoses," *Journal of Nuclear Medicine*, vol. 53, no. 6, pp. 845–855, 2012.

[92] C. Buchbender, T. A. Heusner, T. C. Lauenstein, A. Bockisch, and G. Antoch, "Oncologic PET/MRI, part 1: tumors of the brain, head and neck, chest, abdomen, and pelvis," *Journal of Nuclear Medicine*, vol. 53, no. 6, pp. 928–938, 2012.

[93] P. E. Kinahan, M. Defrise, and R. Clackdoyle, *Emission Tomography : the fundamentals of PET and SPECT*, ch. Analytical reconstruction methods. Elsevier Academic Press, 2004.

[94] L. A. Shepp and Y. Vardi, "Maximum Likelihood Reconstruction for Emission Tomography," *Medical Imaging, IEEE Transactions on*, vol. 1, pp. 113–122, october 1982.

[95] C. C. Watson, "An evaluation of image noise variance for time-of-flight PET," *Nuclear Science, IEEE Transactions on*, vol. 54, no. 5, pp. 1639–1647, 2007.

[96] C. C. Watson, "An improved weighting kernel for analytical time-of-flight PET reconstruction," *Nuclear Science, IEEE Transactions on*, vol. 55, no. 5, pp. 2551–2556, 2008.

[97] M. N. Wernick and J. N. Aarsvold, *Emission tomography: the fundamentals of PET and SPECT*. Access Online via Elsevier, 2004.

[98] S. R. Cherry, M. Dahlbom, and E. J. Hoffman, "3D PET using a conventional multislice tomograph without septa," *Journal of computer assisted tomography*, vol. 15, no. 4, pp. 655–668, 1991.

[99] R. Badawi, P. Marsden, B. Cronin, J. Sutcliffe, and M. Maisey, "Optimization of noise-equivalent count rates in 3D PET," *Physics in medicine and biology*, vol. 41, no. 9, p. 1755, 1996.

[100] C. C. Watson, D. Newport, and M. E. Casey, "A single scatter simulation technique for scatter correction in 3D PET," in *Three-dimensional image reconstruction in radiology and nuclear medicine*, pp. 255–268, Springer, 1996.

[101] C. C. Watson, "Extension of single scatter simulation to scatter correction of time-of-flight PET," *Nuclear Science, IEEE Transactions on*, vol. 54, no. 5, pp. 1679–1686, 2007.

[102] S. Grootoonk, T. Spinks, T. Jones, C. Michel, and A. Bol, "Correction for scatter using a dual energy window technique with a tomograph operated without septa," in *Nuclear Science Symposium and Medical Imaging Conference, 1991., Conference Record of the 1991 IEEE*, pp. 1569–1573, IEEE, 1991.

[103] M. A. King, G. J. Hademenos, and S. J. Glick, "A dual-photopeak window method for scatter correction," *Journal of nuclear medicine: official publication, Society of Nuclear Medicine*, vol. 33, no. 4, pp. 605–612, 1992.

[104] B. Bendriem, R. Trebossen, V. Frouin, and A. Syrota, "A PET scatter correction using simultaneous acquisitions with low and high lower energy thresholds," in *Nuclear Science Symposium and Medical Imaging Conference, 1993., 1993 IEEE Conference Record.*, pp. 1779–1783, IEEE, 1993.

[105] J. M. Ollinger, "Model-based scatter correction for fully 3D PET," *Physics in medicine and biology*, vol. 41, no. 1, p. 153, 1996.

[106] L. Hiltz and B. McKee, "Scatter correction for three-dimensional PET based on an analytic model dependent on source and attenuating object," *Physics in medicine and biology*, vol. 39, no. 11, pp. 2059–71, 1994.

[107] M. J. Lercher and K. Wienhard, "Scatter correction in 3-D PET," *Medical Imaging, IEEE Transactions on*, vol. 13, no. 4, pp. 649–657, 1994.

[108] C. Bai, L. Shao, A. J. Da Silva, and Z. Zhao, "A generalized model for the conversion from CT numbers to linear attenuation coefficients," *Nuclear Science, IEEE Transactions on*, vol. 50, no. 5, pp. 1510–1515, 2003.

[109] P. E. Kinahan, D. W. Townsend, T. Beyer, and D. Sashin, "Attenuation correction for a combined 3D PET/CT scanner," *Medical Physics*, vol. 25, pp. 2046–2053, October 1998.

[110] Y.-C. Tai, K.-P. Lin, M. Dahlbom, and E. Hoffman, "A hybrid attenuation correction technique to compensate for lung density in 3-D

total body PET," *Nuclear Science, IEEE Transactions on*, vol. 43, pp. 323 –330, feb 1996.

[111] M. Xu, P. Cutler, and W. Luk, "Adaptive, segmented attenuation correction for whole-body PET imaging," *Nuclear Science, IEEE Transactions on*, vol. 43, pp. 331 –336, feb 1996.

[112] Y. Censor, D. E. Gustafson, A. Lent, and H. Tuy, "A New Approach to the Emission Computerized Tomography Problem: Simultaneous Calculation of Attenuation and Activity Coefficients," *Nuclear Science, IEEE Transactions on*, vol. 26, pp. 2775 –2779, april 1979.

[113] F. Natterer, *Attenuation correction in emission tomography*. Accademic press, sabatier p ed., 1987.

[114] D. Volker, "A new approach towards simultaneous activity and attenuation reconstruction in emission tomography," *Inverse Problems*, vol. 15, pp. 931–960, 1999.

[115] M. Conti, "Why is TOF PET reconstruction a more robust method in the presence of inconsistent data?," *Physics in Medicine and Biology*, vol. 56, pp. 155–68, Jan 2011.

[116] A. Welch, C. Campbell, R. Clackdoyle, F. Natterer, M. Hudson, A. Bromiley, P. Mikecz, F. Chillcot, M. Dodd, P. Hopwood, S. Craib, G. Gullberg, and P. Sharp, "Attenuation correction in PET using consistency information," *Nuclear Science, IEEE Transactions on*, vol. 45, pp. 3134 –3141, dec 1998.

[117] A. Bromiley, A. Welch, F. Chilcott, S. Waikar, S. McCallum, M. Dodd, S. Craib, L. Schweiger, and P. Sharp, "Attenuation correction in PET using consistency conditions and a three-dimensional template," *Nuclear Science, IEEE Transactions on*, vol. 48, pp. 1371 –1377, aug 2001.

[118] B. A. V., "Reconstruction of Attenuation Map Using Discrete Consistency Conditions," *IEEE Trans Med Imaging*, vol. 19, pp. 451–462, May 2000.

[119] J. Herraiz, S. Espana, E. Vicente, E. Herranz, J. Vaquero, M. Desco, and J. Udias, "Revised consistency conditions for PET data," in *Nuclear Science Symposium Conference Record, 2007. NSS '07. IEEE*, vol. 5, pp. 3865–3870, 26 2007-nov. 3 2007.

[120] M. W. V., "Theradiography of the human body with radioactive isotopes," *British Journal of Radiology*, vol. 25, pp. 517–525, 1952.

[121] D. E. Kuhl, M.D., J. Hale, Ph.D., and M. Walter L. Eaton, "Transmission Scanning: A Useful Adjunct to Conventional Emission Scanning for Accurately Keying Isotope Deposition to Radiographic Anatomy," *Radiology*, vol. 87, pp. 278–284, August 1966.

[122] C. Watson, A. Schaefer, W. Luk, and C.-M. Kirsch, "Clinical evaluation of single-photon attenuation correction for 3D whole-body PET," in *Nuclear Science Symposium, 1998. Conference Record. 1998 IEEE*, vol. 3, pp. 1694 –1701 vol.3, 1998.

[123] C.-H. Tung, G. Gullberg, G. Zeng, P. Christian, F. Datz, and H. Morgan, "Nonuniform attenuation correction using simultaneous transmission and emission converging tomography," *Nuclear Science, IEEE Transactions on*, vol. 39, pp. 1134 –1143, aug 1992.

[124] C. Watson, L. Eriksson, M. Casey, W. Jones, J. Moyers, S. Miller, J. Hamill, A. Van Lingen, B. Bendriem, and R. Nutt, "Design and performance of collimated coincidence point sources for simultaneous transmission measurements in 3-D PET," *Nuclear Science, IEEE Transactions on*, vol. 48, pp. 673 –679, jun 2001.

[125] R. Smith, J. Karp, G. Muehllehner, E. Gualtieri, and F. Benard, "Singles transmission scans performed post-injection for quantitative whole body PET imaging," *Nuclear Science, IEEE Transactions on*, vol. 44, pp. 1329 –1335, jun 1997.

[126] H. Zaidi, M.-L. Montandon, and D. O. Slosman, "Magnetic resonance imaging-guided attenuation and scatter corrections in three-dimensional brain positron emission tomography," *Medical physics*, vol. 30, p. 937, 2003.

[127] G. Wagenknecht, E. R. Kops, L. Tellmann, and H. Herzog, "Knowledge-based segmentation of attenuation-relevant regions of the head in T1-weighted MR images for attenuation correction in MR/PET systems," in *Nuclear Science Symposium Conference Record (NSS/MIC), 2009 IEEE*, pp. 3338–3343, IEEE, 2009.

[128] J. Steinberg, G. Jia, S. Sammet, J. Zhang, N. Hall, and M. V. Knopp, "Three-region MRI-based whole-body attenuation correction for automated PET reconstruction," *Nuclear medicine and biology*, vol. 37, no. 2, pp. 227–235, 2010.

[129] V. Schulz, I. Torres-Espallardo, S. Renisch, Z. Hu, N. Ojha, P. Börnert, M. Perkuhn, T. Niendorf, W. Schäfer, H. Brockmann, *et al.*, "Automatic, three-segment, MR-based attenuation correction for whole-body PET/MR data," *European journal of nuclear medicine and molecular imaging*, vol. 38, no. 1, pp. 138–152, 2011.

[130] V. Keereman, Y. Fierens, T. Broux, Y. D. Deene, M. Lonneux, and S. Vandenberghe, "MRI-based attenuation correction for PET/MRI using ultrashort echo time sequences," *J Nucl Med*, vol. 51, pp. 812–818, May 2010.

[131] C. Catana, A. van der Kouwe, T. Benner, C. J. Michel, M. Hamm, M. Fenchel, B. Fischl, B. Rosen, M. Schmand, and A. G. Sorensen, "Toward implementing an MRI-based PET attenuation-correction method for neurologic studies on the MR-PET brain prototype," *J Nucl Med*, vol. 51, pp. 1431–1438, Sep 2010.

[132] A. Johansson, M. Karlsson, and T. Nyholm, "CT substitute derived from MRI sequences with ultrashort echo time," *Med Phys*, vol. 38, pp. 2708–2714, May 2011.

[133] Y. Berker, J. Franke, A. Salomon, M. Palmowski, H. C. Donker, Y. Temur, F. M. Mottaghy, C. Kuhl, D. Izquierdo-Garcia, Z. A. Fayad, *et al.*, "MRI-based attenuation correction for hybrid PET/MRI systems: a 4-class tissue segmentation technique using a combined ultrashort-echo-time/Dixon MRI sequence," *Journal of Nuclear Medicine*, vol. 53, no. 5, pp. 796–804, 2012.

[134] M. Eiber, A. Martinez-Möller, M. Souvatzoglou, K. Holzapfel, A. Pickhard, D. Löffelbein, I. Santi, E. J. Rummeny, S. Ziegler, M. Schwaiger, *et al.*, "Value of a Dixon-based MR/PET attenuation correction sequence for the localization and evaluation of PET-positive lesions," *European journal of nuclear medicine and molecular imaging*, vol. 38, no. 9, pp. 1691–1701, 2011.

[135] M.-L. Montandon and H. Zaidi, "Atlas-guided non-uniform attenuation correction in cerebral 3D PET imaging," *Neuroimage*, vol. 25, pp. 278–286, Mar 2005.

[136] E. R. Kops and H. Herzog, "Alternative methods for attenuation correction for PET images in MR-PET scanners," in *Nuclear Science Symposium Conference Record, 2007. NSS '07. IEEE*, vol. 6, pp. 4327–4330, Nov. 2007.

[137] E. R. Kops and H. Herzog, "Template based attenuation correction for PET in MR-PET scanners," in *Nuclear Science Symposium Conference Record, 2008. NSS'08. IEEE*, pp. 3786–3789, IEEE, 2008.

[138] M. Hofmann, F. Steinke, V. Scheel, G. Charpiat, J. Farquhar, P. Aschoff, M. Brady, B. Schölkopf, and B. J. Pichler, "MRI-based Attenuation Correction for PET/MRI: A Novel Approach Combining Pattern Recognition and Atlas Registration," *Journal of Nuclear Medicine*, vol. 49, pp. 1875–1883, October 2008.

[139] M. Hofmann, I. Bezrukov, F. Mantlik, P. Aschoff, F. Steinke, T. Beyer, B. J. Pichler, and B. Schölkopf, "MRI-based attenuation correction for whole-body PET/MRI: quantitative evaluation of segmentation-and atlas-based methods," *Journal of Nuclear Medicine*, vol. 52, no. 9, pp. 1392–1399, 2011.

[140] J. S. Karp, G. Muehllehner, H. Qu, and X. H. Yan, "Singles transmission in volume-imaging PET with a 137Cs source," *Phys. Med. Biol.*, vol. 40, pp. 929–944, May 1995.

[141] S. K. Yu and C. Nahmias, "Single-photon transmission measurements in positron tomography using 137Cs," *Physics in Medicine and Biology*, vol. 40, p. 1255, Jul. 1995.

[142] M. E. Daube-Witherspoon, S. Surti, A. Perkins, C. C. M. Kyba, R. Wiener, M. E. Werner, R. Kulp, and J. S. Karp, "The imaging performance of a LaBr3-based PET scanner," *Phys Med Biol*, vol. 55, pp. 45–64, Jan. 2010.

[143] S. Surti, J. S. Karp, and G. Muehllehner, "Image quality assessment of LaBr3-based whole-body 3D PET scanners: a Monte Carlo evaluation," *Phys Med Biol*, vol. 49, pp. 4593–4610, Oct 2004.

[144] K. Lange and R. Carson, "EM reconstruction algorithms for emission and transmission tomography," *J Comput Assist Tomogr*, vol. 8, pp. 306–316, Apr. 1984.

[145] J. Nuyts, B. D. Man, P. Dupont, M. Defrise, P. Suetens, and L. Mortelmans, "Iterative reconstruction for helical CT: a simulation study.," *Phys Med Biol*, vol. 43, pp. 729–737, Apr 1998.

[146] Z.-K. Huang and K.-W. Chau, "A new image thresholding method based on Gaussian mixture model," *Applied Mathematics and Computation*, vol. 205, no. 2, pp. 899 – 907, 2008.

[147] G. Pratx, S. Surti, and C. Levin, "Fast List-Mode Reconstruction for Time-of-Flight PET Using Graphics Hardware," *Nuclear Science, IEEE Transactions on*, vol. 58, pp. 105 –109, feb. 2011.

[148] N. Ojha, J. Griesmer, Z. Hu, L. Shao, D. Izquierdo, J. Machac, O. Ratib, H. Zaidi, V. Fuster, and Z. Fayad, "PET performance of the GEMINI TF PET - MR: The world's first whole body PET - MRI scanner," in *Nuclear Science Symposium Conference Record (NSS/MIC), 2010 IEEE*, pp. 2013 –2015, 30 2010-nov. 6 2010.

[149] "NEMA Standards Publication NU2-2001 : Performance Measurements of Positron Emission Tomographs," 2001.

[150] A. D. Wrixon, "New ICRP recommendations," *Journal of Radiological Protection*, vol. 28, no. 2, p. 161, 2008.

[151] S. Strother, M. Casey, and E. Hoffman, "Measuring PET scanner sensitivity: relating countrates to image signal-to-noise ratios using noise equivalents counts," *Nuclear Science, IEEE Transactions on*, vol. 37, pp. 783–788, Apr 1990.

[152] T.-H. Wu, Y.-H. Huang, J. J. S. Lee, S.-Y. Wang, S.-C. Wang, C.-T. Su, L.-K. Chen, and T.-C. Chu, "Radiation exposure during transmission measurements: comparison between CT- and germanium-based techniques with a current PET scanner," *Eur J Nucl Med Mol Imaging*, vol. 31, pp. 38–43, Jan. 2004.

[153] P. Mollet, V. Keereman, and S. Vandenberghe, "Simultaneous emission and transmission imaging for PET-MRI using time-of-flight information," in *J NUCL MED MEETING ABSTRACTS*, vol. 51, p. 124, 2010.

[154] P. Mollet, V. Keereman, E. Clementel, and S. Vandenberghe, "Simultaneous MR-compatible emission and transmission imaging for PET using time-of-flight information," *Medical Imaging, IEEE Transactions on*, vol. 31, no. 99, pp. 1734–1742, 2012.

[155] H. Derin and H. Elliott, "Modeling and segmentation of noisy and textured images using Gibbs random fields," *Pattern Analysis and Machine Intelligence, IEEE Transactions on*, no. 1, pp. 39–55, 1987.

[156] J. E. Bowsher, V. E. Johnson, T. G. Turkington, R. J. Jaszczak, C. E. Floyd Jr, and R. E. Coleman, "Bayesian reconstruction and use

of anatomical a priori information for emission tomography," *Medical Imaging, IEEE Transactions on*, vol. 15, no. 5, pp. 673–686, 1996.

[157] J. W. Stayman and J. A. Fessler, "Regularization for uniform spatial resolution properties in penalized-likelihood image reconstruction," *Medical Imaging, IEEE Transactions on*, vol. 19, no. 6, pp. 601–615, 2000.

[158] S. Geman and D. Geman, "Stochastic relaxation, Gibbs distributions, and the Bayesian restoration of images," *Pattern Analysis and Machine Intelligence, IEEE Transactions on*, no. 6, pp. 721–741, 1984.

[159] P. J. Green, "Bayesian reconstructions from emission tomography data using a modified EM algorithm," *Medical Imaging, IEEE Transactions on*, vol. 9, no. 1, pp. 84–93, 1990.

[160] T. Hebert and R. Leahy, "A generalized EM algorithm for 3-D Bayesian reconstruction from Poisson data using Gibbs priors," *Medical Imaging, IEEE Transactions on*, vol. 8, no. 2, pp. 194–202, 1989.

[161] L. I. Rudin, S. Osher, and E. Fatemi, "Nonlinear total variation based noise removal algorithms," *Physica D: Nonlinear Phenomena*, vol. 60, no. 1â"4, pp. 259 – 268, 1992.

[162] P. Mollet, V. Keereman, and S. Vandenberghe, "Corrections for simultaneous emission and transmission imaging for TOFPET-MRI," in *PET-MR Workshop at MIC*, 2010.

[163] P. Mollet, V. Keereman, J. Bini, D. Izquierdo, Z. Fayad, and S. Vandenberghe, "Improvement of attenuation correction in tof-pet/mri using a positron emitting source," *Journal of Nuclear Medicine*, vol. 55, pp. 329–336, Feb. 2014.

[164] V. Keereman, R. V. Holen, P. Mollet, and S. Vandenberghe, "The effect of errors in segmented attenuation maps on PET quantification," *Med Phys*, vol. 38, no. 11, pp. 6010–6019, 2011.

[165] V. Keereman, Y. D'Asseler, R. Van Holen, P. Mollet, and S. Vandenberghe, "The effect of inter-patient attenuation coefficient variability on segmented attenuation correction for PET," *J NUCL MED MEETING ABSTRACTS*, vol. 51, no. 2, pp. 1378–, 2010.

[166] B. Zhang, D. Pal, Z. Hu, N. Ojha, T. Guo, G. Muswick, C. hua Tung, and J. Kaste, "Attenuation correction for MR table and coils

for a sequential PET/MR system," in *Nuclear Science Symposium Conference Record (NSS/MIC), 2009 IEEE*, pp. 3303 –3306, Nov. 2009.

[167] C. Burger, G. Goerres, S. Schoenes, A. Buck, A. H. R. Lonn, and G. K. V. Schulthess, "PET attenuation coefficients from CT images: experimental evaluation of the transformation of CT into PET 511-keV attenuation coefficients," *Eur. J. Nucl. Med. Mol. Imag.*, vol. 29, pp. 922–927, July 2002.

[168] Z. Hu, N. Ojha, S. Renisch, V. Schulz, I. Torres, A. Buhl, D. Pal, G. Muswick, J. Penatzer, T. Guo, P. Bonert, C. Tung, J. Kaste, M. Morich, T. Havens, P. Maniawski, W. Schafer, R. Gunther, G. Krombach, and L. Shao, "MR-based attenuation correction for a whole-body sequential PET/MR system," in *Nuclear Science Symposium Conference Record (NSS/MIC), 2009 IEEE*, pp. 3508 –3512, Nov. 2009.

[169] Z. Hu, S. Renisch, B. Schweizer, T. B. t, N. Ojha, J. T. T. Guo, C. . Tung, J. Kaste, V. Schulz, I. . Torres, and L. Shao, "Philips Ingenuity TF PET/MR attenuation correction," tech. rep., Philips Heathcare, Dec 2011.

[170] T. Beyer, A. Bockisch, H. Kühl, and M.-J. Martinez, "Whole-body 18F-FDG PET/CT in the presence of truncation artifacts," *J Nucl Med*, vol. 47, pp. 91–99, Jan 2006.

[171] G. Delso, A. Martinez-Möller, R. A. Bundschuh, S. G. Nekolla, and S. I. Ziegler, "The effect of limited MR field of view in MR/PET attenuation correction," *Med Phys*, vol. 37, pp. 2804–2812, Jun 2010.

[172] A. Martinez-Möller, M. Souvatzoglou, G. Delso, R. A. Bundschuh, C. Chefd'hotel, S. I. Ziegler, N. Navab, M. Schwaiger, and S. G. Nekolla, "Tissue classification as a potential approach for attenuation correction in whole-body PET/MRI: evaluation with PET/CT data," *J Nucl Med*, vol. 50, pp. 520–526, Apr 2009.

[173] P. Mollet, V. Keereman, D. Izquierdo, Z. A. Fayad, and S. Vandenberghe, "Transmission-based attenuation correction in a sequential tof-pet/mri system," in *PSMR, Abstracts*, pp. 102–102, 2012.

[174] M. Daube-Witherspoon, S. Surti, A. Perkins, C. Kyba, R. Wiener, M. Werner, R. Kulp, and J. Karp, "The imaging performance of a

LaBr3-based PET scanner," *Physics in medicine and biology*, vol. 55, no. 1, p. 45, 2010.

[175] S. Surti, J. Karp, and G. Muehllehner, "Image quality assessment of LaBr3-based whole-body 3D PET scanners: a Monte Carlo evaluation," *Physics in medicine and biology*, vol. 49, no. 19, p. 4593, 2004.

[176] P. Mollet, V. Keereman, P. Amy, K. A. Joel, and S. Vandenberghe, "Attenuation correction for TOF-PET with a limited number of stationary coincidence line-sources," in *PSMR, Abstracts*, 2013.

List of Publications

Journal papers

[1] Mollet, P., Keereman, V., Bini, J., Izquierdo, D., Fayad, Z., Vandenberghe, S. Improvement of attenuation correction in TOF-PET/MRI using a positron emitting source. *J Nucl Med* 55.2 (2014): 329-336.

[2] Keereman, V., Mollet, P., Berker, Y., Schulz, V., and Vandenberghe, S. Challenges and Current Methods for Attenuation Correction in PET/MR. *Magnetic Resonance Materials in Physics, Biology and Medicine* 26.1 (2013): 81-98.

[3] Clementel, E., Mollet, P., and Vandenberghe, S. Effect of Local TOF Kernel Miscalibrations on Contrast-noise in TOF PET. *Nuclear Science, IEEE Transactions on* 60.3 (2013): 1578-1588.

[4] Thoen, H., Keereman, V., Mollet, P., Van Holen, R., and Vandenberghe, S. Influence of Detector Pixel Size, TOF Resolution and DOI on Image Quality in MR-compatible Whole-body PET. *Phys Med Biol* 58 (2013): 6459-6479.

[5] Mollet, P., Keereman, V., Clementel, E., and Vandenberghe, S. Simultaneous MR-compatible Emission and Transmission Imaging for PET Using Time-of-flight Information. *Medical Imaging, IEEE Transactions on* 31.9 (2012): 1734-1742.

[6] Tsoumpas C, Buerger C, King AP, Mollet, P., Keereman, V., Vandenberghe, S., Schulz, V., Schleyer, P., Schaeffter, T., and Marsden PK. Fast Generation of 4D PET-MR Data from Real Dynamic MR Acquisitions. *Phys Med Biol* 56.20 (2011): 6597-6613.

[7] Keereman, V., Holen, RV., Mollet, P., and Vandenberghe S. The Effect of Errors in Segmented Attenuation Maps on PET Quantification.

Med Phys 38.11 (2011): 6010-6019.

Conference proceedings

[1] Mollet, P., Keereman, V., Perkins, A., Karp, J., and Vandenberghe, S. (2013). Attenuation correction for TOF-PET with a limited number of stationary coincidence line-sources. *PSMR, Abstracts*. Presented at the PSMR 2013; 4th Jülich MR-PET Workshop:

[2] Thoen, H., Keereman, V., Mollet, P., Van Holen, R., and Vandenberghe, S. (2013). Relative importance of transverse detector pixel size, DOI and TOF in future whole-body PET/MR systems. *PSMR, Abstracts*. Presented at the PSMR 2013?; 4th Jülich MR-PET Workshop:

[3] Vandenberghe, S., Thoen, H., Keereman, V., Karp, J., Schaeffter, T., Tsoumpas, C., King, A., et al. (2012). Optimization and development of high performance TOF PET-MR systems: the sublima project. *PSMR, Abstracts* (pp. 3334). Presented at the PSMR 2012.

[4] Keereman, V., Mollet, P., Izquierdo, D., Bini, J., Fayad, Z. A., and Vandenberghe, S. (2012). Design of a realistic antropomorphic PET-CT-MRI thorax phantom. *PSMR, Abstracts* (pp. 46-46). Presented at the PSMR 2012.

[5] Thoen, H., Keereman, V., Mollet, P., and Vandenberghe, S. (2012). Impact of the crystal pixel size on spatial resolution and contrast recovery in whole-body PET scanners. *J Nucl Med* (Vol. 53). Presented at the 59th Annual meeting of the Society of Nucelar Medicine (SNM 2012).

[6] Thoen, H., Mollet, P., Vandenberghe, S., and Keereman, V. (2012). Influence of PSF-modeling on spatial resolution and contrast recovery of a hybrid PET/MR system. *PSMR, Abstracts* (pp. 68-68). Presented at the PSMR 2012.

[7] Mollet, P., Keereman, V., Izquierdo, D., Fayad, Z. A., and Vandenberghe, S. (2012). Transmission-based attenuation correction in a sequential TOF-PET/MRI system. *PSMR, Abstracts* (pp. 102-102). Presented at the PSMR 2012.

[8] Mollet, P., Izquierdo, D., Keereman, V., Fayad, Z. A., and Vandenberghe, S. (2012). Reconstruction of simultaneous transmission and emission patient data in a sequential TOF-PET/MRI system. *J Nucl Med* (Vol. 53). Presented at the 2012 SNM Annual Meeting.

[9] Keereman, V., Van Holen, R., Vanhove, C., Mollet, P., and Vandenberghe, S. (2011). Absolute quantification for small-animal PET. *IEEE Nuclear Science Symposium Conference Record* (pp. 3715-3719). Presented at the 2011 IEEE Nuclear Science Symposium and Medical Imaging Conference (NSS/MIC 2011), Piscataway, NJ, USA: IEEE.

[10] Mollet, P., Keereman, V., and Vandenberghe, S. (2011). Experimental evaluation of simultaneous emission and transmission imaging using TOF information. *IEEE Nuclear Science Symposium Conference Record* (pp. 2976-2980). Presented at the IEEE Nuclear Science Symposium/Medical Imaging Conference (NSS/MIC)/18th International Workshop on Room-Temperature Semiconductor X-Ray and Gamma-Ray Detectors, New York, NY, USA: IEEE.

[11] Keereman, V., Mollet, P., Fierens, Y., Espana Palomares, S., and Vandenberghe, S. (2011). Design of a realistic PET-CT-MRI phantom. *IEEE Nuclear Science Symposium Conference Record* (pp. 31733177). Presented at the 2011 IEEE Nuclear Science Symposium and Medical Imaging Conference (NSS/MIC 2011), Piscataway, NJ, USA: IEEE.

[12] Thoen, H., Keereman, V., Mollet, P., and Vandenberghe, S. (2011). Determination of the resolution limit of a whole body PET scanner using monte carlo simulations. In M. Nyssen (Ed.), *Belgian day on Biomedical Engineering, 10th, Abstracts*. Presented at the 10th Belgian Day on Biomedical Engineering, Koninklijke Vlaamse Academie (KVAB).

[13] Mollet, P., Keereman, V., and Vandenberghe, S. (2010). Simultaneous emission and transmission imaging for PET-MRI using time-of-flight information. *J Nucl Med* (Vol. 51, pp. 35-35). Presented at the 57th Annual meeting of the Society of Nucelar Medicine (SNM 2010).

[14] Keereman, V., DAsseler, Y., Van Holen, R., Mollet, P., and Vandenberghe, S. (2010). The effect of inter-patient attenuation coefficient variability on segmented attenuation correction for PET. *J Nucl Med*

(Vol. 51, pp. 267-267). Presented at the 57th Annual meeting of the Society of Nucelar Medicine (SNM 2010).

[15] Mollet, P. (2010). Simultaneous emission and transmission imaging for PET-MRI using time-of-flight information. *UGent-FirW Doctoraatssymposium*, 11e (pp. 61-61). Presented at the 11e FirW PhD Symposium, Gent: Universiteit Gent. Faculteit Ingenieurswetenschappen.